Complex fluids and complex flows: applications to transfers in subsurface environments

Yves Méheust

Complex fluids and complex flows: applications to transfers in subsurface environments

Yves Méheust

Thèse d'Habilitation à Diriger des Recherches

Soutenue le 4 mars 2016 à l'*Université de Rennes 1* devant le jury composé de

Jesus Carrera Ramirez (DR CSIC, Barcelone, Espagne)	
Philippe Davy (DR CNRS, Géosciences Rennes)	
Renaud Delannay (Professeur, Univ. Rennes 1)	Président
Insa Neuweiler (Professeur, Univ. Hannover, Allemagne)	Rapporteur
Dani Or (Professeur, ETH Zürich, Suisse)	Rapporteur
André Revil (Professeur, Colorado School of Mines), USA	
Henri Van Damme (Professeur Invité, MIT, USA)	Rapporteur

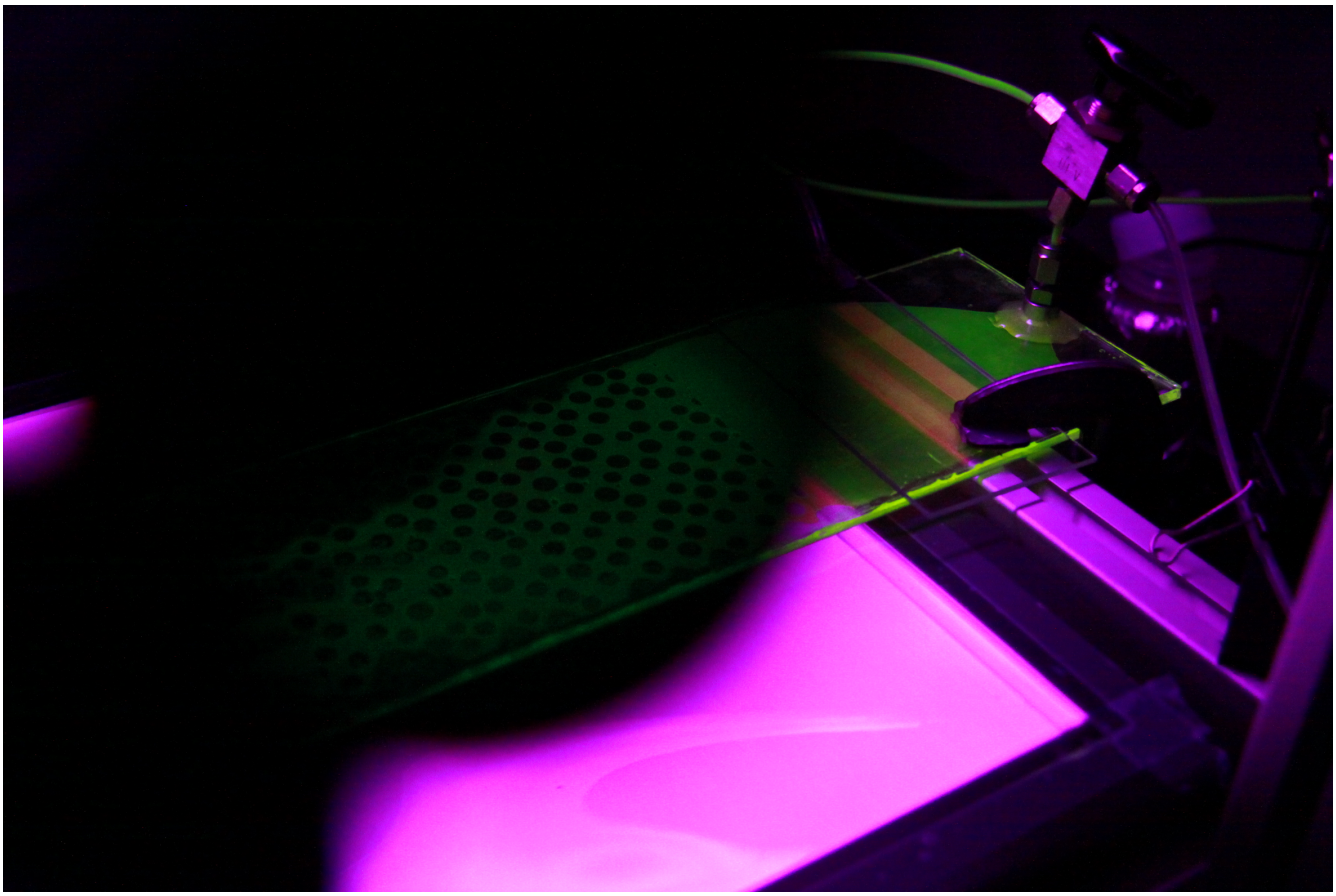

Contents

1 Introduction

This HdR ("Habilitation à Diriger des Recherches) thesis is about complex fluids and complex flows applied to subsurface environments. The term "complex fluid" is rather standard and denotes fluids that consist of a mixture of two phases, solid-liquid, solid-gas or liquid-liquid. In this case I consider suspensions of colloidal particles in a liquid; their self-organization resulting from their interactions in-between them and with the liquid (sections 4.3.3 and 4.3.4), or from an external excitation (section 4.3.5), have a strong influence on the mechanical properties of the mixture and its flow.

The term "complex flow" is to my knowledge no standard term. Here I mean by that a flow with a complex velocity field, in particular a wide distribution of velocities associated with strong spatial heterogeneities of the velocity field. As most of my work applies to subsurface processes, the Reynolds numbers involved are small, so that the flow field complexity can only result from the association of a geometric complexity of the flow boundary conditions and of small typical dimensions of the channels available for flow. It is the case when one considers the flow of a liquid in the pore space of a porous medium of even simple geometry (such as a bead pack), or inside a geological fracture. But it won't be the case as soon as one has averaged local flow properties over a representative elementary volume (REL) to work at the Darcy scale. This means that most of my work involving what I call complex flows has considered flow, transport and reaction at the pore scale or at the scale of a fracture. The flow field complexity at these small scales has consequences at larger scales, be it at the fracture scale on a fracture's transmissivity (section 4.1.2), on the Darcys-scale relationship between pressure drop and saturation during unstable unsaturated flows (section 4.1.3), on the mass of product resulting from the reaction of two solutes transported by the flow (section 4.2.3), on the transit time of a solute transported by an unsaturated flow (section 4.2.4), on the efficiency of mixing in a three-dimensional porous medium (section 4.2.6), on the efficiency of a foam-based soil remediation process (section 4.1.4), or on the Darcy-scale measurement of an unsaturated medium's electrical conductivity (section 6.4).

One characteristics of my research work, for someone whose objects of interest belong to the subsurface, is therefore that I do Fluid Mechanics (in a broad sense) at scales that most hydrogeologists would rate between incredibly small (the nm) and very small (the m). The other characteristics is that most of my work relies on laboratory experiments. For these experiments my approach has always been to build analogue models of a geological object, in order to gain as complete a characterization of the investigated system as possible. In this thesis I shall mainly discuss analog models for two-dimensional porous media, in which we can measure both the spatial distribution of the various solid and fluid phases, the velocity field of liquids, and the concentration field of transported solutes or of solutes resulting from an in situ reaction. Using transparent setups allows the use of optical methods to measure those quantities, even in three dimensions (section 4.2.6). The motivation for this approach is to be able to obtain results as quantitative as possible, if possible with a quantitative theoretical explanation/predictions of the measurements. This perhaps betrays a Physicist's background, but on the other hand I am very much aware of the necessity (and difficulty !) of choosing a suitable compromise between sufficient relevance to the real world object and capacity to infer quantitative findings. In particular, the analogue systems that I develop incorporate some level of disorder, if possible. This means that those systems, as natural systems, feature large fluctuations, which triggers the need for averaging, statistical analyses/models, upscaling schemes, and such.

The document contains a curriculum vitae, a complete list of publications (articles and conference abstracts), a summary of my research activities between 2003 and 2015, a short description of my teaching and editorial activities, a presentation of the prospects for my future research, and a short conclusion. Given the variety of the topics addressed, the environmental context is presented per topic within the sections devoted to the summary of past research and when necessary to the research prospects, rather than inside a general introduction.

2 Curriculum Vitae

REFERENCES:

Family name:	**Méheust**	**Position held:**	Maître de Conférence (Associate Professor)
Given names:	Yves Henri Jean-Pierre	**University**:	Université de Rennes 1, Rennes, France
Birthdate:	05/04/1973	**Institute:**	Géosciences Rennes, UMR CNRS 6118
Family status:	Married, three children (6.5 year, 5 year and 17 month old)		

Email address:	yves.meheust@univ-rennes1.fr
Phone number	02.23.23.62.51
Web page:	http://perso.univ-rennes1.fr/yves.meheust

SCIENTIFIC FIELDS:

Hydrogeology, Fluid Mechanics, Rock Physics, Soft Condensed Matter Physics.

RESEARCH TOPICS:

Flow of foams in porous media (2011-): The relationship between pressure drop and foam structure; local intermittency under stationary forcing; the control on the foam bubble size distribution by the medium's geometry – Laboratory experiments and theory. The motivation is soil remediation and EOR.
Solute transport in two-dimensional porous media (2011-): Influence of water saturation on transport and mixing in the unsaturated zone, influence of incomplete mixing at the pore scale on reactive transport, transport and mixing in 3D grains packs – Laboratory experiments, numerical simulations and theory.
Free surface flows of thixotropic clayey muds (2008-): Characterization of runout lengths and heights as a function of the initial water content and the inclination angle of the slope; phase diagram of the flow regimes as a function of water content and resting time prior to the avalanche – Laboratory experiments, rheology measurements and theory.
Solute transport in fractured media (2006-2012): Influence of buoyant coupling and aperture variability on solute transport in a horizontal fracture; solute exchange between a fracture and the porous matrix – Laboratory experiments and numerical simulations.
Physical properties of smectite clay minerals (2002-): Hydration, anomalous diffusion of humidity (vapor), electro-rheological suspensions, phase diagrams of clay saline suspensions – Experimental studies by X-ray scattering at wide and low angles (WAXS et SAXS), microscopy, small angle light scattering (SALS), rheometry, calorimetry.
Two-phase flows in two-dimensional porous media and fractures (2000-): Viscous fingering i 2D porous media, gravitational stabilization of interface instabilities in 2D porous media, influence of geometric disorder on the displacement process, trapping during drainage in a rough fracture – Laboratory experiments, numerical simulations and theory.
Flow in fractured media (1998-2001 and 2009-): Flow at the fracture scale (influence of fracture wall roughness, channeling and correlations, permeability anisotropy), influence of fracture wall roughness on the flow at the network scale – Laboratory experiments and numerical simulations.

TECHNICAL EXPERTISE:

My work is mostly based on laboratory experiments, with complementing numerical simulations and/or theoretical models. Some studies are solely based on numerical simulations and theory. My technical competences include flow and transport experiments in millifluidic setups, X-ray diffraction and small-angle X-ray scattering, rheometry measurements of complex fluids, image treatment, as well as numerical modeling of saturated Newtonian flows (finite differences and finite element).

EDUCATION:

1998 - 2002: PhD (Laboratoire de Géologie, ENS Paris) in Geophysics; highest distinction.
1997 - 1998: MSc in Statistical Physics and Nonlinear Phenomena (ENS-Lyon); ranking 5.
1996 - 1997: Admitted to the national competitive exam for recruiting senior teachers ("Agrégation de Sciences Physiques"), majoring in physics and minoring in chemistry; national ranking: 39.
1995 - 1996: Undergraduate studies at ENS-Lyon – BSc in fundamental Physics.
1992 - 1994: Admitted as a civil servant student at ENS-Lyon (Physics, Mathematics and Chemistry); national ranking: 33.

POSITIONS HELD AND FUNDING:

2014: Invited Researcher at University of Lausanne (UNIL), fondation Herbette**.**
May 2012: Invited Researcher, Center for Adv. Studies, Norwegian Academy of Science and Univ. of Oslo (4 weeks)
2010 - 2011: Research Scientist, CNRS (leave from University).
2006 - : Associate Professor, Université Rennes 1.
2004 - 2006: Research Scientist ("Forsker"), Norwegian Research Council (NRC).
2002 - 2004: Postdoc, Norwegian Research Council (NRC).
2001 - 2004: French senior teacher in physics (on leave), French Ministry for Higher Education.
2001 - 2002: Research and Teaching Assistant, École Normale Supérieure (Paris, France).
1998 - 2001: PhD Grant, French Ministry for Higher Education.
1998 - 2001: Assistant Lecturer, Université Paris-Sud (Orsay, France).
1994 - 1998: Civil servant student at École Normale Supérieure de Lyon, French Ministry for Higher Education.

PAST PROJECTS FUNDED:

2015 - 2020: Participant in the ERC (European Research Council) project "Reactive Fronts": 2 M€**.**
2015 - 2018: Participant in the ANR (French National Science Foundation) project "Subsurface mixing and reaction": 299 k€.
2014 - 2016: Participant in the NFR (Norsk Forsknigsraadet, Norway) Petromaks2 Institute-based Strategic Project "Particle stabilized emulsions for EOR": 406 k€.
2012 - 2014: PI of INSU/CNRS project "Dispersion and mixing in the unsaturated zone: a pore scale investigation": 40 k€.
2011 - 2014: Participant in CREATE project "Foam flow in porous media": 150 k€.
2009 - 2012: Participant in european INTERREG IV project CLIMAWAT: http://www.climawat.info.
2008 - 2012: Participant in Marie Curie initial training European network IMVUL "Towards improved groundwater vulnerability assessment": http://www.see.leeds.ac.uk/imvul/index.htm.
2009 - 2011: PI of PICS (CNRS) collaboration program involving 3 French laboratories and 3 Norwegian research institutes: "The Physics of geological complex systems": 25 k€.
2008 - 2010: Participant in ANR MOHINI: "Evaluation of crystalline aquifer vulnerability to climate change": 290 k€.
2009 - 2011: Allocation for equipment (Rennes Métropole): "Experimental and numerical modeling of subsurface transport à the scale of a geological fracture": 40 k€.
2008 - 2009: PI of an Aurora (Egide) collaboration program between Geosciences Rennes and the Phyics Institute at NTNU (Trondheim, Norway), "Water transport in clay dual-permeability systems": 20k€.

TEACHING:

Teaching responsabilities:
2006 - : In charge of 5 lecture units per year (on average); currently: *Continuum Mechanics*, *Environmental Risks*, *Flows in Fractured Media*, *Two-phase Flows in Porous Media*, *Surface Hydrology field trip*. All those lecture units belong to one of three MSc Programs at Université Rennes 1: Hydrogeology-Hydrobiogeochemistry-Hydropedology, Complex Systems, and Physics.

2008 - 2012: In charge of subprogram "Terre et Environnement" (Earth and Environment) of the M.Sc. program Systèmes Complexes Naturels et Industriels (SCNI) at Univ. Rennes 1. Cf. http://osur.univ-rennes1.fr/masterSCNI.
2006 - 2008: Member of the committee in charge of setting up the SCNI M.Sc. Program .

Teaching experience:
In addition to the lecture units above, I also lecture on *Transport processes in the subsurface* within the lecture unit *Hydrogeology*. In the past I have taught *Rock Physics* and *Dynamics of the atmosphere* in L3 at Univ. Rennes 1 (2006-2008), as well as *Geodynamics* at École Normale Supérieure (2001-2002), for M1 students, and Mathematics for Geosciences at Univ. Paris-Sud XI, for L1 and L2 (undergraduate) students (1998-2001).
I also hold the French *Aggrégation de Sciences Physiques* habilitation (obtained through a national competitive exam) for teaching undergraduate students.

SUPERVISION OF YOUNG RESEARCHERS:

Postdocs: Aditya Bandopadhyay (2016-2017), Baudouin Géraud (2013-2014 and 2016-2017), Joaquin Jimenez (2010-2014), Siân Jones (2011-2013).
PhD students: Antoine Hubert (2016-, co-supervisor), Benjamin Delfino (2015-, co-supervisor), Régis Turuban (2012-, main supervisor), Pietro de Anna (2010-2012, supervisor on experimental work), Jérémy Bouquain (2008-2012, co-sup.), Laure Michel (2006-2009, co-sup.)

EDITORIAL ACTIVITIES:

2011 - 2016: Associate Editor for the Vadose Zone Journal (two periods).
2003 - : Referee for various Earth Sciences (Water Resour. Res., Adv. Water Resour., J. Hydrol., Int. J. Rock Mech. Mining Sci., J. Contam. Hyd., Comput. Geology), Soil Sciences (Vadose Zone J.), Physics (Phys. Rev. Lett., Phys. Rev. E, European Phys. J., J. Appl. Cryst.), Physical Chemistry (Langmuir, Liquid Crystals), Engineering (Transp. Porous Media) and hard science (Proc. Royal Soc. A) journals.
Since 2012 I have written about one report per month.
2010 - : Referee for 6 research proposals (one for Univ. Europ. de Bretagne in 2010,one for The Petroleum Res. Fund of the Amer. Chem. Soc. In 2011, one for the Binational Agricultural Res. and Development Fund of the US and Israel in 2012, three for Région Ile-de-France in 2014.

ORGANIZATION OF SCIENTIFIC MEETINGS/SESSIONSS:

2016: Convener for Session "Transport Processes in Permeable Media" of the 15ème Journée de la Matière Condensée (JMC) (Bordeaux, France).
2015: Member of the Organization Committee for the 3rd Cargèse Summer School on Flow and Transport in Porous and Fractured Media (Cargèse, Corsica, France).
2013 - 2015: Main organizer of the Rennes Interdisciplinary School on Complex Systems (Rennes, France), held every year.
2009 - 2012: Member of the Organization Committee for the Rennes Interdisciplinary School on Complex Systems (Rennes, France).
2010: Member of the Organization Committee for the 2nd Cargèse Summer School on Flow and Transport in Porous and Fractured Media (Cargèse, Corsica, France).

SCIENTIFIC COMMUNICATION:

Invited talks at international Conferences and Workshops:

1. **May 9 - 12, 2016 (planned):** 8th International Conference on Porous Media (Interpore), in minisymposium "Multiphase flow and reactive transport at the pore scale: direct comparison of experiments and numerical simulations": "Mixing and reactive transport under unsaturated conditions: a pore scale study".
2. **December 14 - 18, 2015:** The AGU Fall Meeting, in session "Persistent Problems in Multiphase Flow and Transport in Porous Media: Modeling and Visualization from Pore to Laboratory and Field Scales": "Foam flows in analog porous media".

3. **July 20 - August 1, 2015:** Third Cargèse Summer School on Flow and Transport in Porous and Fractured Media: “Foam flows in porous media”.
4. **June 9 - 12, 2015:** Nordic Physics Days 2015: “Local rheology of aqueous foams in two-dimensional porous media”.
5. **April 12 - 17, 2015:** The EGU General Assembly, in session “Flow in transforming porous media”: “Local rheology of foams in porous media: intermittency and bubble fragmentation”.
6. **March 16 - 26, 2015:** The Geilo School 2015, Geilo (Norway) (http://www.ife.no/en/ife/departments/physics/the-geilo-school-2015): “The flow of an aqueous foam through a two-dimensional porous medium”.
7. **February 18 - 21, 2014:** 3rd International Workshop on Complex Physical Phenomena in Materials, PUC-Rio, Rio de Janeiro (Brazil): “The flow of foams in porous media: structure effects, elasticity effects, and bubble size selection”.
8. **July 15 - 16, 2013:** Workshop on Complex Systems, UnB, Brasilia (Brazil) : “Transport in a 2D porous medium: an experimental study” (http://trad.fis.unb.br/MiniWorkshopBrasiliaJuly_1516_2013_1.pdf).
9. **July 12, 2013:** Workshop on Complex drops and fluids, PUC-Rio, Rio de Janeiro (Brazil) : “The flow of foams in porous media”.
10. **July 07 - 11 2013**: XVth International Clay Conference, Rio de Janeiro (Brazil): “Self-organization in clay-based complex fluids”.
11. **May 22 - 24 2012:** Soft Matter Physics & Complex Flows, Svolvær, Lofoten (Norway) (http://www.ntnu.edu/physics/nordsoft/nordsoft2): “Flow in fractured geological media: the influence of fracture scale heterogeneity”.
12. **Jan. 31 - Feb. 3 2012:** Complex Physical Phenomena in Materials, 2nd Workshop, Porto de Galinhas (Brazil) (http://blogs.df.ufpe.br/˜complex2012/bookletpdg.pdf): “The viscous instability between two immiscible fluids in a disordered two-dimensional porous medium”.
13. **December 14 - 17 2010:** Complex Physical Phenomena in Materials, Recife (Brazil): “The rheology of quick clays - Implications for landslides of clayey soils”.
14. **December 7 - 10 2010:** CO2 and Fluids in Nanoscience, Brasilia (Brazil) (http://folk.ntnu.no/fossumj/workshops2010/workshopbrasiliadecember2010/WorkshopBrasilia.pdf)“Solute transport in a plane horizontal fracture : influence of density contrasts and fracture-matrix exchange”.
15. **August 16 - 28 2010:** Second Cargèse Summer School on Flow and Transport in Porous and Fractured Media: “Flow and Transport in Fractured Media”
16. **September 6 - 7 2008:** Fifth Nordic Workshop on Scattering from Soft Matter, Trondheim (Norway): “Utilizing WAXS to characterize the orientation distribution of a clay assemblies - Application to electro-rheological suspensions and weakly-hydrated samples”.
17. **September 16 - 18 2004:** Annual meeting of the Norwegian Physical Society (NFS), Wadahl (Norway): "Coupled structural and dynamical properties of nano-layered silicates studied by synchrotron X-Ray scattering techniques".

Contributed conference talks and posters:
122 published contributed abstracts since 1999 (not including those for the invited talks), 56 of which for contributions presented by me.
See the list of contributed abstracts in the publication list.

Invited seminars:
Seminars given in my home institute are not listed.

1. **May 2016 (planned):** Earth & Environmental Sciences, Los Alamos National Laboratory (LANL), “Foam flows in analog porous media”.
2. **December 2015:** Biological and Ecological Engineering, Oregon State University (OSU), “The flow of a foam in a two-dimensional porous medium”.
3. **December 2014:** Earth Systems Science Division, Pacific Northwest National Laboratory, Richland (USA), “Mixing and reaction kinetics in porous media: an experimental pore scale quantification”.
4. **November 2014:** GSE Faculty, UNIL, Lausanne (Switzerland), “The flow of an aqueous foam through a 2D porous medium”.

5. **May 2014:** Gulliver Laboratory, ESPCI, Paris (France), "Mixing and reaction kinetics in porous media: an experimental pore scale quantification".
6. **March 2014:** Physics of Geological Processes (PGP), University of Oslo, Oslo (Norway), "The flow of an aqueous foam through a 2D porous medium".
7. **November 2010:** Physics Institute, Univ. Rennes 1, Rennes, (France), "Micro- et mesoscopic self-organization of smectite clays minerals".
8. **March 2007:** Physics Institute, Univ. Rennes 1, Rennes, (France), "X-ray scattering techniques to study the micro- and meso-structure of clay under poly-crystalline and colloidal form".
9. **March 2006:** Geosciences Rennes, Univ. Rennes 1, Rennes, (France), "Flow through rocks: from the fracture scale to the pore scale".
10. **January 2006:** Department of Physics, Brazilian National University (UnB), Brasilia (Brazil), "Micro- and meso-scopic structural properties of nano-layered silicate systems in polycrystalline and colloidal form - Utilization of X-ray scattering" techniques".
11. **April 2004:** IUSTI (Department of Fluid Mechanics), Univ. Marseille, Marseille (France), "Viscous fingering in random porous media: an experimental study".
12. **March 2004:** Physics Department, University of Oslo, "Viscous fingering in porous media as a Dielectric Breakdown Model".
13. **November 2002:** Physics Department, University of Oslo, "Flow between two self-affine walls: an experimental and numerical study".

CITATION RECORD:

(ISIS Web of Science / *Google Scholar*, Feb. 6, 2016)
Publications: **33** / ***126*** Total citations: **583** / ***957*** Average citation per item: **17.6**7
h-index: **15** / ***19*** g-index: **23** / ***30*** i10-index: **18** / ***24***
2 manuscripts currently in press; 3 manuscripts about to be resubmitted; 2 preprints about to be submitted.

See the complete list of journal articles in the list of publications.

AWARDS:

2013 - 2016: Awarded the salary bonus for Excellence in Research (Prime d'Excellence), awarded to the best 15% of applicants.
May 2012: Invited Researcher at the Center of Advanced Studies of the Norwegian Academy of Science (1 month).
2010 - 2011: Awarded funding by CNRS for a one year leave from teaching ("détachement au CNRS").
2009 - 2013: Awarded the salary bonus for Doctoral Supervision and Research (Prime d'Encadrement Doctoral and Research).
2009: Prize for new faculty members (AIS Rennes Métropole): 40k€ to setup an experimental lab.
2006: The article "Intercalation-enhanced electric polarization and chain formation of nano-layered particles", by J.O. Fossum et al., Europhys. Lett (2006) was selected by European Synchrotron Radiation Facillity for the "ESRF Highlights" (best 10% among papers published in 2006 based on data obtained at the ESRF).
1999: EGS Student Travel Award for the EGS Spring Meeting.

LANGUAGE SKILLS:

French (mother tongue), English (read, written, spoken fluently), Brazilian Portuguese (read, written, spoken fluently), Norwegian (read, written, spoken), German (read, understood).

LEISURES

Reading, swimming, sailing, cross-country skiing.

February 6th, 2016.

3 Publication list

3.1 PhD Thesis

Y. Méheust, *Écoulements dans les Fractures Ouvertes* (partly in French), PhD thesis, Université Paris XI (Orsay), 2002.

3.2 Articles

3.2.1 Articles in international peer-reviewed journal

1 **Y. Méheust** and J. Schmittbuhl, Flow enhancement of a rough fracture, *Geophys. Res. Lett.*, **27**(18), 2989 (2000).

2 **Y. Méheust** and J. Schmittbuhl, Geometrical heterogeneities and permeability anisotropy of a rough fracture, *J. of Geophys. Res.*, **106**(B2), 2089 (2001).

3 **Y. Méheust**, G. Løvoll, K.-J. Maløy and J. Schmittbuhl, Interface scaling in a two-dimensional porous medium under combined viscous, gravity, and capillary effects, *Phys. Rev. E*, **66**, 051603 (2002).

4 **Y. Méheust** and J. Schmittbuhl, Scale effects related to flow in rough fractures, *Pure and Applied Geophysics*, **160**(5-6), 1023-1050 (2003).

5 G. Løvoll, **Y. Méheust**, R. Toussaint, J. Schmittbuhl and K.-J. Måløy, Growth activity during fingering in a porous Hele Shaw cell, *Phys. Rev. E*, **70**(2), 026301 (2004).

6 G. Løvoll, B. Sandnes, **Y. Méheust**, K. J. Måløy, J. O. Fossum, G. J. da Silva, M. S. P. Mundim, R. Droppa and D. M. Fonseca, Dynamics of the water intercalation front in a nano-layered synthetic silicate: A synchrotron X-ray scattering study, *Physica B*, **370**, 90-98 (2005).

7 R. Toussaint, G. Løvoll, **Y. Méheust**, K.-J. Måløy and J. Schmittbuhl, Influence of pore-scale disorder on viscous fingering during drainage, *Europhys. Lett.*, **71**(4), 583-589 (2005).

8 J. O. Fossum, **Y. Méheust**, K. Parmar, K. J. Måløy and D. de Miranda de Fonseca, Intercalation-enhanced particle polarization and chain formation of nano-layered clay platelets in oil, *Europhys. Lett.*, **74**(3), 438–444 (2006).

This article was selected for the **ESRF Highlights 2006** (i.e. the 10% best articles published in 2006 based on data collected at the European Synchrotron Radiation Facility).

9 **Y. Méheust**, K. D. Knudsen and J. O. Fossum, Inferring orientation distributions in anisotropic powders of nano-layered particles from a single two-dimensional WAXS image, *J. Applied. Cryst* **39**, 661–670 (2006).

10 K. P. S. Parmar, **Yves Méheust**, Børge Schjelderupsen, and J. O. Fossum, Electrorheological Suspensions of Laponite in Oil: Rheometry Studies, *Langmuir* **24**, 1814–1822 (2008)

11 D. d. M. Fonseca, **Y. Méheust**, J. O. Fossum, K. D. Knudsen and K. J. Måløy, Phase diagram of polydisperse Na-fluorohectorite–water suspensions: A synchrotron small-angle x-ray scattering study, *Phys. Rev. E* **79**, 021402 (2009)

12 H. Hemmen, N. I. Ringdal, E. N. De Azevedo, M. Engelsberg, E. L. Hansen, **Y. Méheust**, J. O. Fossum and K. D. Knudsen, The Isotropic-Nematic Interface in Suspensions of Na-Fluorohectorite Synthetic Clay, *Langmuir* **25**, 12507–12515 (2009).

13 A. Khaldoun , P. Moller , G. Wegdam , B. de Leeuw , **Y. Méheust**, J. O. Fossum and D Bonn, Quickclay: landslides of clayey soils, *Phys. Rev. Lett.* **103**, 188301 (2009).

14 H. Hemmen, L. R. Alme, J. O. Fossum, **Y. Méheust**, X-ray studies of interlayer water absorption and mesoporous water transport in a weakly hydrated clay, *Phys. Rev. E* **82**(3), 036315 (2010).

15 G. Løvoll, M. Jankov, K. J. Måløy, R. Toussaint, J. Schmittbuhl, G. Shäfer and **Y. Méheust**,, Influence of viscous fingering on dynamic saturation-pressure curves in porous media, *Transp. Por. Media* **86**(1), 335-354 (2011).

16 J. Bouquain, **Y. Méheust**, P. Davy, Horizontal pre-asymptotic solute transport in a model fracture with significant density contrasts, *J. Contaminant. Hyd.* **120**, 184-197 (2011).

17 H. Hemmen, L. R. Alme, J. O. Fossum, **Y. Méheust**, Erratum: X-ray studies of interlayer water absorption and mesoporous water transport in a weakly hydrated clay, *Phys. Rev. E* **83**(1), 019901 (2011).

18 **Y. Méheust**, K. P. S. Parmar, Børge Schjelderupsen and J. O. Fossum (2011), The rheology of electrorheological smectite clay-oil suspensions, *J. Rheol* **55**(4), 809-833.

19 R. Toussaint, K. J. Måløy, **Y. Meheust**, G. Løvoll, M. Jankov, G. Schäfer, J. Schmittbuhl (2012), Two-phase flow: structure, upscaling, and consequences for macroscopic transport properties, *Vadose Zone J.* **11**(3), DOI: 10.2136/vzj2011.0123.

20 J. Bouquain, **Y. Méheust**, D. Bolster, P. Davy (2012), Impact of inertial effects on solute dispersion in channels with a periodically-varying aperture, *Phys. Fluids* **24**(8), 083602.

21 J.-R. de Dreuzy, **Y. Méheust**, G Pichot (2012), Influence of fracture scale heterogeneity on the flow properties of three-dimensional Discrete Fracture Networks (DFN), *J. Geophys. Res.* **117**, B11207.

22 S. A. Jones, B. Dollet, I. Cantat, **Y. Méheust**, S. J. Cox (2013), Structure-dependent mobility of a dry aqueous foam flowing along two parallel channels, *Phys. Fluids* **25**(6), 063101.

23 P. de Anna, J. Jimenez-Martinez, H. Tabuteau, R. Turuban, T. Le Borgne, M. Derrien and **Y. Méheust** (2014), Mixing and reaction kinetics in porous media: an experimental pore scale quantification, *Environ. Sci. Tech.* **48**, 508-516.

24 D. Bolster, **Y. Méheust**, T. Le Borgne, J. Bouquain, P. Davy (2014), Modeling preasymptotic transport in flows with significant inertial and trapping effects – The importance of velocity correlations and a spatial Markov model, *Adv. Water Resour.* **70**, 89-103.

25 B. Dollet, S. A. Jones, **Y. Méheust**, I. Cantat (2014), Influence of the elastic deformation of a foam on its mobility in a model porous medium, *Phys. Rev. E* **90**, 023006.

26 A. Ferrari, J. Jimenez-Martinez, T. Le Borgne, **Y. Méheust**, and I. Lunati (2015), Challenges in modeling unstable two phase flow experiments in porous micromodels, *Water Resour. Res.* **51**(3), 1381-1400.

27 J. Jimenez-Martinez , P. de Anna , H. Tabuteau , R. Turuban , T. Le Borgne, and **Y. Méheust** (2015), Pore-scale mechanisms for the enhancement of mixing in unsaturated porous media and implications for chemical reactions, *Geophys. Rev. Lett.* **42**(13), 5316-5324.

28 B. Géraud, S. A. Jones, I. Cantat, B. Dollet and **Y. Méheust** (2015), The flow of a foam in a two-dimensional porous medium, Water Resour. Res., in press.

29 Yang Z., I. Neuweiler, **Y. Méheust**, F. Fagerlund and A. Niemi (2015), Fluid trapping during capillary displacement in fractures, Advances Water Resour., in press.

3.2.2 Conference proceedings in international peer-reviewed journals

30 G. Løvoll, **Y. Méheust**, K.-J. Måløy, E. Aker and J. Schmittbuhl, Competition of gravity, capillary fluctuations and dissipation forces during drainage in a two-dimensional porous medium, a pore-scale study, *Energy, the International Journal*, **30**(6), 861-872 (2005).

31 J. O. Fossum, E. Gudding, D. de M. Fonseca, **Y. Méheust**, E. Di Masi, T. Gog and C. Ventakaraman, Observations of orientational ordering in aqueous suspensions of a nano-layered silicate, *Energy, the International Journal*, **30**(6), 873-883 (2005).

32 **Y. Méheust**, B. Sandnes, G. Løvoll, K. J. Måløy, G. J. da Silva, M. S. P. Mundim, R. Droppa and D. d. M. Fonseca, Using synchrotron X-ray scattering to study the diffusion of water in a weakly-hydrated clay sample, *Clay Science*, **12** Supplement 2, 66-77 (2006).

33 **Y. Méheust**, S. Dagois-Bohy, K. D. Knudsen and J. O. Fossum, Mesoscopic structure of dry-pressed clay samples from small-angle X-ray scattering measurements, *J. Appl. Cryst.* **40**, s286–s291 (2007).

34 D. M. Fonseca, **Y. Méheust**, J. O. Fossum, K. D. Knudsen, K. J. Måløy and K. P. S. Parmar, Phase behavior of platelet-shaped nanosilicate colloids in saline solutions – a small-angle X-ray scattering study, *J. Appl. Cryst.* **40**, s292–s296 (2007).

35 Z. Rozynek, J. O. Fossum, K. D. Knudsen, **Y. Méheust**, B. Wang, M. Zhou, Dynamic Column Formation of Na-fluorohectorite Clay Particles : Wide Angle X-ray Scattering, rheometry and electrical current, *J. Phys. Condens. Mat.* **22**, 324104 (2010).

3.2.3 Preprints

36 **Y. Méheust**, A. Khaldoun, P. Møller, A. Fall, E. Hansen, G. Wegdam, B. Leeuw, J. O. Fossum, and D. Bonn (2016), Flow regimes of rehydrated quick clay – Implications for mudslides of clayey soils, to be resubmitted.

37 L. Michels, **Y. Méheust**, M. A. S. Altoé, E. C. dos Santos, H. Hemmen, R. Droppa, J. O. Fossum and G. J. da Silva (2016), Water vapor transport in porous swelling clays: Control of normal vs. anomalous

diffusion, to be resubmitted.

38 M. Dentz, I. Neuweiler, **Y. Méheust** and D. M. Tartakovsky (2016), Noise-Driven Interfaces and Their Macroscopic Representation, to be resubmitted.

39 J. Jiménez-Martínez, T. Le Borgne, H. Tabuteau and **Y. Méheust** (2016), Mixing dynamics in unsaturated porous media: Insights from a photo-bleaching pulse line injection, to be submitted.

40 Aditya Bandopadhyay, **Yves Méheust** and Tanguy Le Borgne (2016), Reaction-diffusion of a bimolecular system in a stretching lamella, to be submitted.

3.3 Conference abstracts

3.3.1 Abstracts of invited talks in international conferences/workshops

1 **Y. Méheust**, Coupled structural and dynamical properties of nano-layered silicates studied by synchrotron X-Ray scattering techniques, Annual meeting of the Norwegian Physical Society (NFS), Wadahl (Norway), September 16-18 2004.

2 **Y. Méheust**, J. O. Fossum, K. D. Knudsen, K. P. S. Parmar, K. J. Måløy and G. Helgesen : Utilizing WAXS to characterize the orientation distribution of a clay assemblies – Application to electrorheological suspensions and weakly-hydrated samples, Fifth Nordic Workshop on Scattering from Soft Matter, Trondheim (Norway), 12. September 6 - 7 2008.

3 **Y. Méheust** and P. Davy, Flow and Transport in Fractured Media, Second Cargèse Summer School on Flow and Transport in Porous and Fractured Media, 11. August 16 – 28 2010.

4 **Y. Méheust**, J. Bouquain, L. Michel, J. de Bremond d'Ars and P. Davy, Solute transport in a plane horizontal fracture : influence of density contrasts and fracture-matrix exchange, CO2 and Fluids in Nanoscience, Brasilia (Brazil), December 7-10 2010.

5 **Y. Méheust**, A. Khaldoun, P. Møller, A. Fall, G. Wegdam, B. Leeuw, J. O. Fossum and D. Bonn, The rheology of quick clays – Implications for landslides of clayey soils, Complex Physical Phenomena in Materials, Recife (Brazil), December 14-17 2010.

6 **Y. Méheust**, G. Løvoll, R. Toussaint, K. J. Måløy (2), J Schmittbuhl, The viscous instability between two immiscible fluids in a disordered two-dimensional porous medium, Complex Physical Phenomena in Materials, 2nd Workshop, Porto de Galinhas (Brazil), 8. Jan. 31-Feb. 3, 2012.

7 **Y. Méheust**, J.-R. de Dreuzy and G. Pichot, Flow in fractured geological media: the influence of fracture scale heterogeneity, Soft Matter Physics & Complex Flows, Svolvær, Lofoten (Norway), May 22-24 2012.

8 **Y. Méheust**, K. P. S. Parmar, D. de Miranda Fonseca, H. Hemmen, K. D. Knudsen, K. J. Måløy, J. O. Fossum, Self-organization in clay-based complex fluids, XVth International Clay Conference, Rio de Janeiro (Brazil), July 07-11 2013.

9 P. de Anna, J. Jimenez-Martinez, H. Tabuteau, R. Turuban, T. Le Borgne, M. Derrien and **Y. Méheust**, The flow of foams in porous media, Workshop on Complex drops and fluids, PUC-Rio, Rio de Janeiro (Brazil), July 12, 2013.

10 P. de Anna, J. Jimenez-Martinez, H. Tabuteau, R. Turuban, T. Le Borgne, M. Derrien and **Y. Méheust**, Transport in a 2D porous medium: an experimental study, Workshop on Complex Systems, UnB, Brasilia (Brazil), July 15-16, 2013.

11 B. Géraud, S. A. Jones, B. Dollet, I. Cantat, **Y. Méheust**, The flow of foams in porous media: structure effects, elasticity effects, and bubble size selection, 3rd International Workshop on Complex Physical Phenomena in Materials, PUC-Rio, Rio de Janeiro (Brazil), 3. February 18-21, 2014.

12 B. Géraud, S. A. Jones, B. Dollet, I. Cantat, **Y. Méheust**, The flow of an aqueous foam through a two-dimensional porous medium, The Geilo School 2015, Geilo (Norway), March 16-26, 2015.

13 B. Géraud, S. A. Jones, B. Dollet, I. Cantat, **Y. Méheust**, Local rheology of foams in porous media: intermittency and bubble fragmentation, The EGU General Assembly, in session "Flow in transforming porous media", Vienna (Austria), April 12-17, 2015.

14 **Y. Méheust**, B. Géraud, S. A. Jones, B. Dollet, I. Cantat, Local rheology of aqueous foams in two-dimensional porous media, Nordic Physics Days 2015, Trondheim (Norway), June 9-12, 2015.

15 **Y. Méheust**, "Foam flows in porous media", Third Cargèse Summer School on Flow and Transport in Porous and Fractured Media, Cargèse (France), July 20-31, 2015.

16 **Y. Méheust**, B. Géraud, S. A. Jones, B. Dollet and I. Cantat, Foam flows in analog porous media, The AGU Fall Meeting, in session "Persistent Problems in Multiphase Flow and Transport in Porous Media: Modeling and Visualization from Pore to Laboratory and Field Scales", San Francisco, December 14-18, 2015.

17 (planned) J. Jimenez-Martinez , P. de Anna , H. Tabuteau , R. Turuban , T. Le Borgne, and **Y. Méheust**, Mixing and reactive transport under unsaturated conditions: a pore scale study, 8th International Conference on Porous Media (Interpore), in minisymposium "Multiphase flow and reactive transport at the pore scale: direct comparison of experiments and numerical simulations", Cincinatti (USA), May 9-12, 2016.

3.3.2 Abstracts of contributed talks and posters in international conferences/workshops, presented by me

18 **Y. Méheust** and J. Schmittbuhl, Fluid flow through rough fractures – spatial correlations, channeling, and permeability, *European Geophysical Society (EGS) XXIV General Assembly*, La Haye (Pays Bas), 19-23 april 1999: talk.
This abstract got me a **Young Scientist Travel Award** for the conference.

19 **Y. Méheust** and J. Schmittbuhl, Écoulement dans une fracture rugueuse – corrélations spatiales and chenalisation, *réunion du GdR "Milieux Divisés"*, Carry-le-Rouet (France), may 1999: talk.

20 **Y. Méheust** and J. Schmittbuhl, Influence of fracture roughness on the hydraulic anisotropy of rough fractures, *1st Euroconference on Rock Physics and Rock Mechanics*, Edimburgh (Great-Britain), 1999: poster.

21 **Y. Méheust** and J. Schmittbuhl, Anisotropy of crack roughness, *EGS XXV General Assembly*, Nice (France), 25-29 april 2000: talk.

22 **Y. Méheust** and J. Schmittbuhl, Écoulement dans une fracture rugueuse, *Réunion du PNRH*, 2000: poster.

23 **Y. Méheust** and J. Schmittbuhl, Geometrical heterogeneities and permeability anisotropy of rough fractures, *2nd Euroconference on Rock Physics and Rock Mechanics*, Bonn (Allemagne), 2000: talk.

24 **Y. Méheust**, G. Løvoll, K.-J. Måløy and J. Schmittbuhl, Competition between viscous and gravitational effects during drainage in a 2D porous medium, *EGS XXVI General Assembly*, Nice (France), 25-30 march 2001: talk.

25 **Y. Méheust** and J. Schmittbuhl, Scale effects related to flow in rough fractures, *AGU Fall Meeting*, San Francisco (USA), november 2001: poster.

26 **Y. Méheust**, G. Løvoll, K. J. Måløy and J. Schmittbuhl, Gravity stabilized viscous fingering, *AGU Fall Meeting*, San Francisco (USA), november 2001: poster.

27 J. O. Fossum, K. P. S. Parmar., **Y. Méheust**, K. D. Knudsen, K. J. Måløy and G. J. da Silva, Ordering of nano-layered clay particles in an electric field, *SNBL Highlights Conference*, Tromsø (Norway), june 2003: poster.

28 G. Løvoll, **Y. Méheust**, R. Toussaint, K. J. Måløy and J. Schmittbuhl, Growth activity – From capillary to viscous fingering, *Annual Meeting of the Complex Systems and Soft Materials group*, Lillehammer (Norway), 3-5 february 2004: talk.

29 **Y. Méheust**, J. O. Fossum, K. Knudsen, K. J. Måløy and G. Helgesen, Water intercalation in a dehydrated fluorohectorite under controlled temperature and humidity - A synchrotron study, *Annual Meeting of the Complex Systems and Soft Materials group*, Lillehammer (Norway), 3-5 february 2004: talk.

30 **Y. Méheust**, J. O. Fossum, K. J. Måløy and G. Helgesen, Water intercalation in a dehydrated fluorohectorite under controlled temperature and humidity - A synchrotron study, *Annual Meeting of the Complex Systems and Soft Materials group*, Lillehammer (Norway), 3-5 february 2004: talk.

31 **Y. Méheust**, J. O. Fossum, K. D. Knudsen, K. J. Måløy, G. Helgesen, G. J. da Silva, and E. DiMasi, Complex phenomena in clays I – Water intercalation, *Nanomat Conference*, Oslo (Norway), 3-4 june 2004: poster.

32 G. Løvoll, B. Sandnes, **Y. Méheust**, K. J. Måløy, J. O. Fossum and G. J. da Silva, Complex phenomena in clays II – Nanodiffusion, *Nanomat Conference*, Oslo (Norway), 3-4 june 2004: poster.

33 D. d. M. Fonseca, **Y. Méheust**, J. O. Fossum, K. Parmar, K. D. Knudsen and K. J. Måløy, Complex phenomena in clays III – Phase characterization of suspensions in saline solutions, *Nanomat Conference*, Oslo (Norway), 3-4 june 2004: poster.

34 K. P. S. Parmar, **Y. Méheust**, J. O. Fossum, K. D. Knudsen and K. J. Måløy, Complex phenomena in

clays IV – Electrorheology, *Nanomat Conference*, Oslo (Norway), 3-4 june 2004: poster.

35 **Y. Méheust**, R. Toussaint, G. Løvoll, K. J. Måløy and J. Schmittbuhl, Viscous fingering in a random porous medium, *Complex Motions in Fluids*, Humlebæk (Danemark), 8-14 august 2004: talk.

36 **Y. Méheust**, Structural and dynamic properties of clays studied by synchrotron X-ray scattering techniques, *Réunion annuelle de la NFS (Norwegian Physics Union*, Wadahl (Norway), 16-18 september 2004: invited talk.

37 **Y. Méheust**, K. P. S. Parmar, J. O. Fossum, K. D. Knudsen, K. J. Måløy and D. d. M. Fonseca, Intercalation-enhanced electric polarization and chain formation of nano-layered particles, *NATO Advanced Studies Institute*, Geilo (Norway), 11-21 april 2005: poster.

38 **Y. Méheust**, J. O. Fossum, K. D. Knudsen, K. J. Måløy, and G. Helgesen, Mesostructural changes in a weakly hydrated smectite clay during hydration transitions, *Nanomat Conference*, Trondheim (Norway), 2-3 june 2005: poster.

39 **Y. Méheust**, K. P. S. Parmar, J. O. Fossum, K.-J. Måløy and D. de Miranda de Fonseca, Intercalation-enhanced electric polarization and chain formation of nano-layered clay platelets in oil, *Nanomat Conference*, Trondheim (Norway), 2-3 june 2005: poster.

40 **Y. Méheust**, J. O. Fossum, K. D. Knudsen, K. J. Måløy, and G. Helgesen, Mesostructural changes in a weakly hydrated smectite clay during hydration transitions, *13th International Conference on Clay*, Tokyo (Japan), 21-27 august 2005: talk.

41 K. J. Måløy, G. Løvoll, B. Sandnes, J. O. Fossum, D. d. M. Fonseca, **Y. Méheust**, G. J. da Silva, M. S. P. Mundim, and R. Droppa, Dynamics of a water intercalation front in a nano-layered smectite clay, studied by synchrotron X-ray scattering, *13th International Conference on Clay*, Tokyo (Japan), 21-27 august 2005: talk.

42 **Y. Méheust**, K. P. S. Parmar, J. O. Fossum, K. D. Knudsen, K. J. Måløy, and D. M. Fonseca, Polarization and aggregation of clay particles suspended in oil – A study using X-ray scattering, Bridging Clays, Ile d'Oléron (France), 3-7 june 2006: talk.

43 **Y. Méheust**, G. J. da Silva, J. O. Fossum, K. J. Måløy and K. D. Knudsen, Hydration transitions in a weakly-hydrated fluorohectorite – A Hendricks-Teller analysis, Bridging Clays, Ile d'Oléron (France), 3-7 june 2006: talk.

44 **Y. Méheust**, S. Dagois-Bohy, K. D. Knudsen and J. O. Fossum, Mesoscopic structure of dried-pressed clay samples from SAXS measurements, XIII International Conference on Small-Angle Scattering, Kyoto (Japan), 9-13 July 2006: poster.

45 K. P. S. Parmar, **Y. Méheust**, J. O. Fossum, K. D. Knudsen, K. J. Måløy and D. M. Fonseca, A small angle scattering study of the porous space inside bundles of polarized clay particles, XIII International Conference on Small-Angle Scattering, Kyoto (Japan), 9-13 July 2006: poster.

46 **Y. Méheust**, N. Le Gal, J.-P. Caudal, J. de Bremond d'Ars, Using optical index matching to visualize solute transport and perform particle tracking in a synthetic porous medium, AGU General Assembly 2007 Fall Meeting, San Francisco (USA), 10-14 décembre 2007: poster.

47 L. Michel, **Y. Méheust**, J.-P. Caudal, J. de Bremond d'Ars, J.-R. de Dreuzy, Laboratory experiment of solute transport in a fracture with one porous wall: fracture-matrix interaction, AGU Fall Meeting 2007, San Francisco (USA), 10-14 décembre 2007: talk.

48 L. Michel, **Y. Méheust**, J. Bouquain, J.-P. Caudal, J. de Bremond d'Ars, J.-R. de Dreuzy, P. Davy, Solute exchange between a fracture and the surrounding porous matrix – an analog experiment, EGU General Assembly 2008, Vienne (Autriche), 13-18 April 2008: talk.

49 **Y. Méheust**, N. Le Gal, J.-P. Caudal, J. de Bremond d'Ars, Visualization of solute transport and particle tracking in a three-dimensional porous medium, using optical index matching, EGU General Assembly 2008, Vienne (Autriche), 13-18 April 2008: poster.

50 L. Ramstad Alme, J. O. Fossum, **Y. Méheust**, Transport of water in a weakly-hydrated model clay soil, EGU General Assembly 2008, Vienne (Autriche), 13-18 April 2008: poster.

51 **Y. Méheust**, J. O. Fossum, K. D. Knudsen, K. J. Måløy, G. Helgesen, Mesoscopic changes of a model clay soil due to the microscopic swelling of its crystallites, EGU General Assembly 2008, Vienne (Autriche), 13-18 April 2008: talk.

52 L. Michel, **Y. Méheust**, J. Bouquain, J.-P. Caudal, J. de Bremond d'Ars, J.-R. De Dreuzy and P. Davy, Solute transport in a single fracture with porous walls, Gordon Conference on Flow and Transport in

Permeable Media, Oxford (Royaume-Uni), 13-18 July 2008: poster.

53 L. Michel, **Y. Méheust**, J. Bouquain, J.-P. Caudal, J. de Bremond d'Ars, J.-R. De Dreuzy and P. Davy, Solute exchange at the fracture-matrix wall involving significant buoyancy effects – an analog experiment, AGU Fall Meeting 2008, 15-19 décembre 2008: poster.

54 J. Bouquain, L. Michel, **Y. Méheust**, J.-P. Caudal, T. Le Borgne, J. de Bremond d'Ars, Solute Transport Through a Smooth Fracture in the Pre-asymptotic Taylor Regime, AGU Fall Meeting 2008, 15-19 décembre 2008: poster.

55 H. Hemmen, L. Ramstad Alme, J. O. Fossum and **Y. Meheust**, Space and time resolved X-ray diffraction as a tool to image mesoporous transport of water in a weakly-hydrated swelling clay, AGU Fall Meeting, San Francisco (USA), décembre 2010: poster.

56 **Y. Méheust**, J. Bouquain, L. Michel, J. de Bremond d'Ars, and P. Davy, Solute transport in a plane horizontal fracture: influence of density contrasts and fracture-matrix exchange, EGU General Assembly 2011, Vienne (Autriche), April 2011: talk.

57 A. Khaldoun, **Y. Méheust**, P. Møller, A. Fall, G. Wegdam, B. de Leeuw, J. F., and D. Bonn, Landslides of clayey soils: a dramatic avalanche behavior, EGU General Assembly 2011, Vienne (Autriche), April 2011: talk.

58 H. Hemmen, L. Ramstad Alme, J. O. Fossum, **Y. Méheust**, Diffusion of water in the mesoporosity of a dry clay: an experimental study using space and time resolved X-ray diffraction, EGU General Assembly 2011, Vienne (Autriche), April 2011: talk.

59 **Y. Méheust**, J-R. De Dreuzy, G. Pichot, Influence of fracture scale heterogeneity on the flow properties of 3D Discrete Fracture Networks (DFNs), AGU Fall Meeting 2011, San Francisco (USA), December 2011: talk.

60 S. Jones, I. Cantat, B. Dollet, and **Y. Méheust**, Flow of a two-dimensional aqueous foam in two parallel channels, EGU General Assembly, 22 – 27 April 2012: talk.

61 H. Hemmen, **Y. Méheust**, L. R. Alme, J. O. Fossum, X-ray studies of interlayer water absorption and mesoporous water transport in a weakly hydrated clay, EGU General Assembly, 22 – 27 April 2012: talk.

62 **Y. Méheust**, S. Jones, B. Dollet, S. Cox, I. Cantat, Flow of an aqueous foam through a two-dimensional porous medium: a pore scale investigation, AGU Fall Meeting, December 3-7 2012: talk.

63 R. Turuban, P. de Anna, J. Jimenez-Martinez, H. Tabuteau, T. Le Borgne and **Y. Méheust**, Measuring the heterogeneity of the velocity field in a 2D porous medium, AGU Fall Meeting, December 3-7 2012: poster.

64 **Y. Méheust**, A. Khaldoun, P. Møller, A. Fall, E. L. Hansen, G. Wegdam, B. de Leeuw, J. O. Fossum and D. Bonn, Mudslides of clayey soils, 15th International Clay Conference, July 7-11 2013, Rio de Janeiro (Brazil): talk.

65 **Y. Méheust**, J-R. De Dreuzy, G. Pichot, Flow in fractured geological media: the influence of fracture scale heterogeneity, AGU Fall Meeting, December 9-13 2014, San Francisco (USA): talk.

66 B. Dollet, S. A. Jones, B. Géraud, **Y. Méheust**, S. J. Cox and I. Cantat, The flow of an aqueous foam through a two-dimensional porous medium, AGU Fall Meeting, December 9-13 2014, San Francisco (USA): poster.

67 **Y. Méheust**, R. Turuban, J. Jimenez-Martinez, P. de Anna, H. Tabuteau and T. Le Borgne, Experimental investigation of the link between pore scale velocities, transport and reactivity in porous media, AGU Fall Meeting, December 9-13, San Francisco (USA): talk.

68 A. Ferrari, J. Jimenez-Martinez, T. Le Borgne, **Y. Méheust** and I. Lunati, Challenges in modeling unstable two-phase flow experiments in porous micromodels, AGU Fall Meeting, December 15-19 2014, San Francisco (USA): talk.

69 B. Géraud, S. A. Jones, B. Dollet, I. Cantat and **Y. Méheus**t, Foam flows in 2D porous media: intermittency and bubble fragmentation, AGU Fall Meeting, December 15-19 2014, San Francisco (USA): talk.

70 J. Jimenez-Martinez , P. de Anna , H. Tabuteau , R. Turuban , T. Le Borgne, and **Y. Méheust**, Impact of saturation on dispersion and mixing in porous media, 7th International Conference on Porous Media (Interpore), May 18-21 2015, Padova (Italy): talk.

71 B. Géraud, S. A. Jones, B. Dollet, I. Cantat and **Y. Méheus**t, The local rheology of foam flows in two-dimensional porous media: intermittency and bubble fragmentation, 7th International Conference on

Porous Media (Interpore), May 18-21 2015, Padova (Italy): poster.

72 **Y. Méheust**, R. Toussaint, G. Løvoll, and K. J. Måløy, Saffman-Taylor fingering: why it is not a proper upscaled model of viscous fingering in an (even two-dimensional) random porous medium, AGU Fall Meeting, December 14-18 2015, San Francisco (USA): poster.

73 L. Michels, **Y. Méheust**, M. A. S. Altoé, H. Hemmen, R. Droppa Jr., G. Grassi, J. O.Fossum, G. J. da Silva, Vapor transport in a porous smectite clay: from normal to anomalous diffusion, AGU Fall Meeting, December 14-18 2015, San Francisco (USA): poster.

3.3.3 Abstracts of contributed talks and posters in international conferences/workshops, presented by a co-author

The name of the presenter appears in bold font.

74 **K. P. S. Parmar**, J. O. Fossum, R. K. Sangar and Y. Méheust, Electro-rheological systems of synthetic nano-layered silicate platelets particles, *NATO Advanced Studies Institute*, Geilo (Norway), 2003: poster.

75 **G. Løvoll**, Y. Méheust, K.-J. Måløy and J. Schmittbuhl, Competition of gravity, capillary fluctuations and dissipation forces during drainage in a two-dimensional porous medium, *International Conference on "Transport, dissipation, and turbulence"*, Trondheim (Norway), 2003: talk.

76 **D. d. M. Fonseca**, J. O. Fossum, and Y. Méheust, Experimental studies of transport mechanisms and Onsager nematic ordering of platelet nano-layered silicates, *International Conference on "Transport, dissipation, and turbulence"*, Trondheim (Norway), 2003: poster.

77 **K. P. S. Parmar**, J. O. Fossum, Y. Méheust and R. K. Sangar, Transport properties and structure of electrorheological systems of synthetic nano-layered silicate platelet particles, *International Conference on "Transport, dissipation, and turbulence"*, Trondheim (Norway), 2003: poster.

78 **J. O. Fossum**, D. de Miranda Fonseca, Y. Méheust, K. J. Måløy and K. D. Knudsen, Visual Observations and Synchrotron X-Ray Scattering Studies of Na-Fluorohectorite Smectite Clay Suspensions, *Euroclay 2003*, Modena (Italy), 2003: poster.

79 **J. O. Fossum**, K. P. S. Parmar, Y. Méheust, D. de Miranda Fonseca, K. D. Knudsen and K. J. Måløy, Electrorheological Chain Formation in Systems of Nanolayered Silicates, Annual APS March Meeting, Montréal (Canada), 2004: poster.

80 **D. d. M. Fonseca**, J.O. Fossum, Y. Méheust, K. Parmar, K.D. Knudsen and K.J. Måløy, Synchrotron small Angle X-ray scattering (SAXS) studies of a nanolayered silicate: A New insight in the Phase Diagram of Na-Fluorohectorite in NaCl Aqueous Suspensions, *Réunion annuelle de la NFS (Norsk Fysikk Selskap)*, Wadahl (Norway), 16-18 september 2004: poster.

81 **K. P.S. Parmar**, J. O. Fossum, Y. Méheust, K. D. Knudsen and K. J. Måløy, Synchrotron X-ray scattering studies of electrorheological fluids of nano-layered silicate particles, *Réunion annuelle de la NFS (Norsk Fysikk Selskap)*, Wadahl (Norway), 16-18 september 2004: poster.

82 **K. P. S. Parmar**, Y. Méheust, J. O. Fossum, K. D. Knudsen and K.-J- Måløy, A small Angle Scattering study of the porous space inside electrorheological bundles of platelet-shaped clay particles, *Nanomat Conference*, Trondheim (Norway), 2-3 june 2005: poster.

83 **J. O. Fossum**, Y. Méheust, K. P. S. Parmar, K.-J. Måløy and D. de Miranda de Fonseca, Intercalation-enhanced electric polarization and chain formation of nano-layered clay platelets in oil, *13th International Conference on Clay*, Tokyo (Japan), august 21-27, 2005: talk.

84 D. M. Fonseca, Y. Méheust, **J. O. Fossum**, K. D. Knudsen, K. J. Måløy and K. P. S. Parmar, Phase separation and orientational ordering in aqueous suspensions of fluorohectorite clay, Bridging Clays, Ile d'Oléron (France), 3-7 june 2006: talk.

85 **K. P. S. Parmar**, Y. Méheust and J. O. Fossum, Electro-rheology of smectite clay suspensions submitted to a strong electric field, Bridging Clays, Ile d'Oléron (France), 3-7 june 2006: talk.

86 D. M. Fonseca, Y. Méheust, **J. O. Fossum**, K. D. Knudsen, K. J. Måløy and K. P. S. Parmar, Nematic ordering of platelet-shaped nanosilicate colloids in saline solutions, XIII International Conference on Small-Angle Scattering, Kyoto (Japan), 9-13 july 2006: poster.

87 **J. O. Fossum**, Y. Méheust, K. Parmar, K. J. Måløy and D. de Miranda de Fonseca, Intercalation-enhanced particle polarization and chain formation of nano-layered clay platelets in oil, Fourth Scandinavian Workshop on Scattering from Soft Matter, Lund (Suède), 1-2 February 2007: talk.

88 **L. Michel**, J.-P. Caudal, J. de Bremond d'Ars, Y. Méheust, Laboratory experiment of solute transport

in a fracture with one porous wall, EGU General Assembly 2007, Vienne (Autriche), 15-20 April 2007: poster.

89 H., N.I. Ringdal, E.N de Azevedo, E. L. Hansen, Y. Méheust, J.O. Fossum, M. Engelsberg, and K.D. Knudsen, The Isotropic-Nematic Interface in Suspensions of Na-Fluorohectorite Synthetic Clay, MRS Fall Meeting, 1-5 décembre 2008, Boston, MA, (USA): poster.

90 **J. O. Fossum**, Y. Meheust, B.-X. Wang, K. P.S. Parmar,B. Schelderupsen, Z. Rozynek, M. Zhou, Electrorheology of Clay Particles suspended in Oil, IV Brazilian Conference on Rheology, Rio de Janeiro (Brésil) 2-4 July 2008: talk.

91 L. Ramstad Alme, **J. O. Fossum**, Y. Méheust, Water vapor transport in, and hydration of, a model nano-clay: X-ray studies, VII Encontro da SBPMat (Sociedade Brasileira de Pesquisa em Materiais), Guaruja-SP (Brésil), 28 septembre - 2 octobre 2008: talk.

92 **H. Hemmen**, N. Ringdal, E. N. De Azevedo, E. Lindbo, H. M. Häger, Y. Méheust, J. O. Fossum, M. Engelsberg and K. D. Knudsen, Isotropic-Nematic Interfaces in Suspensions of Na-Fluorohectorite Synthetic Clay, 6th Nordic Workshop on Scattering from Soft Matter, Århus, Denmark, 28-29 January 2009: poster.

93 **E. L. Hansen**, E. N. de Azevedo, Y. Méheust, H. Hemmen, B. M. Kjelling, J. O. Fossum, D. Y. Noh, C. Kim, S. Marathe, I. W. Cho, M. Engelsberg, Liquid Crystalline Ordering In Gravitationally Settled And Evaporating Aqueous Dispersions Of Clay Nanoplatelets Studied By Small Angle X-Ray Scattering, 6th Nordic Workshop on Scattering from Soft Matter, Århus, Denmark, 28-29 January 2009: poster.

94 **J. Bouquain**, L. Michel, Y. Méheust, J.-P. Caudal, T. Le Borgne, J. de Bremond d'Ars, and P. Davy, Solute transport through a fracture with significant density effects and short of the asymptotic Taylor regime, EGU General Assembly 2009, 19-24 April 2009: poster.

95 **D. M. Fonseca**, Y. Meheust, K. D. Knudsen and J. O. Fossum, Phase diagram of polydisperse Na-fluorohectorite-water suspensions: A synchrotron small-angle X-ray scattering stud, 14th International Clay Conference, Castellaneta M., Italy, 14-20 June 2009: poster.

96 **H. Hemmen**, N. Ringdal, E. N. De Azevedo, E. Lindbo, H. M. Häger, Y. Méheust, J. O. Fossum, M. Engelsberg and K. D. Knudsen, Isotropic-Nematic Interfaces in Suspensions of Na-Fluorohectorite Synthetic Clay, 14th International Clay Conference, Castellaneta M., Italy, 14-20 June 2009: talk.

97 **E. L. Hansen**, N. I. Ringdal, B. M. Kjelling, H. Hemmen, J. O. Fossum, E. N. de Azevedo, M. Engelsberg, Y. Méheust, C. Kim, S. Marathe, I. W. Cho, D. Y. Noh, Highly Ordered Nematic Phases and Emerging Positional Ordering in Aqueous Dispersions of Na-Fluorohectorite, Castellaneta M., Italy, 14-20 June 2009: talk.

98 Y. Méheust, K. Parmar, B. Schjelderupsen and **Jon O. Fossum**, The Electro-Rheology of Suspensions of Synthetic Smectites in Oil, 14th International Clay Conference, Castellaneta M., Italy, 14-20 June 2009: talk.

99 A. Khaldoun, **Y. Méheust**, P. Møller, A. Fall, G. Wegdam, B. de Leeuw, J. F., and D. Bonn, Quickclay and Landslides of Clayey Soils, 14th International Clay Conference, Castellaneta M., Italy, 14-20 June 2009: talk.

100 L. Ramstad Alme, Y. Méheust, and **J. O. Fossum**, Humidity Transport in Quasi One-Dimensional Na-Fluorohectorite Powders, 4th International Clay Conference, Castellaneta M., Italy, 14-20 June 2009: poster.

101 **E. L. Hansen**, N. I. Ringdal, B. M. Kjelling, H. Hemmen, J. O. Fossum, E. N. de Azevedo, M. Engelsberg, Y. Méheust, C. Kim, S. Marathe, I. W. Cho, D. Y. Noh, SAXS Studies of Highly Ordered Nematic Phases in Aqeous Dispersions of Sodium-Fluorohectorite Nanodiscs, SAS2009, XIV International Conference on Small-Angle Scattering, Oxford (UK), 13-18 septembre 2009: poster.

102 **H. Hemmen**, N. I. Ringdal, E. N. De Azevedo, M. Engelsberg, E. L. Hansen, Y. Méheust, J. O. Fossum, and K. D. Knudsen, The Isotropic-Nematic interfacde in suspensions of Na-fluorohectorite synthetic clay, Seventh Nordic Workshop on Scattering from Soft Matter . Helsinki, Finland, 27-28 January 2010: talk.

103 L. R. Alme, H. Hemmen, **J. O. Fossum** and Y. Méheust, Humidity Transport in a Material of Interconnected Meso- and Nanopores: X-ray Studies of a Model Clay, MRS Fall Meeting, Boston (USA), 20 novembre 30 - 4 décembre 2009: talk.

104 **E. L. Hansen**, N. I. Ringdal, B. M. Kjelling, H. Hemmen, J. O. Fossum, E. N. de Azevedo, M. Engelsberg, Y. Méheust, C. Kim, S. Marathe, I. W. Cho, D. Y. Noh, Highly Ordered Nematic Phases and

Emerging Positional Ordering of Nanosized Clay Platelets in Water, MRS Fall Meeting, Boston (USA), 20 novembre 30 - 4 décembre 2009: poster.

105 **H. Hemmen**, L. R. Alme, J. O. Fossum, and Y. Meheust, X-ray studies of interlayer water absorption and mesoporous water transport in a weakly hydrated clay, Gordon Research Conference on Flow and Transport in Permeable Media, 10-16 July 2010, Lewiston ME (USA): poster.

106 **D. M. Fonseca**, Y. Meheust, K. D. Knudsen and J. O. Fossum, Phase diagram of polydisperse Na-fluorohectorite-water suspensions: A synchrotron small-angle X-ray scattering stud, International Workshop on CO2 and Fluids in Nanoscience, Brasilia-DF, (Brésil), 7-10 December 2010: poster.

107 **H. Hemmen**, N. I. Ringdal, E. N. De Azevedo, M. Engelsberg, E. L. Hansen, Y. Méheust, J. O. Fossum, and K. D. Knudsen, The Isotropic-Nematic interfacde in suspensions of Na-fluorohectorite synthetic clay, International Workshop on CO2 and Fluids in Nanoscience, Brasilia-DF, (Brésil), 7-10 December 2010: poster.

108 **H. Hemmen**, L. R. Alme, J. O. Fossum, and Y. Meheust, X-ray studies of interlayer water absorption and mesoporous water transport in a weakly hydrated clay, International Workshop on CO2 and Fluids in Nanoscience, Brasilia-DF, (Brésil), 7-10 December 2010: talk.

109 **H. Hemmen**, L. R. Alme, J. O. Fossum, and Y. Meheust, X-ray studies of interlayer water absorption and mesoporous water transport in a weakly hydrated clay, International Workshop on Complex Physical Phenomena in Materials, Recife-PE (Brésil), 14-17 December 2010: talk.

110 **D. M. Fonseca**, Y. Meheust, K. D. Knudsen and J. O. Fossum, Phase diagram of polydisperse Na-fluorohectorite-water suspensions: A synchrotron small-angle X-ray scattering stud, International Workshop on Complex Physical Phenomena in Materials, Recife-PE (Brésil), 14-17 December 2010: poster.

111 **H. Hemmen**, N. I. Ringdal, E. N. De Azevedo, M. Engelsberg, E. L. Hansen, Y. Méheust, J. O. Fossum, and K. D. Knudsen, The Isotropic-Nematic interfacde in suspensions of Na-fluorohectorite synthetic clay, International Workshop on Complex Physical Phenomena in Materials, Recife-PE (Brésil), 14-17 December 2010: poster.

112 **J. Bouquain**, Y. Méheust and P. Davy, Solute transport through a horizontal fracture with significant density effects, AGU Fall Meeting, San Francisco (USA), December 2010: poster.

113 G. Løvoll, M. Jankov, K. Måløy, **R. Toussaint**, J. Schmittbuhl, G. Schäfer, and Y. Méheust, Viscous fingering and dynamic saturation–pressure curves in two-dimensional porous media, EGU General Assembly 2011, Vienne (Autriche), April 2011: poster.

114 **R. Toussaint**, M. Niebling, J. Schmittbuhl, G. Schaefer, K. J. Måløy, E. G. Flekkøy, K. T. Tallakstad, G. Løvoll, M. Jankov, Y. Méheust, Channel formation during biphasic flow in porous media, or during fast monophasic flow and matrix hydrofracture: Consequences on the dynamic pressure-saturation and relative permeability relations, MUSIS workshop, February 2011: talk.

115 **S. Jones**, I. Cantat, B. Dollet, Y. Méheust, Flow of a Two-Dimensional Aqueous Foam through Two Parallel Channels, British Society of Rheology Midwinter Meeting, on Complex fluids and complex flows, London (UK), December 19-20 2011: talk.

116 **J. Bouquain**, Y. Méheust, D. Bolster, P. Davy, Inertial effects in channels with periodically varying aperture and impact on solute dispersion, EGU General Assembly, 22 – 27 April 2012: poster.

117 **S. A. Jones**, B. Dollet, Y. Méheust, I. Cantat, Flow of a two-dimensional aqueous foam through model porous media, Eufoam 2012 (X European Conference on Foams, Emulsions and Applications), July 8-11 2012, Lisboa (Portugal): talk.

118 **J. Bouquain**, Y. Méheust, D. Bolster, P. Davy, Inertial effects in channels with periodically varying aperture and impact on solute dispersion, AGU Fall Meeting, San Francisco (USA), December 3-7 2012: poster.

119 **J. Jiménez-Martínez**, P. Anna, R. Turuban, H. Tabuteau, T. Le Borgne, Y. Méheust, 2D experiments for characterizing solute dispersion in unsaturated heterogeneous porous media, AGU Fall Meeting, December 3-7 2012: poster.

120 **R. Turuban**, P. de Anna, J. Jimenez-Martinez, H. Tabuteau, Y. Méheust and T. Le Borgne, Dispersion upscaling from a pore scale characterization of Lagrangian velocities, EGU General Assembly, Vienna (Austria), April 7-12 2013: talk

121 S. A. Jones, **B. Dollet**, B. Géraud, Y. M\'eheust, I. Cantat, Flow of liquid foams in two-dimensional porous media, 5th Workshop on Viscoplastic Fluids, Rueil-Malmaison (France), 2013: présentation

orale.

122 **S.A. Jones**, B. Dollet, Y. M\éheust and I. Cantat, International Soft Matter Conference, Rome (Italy), September 15-19 2013: talk.

123 **P. de Anna**, J. Jimenez-Martinez, H. Tabuteau, R. Turuban, T. Le Borgne, M. Derrien and Y. Méheust (2013), Mixing and reaction kinetics in porous media: an experimental pore scale quantification, AGU Fall Meeting, December 9-13, San Francisco (USA): poster.

124 **R. Turuban**, P. de Anna, J. Jimenez-Martinez, H. Tabuteau, Y. Méheust and T. Le Borgne, Mixing upscaling from a 2D pore scale characterization of Lagrangian velocities, AGU Fall Meeting, December 9-13 2013, San Francisco (USA): poster.

125 **J.-R. de Dreuzy**, C. Darcel, P. Davy, J. Erhel, R. Le Goc, J. Maillot, Y. Méheust, G. Pichot, B. Poirriez, Origin of permeability and structure of flows in fractured media, AGU Fall Meeting, December 9-13 3013, San Francisco (USA): talk.

126 **J. Jiménez-Martínez**, P. Anna, R. Turuban, H. Tabuteau, T. Le Borgne, Y. Méheust, Pore scale imaging of transport in unsaturated flows, AGU Fall Meeting, December 9-13 2013, San Francisco (USA): poster.

127 **B. Dollet**, S. A. Jones, B. Géraud, Y. Méheust, S. J. Cox and I. Cantat, Flow of an aqueous foam through a two-dimensional porous medium: structure dynamics couplings, Workshop on Foams and Minimal Surfaces - 12 years on, Isaan Newton Institute for Mathematical Science, Cambridge (UK), February 24-28 2014, **invited talk**.

128 **B. Géraud**, S. A. Jones, Y. Méheust, I. Cantat and B. Dollet, Complex flows in 2D-porous media: intermittencies and fragmentation, Eufoam 2014, Thessaloniki (Greece), July 7-10 2014: talk.

129 **B. Dollet**, B. Géraud, S. A. Jones, S. J. Cox, Y. Méheust and I. Cantat, Flow of foams in two-dimensional porous media, 10th European Fluid Mechanics Conference, Copenhagen (Denmark), September 14-18 2014: talk.

130 **D. Jougnot**, J. Jiménez-Martínez, N. Linde, T. Le Borgne, Y. Méheust, Laboratory-scale electrical resistivity and fluorimetric monitoring of saline tracer tests at partial saturation, RST 2014, October 27-31 2014, Pau (France): poster.

131 **Zhibing Yang**, I. Neuweiler, Y. Méheust 3 , A. P. Niemi and F. Fagerlund, Fluid trapping characteristics of immiscible displacement in fractures, AGU Fall Meeting, San Francisco (USA), December 15-19 2014: talk.

132 **J.-R. de Dreuzy**, P. Davy, Y. Méheust and Olivier Bour, From Multi-Porosity to Multiple-Scale Permeability Models of Natural Fractured Media, AGU Fall Meeting, San Francisco (USA), December 15-19 2014: talk.

133 **J. Jiménez-Martínez**, P. Anna, R. Turuban, H. Tabuteau, T. Le Borgne, Y. Méheust, Impact of saturation on dispersion and mixing in porous media, AGU Fall Meeting, San Francisco (USA), December 15-19 2014: talk.

134 **R. Turuban**, P. de Anna, J. Jimenez-Martinez, H. Tabuteau, Y. Méheust and T. Le Borgne, Upscaling of mixing in a 2D porous medium from a characterization of pore scale Lagrangian velocities, AGU Fall Meeting, San Francisco (USA), December 15-19 2014: poster.

135 **T. R. Ginn**, K. Nelson, T. Kamai, A. Massoudieh, T. H. Nguyen, T. Le Borgne, Y. Méheust, R. Turuban, A. Benjamin and A. Palomino, Colloid Transport in Porous Media: A Continuing Survey of Conceptual Model Development, AGU Fall Meeting, San Francisco (USA), December 15-19 2014: **invited talk**.

136 **T. Le Borgne**, P. de Anna, R. Turuban, J. Jimenez-Martinez, H. Tabuteau, Y. Méheust, T. R. Ginn and M. Dentz, The lamellar structure of reactive mixtures in porous media: Pore scale experimental imaging and upscaling, AGU Fall Meeting, San Francisco (USA), December 15-19 2014: talk.

137 **B. Géraud**, S. A. Jones, Y. Méheust, I. Cantat and B. Dollet, Foam flows in 2D porous media, 10th Annual European Rheology Conference, Nantes (France), April 14-17 2015: poster.

138 B. Géraud, S. A. Jones, Y. Méheust, I. Cantat and **B. Dollet**, Flow of foams in two-dimensional disordered porous media, APS Physical Society 68th Annual DFD (Division of Fluid Dynamics) Meeting, November 22-24, 2015: talk.

139 **J.-R. de Dreuzy**, J. Maillot, C. Darcel, P. Davy, R. Le Goc, Y. Méheust and G. Pichot, Power-averaging method to characterize and upscale permeability in DFNs, AGU Fall Meeting, San Francisco (USA), December 14-18 2015: talk.

140 **D. Jougnot**, J. Jiménez-Martínez, Y. Méheust, T. Le Borgne, and N. Linde, Impact of saline tracer

mixing on upscaled electrical resistivity under partially saturated conditions: Insights from a pore-scale fluorimetry study, AGU Fall Meeting, San Francisco (USA), December 14-18 2015: talk.

February 6th, 2016.

4 Research activities

I present below in a concise manner the research activities that I have developed since I defended my PhD thesis in April 2002. They address two types of research topics.

The first type deals with the flow of one or two fluids in subsurface cavities of complex geometry, and/or the transport/mixing/reaction of solute species advected by such flows. We investigate how flow, transport and reaction are impacted by the complexity in the boundary conditions of subsurface flow, in particular their disorder. Since solute transport and mixing have been a major focus in the last years, the studies mostly addressing flow and those mostly addressing transport and reaction have been grouped in separate sections (4.1 et 4.2).

The second type of topics deals with the flow of fluids whose mechanical properties are rendered complex by the fact that they carry solid microscopic particles (colloids). The focus is how the collective organization of the suspended solid particles impacts the mechanical properties of the complex fluid (viscous liquid and colloids). These studiees are presented in section 4.3.

Section 4.4 provides information about the colleagues I have collaborated with through the years, and about funding sources.

4.1 Flows of fluids with complex boundary conditions

4.1.1 Geological and environmental context:

Soils and rocks of the upper crust of the Earth are permeable media, that is, they possess connected cavities through which fluids can flow. Such fluids are for example air, rain water or irrigation water, groundwater, non-aqueous fluid pollutants originating in an industrial spill, drilling muds used for oil extraction, oil being extracted, supercritical CO_2 being injected in an ancien saline aquifer, etc.

Two types of cavities are generally distinguished: (i) pores belonging to the rock matrix, that is, cavities that are present in the undamaged rock, and (ii) fractures/joints, which are quasi-planar cavities resulting from the fracturing of the material, for example due to tectonic constraints. Fractures are distributed within the rock formation as networks with a certain degree of connectivity. Networks of interconnected fractures correspond generally to a low porosity (ratio of the volume of the cavities to the total volume) but to a large permeability (capacity of the rock to let fluids flow through it). The rock matrix, on the contrary, can posses a significative porosity (up to 30% in some sedimentary rocks), but the sub-micrometric size of individual pores limits the permeability of the undamaged material. In most igneous rocks, that is, rocks which were formed by the cooling and solidification of lava or magma, such as granite, the matrix porosity can be considered negligible.

In the vadose zone, which is defined as the region of the subsurface positioned between the water table and the Earth's surface, air coexists with water within the porous space . Water flows are then denoted *insaturated*, and constitute a particular case of immiscible diphasic flow. In this type of flows, capillary forces at the air-water interface play in important role in the interface dynamics. The displacement of oil by an aqueous solution, the understanding of whose dynamics is crucial for Enhanced Oil Recovery (EOR) techniques developed by the oil industry to improve the recovery rate of their oil fields, is another example of an immiscible two-phase flow occurring in the subsurface.

4.1.2 Flows in fractured media:

Networks of interconnected fractures are the main paths for flows in crystalline rock formations (such as granite). Since September 2006 I have been part of the team "Transferts d'eau et de matière dans les milieux hétérogènes complexes" at Géosciences Rennes, which has contributed pioneering work in the modeling of the geometry of such fracture networks (*Bour and Davy*, 1997, 1998, 1999; *Bonnet et al.*, 2001), as well as in the understanding of their connectivity *de Dreuzy et al.* (2001a); *Darcel et al.* (2003c,b) and permeability (*de Dreuzy et al.*, 2001a,b, 2004). These models are Discrete Fracture Networks (DFNs), as they neglect the permeability of the rock matrix and consider each fracture as a link in the network, with a given transmissivity. Traditionally the transmissivity of a fracture is modeled as that of a *parallel plate*, of constant aperture identical to the fracture's mean aperture, and of given shape (usually circular) along the fracture plane. The fracture sizes (disk diameters) are distributed according to a power law, as shown from the mapping of fracture traces in outcrops and core data (*Darcel et al.*, 2003b; *Davy et al.*, 2006), and a non-uniform distribution can also be

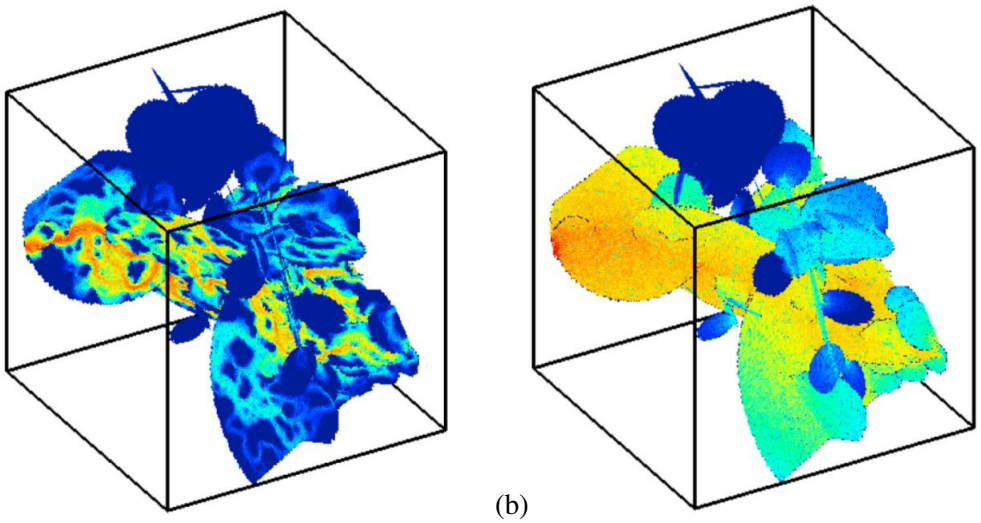

(a) (b)

Figure 1: Two synthetic DFNs with the same network-scale topology. In (a) the fractures are rough, while in (b) each fracture is the parallel plate approximation of a fracture of the medium shown in (b). The local flow rates (velocities integrated on the local fracture aperture) are shown on the fracture planes as colors, red denoting larger magnitudes of the local flow rate and blue smaller magnitudes. Figures from (*de Dreuzy et al.*, 2012).

assigned to the fracture apertures and orientations. Correlations between fracture lengths and positions can also be characterized from field data (*Darcel et al.*, 2003a).

I had devoted my MSc work and a large part of my PhD studies (1998-2002) to the impact of fracture roughness on fracture flow and on the resulting fracture transmissivity. The parallel plate model for the flow and permeability of a rough fracture is a first order approximation; geological fractures are in fact not perfectly planar. Not only does their aperture field vary along the fracture plane, but its distribution possesses well-defined statistical properties. In particular, there exists a *correlation scale* (or *mismatch scale*) L_c above which the two facing fracture walls are identical, while at scales smaller than L_c the two walls can be considered uncorrelated with each other (*Brown et al.*, 1986; *Brown*, 1995; *Glover et al.*, 1998). Furthermore, at these smaller scales the aperture field is self-affine, that is, possesses a particular type of self-invariance that renders its power spectral density a power law of exponent $-2-2\,H$, H being the *Hurst exponent* characteristic of the self-affinity. This particular geometry is responsible for flow channeling, with flow structures as large as the correlation length. If L_c is the fracture scale, the channeling translates into a significant deviation of the fracture transmissivity from that of a parallel plate of identical mean aperture, and this all the more as the fracture closure is increased (*Brown*, 1987). This deviation is not necessarily negative: if large aperture channels are oriented along the direction of pressure head imposed at the fracture scale, roughness may enhance the volumetric flow rate with respect to the parallel plate geometry of identical mean aperture (*Méheust and Schmittbuhl*, 2000). However, for a population of fractures with the same statistical description in terms of Hurst exponent, mean aperture, amplitude of the roughness relative to the fracture length, and correlation length, configurations that are unfavorable to flow are more common than favorable ones *Méheust and Schmittbuhl* (2001). In any case, the correlation length plays a fundamental parameter: the permeability/transmissivity computed at scales significantly larger than the correlation length is the same as that of a smooth fracture of identical mean aperture (*Méheust and Schmittbuhl*, 2003), and the deviation from this ideal behavior is all the larger as L_c is closer to the fracture size.

One open question was the link between (i) this impact of the fracture wall roughness on the flow at the fracture scale and (ii) the possible impact of this roughness on the medium's permeability at the network scale. Let us consider two DFNs with the same network scale topology, such as those featured in Fig. 1: one consisting of rough fractures, the other one of parallel plates which are first order approximation of the fractures in the first DF: to each rough fracture in the DFN of Figure. 1.a corresponds a parallel plate fracture with identical mean aperture in DFN of Figure. 1.b. Can the impact of fracture wall roughness on the permeability of the DFN of Figure. 1.a simply consist in a roughness-controlled factor to be applied to the permeability of the DFN of Figure. 1.b, or does there exist a coupling between (i) and (ii) ? In other words, can the reorganization of the flow within fracture planes impact the way the flow at the network scale is distributed between fractures ?

Do some fracture for example cease to be conductive when their aperture fluctuations are taken into account ? Oviously this depends strongly both on the average fracture closure and on the size of the correlation length L_c relative to the typical distance between fracture intersections within the fracture planes. This question was addressed in collaboration with Jean-Raynald de Dreuzy (Géosciences Rennes), Géraldine Pichot (now at INRIA in Rennes) and Romain Giraud (MSc student) using numerical simulations in which the entire DFN is discretized on a single mesh which is two-dimensional on each of the fracture planes. The flow in each of these planes is solved using the Reynolds equation, that is, in terms of local fluxes, assuming that a local cubic law relates the pressure gradient to the local flux field everywhere. Running simulations over 2 millions of synthetic DFNs, we could gather enough statistics to show that there are conditions for which the topology of the flow at the network scale is coupled to the flow heterogeneity within fracture planes (*de Dreuzy et al.*, 2012). However, configurations for which such effects impact the medium's effective permeability significantly are those with a fracture aperture correlation length less than about 20 times the overall system size, which means that this coupling would not have to be taken into account when simulating the flow through a fractured formation at the scale of a catchment. But it would be relevant when simulating the flow between two boreholes distant by a few meters, or inside a rock core in the laboratory.

4.1.3 Two-phase flows in two-dimensional porous media

Two-phase flows occur when two immiscible fluids flow together. In such flows, the flow is imposed by the joint action of not only viscous forces, pressure forces, and gravity, but also of capillary forces acting at the interfaces between the two fluids. Capillary forces result from the surface tension at fluid-fluid interfaces, which imposes a difference in pressure (the *capillary pressure*) between the two sides of a fluid-fluid interface wherever it has a finite curvature radius R; this pressure difference is proportional to the inverse of R. In porous media, the wetting of solid surfaces by one of the two fluids generally imposes that curvature radii are on the order of the radius of the channels in which they are being displaced, which means that capillary forces are potentially very strong. Another reason why they can have a strong impact on the flow is that they capillary forces are all the stronger (in absolute value) as the interface is displaced along a narrower channel, so that any variability in channel widths within the medium will result in different velocities of fluid-fluid interfaces in different channels. Since in porous media with non completely trivial geometry such channels connect to each other at pore locations, a potential very large complexity of the spatial distribution of the immiscible fluid phases can result. Two-phase flows with initial conditions in which one of the fluids occupies the porous space entirely, and is consequently displaced by the other one, have been studied extensively (*Homsy*, 1987); they are denoted *primary displacements*. The shape of an invasion pattern, and in particular the spatial distribution of the displaced fluid that remains trapped in the medium behind regions invaded by the displacing fluid, strongly depend on whether capillary forces oppose the displacement of fluid-fluid interfaces, or whether they oppose it. In the latter case the displacement is denoted *imbibition*, in the former case *drainage*. Drainage occurs when the fluid that wets the solid walls is the displaced fluid, and imbibition occurs otherwise.

Two-dimensional (2D) porous media have a geological relevance in that they can be viewed as a (strong) idealization of the geometry of a gouge within a fault plane. In addition, they have been used for seminal works on two-phase flow regimes and fluid-fluid interface instabilities in porous media. In particular, the seminal experimental works of Lenormand (*Lenormand and Zarcone*, 1985; *Lenormand et al.*, 1988; *Lenormand and Zarcone*, 1989; *Lenormand*, 1990), which addressed primary drainage or primary imbibition and showed how the interplay between viscous instability of water-air meniscii, capillary forces across them, and the disorder in the pore space contribute to shaping the geometry of the invasion structure, used 2D networks of channel of various widths. Other seminal studies, in particular those by the Oslo group (*Måløy et al.*, 1985, 1987), used porous media consisting of a monolayer of monodisperse glass beads inside a Hele-Shaw cell of thickness equal to the beads' diameter. Results obtained with the two types of systems under similar flow conditions are consistent with each other, which shows that the detail of the pore scale geometry is not what mostly controls the shape of the invasion structure at scales much larger than the pore scale (though for imbibition it can, depending on the flow conditions, see (*Lenormand*, 1990)). These early works contributed in particular to the full understanding of two particular regimes of two-phase flow: (i) capillary fingering, which for drainage occurs at sufficiently low mean displacement velocity and for imbibition at sufficiently low, but not extremely low, mean displacement velocity, and (ii) viscous fingering, which occurs at sufficiently large displacement velocity and at sufficiently low viscosity ratio, that is, when the displaced fluid is sufficiently more viscous than

the displacing fluid for the fluid-fluid interface to be rendered intrinsically unstable (*Saffman and Taylor*, 1958). A concise review on two-phase flows, in particular drainage, and in particular based on findings obtained using 2D measurements, was published a few years ago in collaboration with Renaud Toussaint (Institut de Physique du Globe de Strasbourg) and Knut Jørgen Måløy (University of Oslo) (*Toussaint et al.*, 2012).

The reason why 2D setups were used in those seminal studies is that they allow for full in situ visualization of the two phases. In 2000, during my PhD, I had had the opportunity to work on the setup of the Oslo team and address the gravitational stabilization of viscously-unstable drainage (*Méheust et al.*, 2002). We showed that the competition between these two effects is controlled by the difference between the capillary number (which quantifies the ratio of the typical magnitude of viscous forces to that of capillary forces) and the Bond number (ratio of the typical magnitude of the gravitational force to that of capillary forces). Furthermore, the amplitude of the roughness front between these two fluids, in conditions of stabilized displacement for which gravity dominates viscous forces, is controlled by the same number. Experimental work on 2D drainage has continued in later years in collaboration with Knut Jørgen Måløy and Renaud Toussaint. In particular the experimental findings of *Méheust et al.* (2002) were confirmed by numerical simulations *Løvoll et al.* (2005a). Other questions have been studied over the years, which I present in separate paragraphs, below. It is important to note that all these studies have been performed in porous media that are statistally homogeneous, that is, homogeneous at the Darcy scale, and in which disorder is only found at the pore scale. A Fontainebleau sandstone, for example, can be considered to also exhibit this property, but it is by no means the case in porous media with multiscale heterogeneities, such as soils, where macropores and root channels are Darcy scale heterogeneities (*Beven and Germann*, 1982)Fall.

We have performed a detailed experimental study of the growth of the viscous instability during drainag in a 2D porous medium. When the medium is horizontal, the displacement of an aqueous liquid by air leads to the formation of a branched, percolating, fractal structure which has been well known since the 80s (*Måløy et al.*, 1985). The growth of that invasion pattern has long been considered analog to DLA (diffusion-limited aggregation) (*Arneodo et al.*, 1996). Furthermore, since the pioneering work of *Saffman and Taylor* (1958), the viscous instability in a Hele-Shaw cell has been considered by many physicists as a relevant Darcy scale model of the viscous instability in 2D porous media. We have studied the growth process in a medium consisting of a monolayer of glass beads and for displacement regimes that are neither full capillary fingering, nor full viscous fingering, but correspond to intermediate magnitudes of the imposed displacement velocities. The study has shown that the growth only occurs in a region of fixed area around the tip of the most advanced finger (*Løvoll et al.*, 2004) and that the map of probability densities for the occupation of the medium by the invading fluid provides a topography whose cut at probability 1/2 indeed has a shape resembling a Saffman-Taylor finger (*Løvoll et al.*, 2004; *Toussaint et al.*, 2005). We have termed that shape *en-*

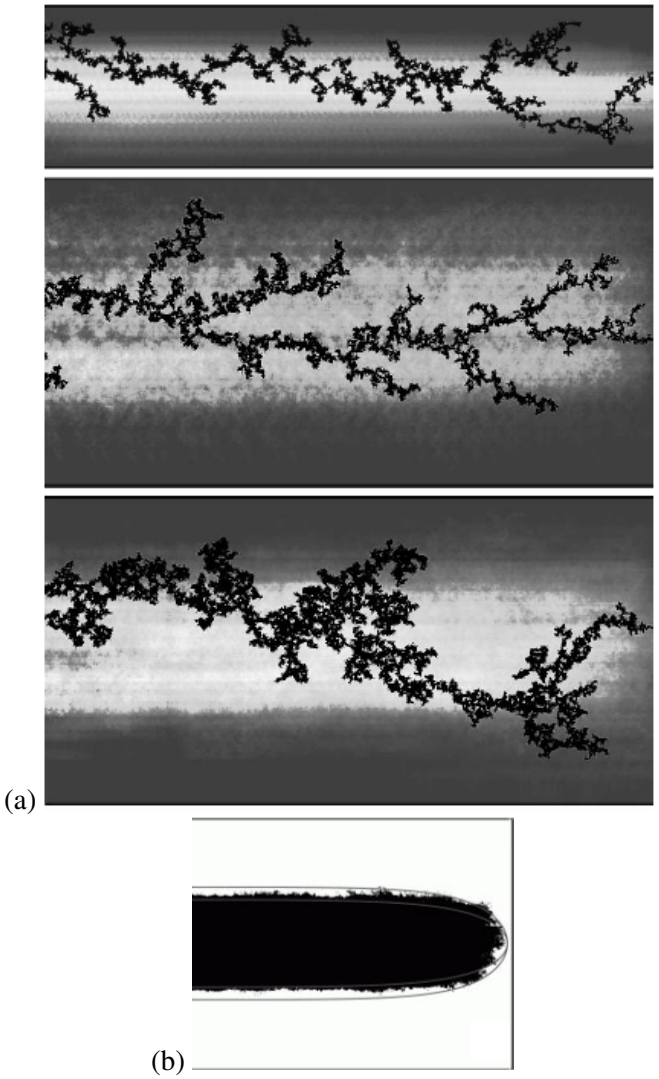

Figure 2: (a) Invasion patterns of air (in black), to which the map of invasion probability densities has been superimposed in gray levels. (b) Envelope of the invasion pattern as inferred from the bottom map in (a), and the superimposed shape of a Saffman-Taylor finger (with uncertainty interval on its width). Figures adapted from (*Toussaint et al.*, 2005).

velope of the invasion pattern. However the width of that envelope, which is one half of the medium's width in the Saffman-Taylor geometry, was consistently measured to 0.4 of the medium's width. By estimating theoretically the relationship between the growth invasion probability ϕ and the pressure gradient in the liquid in the vicinity of the interface, we showed that it corresponds approximately to a dielectric breakdown model (DBM) (*Niemeyer et al.*, 1984) of exponent 2 (*Toussaint et al.*, 2005), that is: $\phi \propto (\nabla P)^2$. Consequently, the growth process is neither equivalent to that of DLA, nor to the growth of the Saffman-Taylor finger, since these processes are laplacian (i. e., their growth probability is proportional to the gradient that is causing it). The main conclusion of those studies is therefore that the Saffman-Taylor finger is not a proper upscaled model for viscously unstable drainage in a 2D porous medium. Another important finding is that the distinction between capillary and viscous fingering is not only a question of mean displacement velocity, but also a question of scale. Indeed, capillary forces dominate viscous forces in controlling the interface evolution at small scales, while the contrary occurs at large scales. Simple theoretical arguments show that the crossover scale between these two regimes scales as the inverse of the capillary number, and appears visually as the typical finger width of the structure (*Toussaint et al.*, 2005). So for sufficiently fast displacements, that crossover scale becomes of the order of the typical pore size, so that no signature of capillary fingering is seen in the growth process. Conversely, for sufficiently slow displacements, the crossover scale becomes of the order of the system size, so that no signature of viscous fingering is seen. In our intermediate regimes we were able to see both signatures (in particular in terms of fractal dimension) and verify that the typical finger width scsales as $1/Ca$.

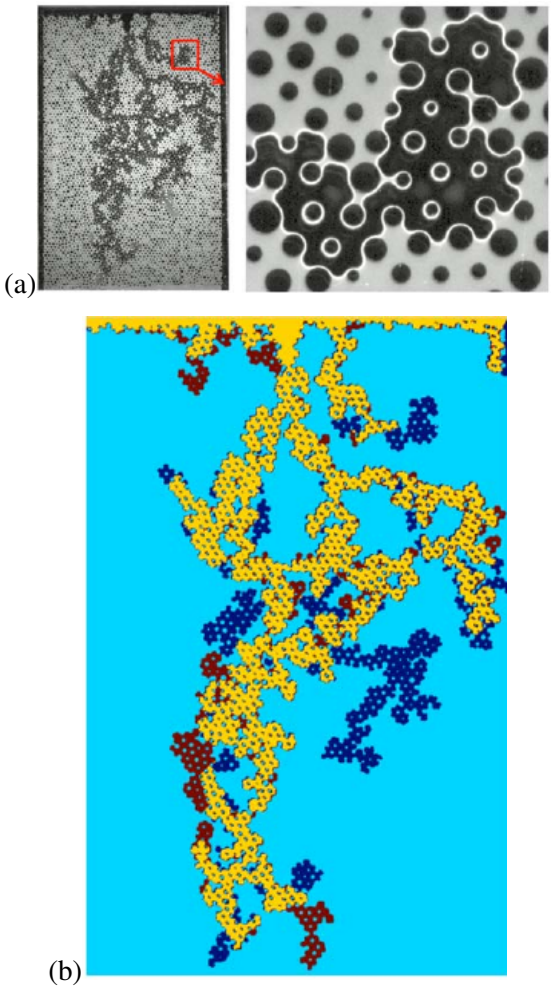

Figure 3: (a) Example of experimental invasion pattern obtained in the Géosciences Rennes setup, with close view image on the right. Air is the dark phase, water the light gray phase. (b) Comparison of experimental and numerical invasion patterns. Figures adapted from (*Ferrari et al.*, 2015).

For this type of unstable displacement, we have also investigated the upscaling of the pressure drop. We obtained a scaling law relating that pressure drop to saturation, the linear size of the medium and the capillary number (*Løvoll et al.*, 2011). If one assumes that the size of the experimental porous medium is what would be taken as the Darcy scale in a much larger medium, then the pressure drop measured in our system is the capillary pressure that would be defined at the Darcy scale, as is customary in Darcy scale models of two-phase flows. Consequently there would be a dependence of the capillary pressure (defined at the Darcy scale) on the capillary number, that is, on the mean flow velocity. This dependence is well known in the literature; it is being accounted for by Darcy scale models of two-phase flows (*Hassanizadeh et al.*, 2002) and termed *dynamic capillary pressure*. It had been assumed that it arises essentially from capillary effect. In this study we showed that it is not necessarily the case and that it can be the consequence of the sole viscous pressure drops at scales smaller than the Darcy scale. In fact, we suggested that its causes were essentially viscous, a proposal that not all referees of the manuscript agreed with at the time.

In recent years a novel experimental setup has been developed at Géosciences Rennes, in collaboration with Tanguy Le Borgne (Géosciences Rennes) and Hervé Tabuteau (Institut de Physique de Rennes). It is based on a medium whose grains are cylindrical pillars positioned in a Hele-Shaw cell, which means that it is a fully-2D porous medium, in contrast to the monolayer of glass beads. This choice was initially made in order to be able to image the inside of pores with a very good resolution and measure concentration fields of solutes within the pore space (see section 4.2.3, 4.2.4 and 4.2.5). The medium is built using soft lithography, a technique borrowed from the field of Microfluidics and which allows to make a physical ren-

dering of a geometry defined numerically. This feature is very promissing since the disorder of the medium can be controlled at will, and, as explained above, pore scale disorder plays a crucial role. The left part of Figure 3.a shows an invasion pattern of air in water, obtained in the viscously-unstable regime. Seen at large scale, it looks similar to the lower pattern of Figure 2, though the viscosity ratio for the latter was $\sim$ 100 times larger. The close view image on the right part of Figure 3.a shows the excellent resolution of the phase geometry. Such patterns were compared to patterns from a numerical simulation based on the volume of fluid method and performed on a numerical geometry that reproduced the experimental geometry. An example of comparison is shown in Figure 3.b. The area where the two experimental and numerical patterns coincide is shown in yellow, while blue and red denote areas occupped by the sole experimental and numerical patterns, respectively. We could explain the differences in pattern geometries and explain them by uncertainties on the experimental characterization of the geometry, which result in small differences between the experimental and numerical geometries in the capillary pressure threshold distributions of the medium's pores (*Ferrari et al.*, 2015). Therefore, the more disordered the medium is, the easier it is to predict the experimental patterns from a numerical simulation, because the uncertainties on the distribution of capillary pressure threshold are absolute, and their relative impact on the shape of that distribution is smaller if the distribution is wider.

Another topic that has been addressed, in collaboration with Zhibing Yang (now at MIT), Insa Neuweiler (Institut für Strömungsmechanik und Umweltphysik im Bauwesen, Hannover), as well as Fritjof Fagerlund and Auli Niemi (Uppsala University, Sweden), is drainage in the plane of a rough fracture and the subsequent trapping of the displaced fluid. Subsurface engineering applications such as oil extraction, geological storage of CO_2, subsurface disposal of nuclear waste, or geothermal exploitation, all possibly involve the joint flow of two immiscible fluids in a fractured media. Understanding the displacement process at the scale of the individual fracture is therefore fundamental. The trapping of the displaced fluid is a major concern: in petroleum recovery and CO_2 sequestration, for example, the trapping should be minimized so as to increase the recovery and the storage capacity of the formation, respectively. Interfacial area is also an important parameter for the interphase mass transfer processes that are critical to contaminant remediation problems (*Detwiler et al.*, 2001; *Yang et al.*, 2012a, 2013). The Physics of the displacement is somewhat different in the plane of a geological fracture from what it is in the 2D porous media discussed until now: there are no grains, but, rather, aperture variations arising from the roughness of the fracture walls, as described in section 4.1.2. Hence, though there can be several separate interfaces (otherwise there would be no trapping), the interface(s) do not consist of meniscii of length of the order of the aperture size, as in classic 2D porous media: their extension along the fracture plane can be much larger, and their principal curvature along that plane (see Figure 4) is imposed not only by the local aperture, but also by the neighboring apertures and by the history of the interface displacement. The resulting flow regimes can range from tortuous fingers and random clusters to piston-like displacement with trapping, depending on the capillary number, Bond number, and viscosity ratio (*Neuweiler et al.*, 2004; *Loggia et al.*, 2009). We have reduced the variety of potential flow regimes by studying drainage at small capillary numbers; the displacement can then be described by an improved invasion percolation (IP) process. In IP the displacement is considered quasi-static, and the interface advances at each time step at the position where the pressure difference across the interface exceeds the defending capillary pressure by the largest amount (*Wilkinson and Willemsen*, 1983). It has been used extensively in the 80s and 90s for the study of capillary fingering and of gravity-induced or viscous forces-induced small deviations to capillary fingering (*Birovljev et al.*, 1991; *Meakin et al.*, 1992; *Schmittbuhl et al.*, 2000). Attempts had also been made to use IP to describe slow displacement in self-affine apertures fields (see among others (*Wagner et al.*, 1997)), in which case the correlated aperture variations were accounted for, as well as possibly the impact of gravity due to the topography of the walls, but in most cases the algorithm did not take into account the in-plane curvature. The first numerical simulation based on IP that considered

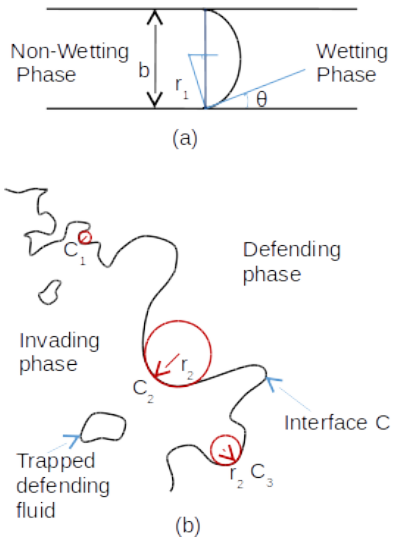

Figure 4: Geometry of the fluid-fluid interface during primary drainage in a fracture. (Top) Side view. (Bottom) Top view. Figure reproduced from (*Yang et al.*, 2016).

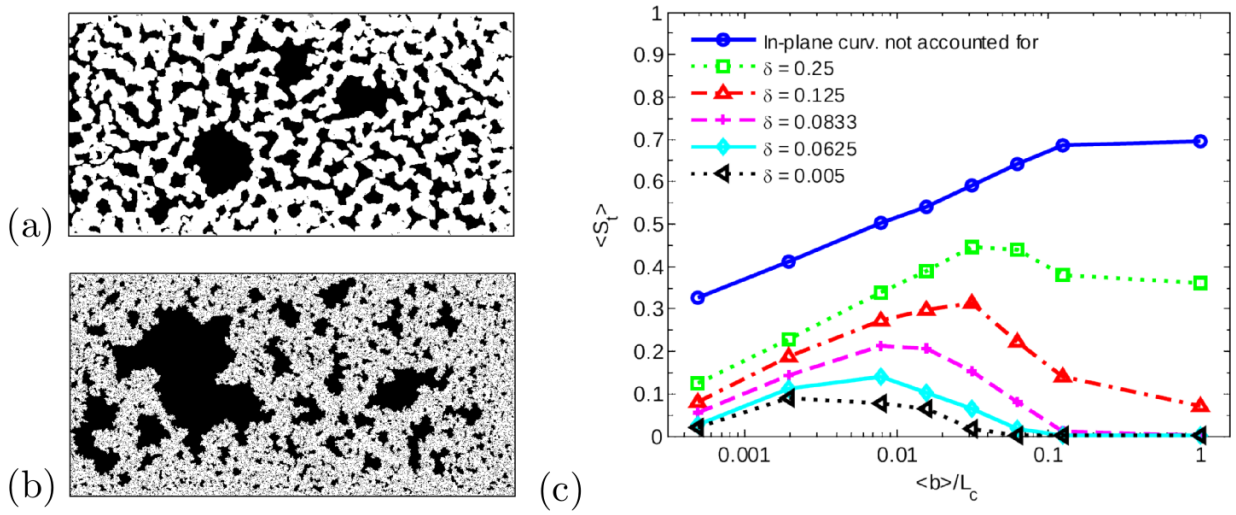

Figure 5: (a) Phase distribution obtained for a topography of closure $1/\delta = 4$ and a correlation length $L_c = L/64$. (b) Phase distribution for $1/\delta = 4$ and a correlation length $L_c = L/256$. (c) Mean saturation as a function of the ratio of the mean aperture to L_c, for various degrees of closure. Figures adapted from *Yang et al.* (2016).

in-plane curvature was performed by *Glass et al.* (1998), who estimated the in-plane curvature based on the existence of an empiric length scale set to half of the correlation length of the aperture field that they were considering. Obviously such an approach was doomed to fail to predict experimentally-observed invasion patterns, since the curvature is in essence a purely geometric quantity, and is not expected to rely on a pre-established length scale. *Neuweiler et al.* (2004) and *Ferer et al.* (2011) improved the method by treating the empirical length scale as a fitting parameter to be determined by trial and error based on a comparison with physical experiments, which is difficult to be generalized. More recently, *Yang et al.* (2012b) proposed a method to compute the in-plane curvature in a purely geometric manner. Their approach was validated against experimental data and shown to be advantageous over previous approaches. The presently discussed study of drainage in a rough fracture in the slow displacement regime is based on the code of Zhibing Yang. The properties of the clusters of trapped displaced fluid have been investigated as a function of the geometry of the fracture, for geometries identical to those presented above in section 4.1.2. We have focused in particular on the roles of the fracture closure and correlation length. A wide spectrum of entrapment morphologies can occur, spanning morphologies consisting of trapped clusters with a power law size distribution, to morphologies consisting of only a few sparse large clusters, and even to situations exhibiting no wetting fluid entrapment. Two of these patterns are shown in Figure 5.a and .b; the corresponding geometries differ only by the ratio of the fracture length L to the correlation length L_c. Figure 5.c shows how the global saturation, averaged over a sufficient number of realizations of the medium, varies as a function of the correlation length. The curve for which "in-plane curvature has not been accounted for" corresponds to a calculation using the standard invasion percolation, only accounting for aperture variations; it does not depend on the fracture closure. For calculations that account for the in-plane curvature, on the contrary, the plots are non-monotonic. The effect of the in-plane curvature is in fact to smoothen the invasion front and to dampen the entrapment of fluid clusters of a certain size range. This size range depends on the combination of the closure and aperture spatial correlation length.

4.1.4 Foam flows in two-dimensional porous media:

Aqueous foams consist of air bubbles separated by films of an aqueous solution (*Weaire and Hutzler*, 1999; *Cantat et al.*, 2013) that contain surfactants to lower the surface tension. They are used in a number of industrial applications, including glass manufacturing, ore flotation or firefighting technology (*Stevenson*, 2012). Enhanced oil recovery (EOR) has been the first application for subsurface environments: injection of surfactant together with gas into the subsurface has been used for 50 years to generate foam in situ and improve oil sweep, in particular in the framework of steam EOR (*Zhdanov et al.*, 1996). More recently, foams have been used to remediate aquifers contaminated with non-aqueous phase liquids (NAPLs), in a manner very similar to EOR (*Hirasaki et al.*, 1997). In both applications the use of foams offers the following advantages: a reduction by

one order of magnitude in the needed volume of solution for a given injection volume, since only about 10% of the foam consists of liquid solution *Chowdiah et al.* (1998), the rest being gas; a reduction of the needed amount of surfactant (*Roy et al.*, 1995b,a), a better sweep of the defending fluid due to a more favorable mobility ratio with respect to the oil (*Huang et al.*, 1986), and diversion mechanisms resulting from the particular dissipation mechanisms at play when a foam flows through a porous medium: the foam tends to first occupy large permeability regions, where its low mobility causes later flow to sweep low permeability regions (*Szafranski et al.*, 1998; *Huang and Chang*, 2000; *Jeong et al.*, 2000; *Jeong and Corapcioglu*, 2003). A more recent application is the remediation of vadose zone environments, and particularly of soils *Chowdiah et al.* (1998); *Jeong et al.* (2000); *Wang and Mulligan* (2004); *Zhong et al.* (2010); *Shen et al.* (2011); *Zhong et al.* (2011). In this context the foam is used as carrier fluid for chemical amendments rather than as displacing fluid. In this respect foams offer several advantages: they can be injected while maintaining a low water content in the treated zones, which is cheaper and particularly useful for remediation of the vadose zone (*Zhong et al.*, 2010); their capacity to transport soil/colloidal particles (*Shen et al.*, 2011) and bacteria (*Wan et al.*, 1994) at air-water interfaces is high; transport of air along with the aqueous solution may enhance the efficiency of biodegradation (*Rothmel et al.*, 1998; *Jenkins et al.*, 1993); in the case of *in situ* stabilization (of heavy metals, for example), a foam does not displace the target chemicals as much as a solution (*Zhong et al.*, 2009, 2011); they present a better sweeping efficiency than aqueous solutions due to a moderate sensitivity to gravity (*Zhong et al.*, 2011). In column experiments, a breaking of the foam front and the consequent propagation of a wetting front ahead of the foam, which may help to optimally deliver the amendments in case of a heterogeneous reaction, has also been reported (*Zhong et al.*, 2010).

Since 2011 I have collaborated with Isabelle Cantat and Benjamin Dollet (Institut de Physique de Rennes), as well as Baudouin Géraud (now at Géosciences Rennes) and Siân A. Jones (now a Technical University Delft). Our main focus has been to understand the local rheology of aqueous foams in porous media, with a motivation mostly oriented towards the remediation of the vadose zone. The flow of bulk foams has been the subject of a vast amount of literature from the foam Physics community through the years (*Heller and Kuntamukkula*, 1987; *Weaire*, 2008; *Dollet and Raufaste*, 2014), but not so much so for the flow of foams in porous media. The dissipation mechanisms are quite different in bulk foam flows and in foam flows through porous media, because in the latter a large part of the dissipation occurs in the wall films and in the regions of the films (called Plateau borders) that connect these films to the lamellae separating the flowing bubbles, while in bulk foam flow dissipation within the films/lamellae separating bubbles is the dominant dissipation mechanism. Three fundamental mechanisms of lamella/film creation are known to occur during foam generation within a porous medium: *leave-behind*, in which two gas fingers invade two adjacent and communicating liquid-filled pores, trapping a film of liquid in-between them after the pores have been fully invaded; capillary snap-off (*Kovscek and Radke*, 1994), in which the snap-off of liquid films at the throat between two pores separates a gas bubble in two (*Roof et al.*, 1970; *Gauglitz and Radke*, 1990; *Kovscek and Radke*, 1994; *Kovscek et al.*, 2007); *lamella division*, in which a liquid film touching a solid grain while still attached to other grains on this perimeter separates into two films that travel on either side of the dividing grain (*Kovscek and Radke*, 1994). Mechanisms of bubble disappearance are also at play when a foam flows through a porous medium; they consist mostly in (i) coarsening through gas diffusion and (ii) bubble coalescence by capillary suction. Bubble coarsening results from the diffusion of gas from smaller bubbles where the pressure and chemical potential are larger, to neighboring larger bubbles; it has been studied extensively in the context of bulk foams (*Cantat et al.*, 2013). In porous media it is observed at locations where bubbles are trapped (*Kovscek and Radke*, 1994). Bubble coalescence by capillary suction involves the sudden rupture of a lamella; it occurs when a lamella/film that has been sitting at a pore throat is displaced quickly into a pore volume much wider than the throat, and cannot adjust its liquid volume sufficiently fast to avoid rupturing (*Khatib et al.*, 1988).

We are using two-dimensional (2D) porous media in which the foam structure can be monitored in situ. This experiment is to my knowledge the only existing one in which the foam's local rheology (deformation of the bubble and interaction between them and with the solid walls) can be related to macroscopic properties of the flow (effective viscosity of the foam, pressure drop across the medium, etc...). The impact of the foam's texture or structure on the pressure drop across a porous medium, and, consequently, on flow through that medium, had until now been examplified in experimental and theoretical studies performed on systems of aqueous films confined in simple geometries: single film flowing across a bi-conical pore (*Rossen*, 1990; *Cox et al.*, 2004; *Ferguson and Cox*, 2013), single bubble (*Bretherton*, 1961) or bubble trains (*Cantat*, 2004;

Terriac et al., 2006) flowing in capillaries, two-dimensional monodisperse foams of various structures (e.g. staircase structures) flowing in a single channel (*Raven and Marmottant*, 2009; *Marmottant and Raven*, 2009). On the other hand, experimental studies performed on porous media have involved the use of core flooding units (*Fergui et al.*, 1998; *Apaydin and Kovscek*, 2001; *Pang*, 2010) from which it is difficult to obtain detailed information on the local foam structure (only global quantities can be measured), and where only qualitative information on local displacement dynamics is inferred. In recent years, the use of X-ray microtomography (*Apaydin and Kovscek*, 2001; *Zitha et al.*, 2006; *Nguyen et al.*, 2007; *Du et al.*, 2008; *Simjoo et al.*, 2012) or γ-ray attenuation (*Fergui et al.*, 1998), has enabled limited visualization of foam flows, revealing regions of preferential occupation of the medium by the foam and providing spatially-resolved measurement of liquid fractions, also under conditions of oil sweep (*Simjoo et al.*, 2013). Experiments based on micromodels consisting of pore networks (*Jeong et al.*, 2000; *Chen et al.*, 2005; *Ma et al.*, 2012; *Jeong and Corapcioglu*, 2003), on the other hand, have mainly been used to investigate oil or NAPL sweep, and have not allowed precise bubble-scale observation of the foam kinematics, or only on a small subpart of the system (*Jeong and Corapcioglu*, 2005), for example in order to assess the role of capillary snap-off on foam generation (*Kovscek et al.*, 2007). Our experiments combine a detailed pore scale characterization of the foam's structure and a structural complexity of the medium that is intermediate between the idealized geometries of foam physicists and the micromodel studies performed by petroleum engineers. The experimental setup is based on a Hele-Shaw cell containing obstacles, which constitute the solid grains of the porous medium. The top and bottom plates are close enough, so that the foam's bubbles be squeased in-between them, making the foam two-dimensional.

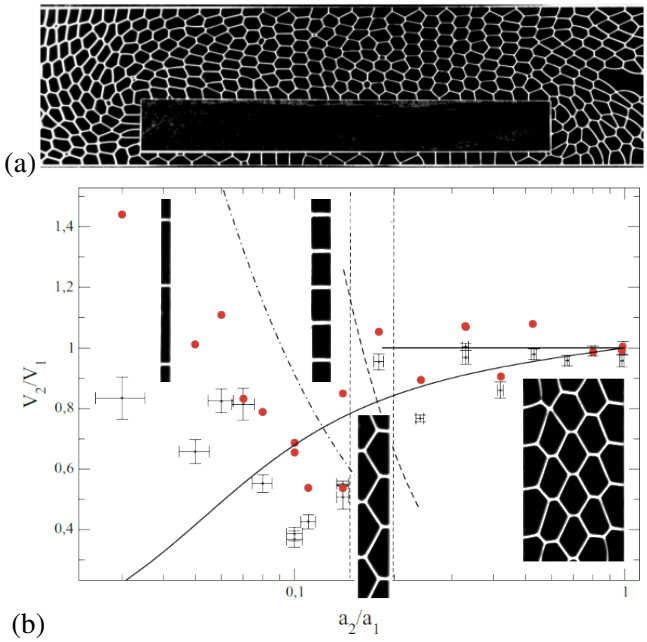

Figure 6: (a) Structure of the foam inside the flow cell during an experiment with two parallel channels. (b) Dependence of the ratio of the mean velocity in the wider channel to that in the narrower channel, as a function of the ratio a_2/a_1 of their widths. Figures adapted from (*Jones et al.*, 2013).

Our first study has addressed the role of structural changes in the foam on the distribution of fluxes in-between two parallel straight channels (*Jones et al.*, 2013). An rectangular obstacle was placed inside the main channel, oriented parallel to it, thus creating two parallel channels (see Figure 6.a). By translating the obstacle in the transverse direction, the ratio of the channel widths a_1 and a_2 could be changed. In Figure. 6.a the structure of the foam in the wider channel is that of a bulk 2D foam, while in the narrower it is a combination of *bamboo* structure (the films span the entire width of the channel) and *staircase* structure. By sufficiently reducing the width of the narrower channel, one changes the foam structure inside it from bulk to staircase and then bamboo. At each of these structural transition the distribution of fluxes between the two channels, under conditions of imposed total volumetric flow rate, is subjected to a discontinuity (see Figure 6.b). The resulting dependence of the ratio of mean velocities, V_2/V_1, as a function of the width ratio, a_2/a_1, is non-monotonic, as shown in Figure 6.b, in which experimental points appear as isolated dots with error bar, while the thin solid line shows the behavior expected for a Newtonian fluid. This unexpected behavior could be explained by modeling the link between the pressure drops in the two channels and the lamella velocities. The thick solid line, dot-dashed line and dashed line in Figure 6.b show the fully-analytical prediction of the behavior for the bulk, single staircase and bamboo structures. The red solid circles correspond to analytical predictions using prefactors inferred from the foam structure measured on the data.

A second study, using a geometry similar to that of Figure 6 but in which the obstacle was inclined, allowed us to evidence the impact of elastic effects on the distribution of fluxes between channels. Figure 7.a shows a snapshot of the foam structure while a foam is flowing around a tilted obstacle that is centered in the flow cell. The corresponding bubble velocity field (Figure 7.b) shows that the converging channel sustains more flux than the diverging one, due to the different elastic deformations of the bubbles in the two channels (see also

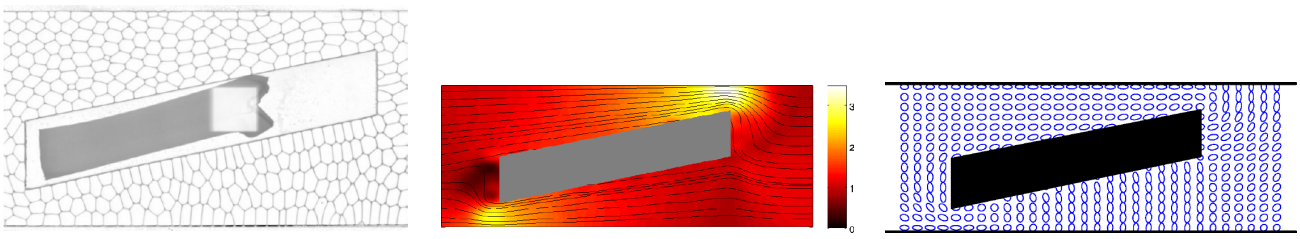

(a) (b) (c)

Figure 7: (a) Snapshot of the foam structure during the flow around a tilted obstacle, in a configuration for which the geometry is symmetrical with respect to the center of mass of the obstacle. (b) Bubble velocities measured inside the Hele-Shaw cell in the same geometry as in (a). (c) Representation of the corresponding elastic stress. Figures adapted from (*Dollet et al.*, 2014).

the elastic stress map of Figure 7.c) (*Dollet et al.*, 2014). Incidentally this also indicates that there is no flow reversibility for the foam. In this situation, the flow kinematics and constraint of flow incompressibility control the bubble deformation, which impacts the viscous friction, which in turn controls the distribution of fluxes between the two channels, and therefore the flow field.

We then proceeded with studying geometries consisting of cylindrical grains in-between which the foam is flowing (see Figure 8.a). The maps of bubble velocities evidence preferential flow paths corresponding to series of connected pores with a size larger than the average (Figure 8.b). Bubble velocities are also observed to be intermittent: some of the preferential flow channels exist for a number of seconds and then disappear, other preferential paths appearing at other places. This is due to the strong fluctuations in the capillary forces felt by the films/lamellas as they travel through the medium. Maps of bubble sizes evidence a correlation with the corresponding velocity maps (compare Figure 8.c versus .b). Figure 8.c also evidences a continuous decrease of the foam's average bubble size and an overall modification of the bubble size distribution as the foam flows through the medium.This is due to bubble fragmentation, which occurs as a consequence of lamella division. In this geometry and over this time scale, mechanisms responsible for lamellar destruction (foam coarsening and capillary snap-off) do not occur, and the dominant mechanism for lamella creation is lamella division. The resulting evolution of the probability density function for bubble sizes as a function of the longitudinal coordinate is shown in Figure 9.a (*Géraud et al.*, 2016). The original narrow symmetrical peak corresponding to the injected quasi-monodisperse foam disappears and another distribution, selected by the medium, appears. By running 45 experiments with different control parameters we could show that the fragmentation efficiency is mostly controlled by the average bubble area of the injected foam and by its water content. The fragmentation process can be modeled in terms of the probability density function (PDF) $n(a, x)$ of bubbles of size in the range $[a; a + da]$ in the longitudinal coordinate

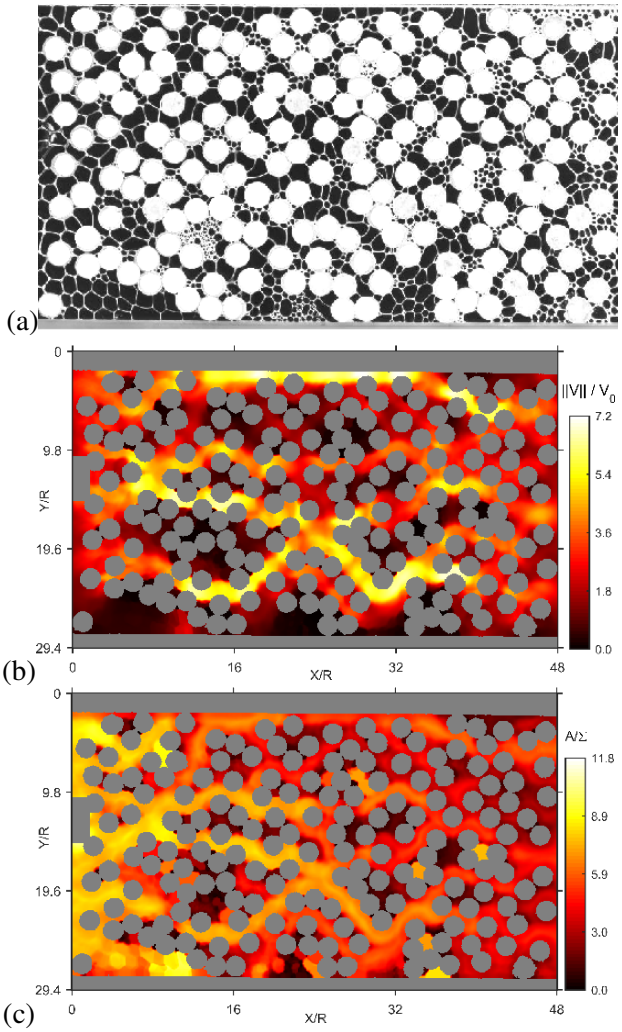

Figure 8: (a) Snapshot of a foam's structure as it flows through the 2D porous medium. (b) Corresponding map of bubble velocities normalized by the average velocity, V_0. (c) Corresponding map of bubble areas, normalized by a typica length of the porous geometry.

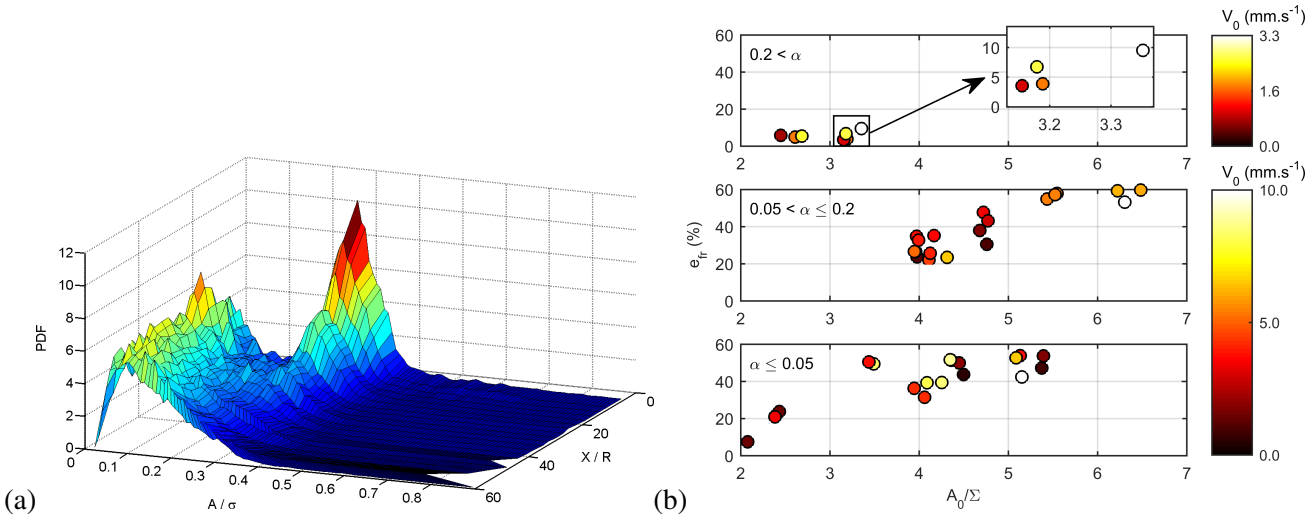

Figure 9: (a) Evolution of the bubble size probability density function along the porous medium length. (b) Dependence of the fragmentation efficiency on the three control parameters: normalized bubble area A_0/Σ, mean velocity V_0 and solution-to-air flux ratio α (indicating the water content). Figures taken from (*Géraud et al.*, 2016).

range $[x; x + dx]$. The conservation law for the bubble population translates into an evolution law for $n(a, x)$, which involves two statistical functions: the fragmentation frequency and the conditional PDF of daughter-bubbles area for a given area of the mother-bubble. Estimates of these two functions can be inferred from the experimental data, providing a rather satisfying match between the simulated evolution of the bubble size distribution and the one shown in Figure 9.a.

4.2 Transport and mixing of solute by flows with complex boudary conditions, and their consequences on reactivity

4.2.1 Environmental context

The processes controlling the transport, mixing, and reaction of solute species in subsurface water, are related to a number of environmental issues of major importance, such as the pollution of aquifers by agricultural fertilizers or chemical spills from the surface, the efficiency of underground nuclear waster storage sites or of CO_2 sequestration. In addition, the upper subsurface is an environment where bio-geochemical activity is very high. Although reactions involving living organisms take place at the pore scale within the porous and fractured media that are constitutive of the subsurface, between solute species or between such species and the solid phase (rock matrix or soil), they impact geochemical cycle and subsurface flows at much larger scales. For example the clogging of geothermal doublets by biological activity, which promotes the growth of biofilms within the porous space and is enhanced by the presence of oxygen in the injected water, can endanger the commercial viability of geothermal sites; the Antea groups considers that one out of three of its geothermal sites is concerned by this issue. Similarly, the quality of the water extracted from the hydrogeological site of Ploemer (near Lorient, French Brittany), which has been a long time study and research site for our research team at Géosciences Rennes, is be garanteed by an in situ denitrification process involving bacteria. From an even more global point of view, it has been stated that the mixing of chemical elements and nutrients in the subsurface (soils, vadose zone, groundwater) is a primary controlling process for biogeochemical cycles and contaminant transport in continental systems (*Grathwohl et al.*, 2013). At a more local scale, the efficiency of subsurface remediation based on chemical amendments is dependent on the efficiency of chemical reactions that occur between the amendments and the pollutant; the mixing of reactants potentially controls that efficiency.

4.2.2 Solute transport in a horizontal fracture

The physical processes that are responsible for solute dispersion in a flow are well known: advection and molecular diffusion. For a horizontal rough fracture with impermeable walls sustaining a low Reynolds number flow, their action leads to well-known longitudinal dispersion mechanisms (*Dronfield and Silliman*, 1993; *Roux et al.*,

1996; *Keller et al.*, 1999): longitudinal molecular diffusion, Taylor dispersion resulting from the interaction between the transverse heterogeneity of the advecting flow and transverse molecular diffusion (*Taylor*, 1954; *Aris*, 1956), geometrical dispersion arising from flow channeling in the fracture plane. If one neglects the aperture fluctuations, the dominant mechanism is Taylor-Aris dispersion, which settles to its well-known asymptotic regime over a time scale necessary for the solute to sample the entire distribution of velocities across the fracture thickness (*Dentz and Carrera*, 2007). The asymptotic regime can be described as a purely one-dimensional, longitudinal, Fickian process (which means that the solute cloud is invariant along the transverse direction) with a dispersion coeffcient $D_{\mathrm{T}} = D_{\mathrm{m}}\left(1 + \chi \mathcal{P}e^2\right)$, where D_{m} is the molecular diffusion coefficient, $\mathcal{P}e$ the Péclet number and χ a prefactor dependent on the geometry ($\chi = 2/105$ in the plane fracture geometry). The preasymptotic regime has also been computed analytically (*Gill and Sankarasubramanian*, 1970; *Berkowitz and Zhou*, 1996). We have seeked to generalize the classic Taylor-Aris configuration along to three lines:

(i) During the PhD of Laure Michel (2009, co-supervised with Jean de Bremond d'Ars), we showed that an even moderate density contrast between the carrier fluid and the fluid-solute mixture can play a significative role in the longitudinal dispersion of the solute. This discovery led to a numerical study of the role of density/buoyant coupling in a horizontal fracture (PhD thesis of Jérémy Bouquain in 2012, co-supervised with Philippe Davy), based on the Boussinesq approximation. We considered the question initially tackled by Taylor and Aris in their seminal papers (*Taylor*, 1954; *Aris*, 1956), but incorporating one more ingredient, namely the coupling between flow and transport. Buoyant coupling impacts only the preasymptotic regime, as seen in Figure 10. We define a reduced time τ such that transverse mixing is fully achieved for $\tau \gg 1$. The injected solute cloud is a very narrow vertical line spanning the entire fracture width, at longitudinal position 0. Figures 10.a and .b show the solute cloud at reduced time $\tau = 2 \cdot 10^{-3}$, that is, very early after injection. The magnitude of buoyant coupling is quantified by the value of the non-dimensional number $\mathcal{A}r^*$, which we have called *convective Archimedes number*: it is an estimate of the ratio of the buoyant term to the viscous term in the Navier-Stokes equation. In Figure 10.a, $\mathcal{A}r^*$ is close to 0, so no buoyant coupling is present (standard Taylor-Aris configuration): only longitudinal molecular diffusion and advection by the parabolic velocity profile have impacted the solute cloud. In Figure 10.b, on the contrary, $\mathcal{A}r^*$ is close to 2000, so that a large part of the solute has gone down due to its negative buoyancy and therefore has spread longitudinally on the bottom wall of the fracture. This has consequences on the time evolution of the apparent dispersion coefficient, which we compute during the preasymptotic regime as $(1/2)\, d\mathcal{V}/dt$, where $\mathcal{V}$ is the longitudinal variance of the solute cloud. Figure 10.a shows the evolution in time of the effective dispersion coefficient as a function of τ. The apparent dispersion coefficient (corresponding to the green plot in Figure 10.c) goes to D_{T} for $\tau \gg 1$ for all values of $\mathcal{A}r^*$, but the preasymptotic regime is strongly impacted by buoyant effects when $\mathcal{A}r^*$ is significant. The green plot corresponds to the solute cloud shown in Figure 10.a, while the red one corresponds to that shown in Figure 10.b. In the latter, the peak observed at $\tau < 0.01$ is due to the gravity-induced spreading seen in Figure 10.b. Further quantitative analysis shows that buoyant effects induce a time shift both in the position of the center of mass of the solute cloud and in the development of its longitudinal dispersion (*Bouquain et al.*, 2011).

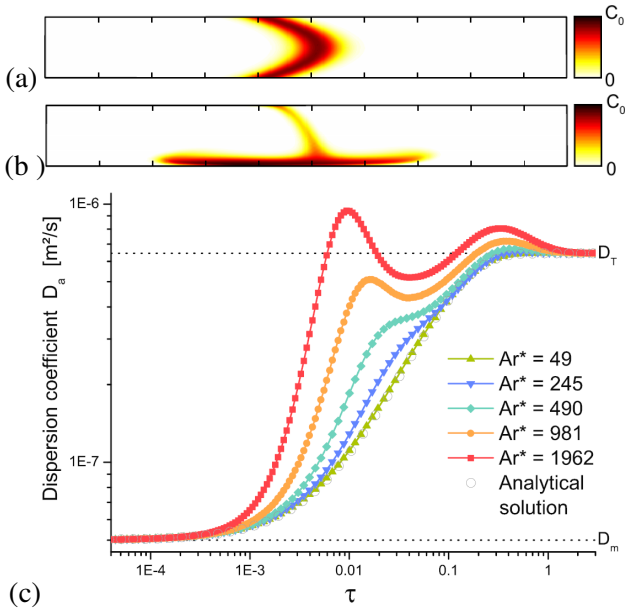

Figure 10: (a) Concentration map of the solute cloud at $\tau = 2 \cdot 10^{-3}$ for $\mathcal{A}r^* = 49$. (b) Same information shown for $\mathcal{A}r^* = 1962$. (c) Time evolution of the apparent dispersion coefficient during Taylor dispersion with buoyant coupling, for a Péclet 50 and various values of the advective Archimedes number.

(ii) Solutes transported by water can be exchanged between fractures and the interstitial porous space of the solid matrix. In general, the advection of solutes is fast along fracture networks, but the matrix can act as a trap for part of the solute, as its very low permeability makes solute transport through it only possible by molecular

diffusion. The PhD thesis of Laure Michel has shown that buoyant coupling, as well as effects related to the roughness of the porous walls, can significantly impact the fracture-matrix exchange (*Michel*, 2009). On the one hand the exchange is made possible at the bottom wall by negative buoyancy effects, on the other hand it remains mostly interfacial: there is no penetration of the solute by diffusion farther than a distance of the order of the pore size.

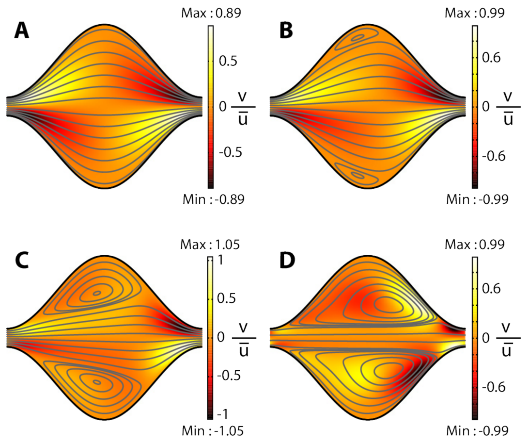

Figure 11: Recirculation zones observed in a 2D sinusoidal unit flow cell for various Reynolds numbers: (A) $\mathcal{R}e = 0.1$, (B) $\mathcal{R}e = 10$, (C) $\mathcal{R}e = 20$, (D) $\mathcal{R}e = 100$. The entire flow cell consists of the repetition of this unit cell for as many times as necessary.

(iii) We have also investigated the influence of local aperture fluctuations on the longitudinal dispersion of a passive (not buoyant) solute, in a 2D fracture with a sinusoidally-varying aperture field (*Bouquain et al.*, 2012) and under laminar but inertial flow conditions (Reynolds numbers ranging between 1 and 100). This study was carried out in collaboration with Diogo Bolster (Univ. Notre-Dame, USA), on a geometry that he had used previously used (*Bolster et al.*, 2009), but extending his study to inertial flows. The flow non-linearity is responsible for the existence of asymetric recirculation zones, which render the flow non-reversible and trap a large amount of solute. These recirculation zones, as well as the mere curvature of the flow (for configurations of lower Reynolds and small aspect ratio of the flow cell in which there is no circulation zone), impacts the longitudinal dispersion, and this all the more as the Reynolds is larger. Defining the apparent dispersion coefficient as explained above in (i), we proposed a law for the scaling of the asymptotic apparent dispersion coefficient as a function of both Péclet number and Reynolds number, in the form $D_a = D_m \left(1 + (2/105)\,\alpha\,\mathcal{P}e^{2+\beta}\,f(\mathcal{R}e)\right)$, where α and β are numerical constants that depend on the detail of the geometry (mean aspect ratio ε of the unit flow cell and ratio a of the aperture variation amplitude to the average aperture) and f is a master function that goes to 1 for very small values of the Reynolds number (see Figure 12.a) . This relation is a generalization of the Taylor-Aris relation for this sinusoidal geometry and for magnitudes of the Reynolds number ranging from the Stokes regime to laminar flows with significant inertia. Consequently, for a fracture of constant aperture α goes to 1 and β to 0. The dependence of α and β as a function of a and ε, consistent with these limits, are shown in Figure 12.b) (*Bouquain et al.*, 2012). β is negative, which shows that the deviation from the exponent 2 typical of the Taylor-Aris relation is negative, and this all the more as the cell aspect ratio is larger. Furthermore, we have modeled the transport by a continuous time random walk (CTRW) *Bolster et al.* (2014), and showed that for sufficiently large Péclet numbers and significant inertial effects, CTRW modeling cannot only be successful at predicting the dispersion process if correlations in the lagrangian velocities *Le Borgne et al.* (2008) are accounted for. In addition, if buoyant coupling is taken into account, the observed trapping of solute

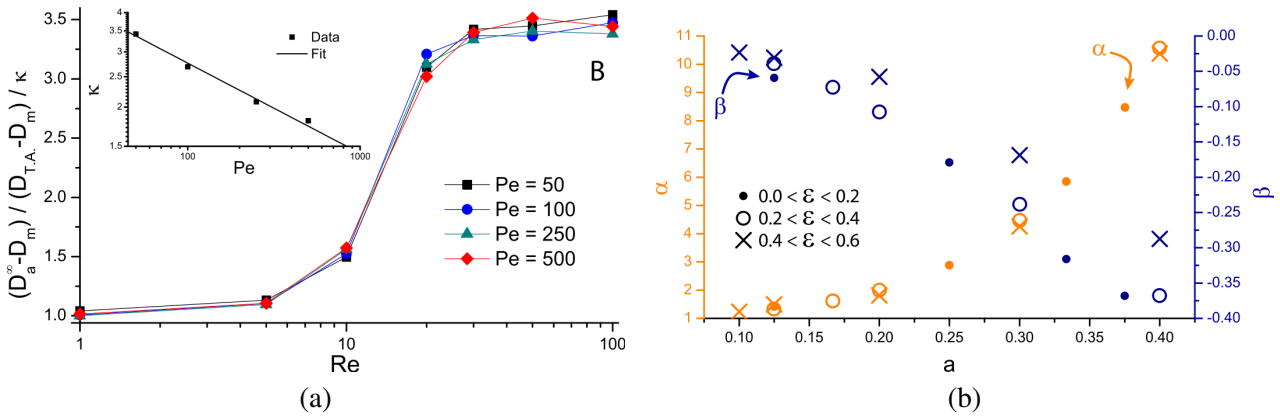

Figure 12: (a) Dependence of the master curve f on the Reynolds number. (b) Dependence of the α and β on the geometrical parameters of the unit flow cell.

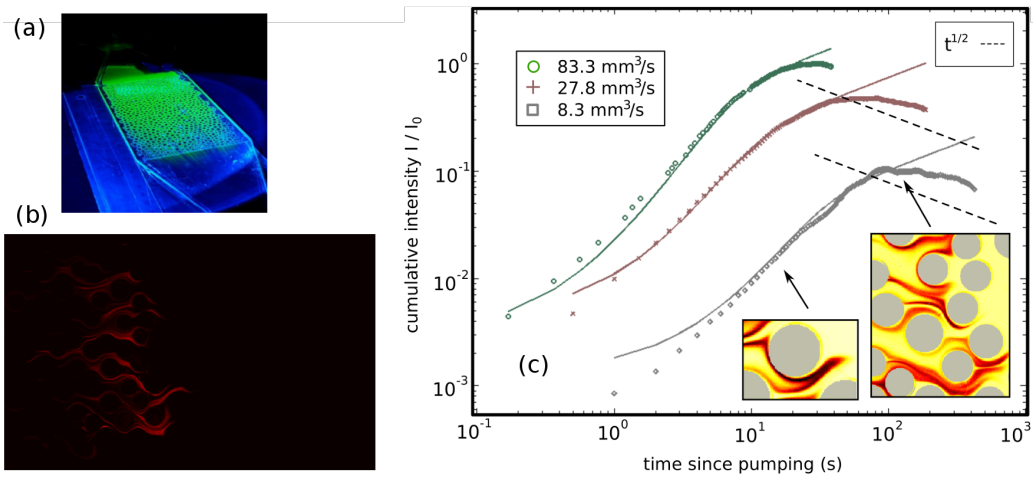

Figure 13: 13(a) Photo of the experimental setup at the end a conservative solute transport experiment. (b) Image of the local reaction rate during a chemoluminescent $A + B \longrightarrow C$ reaction. (c) Corresponding time evolution of themass of reaction product (symbols), confronted to continuous plots obtained from an upscaling theory developed by *de Anna et al.* (2014a). Figures adapted from (*de Anna et al.*, 2014b).

within low velocity and recirculation zones is more radical *Bouquain* (2012).

4.2.3 Reactive transport and solute mixing in a 2D saturated porous medium

The reaction between solute species transported by a liquid inside a poroud medium is only possible if they come in contact. It is therefore potentially dependent on the mixing of the two reactants: if the time characteristic of mixing if much shorter than that characteristic of the reaction's chemical kinetics (very low Damköhler number), the system is *well-mixed*, and reaction rates measured in situ should correspond to those expected from the chemical kinetics. If not, mixing is expected to limit in situ reaction rate. It is often the case in porous media, because the pore scale velocity field is very heterogeneous due to the no-flow boundary condition at the solid walls (*de Anna et al.*, 2013), so that the geometry of the mixing fronts is very complex. This is why reaction rates measured in subsurface media depend on the observation scale (*Meile and Tuncay*, 2006; *Lichtner and Kang*, 2007), while reaction rates measured in well-mixed reactors (*batchs*) in the laboratory are several orders of magnitude larger than those measured in the field.

This limitation of reaction by mixing at large enough Damköhler numbers had been studied in the laboratory by (*Gramling et al.*, 2002) using a Hele-Shaw cell filled with sand and a Darcy scale measurement of the reaction product's concentration based on colorimetry techniques. These authors could evidence that Fickian theories would not provide them with a model consistent with their data, and rightfully attributed this inconsistency to incomplete pore scale mixing. During his PhD, Pietro de Anna and his advisor Tanguy Le Borgne had performed a numerical study of the same process in a two-dimensional (2D) porous medium, and developed an upscaling theory predicting the time evolution of the mass of product (*de Anna et al.*, 2014a) for a very fast reaction (very large Damköhler number), based on an analysis of the mixing interface in terms of stretching lamella. We then set up an experiment to test their theoretical and numerical predictions (also in collaboration with Hervé Tabuteau, of the Institut de Physique de Rennes). It is the same setup that was later used for two-phase flow studies (see section 4.1.3 and Figure 3), but with much larger pores so as to optimally measure the concentration field at the pore scale (see Figure 13.a). The measurement of the local reaction rate is done using a chemolumniscent reaction of the type $A + B \longrightarrow C + \nu$, ν denoting a number of photons (*de Anna et al.*, 2014b), and a very sensitive camera (sCMOS). Solute transport first occurs in fingers that progress along the longitudinal direction (coalescence regime, see Figure 13.b), after which they start coalescing along the transverse direction through molecular diffusion (*stretching regime*). For this regime the stretching of the lamellar interface that is at the heart of the mixing volume, is linear, which allows solving for the equation that controls the time evolution of the lamella thickness. We thus obtain a prediction of the time evolution of the mass of product in that regime. In Figure 13.c the data and the theoretical predictions are superimposed. The $\sqrt{t}$ regime is what would be observed if mixing was complete at the pore scale. In the coalescence regime, the time evo-

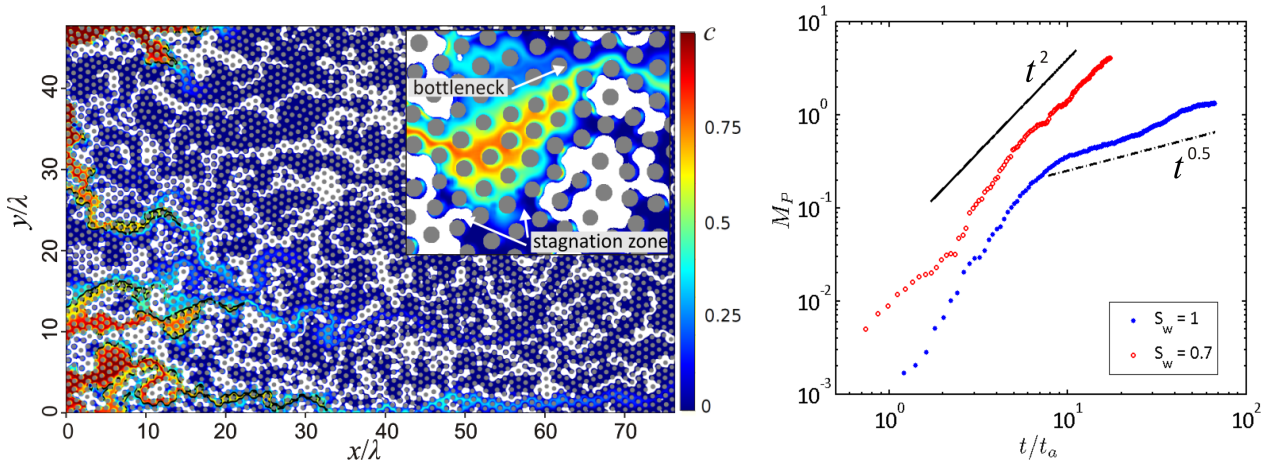

(a) (b)

Figure 14: (a) Snapshot of the concentration field during solute transport through a 2D unsaturated porous medium. The air appears in white, the solid grains in gray. The inset shows a closeview of a subpart of the medium. (b) Time evolution of the total mass of product. Figures adapted from (*Jiménez-Martínez et al.*, 2015).

lution of the mass product can also be predicted from the measurement of the mixing volume during a separate experiment of passive transport conducted in the same porous medium (*de Anna et al.*, 2014b).

Up to very recently, these studies, either theoretical or experimental, only considered the limit of very large Damköhler numbers, for which the local reactivity is completely controlled by local mixing. Further developement of the theory, addressing the effective reaction kinetics at intermediate Damköhler numbers for a simple shear flow in 2D, has been recently undertaken by Aditya Bandopadhyay in the framework of his postdoc (co-supervised by Tanguy Le Borgne and myself). Using the one-dimensional (1D) lamellar theory, scaling laws and crossover times for the product mass could be inferred theoretically and modeled numerically, as a function of Damköhler and Péclet numbers (*Bandopadhyay et al.*, 2016).

4.2.4 Transport and mixing in the unsaturated zone

The unsaturated zone, or vadose zone, in particular, plays a fundamental role in the transfer of chemical substances from the surface to ground water resources. It is formally defined as the zone in-between the water table and the Earth's surface, where air and water coexist in the porous space. The presence of air complexifies water flow lines to a great extent, and widens the velocity distribution. The question of how transport, mixing, and, consequently, reactions, are impacted by the presence of air, is still very open. During the postdoc of Joaquin Jimenez (2011-2014), and in collaboration with Tanguy Le Borgne and H. Tabuteau (IPR), we have attempted to answer that question in a 2D porous medium with pore scale heterogeneities but no macro-heterogeneities. The experimental setup is similar to the one described in section 4.2.3, but the medium has much more grains (~ 4500) and air can be injected together with the liquid. The two fluids are flown jointly into the medium until a *stationary two-phase flow* (whose properties have been studied by *Tallakstad et al.* (2009)) is established in the medium in order to obtain a homogeneous Darcy scale saturation, with reproducible statistical properties of the phase distribution, in the medium. The flow of gas is then interrupted, and the solute is injected continuously in the liquid flow at the medium inlet. The solute is fluorescein, which allows measuring its concentration field at regular time intervals. We observed that in unsaturated conditions, local concentration gradients, which are the driving force of mixing, are sustained for a longer time (*Jiménez-Martínez et al.*, 2015). The resulting mixing behavior can be measured in terms of the scalar mixing rate, which is the integral over the entire system of the square of the concentration gradient. In this experiment there is no reaction. Let us now imagine that the resident liquid and the injected one react according to a bimolecular, irreversible, quasi-instantaneous (very high Damköhler), reaction, the product of which would not impact the subsequent transport of the reactant. The local reaction rate can then be computed from the sole knowledge of the mixing of the two liquids, following the theory derived by *de Simoni et al.* (2007) (see also (*Willmann et al.*, 2010)). The resulting time evolution of the mass of product is shown in Figure 14.b, for for a water saturation $S = 0.7$ and in saturated conditions ($S = 1$): while under saturated conditions the Fickian scaling in $\sqrt{t}$ is reached after the time neede for the flow

to advance by one typical grain size, for unsaturated conditions the product mass grows as t^2 (*Jiménez-Martínez et al.*, 2015). Recent results obtained in the same experimental setup but using a finite injected volume of solute show that the continuous injection is actully a fundamental prerequisite for this regime of sustained mixing and reaction (*Jiménez-Martínez et al.*, 2016).

4.2.5 Upscaling of mixing in porous media from the knowledge of the lagrangian flow velocities

During the PhD of Régis Turuban (2012-2016, co-supervised by Tanguy Le Borgne), we are attempting to characterize solute mixing in a 2D porous medium from the knowledge of the lagrangian velocities of fluid particles, using the same type of 2D porous medium as presented above. They are measured from the optical particle tracking of purely advective solid particles. From this velocity field we can analyze the stretching of the fluid and link it to the mixing process occurring when a conservative solute tracer is injected in the same medium, using for this the lamellar theory as proposed by *Le Borgne et al.* (2013).

4.2.6 Nature of the mixing in 3D

While the 2D systems presented above provide a full experimental characterization of flow and transport, ideal for testing mixing and reactive transport models, most relevant applications, in particular in the subsurface, involve three dimensional (3D) flows. A theoretical study by *Lester et al.* (2013) has suggested that the additional degree of freedom offered by the third dimension may generate chaotic advection. In other words, the fluid line separating two fluid particles initially very close to each other is expected to be stretched continuously in such a manner that its length grows exponentially in time. Such a flow would strongly enhance mixing, and consequently the local effective chemical reaction rates. The chaotic nature of 3D porous media flows, if verified, would have profound implications for reaction kinetics and biological activity as discussed in the review of *Tél et al.* (2005). Since 2013 this still rather open question has been the motivation behind a collaboration with Daniel Lester (then CSIRO Melbourne, now at the RMIT university in Melbourne), and the main topic of Régis Turuban's PhD (co-supervisor Tanguy Le Borgne, Géosciences Rennes).

Chaotic flows can only be obtained if the topology of the flow follows a baker's map of some sort, that is, if fluid particles get separated in some regions of the medium by a virtual interface (called a 2D manifold) that they cannot cross and if manifolds that are locally non parallel to each other interact. One part of our efforts has therefore been devoted to developing very finely meshed numerical simulation of Stokes flow in various types of regular bead packs (simple cubic, centered face cubic, centered cubic), as well as periodical random bead packs, and an effective particle tracking scheme, in order to understand under which conditions such topological structures arise in the flow. One way to do this is to study the maps of skin friction at the surface of the spheres

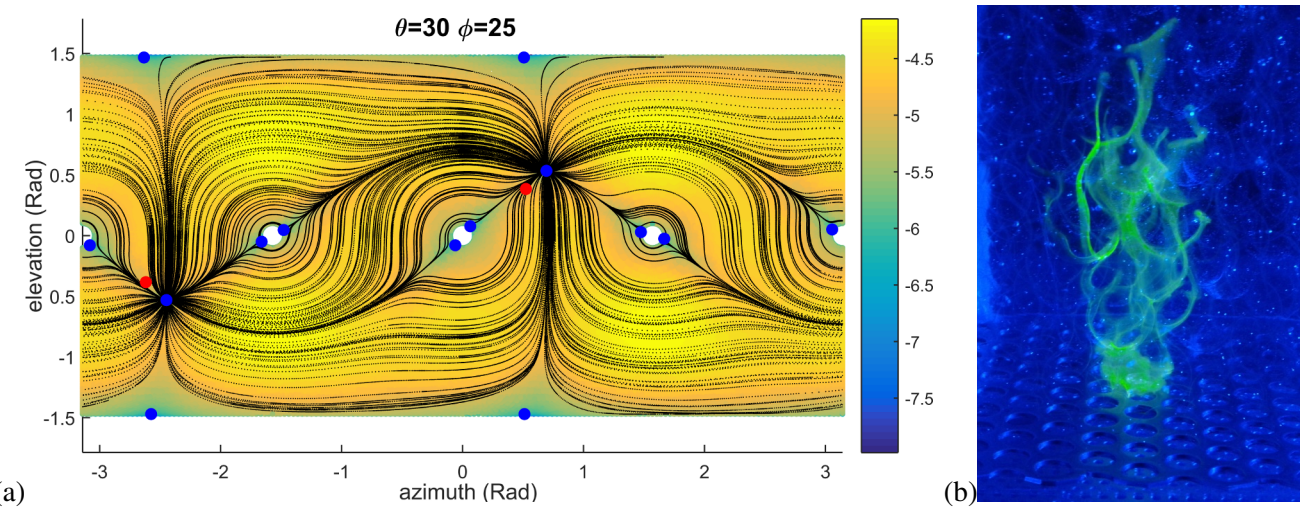

(a) (b)

Figure 15: (a) Map of the skin friction at the surface of a sphere within a simple cubic packing. The red dots indicate the average flow direction, and the blue dots indicate the position of the critial points, either node points or saddle points. Field lines of the skin friction field are superimposed. (b) Spreading of a conservative solute inside an index-match glass bead pack.

(see Figure 15.a). Skin friction is the shear stress measured on the surface, that is, it is proportional to the derivative of the velocity component tangent to the sphere with respect to the radial coordinate. The critical points (in blue) are locations at which the skin friction vanishes. They are of two kinds: node points, at which all stream lines converge, and saddle points, which some stream line converge to and others tend to avoid. The stream lines that go out of the sphere's surface in the vicinity of a saddle point define a 2D manifold (*Surana et al.*, 2006). If by combination of the medium's periodicity and orientation of the average flow a manifold connects to the same manifold on a sphere belonging to the next unit sphere, then no chaos is generated. If not, chaos will be generated. Régis is currently mapping the orientational space to determine which orientations of the average flow lead to chaos generation in the various bead packings considered.

Another objective of the project was to develop a 3D setup in order to perform 3D measurements analogue to those performed on the 2D setup. This has been tackled using optical matching of the fluid with the solid phase: the liquid consists of a mixture whose components' concentrations can be adjusted so as to bring the mixture's optical index as close as possible to that of the solid grains (in our case, glass beads). Figure 15.b shows an example of 3D cloud of solute injected into an optically-matched packing of glass beads. Flow velocities are measured from the tracking of solid particles with two cameras that record the projections of the particles' positions in two perpendicular planes. Three-dimensional concentrations fields are reconstructed from the recording of slices of the medium illuminated by a laser sheet; the data will be confronted to our theoretical/numerical predictions.

4.2.7 Diffusive transport of water vapor through a weakly-hydrated clay

Clay minerals are finely-divided and nano-organized materials, whose structural properties I describe in detail in section 4.3.2 below. For the purpose of this paragraph it is sufficient to say that weakly-hydrated samples of swelling clays are porous materials possessing a connected mesoporosity in the micrometer range, in-between mineral grains, and a nanoporosity inside the grains. The mineral grains are stacks of individual 1 nm-thick clay particles (the layers) and have the ability to swell by incorporating H_2O molecules (or other molecules such as CO_2) in-between the layers, depending on the ambiant temperature and on the humidity present in the mesoporosity surrounding the grain.

The question of vapor transport in soils is traditionally associated to that of evaporation, which consumes about 25% of solar energy input (*Or et al.*, 2013). In this study, however, there is only one fluid phase; imposing a gradient of relative humidity (RH) along a temperature- controlled dry sample of swelling clay, we have investigated the diffusive transport of water molecules in vapor phase through the material. As water molecules diffuse through the mesoporosity, some of them intercalate into the nanoporosity, causing the grains to swell and therefore a decrease in the mesoporous volume available for vapor diffusion. These two effects render the transport process potentially anomalous. We monitor it using space- and time-resolved X-ray diffraction at a synchrotron source; sparticle swelling results in a shift in the scattering angle characteristic of the main diffraction peaks. We can thus follow the advancement of the intercalation front inside the material (*Løvoll et al.*, 2005b; *Méheust et al.*, 2006). Furthermore, using static hydration experiments we can map out the subtle changes (~ 0.1 Å) in interlayer thickness associated to changes of relative humidity that occur in the mesoporous space, in the vicinity of the clay grains, between two hydration transitions. We can thus convert the measured interlayer spaces into a relative humidity measurement in the mesoporous space (*Hemmen et al.*, 2010). Longitudinal RH profiles recorded in time are then analyzed using a generalized Boltzmann-Matano analysis (*Crank*, 1979). If the transport process can be described by a fractional time diffusion equation with characteristic exponent γ ($\gamma = 1$ for standard Fickian diffusion), we can collapse all humidity profiles onto a single master curve by plotting them as a function of the reduced coordinate $x/t^{\gamma/2}$. Our first such study, performed using Na-fluorohectorite (that is, fluorohectorite for which the cation intercalated in the nanoporous space is Na^+), concluded that the diffusion was either normal or weakly-anomalous (*Hemmen et al.*, 2010). This was confirmed by a recent study, in which we also performed measurments on Li-fluorohectorite. We

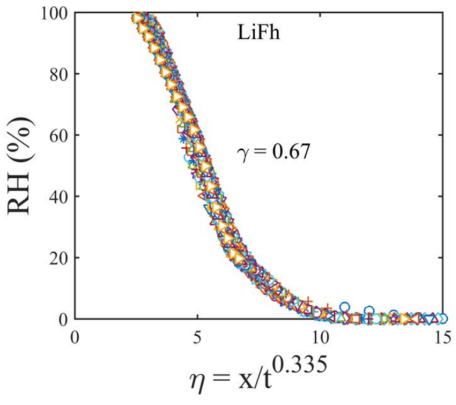

Figure 16: Humidity profiles recorded with Li-fluorohectorite, rescaled and collapsed onto a unique master curve.

found a significantly subdiffusive behavior ($\gamma = 0.335$, see Figure 16) for Li-fluorohectorite (*Michels et al.*, 2016). The different nature of the longitudinal diffusion process is due to a different dynamics of the water intercalation into the clays nano-stacks, as otherwise inferred from static experiments. Note that in both cases we infer the functional dependence of the effective diffusion coefficient on the relative humidity, from the data.

4.3 Clay-based complex fluids

4.3.1 Environnemental and industrial context

The complex fluids that I am considering here are suspensions of smectite clays (also called *swelling clays*) either in aqueous (saline solutions) or non-aqueous (silicon oils) liquids. Clays minerals arise from the hydrolysis of silicate minerals (*Velde*, 1992) and are found on a large portion of the Earth's surface. They are phyllosilicates, which means that the basic crystalline structure is a *platelet* of about 1 nm thickness. This extremely divided nature, in combination with the strong colloidal interaction when suspended in an aqueous liquid, provides them with very interesting physico-chemical properties, which explain why they are being used in a large number of industrial applications (rheology control of paints, catalysis, paper filling, drilling muds for the petroleum industry, fillers in a number of composite materials). It also provides them with a peculiar property as a subsurface formation: they have a very large porosity, but consisting mostly of cavities in the nano-meter to micro-meter range, and a very small permeability. For this reason clay minerals are often constitutive of cap rocks above oil reservoirs or deep aquifers. The French Underground Research Laboratory dedicated to preparing the undergroud storage of high-level and long-lived medium-level radioactive waste, is being developed in shale/argillite formation for the same reason.

The study of the Physics of clay colloids was my main research topic when I was a Postdoc and then Research Scientist at the Norwegian University of Science and Technology (Trondheim, Norway). The work summarized below has been undertaken either within or in collaboration with the group of Jon Otto Fossum (Laboratory for Soft and Complex Matter Studies at NTNU).

4.3.2 Swelling clay minerals: a complex type of colloids

Smectites, or swelling 2:1 clays, have a base structural unit which is a phyllosilicate platelet formed by two inverted silicate tetrahedral sheets that share their apical oxygens with a tetrahedral sheet sandwitched in between (*Velde*, 1992), as shown in Figure 17.d. We have used two types of smectites: laponite and fluorohectorite. Laponite is a synthetic smectite, which is monodisperse (with a platelet size 25 µm) and has been the favorite anisotropic colloid of physicists for two decades. Fluorohectorite clays have a chemical formula per unit cell X_x-$Mg_{3-x}Li_xSi_4O_{10}F_2$. As for natural hectorites, substitutions of Li^+ for Mg^{2+} in part of the fully occupied octahedral sheet sites within each platelet, are responsible for a negative surface charge along the platelets. Fluorohectorites differ from natural hectorites in that hydroxyl groups have been replaced by fluorine atoms. The large surface charge of fluorohectorites (1.2 e^- as opposed to 0.4 e^- for laponite) allows the platelets to stack by sharing an intercalated cation (denoted X in the formula above), which can be for example Na^+, Ni^{2+} or Fe^{3+}. In contrast to laponite, these decks of cards remain stable in suspension, even at low ionic strength of the solvent. However water molecules can enter the interlayer space; this hydration process occurs with thermodynamically-favored molecular packings which are denoted *water layers* (nWL). The hydration transition between nWL and $(n+1)$WL ($n = 1$ to 3) is a first order phase transition that results in swelling of the particle (*Salles et al.*, 2009), hence the denomination of swelling clays. The mean thickness of the nano-layered particles in saline gel/sol has been measured by wide angle X-ray scattering experiments to consist of 20 to 100 stacked platelets (*DiMasi et al.*, 2001; *da Silva et al.*, 2002; *Hemmen et al.*, 2009). An interesting feature of

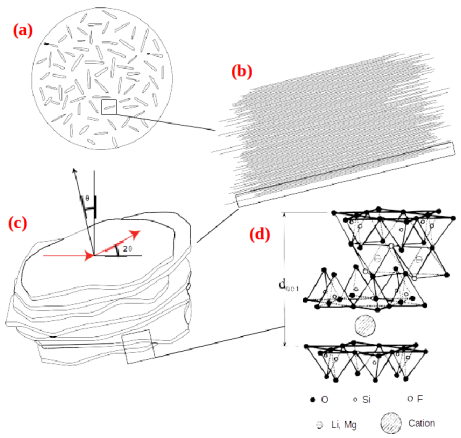

Figure 17: Structural organization of a suspension (a) of clay fluorohectorite colloids. (b-c) The flurohectorite in suspension consist of deck-of-cards where the cards are the individual platelets. Each of these platelets is a crystallite (d) of well-defined structure. Adjacent platelets are held together by sharing intercalated cations.

these fluorohectorite suspensions is that, as most natural clay systems and in contrast to laponite systems, they are polydisperse (*Kaviratna et al.*, 1996; *DiMasi et al.*, 2001).

4.3.3 Collective self-organization of clay colloids in saline solutions

When suspended in a saline solution, clay particles present a wide range of phase behaviors, depending on (i) the concentration in salt, which controls the thickness of electric double layers at the clay-water interface, and therefore the manner in which the colloidal interaction between two particles depends on the distance between them, and (ii) the concentration in clay particles, which controls the typical distance between adjacent particles. Laponite is the best characterized system in this respect (*Levitz et al.*, 2000; *Mourchid et al.*, 1995, 1998). In particular, laponite is well known for giving rise to nematic phases, that is, phases in which the platelets are lying parallel to each other but without a particular positional order, for suitable concentrations in salt and colloids.

We have studied the colloidal and phase behavior of polydisperse suspensions of Na-Fluorohectorite. The samples' polydispersity, with the largest particules of size of order 1 µm, is responsible for a spontaneous heterogeneous sedimentation, which occurs in competition to gelation. This process leads to the formation of gel and sol phases on top of each other, including a nematic sol phase which is denser than the isotropic sol phase, and features clay particles oriented with their planes along the vertical direction. We have characterized the vertical extent of the different phases as a function of the concentrations in salt and clay, using visual observation under polarized light (*Fossum et al.*, 2005; *Fossum*, 1999) and synchrotron small angle X-ray diffusion (WAXS) (*Fonseca et al.*, 2007). By measuring the local concentration in clay particles from the absorption of the X-ray signal, we could convert the vertical position in the sample tubes into the concentration in clay particles, and therefore obtain a phase diagram that can be compared to that of laponite (*Fonseca et al.*, 2009). A further study resorting to the additional aid of NMR (nuclear magnetic imaging), in collaboration with the group of Mario Engelsberg at the University of Recife (Brazil), evidenced another nematic phase consisting of horizontal-lying platelets (*Hemmen et al.*, 2009), and positined between the sol phase and the nematic phase discussed above. Note that since Na-fluorohectorite particles are nano-stacks of individual platelets, they diffract X-ray mostly as one-dimensional diffraction gratings. Using this property I have developed a method to infer the angular probability density function of the clay particles from the anisotropy of 2D diffractograms (*Méheust et al.*, 2006). This technique works for angular orientational orders that can be described with only one angle, such as in nematic or anti-nematic phases (*de Gennes and Prost*, 1993). The model has now been used by a number of other groups. In the study by *Hemmen et al.* (2009) it was used to measure the nematic order parameter of the newly-discovered nematic phase.

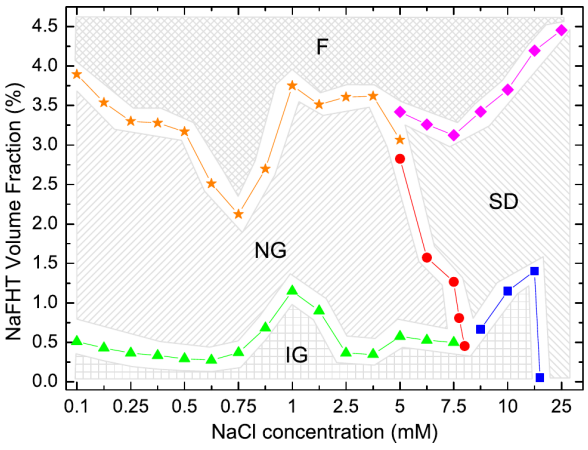

Figure 18: Phase diagram of Na-Fluorohectorite.

4.3.4 Free surface flows of clayey muds

The rheology of smectite clay suspensions is both shear-thinning and thixotropic, which means that the suspensions' microstructure is subjected to two antagonistic processes: aging and shear rejuvenation. Aging is observed when the sample is left to rest, and consists in a self-organization of clay particles under the effect of their colloidal interactions, leading to a strengthening in time of the sample's cohesion, and therefore of the yield stress that one shall have to impose on the material to make it flow. Shear rejuvenation, on the other hand, is the destruction by shear of this self-organization of the microstructure when the material is forced to flow and therefore subjected to shear. A nice synthesis on the topic of these antogonistic effects can be found in (*Møller et al.*, 2006). We have performed experiments on samples of the marine clay from the Trondheim region, in Norway. This is a so-called *quick clay*, which has the ability to suddenly liquefy when the stress conditions imposed on it changes abruptly. The infamous Rissa landslide (Norway, 1978) is a famous example of such a catastrophic behavior. Our avalanche experiments consisted in suddenly inclining at a controlled angle from

the horizontal the plane onto which a clay heap had previously been resting. We then measured the position of the most advanced tip of the flowing fluid in time, as well as the runout length and height of the final deposit, for various initial water contents of the material. This means that the material was remoulded, that is, that the in situ samples had been dried and subsequently rehydrated with a controlled water content. The avalanche experiments evidenced three types of flow regimes: (i) a liquid flow regime, similar to that of a Newtonian fluids, for suspensions with a very small initial yield stress; (ii) a yield stress fluid regime, for suspensions with a sufficiently large initial yield stress; in this regime the heterogeneity in the flow distribution is not too large; and a (iii) mudflow regime, for suspensions with an intermediate initial yield stress; in this regime the flow is strongly localized in a liquefaction layer in the vicinity of the supporting plane's surface. For a range of initial yield stresses the mudflow regime was observed to be more efficient to transfer material down the slope. A simple heuristical model explained the measured runout lengths and height deposits (*Khaldoun et al.*, 2009). Recent further work has provided a phase diagram for the flow regimes in the parameter space formed by the water content of the material and its initial resting time.This diagram is shown in Figure 19. It is similar to that observed in earlier study on bentonite/montmorillonite muds (*Coussot et al.*, 2005).

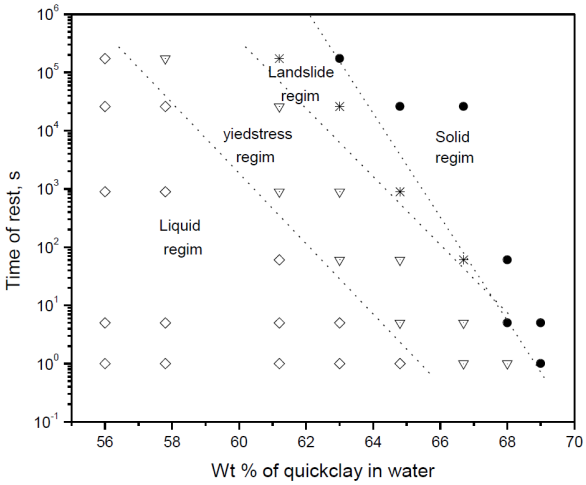

Figure 19: Phase diagram for the flow regimes of the Tiller marine clay as a function of its solid content and resting time. From (*Méheust et al.*, 2016).

4.3.5 Electro-rheology of clay suspensions in silicon oil

Clay particles are electrically-polarizable. When suspended in a fluid with a low electrical conductivity, such as a silicon oil, and subjected to a strong electric field ($\gtrsim$ 1 kV/mm), they behave as small electric dipoles which interact with each other and form chains parallel to the applied electric field. This process is called electrorheology (*Halsey*, 1992); it results in a radical modification of the mechanical properties of these suspensions, in particular with a strong increase of the yield stress. For this reason they would potentially be very useful to design smart materials whose mechanical properties could be tuned with an electric field. We have measured the rheology of such electrorheological fluids, either laponite-based (*Parmar et al.*, 2008) of Na-Fluorohectorite-based (*Méheust et al.*, 2011). We have in particular measured the dependence of the yield stress on the strength of the electric field E and initial clay particle concentration Φ, and obtained for laponite a scaling law in the form $E^{1.85}\,\Phi^{1.70}$ (see Figure 20). Particle polydispersity was observed to weaken the electrorheological structure. A study based on X-ray diffraction has allowed us to characterize the orientation of the clay particles within the chains, based on the method presented above (*Méheust et al.*, 2006), to subsequently find the direction of polarization of the clay crystallites with respect to their crystalline structure. We have also shown that the polarization not only concerns surface charges adsorbed to the outer surfaces of the particles, but also the ions intercalated within them (*Fossum et al.*, 2006).

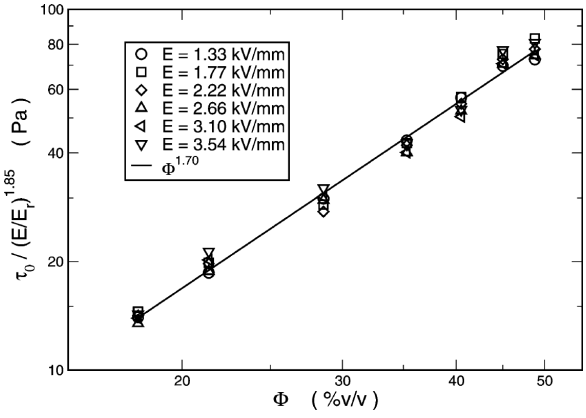

Figure 20: Experimental data showing the scaling of the static yield stress of electrorheological suspensions of laponite as a function of the imposed yield stress E and of the mean concentration in colloidal particles, Φ. Figure from (*Parmar et al.*, 2008).

4.4 Collaborations and funding

4.4.1 Applications for funding and funding sources

The list of projects funded, their title and the associated amount of funding, have been given in my CV (section 2). However I want to give here a circumstantial description of the successful grants that I have been associated to since I became Maître de Conférence at Université Rennes 1. I consider that they belong to three categories:

- Grants devoted to funding travels, which have allowed me to maintain long lasting international collaborations, most particularly with colleagues in Norway and Brazil.

They did not necessarily involve a large funding, but have been crucial, as there is basically no yearly travel money associated to academic positions in France. Such are the Egide project (2008-2009, 20k€) and the PICS program (2009-2011, 25k€ for three French teams), both between France and Norway and both of which I was P.I. for. The Norsk Forskningsraadet project of 2014-2016 is different since it is a Norway-based project which I supported officially but did not write; its objectives were to fund international collaborations and conferences between Norway, France and Brazil, and it has funded a number of my trips to either Norway or Brazil.

- Grants devoted to funding a specific item, either equipment or a young researcher position.

In 2009 I was awarded an "Allocation Rennes-Métropole" for equipment (40 k€), which allowed me to upgrade the Laboratory for Analogue Experiments in Hydrology significantly; in particular I could buy my first good camera, optical tables and displacement stages etc. We then obtained funding from INSU/CNRS (2012-2014), also for equipement, to study solute dispersion and mixing in the unsaturated zone. This allowed us to double our budget for equipment in the lab.

Another funding that has played an important role is the CREATE granted by Région Bretagne in 2011 for a proposal that I had written with Isabelle Cantat (Institut de Physique de Rennes). It gave us a 3 year postdoc position, and allowed us to start a fruitful collaboration on foam flows though porous media.

- Large grants including the funding of both researcher positions, equipment, consumables, and travel.

As a new permanent researcher in the team Transferts d'eau dans les milieux hétérogènes complexes at Géosciences Rennes, I have been lucky to be part of a dynamic reseach group, well funded by ANR (Agence Nationale de la Recherche) and the EU. I was associated to ANR Mohimi (2008-2010) and though taking a modest part in it I have benefited from it. I was more significantly involved in european ITN network IMVUL (2008-2012), which has funded Pietro de Anna's PhD, and in european Interreg project CLIMAWAT, which has funded part of Joaquin Jimenez's postdoc (2011-2014) as well as consumables for the laboratory.

In the last year and a half, Tanguy Le Borgne was awarded an ANR Jeunes Chercheurs (2015-2018, 406 k€) and then an ERC Consolidator grant of the EU (2015-2020, 2 M€) on the topics that we collaborate on. This puts us in a very good position to develop, among others, some of the experimental projects that I shall discuss in section 6 of this thesis. The lab-experimental aspect was fundamental in granting the funding, as expressed by these sentences extracted from the ERC panel's comment on the proposal: "The panel has appreciated the complexity of the underlying issues, in particular the experimental arrangement needed in order to achieve 3D visualisation of transient reactive flows. The panel found the combination of experimental and computational approaches to be a particular strength of the project, with a potential to advance the understanding of reactive mixing in porous media flow."

4.4.2 Collaborations

Through the years many collaborations have been initiated with established researchers, several of which have been long-lasting.

At Géosciences Rennes:
Jean de Bremond d'Ars (2006-2009): solute exchange between fractures and the rock matrix.
Philippe Davy (2008-): flow and transport in fractured media.
Jean-Raynald de Dreuzy (2010-): flow and transport in fractured media.
Tanguy Le Borgne (2011-): transport, mixing and reactivity in porous media.

At other French universities or research institutions:
Isabelle Cantat (Institut de Physique de Rennes, 2011-): foam flows in porous media.
Benjamin Dollet (IPR, 2011-): foam flows in porous media.
Damien Jougnot (UPMC, 2014-): electrical measurements of solute transport in porous media.
Hervé Tabuteau (IPR, 2011-): transport, mixing and reactivity in porous media.
Renaud Toussaint (IPG Strasbourg, 2003-): two-phase flows in porous media.
Jean Schmittbuhl (IPG Strasbourg, 1998-2005): flow in rough fractures; two-phase flows in porous media.

At universities or research institutions abroad:
Pietro de Anna (now at UNIL Lausanne, 2011-): transport, mixing and reactivity in porous media.
Diogo Bolster (University of Notre-Dame, 2011-2014): transport in fractures.
Daniel Bonn (University of Amsterdam, 2009-): free surface flows of clayey muds.
Geraldo Jose da Silva (UnB Brasilia, 2004-2006 and 2015-): vapor transport in weakly-hydrated clays.
Marco Dentz (CSIC Barcelona, 2013-): transport, mixing and reactivity in porous media; displacement of interfaces in heterogeneous media.
Jon Otto Fossum (NTNU Trondheim, 2002-): clay-based complex fluids, vapor transport in weakly-hydrated clays, clay-based electrorheological fluids, free surface flows of clayey muds.
Joaquín Jiménez-Martínez (now at Los Alamos National Laboratory, 2011-): transport, mixing and reactivity in porous media.
Kenneth Knudsen (Institutt for Energiteknologi, Kjeller, 2002-2008): clay-based complex fluids, clay-based electrorheological fluids.
Daniel Lester (RMIT Melbourne, 2013-): solute mixing in 3D porous media.
Niklas Linde (UNIL Lausanne, 2014-): electrical measurements of solute transport in porous media.
Ivan Lunati (UNIL Lausanne, 2014-2015): two-phase flows in porous media.
Knut Jørgen Måløy (University of Oslo, 2000-): two-phase flows in porous media.
Insa Neuweiler (Leibniz Universität Hannover, 2014-): two-phase flows in porous media; displacement of interfaces in heterogeneous media.
Bjørnar Sandnes (now at Swansea University, 2004-2006): vapor transport in weakly-hydrated clays.
John Selker (Oregon State University, 2015-): flow of non-Newtonian fluids in fractures.
Zhibing Yang (MIT, 2014-): two-phase flows in porous media.
Lirong Zhong (Pacific North-west National Laboratory, Richland, 2014-): foam flows in porous media.

4.4.3 Work with PhD students and postdocs

I have had the chance to collaborate with various younger researchers. The ones that I have advised are cited earlier in the CV part of this thesis (section 2), but I have not officially been advisers to all of those I have collaborated with. I acknowledge them all below, as the research activities presented in section 4 above owe them a lot. This constant collaboration with younger people is to me one of the most stimulating and enriching aspect of being a researcher. Here is therefore a list of all the colleagues I have collaborated with either when they were undertaking their PhD, or when they were postdoctoral researchers while I was myself already on an academic position.

PhD students:
Kanak Parmar (2002-2006) and Davi de Miranda Fonseca (2002-2007) started a PhD with Jon Otto Fossum (NTNU Trondheim, Norway) soon after I arrived in Jon Otto's group to begin a postdoc (autumn 2002). I worked with Kanak and Davi on all studies featured in their PhDs, respectively clay-based electrorheology and the phase behavior of clay suspensions in saline solutions. I consider that a large part of my training in young researcher supervision was acquired at that time. Kanak is now an Assistant Professor at the University of Petroleum and Energy Studies in Dehradun, India, while Davi is the General Manager of the Proteomics and Metabolomics Core Facility at the Department of Cancer Research and Molecular Medicine of NTNU.

Laure Michel 2006-2009, co-supervision with Jean de Bremond d'Ars) was the first PhD student that I co-supervised at University of Rennes 1. Her PhD project was about fracture-matrix exchange. Laure is now working in a consulting company in Rennes, which addresses water quality issues.

Jérémy Bouquain (2008-2012, co-supervision with Philippe Davy) performed numerical simulation of solute transport in fracture geometries.

Henrik Hemmen (2008-2012) did a PhD with Jon Otto Fossum at NTNU. We worked together on the phase behavior of clay suspensions in saline solutions and on vapor transport in dry clays. He is now the CTO at Condalign AS, in the Oslo area (Norway).

Elisabeth Lindbo Hansen (2009-2013) did her PhD student with Jon Otto Fossum at NTNU. We worked together on the rheological properties of quick marine clay. She is now a postdoctoral researcher working for the Norwegian Radiation Protection Authority.

Pietro de Anna (2010-2012) did his PhD with Tanguy Le Borgne and Philippe Davy. I supervised the experimental work that he performed in the second half of his PhD.

Andrea Ferrari (2010-2014) did his PhD at UNIL Lausanne with Ivan Lunati. We collaborated on the sensitivity of two-phase flow simulations on geometrical uncertainties, comparing their simulations with our experiments.

Leander Michel (2011-2015) did his PhD student with Jon Otto Fossum at NTNU. We collaborated on vapor transport in dry clays. He is now a postoctoral researcher.

Régis Turuban (2012-2016, cosupervivision with Tanguy Le Borgne) works on mixing in porous media flows.

Benjamin Delfino (2015- cosupervision with Jocelyne Erhel and Jean-Raynald de Dreuzy) has recently started a PhD on reactive transport in fractured media.

Antoine Hubert (2016-, cosupervision with Tanguy Le Borgne) has just started a PhD on the interaction between flow, solute mixing and bioactivity in porous media.

Postdocs:

Siân Jones (2011-2013) was a postdoctoral researcher at Institut de Physique de Rennes, working with Isabelle Cantat, Benjamin Dollet and myself on the flow of foams in porous media. She is now a postdoctoral researcher at TU Delft.

Joaquin Jimenez-Martinez (2010-2014) was a postdoctoral researcher at Géosciences Rennes, working with us mostly on solute transport and mixing in unsaturated porous media and the link between electrical measurements and flow measurements. He is now a postdoctoral research associate at the Los Alamos National Laboratory (LANL).

Baudouin Géraud (2013-2014 and 2016-2017) was a postdoctoral researcher at Institut de Physique de Rennes, working with Isabelle Cantat, Benjamin Dollet and myself on the flow of foams in porous media. He came back recently to Rennes to work with Tanguy Le Borgne and myself in the framework of the ERC project ReactiveFronts.

Clément Roques (2015-) is a postdoctoral researcher in John Selker's group at Oregon State University, with whom I collaborate on the flow of non-Newtonian fluids in rough fractures.

Aditya Bandopadhyay (2016-2017) is a postdoctoral researcher, part of the ReactiveFronts team.

5 Other activities

5.1 Teaching

Since the autumn of 2006, and except during the year 2010-2011 when I was on leave from Université de Rennes 1 at CNRS, I have taught an average of around 200 hours a year and have been responsible for 5 teaching units per year (see the CV, section 2 where the topics that I have taught are listed). The official amount of hours that a Maître de Conférence must teach in France is 192h per year; the lectures, their preparation and organization are supposed to correspond to 50% of the position.

During the year 2007-2008 I have had the chance to be involved in the development of a new master program, "Systèmes Complexes Naturels et Industriels", under the coordination of Renaud Delannay (professeur at the Institut de Physique de Rennes). This is to me one of the most interesting experiences I have had in relation to teaching. One of the subprograms is dedicated to the modeling of environmental issues. Between 2009 and 2012 I was in charge of that subprogram. Another similar experience has been my participation in the committee in charge of setting up a teaching program for the future Department of Environmental Sciences of the new École Normale Supérieure (ENS) de Rennes, in 2011-2012. Unfortunately, though the program was approved both at the level of the ENS and at that of the Department for National Education and Research, its creation has until now not been funded by that Department.

5.2 Editorial work

I devote a fair amount of time to the peer-reviewing of articles by other researchers. I do not review a large number of papers each year (about 1 per month), but I usually spend a significant amount of time on each review: between one and two full days of work, usually. Due to my interdisciplinary background the review request that I receive are both from Physics/Mechanics and Geosciences/Hydrology/Soil Science journals (a few from Physical Chemistry journals).

Since January 2011 I have been Associate Editor for the Vadose Zone Journal. I manage only about two manuscripts per year. It seems to me that this experience has helped me improve both as a reviewer and an author. In addition, in view of the topic covered by the journal, it has significantly broadened my scientific culture towards soil sciences.

5.3 Organization of thematic schools and conference sessions

In relation to the creation of the SCNI master program in the autumn of 2008, we started organizing an interdisciplinary school in Rennes every year, on various aspects of complex systems. Since 2013 I have coordinated the organization. The program of the seven schools that have taken place can be found here: `http://risc-e.univ-rennes1.fr/ecoleSC`.

I have not been active in organizing sessions in big conferences such as the AGU Fall Meeting and the EGU General Assembly, mainly for two reasons: (i) I think that one should propose sessions on topics one has a broad knowledge of, and (ii) I do not see the point in proposing a session on a topic that is already well represented in sessions previously existing and which are likely to be proposed again. In the future I hope to be able to contribute more in this respect. I was recently sollicited to organize a session on tranport processes in permeable media at the JMC 2016 (Journées de la Matière Condensée).

6 Research prospects

In the future I plan to further develop my research along five directions.

Firstly, the work on multiphase flows and flow instabilities in porous and fractured media will be further continued, in particular towards processes related to CO_2 subsurface remediation. These research lines are presented in section 6.1. Secondly, I shall gather my backgrounds in flows with complex boundary conditions and in complex fluids and soft matter (presented respectively in sections 4.1 and 4.3 above) to tackle flows of non-Newtonian fluids in permeable media. This includes the continuation of the studies on foam flows in porous media, but other studies are also planned. These research lines are presented in section 6.2. The third direction concerns the link between flow, solute mixing and reactions in porous media. It is the continuation and further development of the studies presented in section 4.2 and which have recently been put under good auspices by the funding by the ERC of the project ReactiveFronts, in which I am strongly involved. These research lines are presented in section 6.3. The fourth direction, presented in section 6.4, will aim at relating fluid and solute transport to electrical transport. The fifth direction, presented in section 6.5, concerns projects addressing flow and (reactive) transport in fractured media.

6.1 Multiphase flows and flow instabilities in porous media

6.1.1 Two-phase flows in porous media

Fundamental studies on two-phase flows are being continued in the background. In particular the studies on unstable drainage can now be complemented since our experimental setup at Géosciences Rennes allows to control the disorder of the porous medium from a numerical model.

The recent study on drainage in rough fractures (see section 4.1.3), with Zhibing Yang (MIT) and Insa Neuweiler (University of Hannover), is also being continued. It has led to ongoing developments involving the role of buoyancy in such displacements, not only as a consequence of a tilt of the fracture plane with respect to the horizontal, but also for horizontal fractures, as a consequence of the fracture walls' topography. The latter configuration is particularly interesting, as it couples the detail of the wall topography to the displacement process: two fractures with the same aperture field but different wall topographies are not equivalent anymore from the hydraulic point of view. In order to take such effects into account, the invasion percolation algorithm has to be complemented by introducing a correlation between the percolation probability and the topography; this technique has been used extensively on two-dimensional porous media (*Hulin et al.*, 1988; *Frette et al.*, 1992), but to our knowledge not for geometries and with algorithms relevant for fracture flow.

A general and still very open question relative to two-phase flows in porous media, is the relationship between pore scale models and Darcy scale models. While pore scale models are based on first principles, Darcy scale models are based on Darcy laws applied to two-phase flows via the concept of relative permeability, the relationship of which to first principles is debatable. The latter models are not well suited to describing physical instabilities of fluid-fluid interfaces, such as the one discussed in section 4.1.3. Discussions have been ongoing for a while with Marco Dentz (CSIC Barcelona) and Insa Neuweiler on how continuum modeling could be used to describe unstable two-phase flow in porous media. The efforts so far have led to a very interesting work on the relationship between interface statistics and saturation in a stochastic growth model, which for the moment is not applicable to two-phase flows (*Dentz et al.*, 2015). But this question deserves further scutiny.

6.1.2 CO_2 remediation by solubility trapping

Since this is a topic whose environmental context has not been presented yet in this thesis, I am devoting in the following some efforts to summarize that context. It is now generally accepted that a global warming of the atmosphere has been occurring for 150 years, and that its acceleration in the last 30 years will result in a further increase of average annual temperatures in the range 1.1 to 6.3°C (*panel on climate change (IPCC)*, 2007), with devastating consequences in terms of climate, sea level rise and their various consequences. The main cause for this global warming is the increase in the atmospheric concentrations of greenhouse gases since the beginning of the industrial area. Since Carbon dioxide (CO_2) alone is responsible for about two thirds of the enhanced greenhouse effect, it was proposed less than 20 years ago to capture the carbon dioxide generated by large industrial facilities and inject it into deep geological formations where it would remain trapped for a time much larger than its residence time of 50 years in the atmosphere (*Bachu*, 2008). However, despite

the now widely-admitted technical feasibility of CO_2 capture and subsurface storage, assessing under which circumstances such a storage procedure can be successful in keeping CO_2 sequestrated on a times scale of centuries to milleniums, and what are the potential associated risks, is not an easy task, due to the complex fluid mechanics processes involved in the procedure.

The storage procedure indeed consists in injecting carbon dioxide into a permeable formation that is confined by a mostly impermeable formation, the caprock, above it. Rocks formation suitable for storage are mostly old oil reservoirs and deep saline aquifers consisting of sandstone and carbonate, while typical cap rocks consist of mudstone. The injection is performed at depths greater than approximately 800 m (depending on the temperature), at which CO_2 is in its supercritical state: it has a density akin to that of its liquid state, but a much smaller viscosity, and its dynamics can be modeled using standard fluid dynamics. In storage conditions it is less dense and less viscous than the interstitial fluid (that is, the fluid that initially occupies the cavities of the formation), usually water or brine, or light oil. The density ratio and viscosity ratio (M) between the injected CO_2 and the resident fluid are typically in the range $0.22 - 0.75$ and $0.026 - 0.22$, respectively (*Huppert and Neufeld*, 2014). So the CO_2 is buoyant and rises in the formation upon injection, until it reaches the base of the cap rock, after which it is subjected to a lateral buoyancy-driven migration along that base. As the resident fluid is being displaced laterally, viscous fingers then tend to develop (since $M < 1$), so the complex dynamics of the interface inside the porous space of the medium is controlled at small scales by capillary forces involving the surface tension between the two fluid phases. Furthermore, CO_2 is partially soluble in water (up to 3 wt%), so partial mixing occurs at the interface, resulting in a mixture that happens to be denser than both the CO_2 and the resident fluid; hence, under certain conditions the interface destabilizes and a density difference-triggered convection develops. In addition, for brine, the solubility of CO_2 depends on the concentration of salt in the brine.

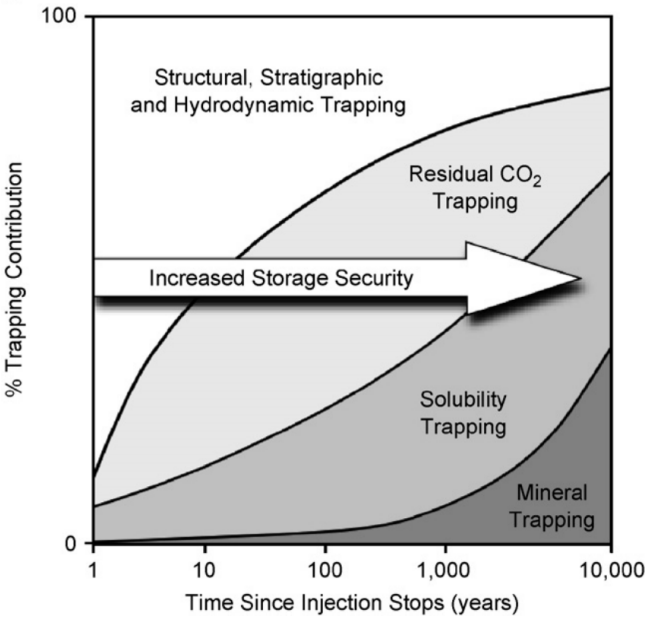

Figure 21: Time evolution of the contributions to trapping of the various trapping mechanisms (adapted from (*Bachu*, 2008)).

As a result of this complex set of hydrodynamic processes, four types of trapping mechanisms can be distinguished: (i) Static structural/stratigraphic trapping is the trapping of the gas below the low-permeability cap rock; (ii) Residual trapping is the trapping of disconnected gas bubbles inside cavities of the medium, when the injected gas is displaced by the resident fluid (from now on we shall consider that it is brine) after the injection has stopped (*Juanes et al.*, 2006); (iii) Solubility trapping occurs when brine mixed with CO_2, and therefore denser than unmixed brine, goes to the bottom of the formation by gravity. (iv) Mineral/chemical trapping occurs when CO_2 is involved into chemical reactions with the host rock and remains bound to it chemically or through physico-chemical forces. As shown in Figure 21, the trapping mechanisms act over different time scales in the order given above, the most perennial forms of trapping overtaking structural trapping as time passes.

We shall focus our efforts on solubility trappping, which is particularly interesting as it provides a way of storing carbon dioxide at the bottom of the host formation, in a configuration where it will remain sequestrated for a very long time. It has already been the subject of a large amount of literature (*Emami-Meybodi et al.*, 2015) but is still far from fully understood, as it involves a hydrodynamic instability and the subsequent development of a convection within the host formation. Indeed, the dissolution of the supercritical CO_2 into the brine at the interface between them creates a thin layer of CO_2-brine mixture, whose thickness increases with time. This layer is denser than the brine underneath and thus becomes unstable when the layer becomes large enough. The subsequent development of this gravitational instability generates convective rolls, which evolve into fingers of CO_2-brine mixture that sink into the brine layer (*Elenius and Johannsen*, 2012). The fingers are mostly located within the brine layer since the interface between the supercritical CO_2 and the CO_2-brine mixture,

being gravitationally extremely stable, remains flat. This convective dissolution, which involves a coupling between the mixing of CO_2 with the brine and the resulting convection, is one of the most challenging aspects of solubility trapping.

A lot of efforts have until now been devoted to studying the gravitational instability in a two-dimensional (2D) geometry. Most of the results were obtained through Darcy-scale numerical simulations. Many papers have tried to predict the onset time of the linear instability (*Rees et al.*, 2008; *Tilton et al.*, 2013). However, the onset time of the nonlinear regime, potentially much larger than that of the linear instability, is more relevant to the trapping of CO_2 since the flux of CO_2 is more enhanced by the presence of non-linearities resulting from the instability than by the linear instability phase(*Elenius and Johannsen*, 2012; *Tilton and Riaz*, 2014). In comparison to numerical studies, experimental studies of the dissolution-induced gravitational instability are scarce. They are usually performed in Hele-Shaw cells, that is, by confining the flow between two parallel plates, which imposes a parabolic velocity profile along the direction transverse to the plate. For saturated flows with no density contrasts the Hele-Shaw is a good analog model for a 2D porous medium (*Hele-Shaw*, 1898), but for saturated flows with significant density-driven convection it is still an open question (*Zeng et al.*, 2003). There have been, on the contrary, very few studies addressing 3D geometries, but recent 3D simulations (*Pau et al.*, 2010; *Fu et al.*, 2013) suggest that the dynamics of convective dissolution may be very different in 3D geometries compared to 2D systems. The convection rolls are limited to the top part of the 3D flow cell, while in the lower part of that cell the rolls give birth to plumes, as in the Rayleigh-Bénard convection. This remains to be confirmed through experiments.

3D experiments are very challenging because they require (i) a porous medium that is transparent when saturated with the flowing fluids, and (ii) an imaging system able to capture the entire 3D structure of the convection rolls/plumes. To our knowledge, no such 3D experiment addressing convective dissolution has been reported in the literature up to now. Observation in porous media usually consist of cuts of the "frozen" final state rather than in a time-resolved imaging of the flow structure (*Held and Illangasekare*, 1995). We have performed preliminary 3D experiments with pure water and no solid grains. They suggest, in agreement with the recent simulations mentioned above, that predictions based on 2D models may be totally inadequate for the trapping of CO_2 in 3D aquifers. We therefore propose to perform 3D experiments of convective dissolution with a granular porous medium of optical index matched to that of the fluids, in order to fully characterize the 3D process experimentally. Obviously the method and technical challenges involved are very similar to those in most part already overcome in the framework of our 3D setup aiming at measuring the mixing of solutes (see section 4.2.6).

Despite the technical challenges involved, such experiments will not only represent a progress with respect to 2D experiments, but they may also uncover issues in numerical studies, either 2D or 3D. Indeed, given the enormous range of scales between the pore scale (≤ 0.1 mm) and the size of the aquifer, all numerical studies are performed at the Darcy scale, thus discarding all the physics potentially occurring at the pore scale. It is thus possible that the dynamics of the instabilities may be influenced by the presence of a porous medium, through enhanced mixing between water and CO_2 due to pore scale flow heterogeneity (a feature that is well known in the context of solute transport(*de Anna et al.*, 2014b)), and thickening of the diffusing fronts. Several questions remain unanswered. Are the gravitational instabilities 2D or 3D? What is the onset time of linear instabilities? What is the onset time of the nonlinear regime of instability? What is the increase in CO_2 flux due to the convective dynamics. All these questions, in particular the latter one, are essential for the prediction of the rate at which CO_2 will sink to the bottom of the saline aquifer to remain trapped over geological times.

The project will be tackled in collaboration with Patrice Meunier (IRPHE, CNRS and Université d'Aix-Marseille) and François Nadal (CEA Bordeaux), who have developed the preliminary experimental setup and developed a theoretical study of the instability. Tanguy Le Borgne (Géosciences Rennes) will bring to the project his expertise in mixing processes.

6.2 Flows of complex fluids in porous media

6.2.1 Foam and emulsion flows for remediation

I shall continue to investigate complex fluids in relation to subsurface remediation, in particular the remediation of the vadose zone. A common feature to many of those methods is the need to bring chemical amendments to the pollutants; to carry these amendments, foams can be used, as mentioned in section 4.1.4. Another type

of fluids with a complex rheology owing to their mesoscopic mesostructure, is emulsions. They consist of drops of a liquid dispersed inside another liquid to which it is immiscible. Emulsions of vegetable oils are used to decontaminate subsurface environments, because they can act as electron doners to allow micro-organims to degrade or sequestrate various contaminants *Hunter* (2005). To that purpose they are often injected using a precise spatial injection scheme so as to create permeable stationary barriers of oil in some regions of an aquifer. However, the use of such techniques for vadose zone environments is little documented.

Using foams: Foam flows in 2D porous media will be further investigate. The first research line that we shall follow is to further investigate the phenomena addressed by *Géraud et al.* (2016), using more disordered porous media. In particular we would like to investigate media where the ratio of the pore size to the pore throat size is larger, so that lamella-destroying processes such as capillary snap-off are not dominated by lamella-creating processes such as lamella division. We expect the process of bubble size selection to be strongly impacted. We also want to investigate the effect of changing the disorder in the system, that is, changing the width of the pore size distribution. We shall also investigate the selection of bubble sizes by the medium in three-dimensional systems.

Another aspect of the project will involve analog experiments of foam flows through an unsaturated porous medium. An interesting application is the remediation of the vadose zone (*Zhong et al.*, 2010). Often, for example when heavy metals are involved, the remediation aims at stabilizing the polluting species in situ, preventing them from reaching the aquifer (*Morse et al.*, 2007), by transforming them into another much less mobile chemical component (*Wellman et al.*, 2007; *Zhong et al.*, 2010, 2011; *Ding et al.*, 2013). The amendments must therefore be injected without wiping the target species away into the aquifer. Foams have been shown, using column experiments, to optimize chemical fixation for the reduction of Cr VI into Cr III (*Zhong et al.*, 2009). In addition, a rupture front of foam bubbles (that is, a separation between the solution and gaz phases) is observed as the foam progresses into the unsaturated porous medium, resulting in the formation of a wetting film of the foaming solution ahead of the foam itself, preceding it and maximizing the contact between the solid phase and amendments contained in the solution. This complex mechanism was characterized qualitatively by Lirong Zhong (Pacific Northwest National Laboratory, Richland, USA) using a column filled with sediments contaminated with Cr VI. In-depth understanding of the process requires a visualization of the processes at play in the medium, which is possible with our 2D experimental setup. A collaboration has already been initiated with Lirong Zhong to that purpose.

Using emulsions: Laboratory studies using columns show that the injection of oil in the form of an oil-in-water emulsion allows for a maximization of the volume of the aquifer visited by the oil, or if needed for a better control of the spatial extent of permeable stationary barriers in the subsurface (*Borden*, 2007). The existing field experiments (*Borden*, 2007) and laboratory experiments (*Hunter*, 2005) have to my knowledge only tackled saturated conditions. I thus first plan to perform the same type of experiments with emulsions as already performed with foams, and then to investigate emulsion flows through an unsaturated medium. A collaboration with the group of Marcio Carvalho at PUC in Rio de Janeiro (Brazil), who works on emulsion flows in confined geometries for Enhanced Oil Recovery (*Guillen et al.*, 2012; *Cobos et al.*, 2009), would be of great help. There have been casual discussions with Prof. Carvalho about this possibility since we met at a worshop at PUC in 2014.

6.2.2 Non-newtonian fluids for the characterization of fractured aquifer properties

Transport in fractured media is characterized by strongly heterogeneous flow path distributions (*Becker and Shapiro*, 2003). While hydrogeophysical methods to characterize fractured media at the borehole scale are relatively mature, the characterization of the geometries of flow paths and their hydraulic properties between boreholes is still remains subject to considerable uncertainty (*Neuman*, 2005), despite recent development in flow tomography techniques (*Le Borgne et al.*, 2006) to infer the properties of fractured reservoirs, fiber optic measurements of temperature to investigate vertical flow in boreholes (*Read et al.*, 2014), and hydrogeophysical methods such as ground penetrating radar (GPR), which provides a qualitative description of the fracture network from the imaging of tracer displacement (*Dorn et al.*, 2011). In collaboration with Clément Roques and John Selker of Oregon State University, Majdi Abou Najm of the American University of Beirut, as well as Olivier Bour, Tanguy Le Borgne and Philippe Davy of Géosciences Rennes, we have been working towards

using non-Newtonian fluids to improve the characterization of fractured aquifers. These tests will be coupled to geophysical measurements performed in collaboration with Niklas Linde of UNIL (Lausanne). We aim at inferring geometric information about the fracture networks from field experiments (flow tests and tracer tests) using shear-thinning fluids. Since these fluids are all the less viscous as they are more sheared, they are subjected to a channeling more profound in heterogeneous media than that sustained by a Newtonian fluid (*Auradou et al.*, 2008). This property is expected to impact both the hydraulic conductance of the medium and the results of tracer tests. Our objective is to be able to obtain characteristic signatures in the flow test and tracer test data, that can be inversed to characterize the geometry. When using biopolymers such a guar gum or xanthan gum, varying the concentration provides several different rheologies, all of the same type but with different values of the rheological parameters. For guar gum and xanthan gum the relevant rheological model is that of Carreau, with a viscosity that reaches a higher limit at infinitely low shear rates and a fixed (much) lower limit at infinitely high shear rates.

Given the complexity of this ambitious task we had to first focus our efforts onto the simplest configuration possible. My implication in the project has been mostly to help Clément Roques to develop a three-dimensional numerical simulation for the flow of a fluid with a Carreau rheology in a realistic geometry such as those used by *Méheust and Schmittbuhl* (2003). Though a few theoretical or numerical (*Lavrov*, 2014) studies exist, all of them address power law fluids, and a majority of them tackles simplified geometries (*di Federico*, 1997, 1998, 2001). In order to characterize the effect of the geometry on flow and on fracture transmissivity, a statistical study must be undertaken (see *Méheust and Schmittbuhl* (2001) for such a study with Newtonian flows).

6.3 Mixing and reactions in heterogeneous flows

The different research lines presented in this section are related to the ERC project ReactiveFronts. Various development to the studies that I have presented in section 4.2.3, are planned.

The main challenge of the project lies in uncovering the coupling between fluid dynamics and biological activity. Biological activity indeed plays a key role in triggering chemical reactions, producing catalysts or degrading pollutants (*Bekins et al.*, 2001). The production of biomass can also dramatically impact flow properties by changing the boundary conditions of the flow, creating preferential flow paths (*Durham et al.*, 2012) and even leading to pore clogging (*Seymour et al.*, 2004). On the other hand, mixing fronts offer particularly favorable conditions for micro-organisms to develop since they prevent the metabolic elements that are necessary to their metabolic function from being seggregated (*McClain et al.*, 2003). These two aspects of the coupling will have to be investigated: (i) how fluid stretching shapes the distribution of micro-organisms, through the control of the spatial gradients in nutriment and concentrations, and ii) how biofilm growth impacts the flow, in particular in terms of spatial heterogeneity and velocity distribution. From an experimental point of view we are facing a double challenge. First, since the bacteria cannot be upscaled, we need to more from millifluidics to microfluidics and work under the microscope (*Rusconi et al.*, 2014). We shall have to resolve both concentration films of nutriments, biofilm growth patterns, flow structures and permeability changes. Second, we shall have to deal with microbiology, in which we shall be greatly helped by our collaboration with our colleague from the Ecobio Lab, Alexis Dufresne. A PhD has just started on this aspect (Antoine Hubert, 2016-2018).

The three-dimensional (3d) experimental setup will be further developed, in order to image the spatial distribution of reactive tracers in a 3D porous medium. For this we shall need to consider reactions with a fluorescent product (different from the chemiluminescent reactions discussed in section 4.2.3). We also plan to address two-phase flows. In 3D we expect this aspect to be quite challenging since optical matching needs to be ensured everywhere between the solid phase and both fluids, so the use of air as one of the two fluids will not be possible.

The investigations of transport and mixing in unsaturated conditions will be first extended to 3D porous media, and then to reactive transport, both in 2D and 3D. The additional dimension changes the connectivity of pores dramatically, which may impact the mechanisms proposed by *Jiménez-Martínez et al.* (2015) from 2D data.

On the theoretical side, the lamella-based theory to quantify the deformation of mixing interfaces under fluid stretching and the consequent distribution of chemical gradients (*Le Borgne et al.*, 2013, 2015) is now being expanded to consider reactions, in particular for finite Dahmköhler numbers. As mentioned in section 4.2.3, a first investigation has addressed configurations of linear shear flow. Later studies will aim at generalizing the theory to other types of streching dynamics, as well as at addressing the regime in which the front geometry

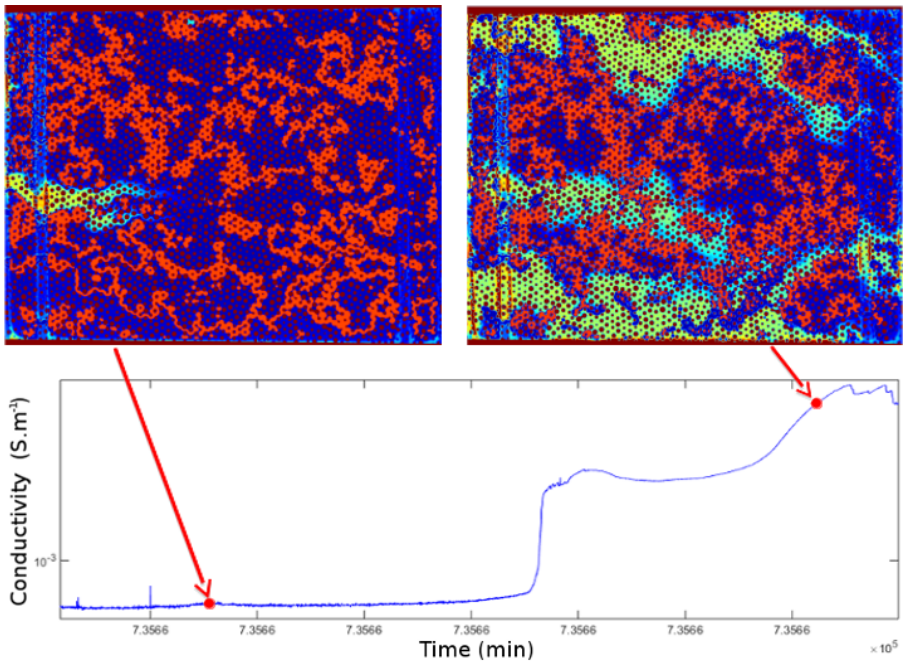

Figure 22: (Top) Two maps of solute transport in an unsaturated 2D porous medium; the air appears in orange, solid grains in dark red, and the solute concentration within the liquid phase in a color scale ranging from blue to yellow. (Bottom) Measured electrical conductivity as a function of time. The red points denote the times at which the two maps above have been recorded.

has become so intricate that adjacent lamellae start coalescing. Ultimately we would like to understand how the medium's geometry controls the stretching dynamics, so as to be able to make predictions on effective chemical dynamics from the sole knowledge of the geometry.

6.4 Monitoring of solute tranport in the vadose zone from electrical methods

On the field, measurements of flow velocities and solute concentrations are only possible at boreholes, which makes the monitoring of pollutant plume extension by conventional subsurface measurement approaches difficult. Among the available geophysical methods, time-lapse electrical resistivity tomography (ERT) is widely used to image the water saturation of the near subsurface or the spatial extension of pollutant plumes (*Binley and Kemna*, 2005; *Doetsch et al.*, 2012). Inferring hydrogeological information from the electric data, however, requires petrophysical relations that have been derived for saturated porous media. These procedures do not account for a possible heterogeneity of the solute spatial distribution, nor of that of the air- and water phases. Their use for unsaturated systems is therefore debatable, and their application not only leads to greater apparent dispersion than otherwise inferred from breakthrough curves measured at pumping wells or from numerical simulations, but even to a strong underestimation of the total solute mass. A collaboration on this topic was initiated in 2014 between our group in Rennes (namely, Joaquin Jimenez, now at LANL in Los Alamos, Tanguy Le Borgne and myself) and the Hydrogeophysics group at UNIL (Damien Jougnot, now at CNRS in Paris, and Niklas Linde). We have complemented the setup for the study of solute transport by 2D unsaturated flows (see Figure 14) with two sets of electrodes, one to impose a voltage across the medium, the other to measure the electrical current. The top part of Figure 22 shows two maps of solute concentration at two different times during the injection of a saline tracer, while the bottom part shows the measured electrical conductivity as a function of time. Clearly the conductivity is strongly impacted by the presence of the conductive tracer in the porous space, and clearly since the flow paths available for the liquid phase are constrained by the presence of the air clusters, whose electrical conductivity is very small, the spatial distribution of the air also impacts the measured conductance significantly. From maps of the phase distributions and solute concentration field such as those shown in Figure 22, the electric current inside the flow cell can be modeled, which provides a prediction of the system's conductance that we can confront to the measurements. Ultimately we hope to propose petrophysical models that are better adapted to the description of unsaturated systems. These are extremely

open questions and for which a large range of developments are possible.

Among the planned developments, one involves the use of spectral induced polarization (SIP), which has been shown by *Revil et al.* (2013) to be able to monitor salt tracer tests in shallow aquifers. SIP provides the measurement of a complex conductivity, thus also measuring the phase lag between the injected current and the measured electrical field. It is complementary to ERT in that ERT measurements result both from the bulk conductivity of the liquid and the surface conductivity at the interface between the pore water and the mineral interface, while SIP offers an independent way of estimating surface conductivity, in particular changes in that conductivity associated with changes in salinity (*Revil et al.*, 2013). SIP is also used to detect bacterial activity (*Davis et al.*, 2006; *Atekwana and Slater*, 2009; *Williams et al.*, 2009) in a quantitative manner, for example to obtain the growth rate and endogenous decay coefficients of bacteria whose population evolution is described by Monod kinetics (*Revil et al.*, 2012). In the 2D experiments with biofilm growth discussed in section 6.3 we should be able to monitor the surface on which biofilms have grown or the total mass of biofilm. Spectral induced polarization is also expected to be able to detect a signature for redox reactions, which would allow us to monitor reactive transport experiments from an electrical measurement, again complementing that information by optical characterization of the reaction.

Eventually i would like to combine the question of the link between electrical transport and mass transport with that of foams and emulsion flows in unsaturated porous media (section 6.2.1), and investigate the monitoring of those flows by electrical methods. Self-potential measurements have been shown to be correlated to the displacement of primary drainage and experiments in a sandbox experiment (*Haas and Revil*, 2009), and could potentially provide interesting information about foam flows (if not emulsion flows). Discussions with André Revil (CNRS and Université de Savoie), have started on this aspect.

6.5 Flow and transport in fractured media

The studies on the coupling between fracture scale flow heterogeneity and network scale flow heterogeneity (see section 4.1.2) have showed that the fracture-scale correlation length plays a crucial role in that coupling. This correlation length is related to the fracture wall topography, and therefore to the fragmentation process. Various hypotheses can be made in this respect, among which that the correlation length could be correlated to individual fracture parameters such as the fracture orientation. A directional fracturing process would certainly result in a correlation length that depends on the fracture orientation, and it would be interesting to understand under which conditions this fracture scale anisotropy would translate into a network scale anisotropy.

A project on diffusively-dominated reactive transport in fractured media has also started in the spring of 2015 (PhD of Benjamin Delfino, co-supervised with Jean-Raynald de Dreuzy of Géosciences Rennes and Jocelyne Erhel a INRIA Rennes). It is motivated by an application to radioactive waste storage studies, in collaboration with the French national agency for the management of nuclear waste (ANDRA). It will involve a combined numerical and experimental approach to determine the influence on reactivity of typical fracture patterns classically found in radioactive waste applications. The relevant hypotheses in this context are (i) mostly diffusive transport, much faster in the fracture than in the porous matrix, (ii) a much larger reactivity in the matrix because of the large surface to volume ratio, and (iii) a very low Damköhler number, that is, reactions that are instantaneous with respect to typical transport times. Numerical simulations will simulate reactivity over long periods of times, while experiments will investigate which is the most critical limiting parameter with respect to reactivity, of which we suspect that it is the exchange law at the fracture-matrix interface. The chemical conditions considered will be as close as possible to the conditions met during the main operational phases of a radioactive waste repository.

7 Conclusion

What general scientific conclusions can one draw from as diverse a set of studies as that which I have reported on here ? First of all, several of these studies have evidenced how pore scale phenomena have consequences at larger scales, in particular at the Darcy scale, but also potentially at much larger scales. Another conclusion is that disorder matters, even disorder below the Darcy scale. At least it matters for unstable two-phase flow; for solute spreading and mixing in unsaturated porous media and more generally for mixing at times scales smaller than the time necessary for the Fickian regime to settle; consequently it matters for reaction, which is by definition a non-stationary property; it also matters for electrical measurements of saturation or solute concentration in unsaturated subsurface environments. This confirms that the only Darcy scale descriptions that are correct upscalings of pore scale processes are those that consider saturated flow and passive transport by such flows. Of course I am aware that Darcy scale heterogeneities exist in the real subsurface world and that their consequences in many cases may vastly dominate the consequences of pore scale processes. However my feeling is that several of the studies presented here call for the necessity of better upscaling pore scale properties/processes to the Darcy scale and above. Actually several of these studies, be they dealing with two-phase flow, solute mixing, foam flow or electrical measurements on unsaturated media, are modest attempts at such an upscaling. As a side conclusion of a practical nature, my experience is that pore scale studies should always incorporate a measurable degree of disorder, because no apparent disorder means a disorder that is too small to be characterized but that may still impact the processes under investigation. Our comparison of two-phase flow experiments and full 3D numerical simulations have provided a nice example of this (section 4.1.3).

In addition to my two pet topics, namely two-phase flows in porous media and transfers in fractured media, my future research activities will be mainly structured around the investigation of complex fluid flows in permeable media, that of the link between flow heterogeneity and reactivity, including biological activity-mediated reactions, and the investigation of the link between the transports of mass and electricity. These three main research directions all involve an ambitious program and significant scientifical and technical challenges. If their outcomes fulfill my expectations, they will ultimately allow us to bridge the laboratory scale and the field scale, something which I am very much looking forward to.

8 Bibliography and list of figures

References

Apaydin, O. G., and A. R. Kovscek (2001), Surfactant concentration and end effects on foam flows in porous media, *Transp. Por. Med.*, *43*(3), 511–536.

Aris, R. (1956), On the dispersion of a solute in a fluid moving through a tube, *Proc. R. Soc.London A*, *235*(1200), 67–77.

Arneodo, A., J. Elezgaray, M. Tabard, and F. Tallet (1996), Statistical diffusion of off-lattice diffusion-limited aggregates in channel and sector geometries, *Phys. Rev. E*, *53*(6), 6200.

Atekwana, E. A., and L. D. Slater (2009), Biogeophysics: A new frontier in earth science research, *Rev. Geophys.*, *47*(4).

Auradou, H., A. Boschan, R. Chertcoff, S. Gabbanelli, J. Hulin, and I. Ippolito (2008), Enhancement of velocity contrasts by shear-thinning solutions flowing in a rough fracture, *J. Non-Newtonian Fluid Mech.*, *153*(1), 53–61.

Bachu, S. (2008), CO_2 storage in geological media: Role, means, status and barriers to deployment, *Progress in Energy and Combustion Science*, *34*(2), 254–273.

Bandopadhyay, A., Y. Méheust, and T. Le Borgne (2016), Reaction kinetics of a front under shear flow fo abritrary damköhler numbers, to be submitted.

Becker, M. W., and A. M. Shapiro (2003), Interpreting tracer breakthrough tailing from different forced-gradient tracer experiment configurations in fractured bedrock, *Water Resour. Res.*, *39*(1).

Bekins, B. A., I. M. Cozzarelli, E. M. Godsy, E. Warren, H. I. Essaid, and M. E. Tuccillo (2001), Progression of natural attenuation processes at a crude oil spill site: II. controls on spatial distribution of microbial populations, *J. Contam. Hydrol.*, *53*(3), 387–406.

Berkowitz, B., and J. Zhou (1996), Reactive solute transport in a single fracture, *Water Resour. Res.*, *32*(4), 901–913.

Beven, K., and P. Germann (1982), Macropores and water flow in soils, *Water Resour. Res.*, *18*(5), 1311–1325.

Binley, A., and A. Kemna (2005), DC resistivity and induced polarization methods, in *Hydrogeophysics*, pp. 129–156, Springer.

Birovljev, A., L. Furuberg, J. Feder, T. Jøssang, K. J. Måløy, and A. Aharony (1991), Gravity invasion percolation in 2 dimensions – experiment and simulation, *Phys. Rev. Lett.*, *67*(5), 584–587.

Bolster, D., M. Dentz, and T. Le Borgne (2009), Solute dispersion in channels with periodically varying apertures, *Phys. Fluids*, *21*(5), 056,601, doi:10.1063/1.3131982.

Bolster, D., Y. Méheust, T. Le Borgne, J. Bouquain, and P. Davy (2014), Modeling preasymptotic transport in flows with significant inertial and trapping effects–the importance of velocity correlations and a spatial markov model, *Advances in Water Resources*, *70*, 89–103.

Bonnet, E., O. Bour, N. E. Odling, P. Davy, I. Main, P. Cowie, and B. Berkowitz (2001), Scaling of fracture systems in geological media, *Rev. Geophys.*, *39*(3), 347–383.

Borden, R. C. (2007), Effective distribution of emulsified edible oil for enhanced anaerobic bioremediation, *J. Contam. Hydrol.*, *94*(1), 1–12.

Bouquain, J. (2012), Etude numérique de l'impact des effets densitaires et inertiels sur le transport en milieu chenalisé, Ph.D. thesis, Université de Rennes 1.

Bouquain, J., Y. Méheust, and P. Davy (2011), Horizontal pre-asymptotic solute transport in a model fracture with significant density contrasts, *J. Contaminant. Hyd.*, *120-121*, 184–197.

Bouquain, J., Y. Meheust, D. Bolster, and P. Davy (2012), The impact of inertial effects on solute dispersion in a channel with periodically varying aperture, *Phys. Fluids*, *24*, 083,602.

Bour, O., and P. Davy (1997), Connectivity of random fault networks following a power law fault distribution, *Water Resour. Res.*, *33*(7), 1567–1583.

Bour, O., and P. Davy (1998), On the connectivity of three-dimensional fault networks, *Water Resour. Res.*, *34*(10), 2611–2622.

Bour, O., and P. Davy (1999), Clustering and size distributions of fault patterns: Theory and measurements, *Geophys. Res. Lett.*, *26*(13), 2001–2004.

Bretherton, F. (1961), The motion of long bubbles in tubes, *J. Fluid Mech.*, *10*(02), 166–188.

Brown, S. R. (1987), Fluid flow through rock joints: the effect of surface roughness, *J. Geophys. Res.*, *92*, 1337–1347.

Brown, S. R. (1995), Simple mathematical model of a rough fracture, *J. Geophys. Res.*, *100*(B4), 5941–5952.

Brown, S. R., R. L. Kranz, and B. P. Bonner (1986), Correlation between the surfaces of natural rock joints, *Geophys. Res. Lett.*, *13*, 1430–1433.

Cantat (2004), Dissipation in foam flowing through narrow channels, *Europhys. Lett. (EPL)*, *65*(5), 726.

Cantat, I., S. Cohen-Addad, F. Elias, F. Graner, R. Hœhler, O. Pitois, F. Rouyer, and A. Saint-Jalmes (2013), *Foams. Structure and dynamics.*, Oxfort University Press, translated by Ruth Flatman.

Chen, M., Y. Yortsos, and W. Rossen (2005), Insights on foam generation in porous media from pore-network studies, *Colloid. Surf. A: Physicochemical and Engineering Aspects*, *256*(2), 181–189.

Chowdiah, P., B. R. Misra, J. J. Kilbane, V. J. Srivastava, and T. D. Hayes (1998), Foam propagation through soils for enhanced in situ remediation, *J. Hazard. Mater.*, *62*, 265–280.

Cobos, S., M. Carvalho, and V. Alvarado (2009), Flow of oil–water emulsions through a constricted capillary, *Int. J. Multiphase Flow*, *35*(6), 507–515.

Coussot, P., N. Roussel, S. Jarny, and H. Chanson (2005), Continous or catastrophic solid-liquid transition in jammed systems, *Phys. Fluids*, *17*, 011,704.

Cox, S. J., S. Neethling, W. R. Rossen, W. Schleifenbaum, P. Schmidt-Wellenburg, and J. J. Cilliers (2004), A theory of the effective yield stress of foam in porous media: the motion of soap film traversing a three-dimensional pore, *Colloid. Surf. A*, *245*(1-3), 143–151.

Crank, J. (1979), *The mathematics of diffusion*, Oxford university press.

da Silva, G. J., J. O. Fossum, E. DiMasi, K. J. Måloy, and S. B. Lutnæs (2002), Synchrotron x-ray scattering studies of water intercalation in a layered synthetic silicate, *Phys. Rev. E*, *66*(1), 011,303.

Darcel, C., O. Bour, and P. Davy (2003a), Cross-correlation between length and position in real fracture networks, *Geophys. Res. Lett.*, *30*(12), 1650.

Darcel, C., O. Bour, and P. Davy (2003b), Stereological analysis of fractal fracture networks, *J. Geophys. Res.*, *108*(B9), 2451.

Darcel, C., O. Bour, P. Davy, and J. R. de Dreuzy (2003c), Connectivity properties of two-dimensional fracture networks with stochastic fractal correlation, *Water Resour. Res.*, *39*(10).

Davis, C. A., E. Atekwana, E. Atekwana, L. D. Slater, S. Rossbach, and M. R. Mormile (2006), Microbial growth and biofilm formation in geologic media is detected with complex conductivity measurements, *Geophys. Res. Lett.*, *33*(18).

Davy, P., C. Darcel, O. Bour, R. Munier, and J.-R. De Dreuzy (2006), A note on the angular correction applied to fracture intensity profiles along drill core, *J. Geophys. Res.: Solid Earth (1978–2012)*, *111*(B11).

de Anna, P., T. Le Borgne, M. Dentz, A. M. Tartakovsky, D. Bolster, and P. Davy (2013), Flow intermittency, dispersion, and correlated continuous time random walks in porous media, *Phys. Rev. Lett.*, *110*(18), 184,502.

de Anna, P., M. Dentz, A. Tartakovsky, and T. Le Borgne (2014a), The filamentary structure of mixing fronts and its control on reaction kinetics in porous media flows, *Geophys. Res. Lett.*, *41*(13), 4586–4593.

de Anna, P., J. Jimenez-Martinez, H. Tabuteau, R. Turuban, T. Le Borgne, M. Derrien, and M. Y. (2014b), *Environ. Sci. Technol.*, *48*, 508–516.

de Dreuzy, J. R., P. Davy, and O. Bour (2001a), Hydraulic properties of two-dimensional random fracture networks following a power law length distribution – 1. effective connectivity, *Water Resour. Res.*, *37*(8), 2065–2078.

de Dreuzy, J. R., P. Davy, and O. Bour (2001b), Hydraulic properties of two-dimensional random fracture networks following a power law length distribution – 2. permeability of networks based on lognormal distribution of apertures, *Water Resour. Res.*, *37*(8), 2079–2095.

de Dreuzy, J.-R., C. Darcel, P. Davy, and O. Bour (2004), Influence of spatial correlation of fracture centers on the permeability of two-dimensional fracture networks following a power law length distribution, *Water Resour. Res.*, *40*, W01,502.

de Dreuzy, J.-R., Y. Méheust, and G. Pichot (2012), Influence of fracture scale heterogeneity on the flow properties of three-dimensional discrete fracture networks (DFN), *J. Geophys. Res.: Solid Earth*, *117*(B11), n/a–n/a, doi:10.1029/2012JB009461.

de Gennes, P. G., and J. Prost (1993), *The Physics of Liquid Crystals*, chap. 2.1, pp. 41–42, 2nd ed., Oxford Science Publications.

de Simoni, M., X. Sanchez-Vila, J. Carrera, and M. Saaltink (2007), A mixing ratios-based formulation for multicomponent reactive transport, *Water Resour. Res.*, *43*, W07,419.

Dentz, M., and J. Carrera (2007), Mixing and spreading in stratified flow, *Phys. Fluids*, *19*, 017,107.

Dentz, M., I. Neuweiler, Y. Méheust, and D. M. Tartakovsky (2015), Interface statistics and saturation dynamics in a stochastic interface growth model, to be resubmitted.

Detwiler, R. L., H. Rajaram, and R. J. Glass (2001), Nonaqueous-phase-liquid dissolution in variable-aperture fractures: Development of a depth-averaged computational model with comparison to a physical experiment, *Water Resour. Res.*, *37*(12), 3115–3129.

di Federico, V. (1997), Estimates of equivalent aperture for non-newtonian flow in a rough-walled fracture, *Int. J. Rock Mech. Mining Sci.*, *34*(7), 1133–1137.

di Federico, V. (1998), Non-newtonian flow in a variable aperture fracture, *Trans. Por. Med.*, *30*(1), 75–86.

di Federico, V. (2001), On non-newtonian fluid flow in rough fractures, *Water Resour. Res.*, *37*(9), 2425–2430.

DiMasi, E., J. O. Fossum, T. Gog, and C. Venkataraman (2001), Orientational order in gravity dispersed clay colloids: A synchrotron x-ray scattering study of na fluorohectorite suspensions, *Phys. Rev. E*, *64*, 061,704.

Ding, D., B. Liu, X. Shen, L. Zhong, and X. Li (2013), Foam-assisted delivery of nanoscale zero valent iron in porous media, *J. Environ. Eng.*, *139*(9), 1206–1212.

Doetsch, J., N. Linde, T. Vogt, A. Binley, and A. G. Green (2012), Imaging and quantifying salt-tracer transport in a riparian groundwater system by means of 3d ert monitoring, *Geophysics*, *77*(5), B207–B218.

Dollet, B., and C. Raufaste (2014), Rheology of aqueous foams, *Comptes Rendus Physique*, *15*(8), 731–747.

Dollet, B., S. A. Jones, Y. Méheust, and I. Cantat (2014), Influence of the elastic deformation of a foam on its mobility in a model porous medium, *Phys. Rev. E*, *90*, 023,006.

Dorn, C., N. Linde, T. Le Borgne, O. Bour, and L. Baron (2011), Single-hole GPR reflection imaging of solute transport

in a granitic aquifer, *Geophys. Res. Lett.*, *38*(8).

Dronfield, D. G., and S. E. Silliman (1993), *Water Resour.Res.*, *29*(10), 3477–3483.

Du, D.-X., A. N. Beni, R. Farajzadeh, and P. L. Zitha (2008), Effect of water solubility on carbon dioxide foam flow in porous media: an x-ray computed tomography study, *Industrial & Eng. Chem. Res.*, *47*(16), 6298–6306.

Durham, W. M., O. Tranzer, A. Leombruni, and R. Stocker (2012), Division by fluid incision: Biofilm patch development in porous media, *Phys. Fluids*, *24*(9), 091,107–091,107.

Elenius, M., and K. Johannsen (2012), On the time scales of nonlinear instability in miscible displacement porous media flow, *Computational Geosciences*, *16*, 901–911.

Emami-Meybodi, H., H. Hassanzadeha, C. Green, and J. Ennis-King (2015), Convective dissolution of CO_2 in saline aquifers: Progress in modeling and experiments, *International Journal of Greenhouse Gas Control*, *40*, 238–266.

Ferer, M., D. Crandall, G. Ahmadi, and D. H. Smith (2011), Two-phase flow in a rough fracture: Experiment and modeling, *Phys. Rev. E*, *84*(1), 016,316.

Fergui, O., H. Bertin, and M. Quintard (1998), Transient aqueous foam flow in porous media: experiments and modeling, *J. Petrol. Sci. Eng.*, *20*(1), 9–29.

Ferguson, D., and S. Cox (2013), The motion of a foam lamella traversing an idealised bi-conical pore with a rounded central region, *Colloid. Surf. A: Physicochemical and Engineering Aspects*, *438*, 56–62.

Ferrari, A., J. Jimenez-Martinez, T. Le Borgne, Y. Méheust, and I. Lunati (2015), Challenges in modeling unstable two-phase flow experiments in porous micromodels, *Water Resour. Res.*, *51*, 1381–1400.

Fonseca, D. M., Y. Méheust, J. O. Fossum, K. D. Knudsen, K. J. Måløy, and K. P. S. Parmar (2007), Phase behavior of platelet-shaped nanosilicate colloids in saline solutions – a saxs study, *J. Appl. Cryst.*, *40*, s292–s296.

Fonseca, D. M., Y. Méheust, J. O. Fossum, K. Knudsen, and K. P. S. Parmar (2009), Phase diagram of polydisperse na-fluorohectorite–water suspensions: A synchrotron small-angle X-ray scattering study, *Phys Rev. E*, *79*, 021,402.

Fossum, J. O. (1999), Physical phenomena in clays, *Physica A*, *270*(1-2).

Fossum, J. O., E. Gudding, D. de M. Fonseca, Y. Méheust, E. Di Masi, T. Gog, and C. Ventakaraman (2005), Observations of orientational ordering in aqueous suspensions of a nano-layered silicate, *Energy*, *30*(6), 861–872.

Fossum, J. O., Y. Méheust, K. P. S. Parmar, K. Knudsen, and K. J. Måløy (2006), Intercalation-enhanced particle polarization and chain formation of nano-layered particles, *Europhys. Lett.*, *74*(3), 438–444.

Frette, V., J. Feder, T. Jøssang, and P. Meakin (1992), Boyancy-driven fluid migration in porous media, *Phys. Rev. Lett.*, *68*(21), 3164–3167.

Fu, X., L. Cueto-Felgueroso, and R. Juanes (2013), Pattern formation and coarsening dynamics in three-dimensional convective mixing in porous media, *Philosophical Transactions of the Royal Society of London A: Mathematical, Physical and Engineering Sciences*, *371*(2004), 20120,355.

Gauglitz, P., and C. Radke (1990), The dynamics of liquid film breakup in constricted cylindrical capillaries, *Journal of Colloid and Interface Science*, *134*(1), 14–40.

Gill, W. N., and R. Sankarasubramanian (1970), Exact analysis of unsteady convection diffusion, *Proc. R. Soc. Lond. A*, *316*, 341–350.

Glass, R. J., M. J. Nicholl, and L. Yarrington (1998), A modified invasion percolation model for low-capillary number immiscible displacements in horizontal rough-walled fractures: Influence of local in-plane curvature, *Water Resour. Res.*, *34*(12), 3215–3234.

Glover, P. W. J., K. Matsuki, R. Hikima, and K. Hayashi (1998), Synthetic rough fractures in rocks, *J. Geophys. Res.*, *103*(B5), 9609–9620.

Gramling, C. M., C. F. Harvey, and L. C. Meigs (2002), Reactive transport in porous media: A comparison of model prediction with laboratory visualization, *Environ. Sci. & Technol.*, *36*(11).

Grathwohl, P., et al. (2013), Catchments as reactors: a comprehensive approach for water fluxes and solute turnover, *Environmental Earth Sciences*, *69*(2), 317–333.

Guillen, V., M. Carvalho, and V. Alvarado (2012), Pore scale and macroscopic displacement mechanisms in emulsion flooding, *Trans. Por. Med.*, *94*(1), 197–206.

Géraud, B., S. A. Jones, I. Cantat, B. Dollet, and Y. Méheust (2016), The flow of a foam in a two-dimensional porous medium, *Water Resour. Res.*, in press.

Haas, A., and A. Revil (2009), Electrical burst signature of pore-scale displacements, *Water Resour. Res.*, *45*(10).

Halsey, T. C. (1992), Electrorheological fluids, *Science*, *258*(5083), 761–766.

Hassanizadeh, S. M., M. A. Celia, and H. K. Dahle (2002), Dynamic effect in the capillary pressure–saturation relationship and its impacts on unsaturated flow, *Vadose Z. J.*, *1*(1), 38–57.

Held, R., and T. Illangasekare (1995), Fingering of dense nonaqueous phase liquids in porous media: 1. experimental investigation, *Water Resources Res.*, *31*, 1213–1222.

Hele-Shaw, H. S. S. (1898), *Trans. Instn. Nav. Archit.*, *40*, 21.

Heller, J. P., and M. S. Kuntamukkula (1987), Critical review of the foam rheology literature, *Industrial & Eng. Chem. Res.*, *26*(2), 318–325.

Hemmen, H., N. I. Ringdal, E. N. de Azevedo, M. Engelsberg, E. L. Hansen, Y. Méheust, J. O. Fossum, and K. D. Knudsen (2009), The isotropic-nematic interface in suspensions of Na-fluorohectorite synthetic clay, *Langmuir*, *25*(21), 12,507–12,515.

Hemmen, H., L. R. Alme, J. O. Fossum, and Y. Meheust (2010), X-ray studies of interlayer water absorption and meso-porous water transport in a weakly hydrated clay, *Phys. Rev. E*, *82*, 036,315.

Hirasaki, G., et al. (1997), Field demonstration of the surfactant/foam process for aquifer remediation, in *SPE Annual Technical Conference and Exhibition*, Society of Petroleum Engineers.

Homsy, G. M. (1987), Viscous fingering in porous media, *Annu. Rev. Fluid Mech.*, *19*, 271–311.

Huang, C.-W., and C.-H. Chang (2000), A laboratory study on foam-enhanced surfactant solution flooding in removing n-pentadecane from contaminated columns, *Colloid. Surf. A: Physicochemical and Engineering Aspects*, *173*(1), 171–179.

Huang, D. D., A. Nikolov, and D. T. Wasan (1986), Foams: basic properties with application to porous media, *Langmuir*, *2*(5), 672–677.

Hulin, J., E. Clement, C. Baudet, J. Gouyet, and M. Rosso (1988), Quantitative analysis of an invading-fluid invasion front under gravity, *Phys. Rev. Lett.*, *61*(3), 333.

Hunter, W. J. (2005), Injection of innocuous oils to create reactive barriers for bioremediation: Laboratory studies, *J. Contam. Hydrol.*, *80*(1), 31–48.

Huppert, H., and J. Neufeld (2014), The fluid mechanics of carbon dioxide sequestration, *Annu. Rev. Fluid Mech.*, *46*, 255–72.

Jenkins, K. B., D. L. Michelsen, and J. T. Novak (1993), Application of oxygen microbubbles for in situ biodegradation of p-xylene-contaminated groundwater in a soil column, *Biotechnology progress*, *9*(4), 394–400.

Jeong, S.-W., and M. Y. Corapcioglu (2003), A micromodel analysis of factors influencing napl removal by surfactant foam flooding, *J. Contam. Hydrol.*, *60*(1), 77–96.

Jeong, S.-W., and M. Y. Corapcioglu (2005), Force analysis and visualization of napl removal during surfactant-related floods in a porous medium, *Journal of hazardous materials*, *126*(1), 8–13.

Jeong, S.-W., M. Y. Corapcioglu, and S. E. Roosevelt (2000), Micromodel study of surfactant foam remediation of residual trichloroethylene, *Environ. Sci. & Technol.*, *34*(16), 3456–3461.

Jiménez-Martínez, J., P. d. Anna, H. Tabuteau, R. Turuban, T. L. Borgne, and Y. Méheust (2015), Pore-scale mechanisms for the enhancement of mixing in unsaturated porous media and implications for chemical reactions, *Geophys. Res. Lett.*, *42*(13), 5316–5324.

Jiménez-Martínez, J., T. Le Borgne, H. Tabuteau, and Y. Méheust (2016), Mixing dynamics in unsaturated porous media: Insights from a photo-bleaching pulse line injection, preprint.

Jones, S. A., B. Dollet, Y. Méheust, S. J. Cox, and I. Cantat (2013), Structure-dependent mobility of a dry aqueous foam flowing along two parallel channels, *Phys. Fluids*, *25*, 063,101.

Juanes, R., E. Spiteri, F. Orr, and M. Blunt (2006), Impact of relative permeability hysteresis on geological CO_2 storage, *Water Resour. Res.*, *42*(12).

Kaviratna, P. D., T. J. Pinnavaia, and P. A. Schroeder (1996), Dielectric properties of smectite clays, *J. Phys. Chem. Solids*, *57*, 1897–1906.

Keller, A. A., P. V. Roberts, and M. J. Blunt (1999), Effect of fracture aperture variations on the dispersion of contaminants, *Water Resour. Res.*, *35*(1), 55–63.

Khaldoun, A., P. Moller, G. Wegdam, B. de Leeuw, Y. Méheust, J. O. Fossum, and D. Bonn (2009), Quickclay : landslides of clayey soils, *Phys. Rev. Lett.*, *103*, 188,301.

Khatib, Z., G. Hirasaki, A. Falls, et al. (1988), Effects of capillary pressure on coalescence and phase mobilities in foams flowing through porous media, *SPE reservoir engineering*, *3*(03), 919–926.

Kovscek, A., G.-Q. Tang, and C. Radke (2007), Verification of roof snap off as a foam-generation mechanism in porous media at steady state, *Colloid. Surf. A: Physicochemical and Engineering Aspects*, *302*(1), 251–260.

Kovscek, A. R., and C. J. Radke (1994), Fundamentals of foam transport in porous media, in *Foams: Fundamentals and Applications in the Petroleum Industry*, edited by L. L. Schramm, chap. 3, pp. 115–163, ACS Publications.

Lavrov, A. (2014), Radial flow of non-newtonian power-law fluid in a rough-walled fracture: Effect of fluid rheology, *Trans. Por. Med.*, *105*(3), 559–570.

Le Borgne, T., F. Paillet, O. Bour, and J.-P. Caudal (2006), Cross-borehole flowmeter tests for transient heads in heterogeneous aquifers, *Ground Water*, *44*(3), 444–452.

Le Borgne, T., M. Dentz, and J. Carrera (2008), Lagrangian statistical model for transport in highly heterogeneous velocity fields, *Phys. Rev. Lett.*, *101*(9), 090601, doi:10.1103/PhysRevLett.101.090601.

Le Borgne, T., M. Dentz, and E. Villermaux (2013), Stretching, coalescence and mixing in porous media, *Phys. Rev. Lett.*, *110*, 204,501.

Le Borgne, T., M. Dentz, and E. Villermaux (2015), The lamellar description of mixing in porous media, *J. Fluid Mech.*, *770*, 458–498.

Lenormand, R. (1990), Liquids in porous media, *Journal of Physics: Condensed Matter*, *2*(S), SA79.

Lenormand, R., and C. Zarcone (1985), Invasion percolation in an etched network: measurement of a fractal dimension, *Phys. Rev. Lett.*, *54*(20), 2226–2229.

Lenormand, R., and C. Zarcone (1989), Capillary fingering: Percolation and fractal dimension, *Trans. Por. Med.*, *4*, 599–612.

Lenormand, R., E. Touboul, and C. Zarcone (1988), Numerical models and experiments on immiscible displacement in

porous media, *J. Fluid Mech.*, *189*, 165–187.

Lester, D., G. Metcalfe, and M. Trefry (2013), Is chaotic advection inherent to porous media flow?, *Phys. Rev. Lett.*, *111*(17), 174,101.

Levitz, P., E. Lecolier, A. Mourchid, A. Delville, and S. Lyonnard (2000), Liquid-solid transition of laponite suspensions at very low ionic strength: Long-range electrostatic stabilisation of anisotropic colloids, *Europhys. Lett.*, *49*(5), 672.

Lichtner, P. C., and Q. Kang (2007), Upscaling pore-scale reactive transport equations using a multiscale continuum formulation, *Water Resour. Res.*, *43*(12).

Loggia, D., Z. Bo, L. Xiaorong, and G. Vasseur (2009), Experimental study of upward oil migration in a fracture, *Trans. Por. Med.*, *80*(1), 1–16.

Løvoll, G., Y. Méheust, R. Toussaint, J. Schmittbuhl, and K. J. Måløy (2004), Growth activity during fingering in a porous hele-shaw cell, *Phys. Rev. E*, *70*, 026,301.

Løvoll, G., Y. Méheust, K. J. Måloy, E. Aker, and J. Schmittbuhl (2005a), Competition of gravity, capillary and viscous forces during drainage in a two-dimensional porous medium, a pore-scale study, *Energy*, *30*, 861–872.

Løvoll, G., B. Sandnes, Y. Méheust, K. J. Måløy, J. O. Fossum, G. J. da Silva, M. S. P. Mundim, R. Droppa, and D. d. M. Fonseca (2005b), Dynamics of water intercalation fronts in a nano-layered synthetic silicate: a synchrotron x-ray scattering study, *Physica B*, *370*, 90–98.

Løvoll, G., M. Jankov, K. J. Måløy, R. Toussaint, J. Schmittbuhl, G. Schäfer, and Y. Méheust (2011), Influence of viscous fingering on dynamic saturation-pressure curves in porous media, *Trans. Por. Med.*, *86*, 305–324.

Ma, K., R. Liontas, C. A. Conn, G. J. Hirasaki, and S. L. Biswal (2012), Visualization of improved sweep with foam in heterogeneous porous media using microfluidics, *Soft Matter*, *8*(41), 10,669–10,675.

Måløy, K. J., J. Feder, and T. Jøssang (1985), Viscous fingering fractals in porous media, *Phys. Rev. Lett.*, *55*, 2688–2691.

Måløy, K. J., F. Boger, J. Feder, T. Jøssang, and P. Meakin (1987), Dynamics of viscous-fingering fractals in porous-media, *Phys. Rev. A*, *36*, 318–324.

Marmottant, P., and J.-P. Raven (2009), Microfluidics with foams, *Soft Matter*, *5*(18), 3385–3388.

McClain, M. E., et al. (2003), Biogeochemical hot spots and hot moments at the interface of terrestrial and aquatic ecosystems, *Ecosystems*, *6*(4), 301–312.

Meakin, P., A. Birovljev, V. Frette, J. Feder, and T. Jøssang (1992), Gradient stabilized and destabilized invation percoation, *Physica A*, *191*, 227–239.

Méheust, Y., and J. Schmittbuhl (2000), Flow enhancement of a rough fracture, *Geophys. Res. Lett.*, *27*(18), 2989–2992.

Méheust, Y., and J. Schmittbuhl (2001), Geometrical heterogeneities and permeability anisotropy of rough fractures, *J. Geophys. Res.*, *106*(B2), 2089–2102.

Méheust, Y., and J. Schmittbuhl (2003), Scale effects related to flow in rough fractures, *Pure Appl. Geophys.*, *160*(5-6), 1023–1050.

Méheust, Y., G. Løvoll, K. J. Måløy, and J. Schmittbuhl (2002), Interface scaling in a two-dimensional porous medium under combined viscous, gravity and capillary effects, *Phys. Rev. E*, *66*, 051,603.

Méheust, Y., K. Knudsen, and J. O. Fossum (2006), Inferring orientation distributions in anisotropic powders of nanolayered crystallites from a single 2d waxs image, *J. Appl. Cryst.*, *39*, 661–670.

Méheust, Y., G. Løvoll, B. Sandnes, K. J. Måløy, J. O. Fossum, G. J. da Silva, M. S. P. Mundim, and D. Droppa, R.and d. M. Fonseca (2006), Using synchrotron x-ray scattering to study the diffusion of water in a weakly hydrated clay sample, *Clay Science*, *12*(Supp. 2), 66–70.

Méheust, Y., K. P. S. Parmar, B. Schjelderupsen, and J. O. Fossum (2011), The electrorheology of suspensions consisting of Na-fluorohectorite synthetic clay particles in silicon oil, accepted.

Meile, C., and K. Tuncay (2006), Scale dependence of reaction rates in porous media, *Advances in Water Resources*, *29*(1), 62–71.

Michel, L. (2009), Transport en fracture et interaction avec la matrice : une expérience analogique, Ph.D. thesis, Université de Rennes 1.

Michels, L., Y. Méheust, M. Altoé, E. dos Santos, H. Hemmen, R. D. Jr., J. Fossum, and G. da Silva (2016), Water vapor transport in porous swelling clays: Control of normal vs. anomalous diffusion, to be resubmitted.

Morse, J. G., S. W. Petersen, M. J. Truex, and G. V. Last (2007), Treatability test plan for deep vadose zone remediation at the hanford's site central plateau, sgw-35774-fp, revision 0, *Tech. rep.*, Fluor Hanfort, Richland, WA.

Mourchid, A., A. Delville, J. Lambard, E. LeColier, and P. Levitz (1995), Phase diagram of colloidal dispersions of anisotropic charged particles: Equilibrium properties, structure, and rheology of laponite suspensions, *Langmuir*, *11*(6), 1942–1950.

Mourchid, A., E. Lecolier, H. van Damme, and P. Levitz (1998), On viscoelastic, birefringent, and swelling properties of laponite clay suspensions: revisited phase diagram, *Langmuir*, *14*, 4718–4723.

Méheust, Y., A. Falls, E. L. Hansen, J. O. Fossum, and D. Bonn (2016), Flow regimes of rehydrated quick clay – Implications for mudslides of clayey soil, to be resubmitted.

Møller, P. C. F., J. Mewis, and D. Bonn (2006), Yield stress and thixotropy: on the difficulty of measuring yield stresses in practice, *Soft Matter*, *2*, 274–283.

Neuman, S. P. (2005), Trends, prospects and challenges in quantifying flow and transport through fractured rocks, *Hydrogeology Journal*, *13*(1), 124–147.

Neuweiler, I., I. Sorensen, and W. Kinzelbach (2004), Experimental and theoretical investigations of drainage in horizontal rough-walled fractures with different correlation structures, *Advances in water resources*, *27*(12), 1217–1231.

Nguyen, Q. P., P. K. Currie, M. Buijse, and P. L. Zitha (2007), Mapping of foam mobility in porous media, *J. Petrol. Sci. Eng.*, *58*(1), 119–132.

Niemeyer, L., L. Pietronero, and H. Wiesmann (1984), Fractal dimension of dielectric breakdown, *Phys. Rev. Lett.*, *52*(12), 1033.

Or, D., P. Lehmann, E. Shahraeeni, and N. Shokri (2013), Advances in soil evaporation physics—a review, *Vadose Z. J.*, *12*(4).

panel on climate change (IPCC), I. (2007), Climate change 2007: The physical science basis. fourth assessment report, *Tech. rep.*, IPPCC Secretariat, Geneva, Switzerland.

Pang, Z.-X. (2010), The blocking ability and flowing characteristics of steady foams in porous media, *Transp. Porous Med.*, *85*(1), 299–316.

Parmar, K. P. S., Y. Méheust, and J. O. Fossum (2008), Electrorheological suspensions of laponite in oil: rheometry studies, *Langmuir*, *24*, 1814–1822, doi:10.1021/la702989u.

Pau, G., J. Bell, K. Pruess, A. Almgren, M. Lijewski, and K. Zhang (2010), High-resolution simulation and characterization of density-driven flow in CO_2 storage in saline aquifers, *Advances in Water Resources*, *33*, 443–455.

Raven, J.-P., and P. Marmottant (2009), Microfluidic crystals: dynamic interplay between rearrangement waves and flow, *Phys. Rev. Lett.*, *102*(8), 084,501.

Read, T., O. Bour, J. Selker, V. Bense, T. L. Borgne, R. Hochreutener, and N. Lavenant (2014), Active-distributed temperature sensing to continuously quantify vertical flow in boreholes, *Water Resour. Res.*, *50*(5), 3706–3713.

Rees, D., A. Selim, and J. Ennis-King (2008), The instability of unsteady boundary layers in porous media, *Emerging Topics in Heat and Mass Transfer in Porous Media (from the series Theory and Applications of Transport in Porous Media)*, *22*, 85–110.

Revil, A., E. Atekwana, C. Zhang, A. Jardani, and S. Smith (2012), A new model for the spectral induced polarization signature of bacterial growth in porous media, *Water Resour. Res.*, *48*(9).

Revil, A., J. Eppehimer, M. Skold, M. Karaoulis, L. Godinez, and M. Prasad (2013), Low-frequency complex conductivity of sandy and clayey materials, *Journal of colloid and interface science*, *398*, 193–209.

Roof, J., et al. (1970), Snap-off of oil droplets in water-wet pores, *Society of Petroleum Engineers Journal*, *10*(01), 85–90.

Rossen, W. R. (1990), Theory of mobilization pressure gradient of flowing foams in porous media: III. asymmetric lamella shapes, *Journal of Colloid and Interface Science*, *136*(1), 38 – 53.

Rothmel, R. K., R. W. Peters, E. St. Martin, and M. F. DeFlaun (1998), Surfactant foam/bioaugmentation technology for in situ treatment of tce-dnapls, *Environ. Sci. & Technol.*, *32*(11), 1667–1675.

Roux, S., F. Plouraboué, and J. P. Hulin (1996), Tracer dispersion in rough open cracks, *Transp. Por. Med.*, *32*(1), 97–116.

Roy, D., R. R. Kommalapati, K. T. Valsaraj, and W. D. Constant (1995a), Soil flushing of residual transmission fluid: application of colloidal gas aphron suspensions and conventional surfactant solutions, *Water Research*, *29*(2), 589–595.

Roy, D., S. Kongara, and K. Valsaraj (1995b), Application of surfactant solutions and colloidal gas aphron suspensions in flushing naphthalene from a contaminated soil matrix, *Journal of hazardous materials*, *42*(3), 247–263.

Rusconi, R., M. Garren, and R. Stocker (2014), Microfluidics expanding the frontiers of microbial ecology, *Annual review of biophysics*, *43*, 65.

Saffman, P. G., and G. Taylor (1958), The penetration of a fluid into a porous medium or hele-shaw cell containing a more viscous liquid, *Proc. Soc. London*, *Ser. A 245*, 312–329.

Salles, F., J.-M. Douillard, R. Denoyel, O. Bildstein, M. Jullien, I. Beurroies, and H. Van Damme (2009), Hydration sequence of swelling clays: Evolutions of specific surface area and hydration energy, *Journal of Colloid and Interface Science*, *333*(2), 510–522.

Schmittbuhl, J., A. Hansen, H. Auradou, and K. J. Måløy (2000), Geometry and dynamics of invasion percolation with correlated buoyancy, *Phys. Rev. E*, *61*(4), 3985–3995.

Seymour, J. D., J. P. Gage, S. L. Codd, and R. Gerlach (2004), Anomalous fluid transport in porous media induced by biofilm growth, *Phys. Rev. Lett.*, *93*(19), 198,103.

Shen, X., L. Zhao, Y. Ding, B. Liu, H. Zeng, L. Zhong, and X. Li (2011), Foam, a promising vehicle to deliver nanoparticles for vadose zone remediation, *J. Hazard. Mater.*, *186*, 1773–1780.

Simjoo, M., Q. Nguyen, and P. Zitha (2012), Rheological transition during foam flow in porous media, *Industrial & Eng. Chem. Res.*, *51*(30), 10,225–10,231.

Simjoo, M., Y. Dong, A. Andrianov, M. Talanana, and P. Zitha (2013), Ct scan study of immiscible foam flow in porous media for enhancing oil recovery, *Industrial & Eng. Chem. Res.*, *52*(18), 6221–6233.

Stevenson, P. (2012), *Foam engineering: fundamentals and applications*, John Wiley & Sons.

Surana, A., O. Grunberg, and G. Haller (2006), Exact theory of three-dimensional flow separation. part 1. steady separation, *J. Fluid Mech.*, *564*(10), 57–103.

Szafranski, R., J. Lawson, G. Hirasaki, C. Miller, N. Akiya, S. King, R. Jackson, H. Meinardus, and J. Londergan (1998), Surfactant/foam process for improved efficiency of aquifer remediation, *Prog. Colloid. Polym. Sci.*, *111*, 162 –167.

Tallakstad, K. T., H. A. Knudsen, T. Ramstad, G. Løvoll, K. J. Måløy, R. Toussaint, and E. G. Flekkøy (2009), Steady-

State Two-Phase Flow in Porous Media: Statistics and Transport Properties, *Phys. Rev. Lett.*, *102*, 074,502.

Taylor, G. I. (1954), Diffusion and mass transport in tubes, *Proc. Phys. Soc.*, *67*(12), 857.

Tél, T., A. de Moura, C. Grebogi, and G. Károlyi (2005), Chemical and biological activity in open flows: A dynamical system approach, *Physics reports*, *413*(2), 91–196.

Terriac, E., J. Etrillard, and I. Cantat (2006), Viscous force exerted on a foam at a solid boundary: Influence of the liquid fraction and of the bubble size, *EPL (Europhys. Lett.)*, *74*(5), 909.

Tilton, N., and A. Riaz (2014), Nonlinear stability of gravitationally unstable, transient, diffusive boundary layers in porous media, *J. Fluid Mech.*, *745*, 251.

Tilton, N., D. Daniel, and A. Riaz (2013), The initial transient period of gravitationally unstable diffusive boundary layers developing in porous media, *Phys. Fluids*, *25*, 092,107.

Toussaint, R., G. Løvoll, Y. Méheust, J. Schmittbuhl, and K. J. Måløy (2005), Influence of pore-scale disorder on viscous fingering during drainage, *Europhys. Lett.*, *71*(4), 583–589.

Toussaint, R., K. J. Måløy, Y. Méheust, G. Løvoll, M. Jankov, G. Schäfer, and J. Schmittbuhl (2012), Two-phase flow: structure, upscaling, and consequences for macroscopic transport properties, *Vadose Zone J.*, *11*(3).

Velde, B. (1992), *Introduction to Clay Minerals*, Chapman and Hall.

Wagner, G., P. Meakin, J. Feder, and T. Jøssang (1997), Invasion percolation on self-affine topographies, *Phys. Rev. E*, *55*(2), 1698–1703.

Wan, J., J. L. Wilson, and T. L. Kieft (1994), Influence of the gas-water interface on transport of microorganisms through unsaturated porous media, *Applied and Environmental Microbiology*, *60*(2), 509–516.

Wang, S., and C. N. Mulligan (2004), An evaluation of surfactant foam technology in remediation of contaminated soil, *Chemosphere*, *57*(9), 1079 – 1089.

Weaire, D. (2008), The rheology of foam, *Current Opinion in Colloid & Interface Science*, *13*(3), 171–176.

Weaire, D., and S. Hutzler (1999), *The physics of foams*, Oxford University Press.

Wellman, D. M., et al. (2007), Uranium stabilization throgh polyphosphate injection: 300 area uranium plume treatability demonstration project. interim rep. pnnl-16683, *Tech. rep.*, Northw. Natl. Lab., Richland, WA.

Wilkinson, D., and J. Willemsen (1983), Invasion percolation: A new form of percolation theory, *J. Phys. A*, *16*, 3365–3376.

Williams, K. H., A. Kemna, M. J. Wilkins, J. Druhan, E. Arntzen, A. L. N'Guessan, P. E. Long, S. S. Hubbard, and J. F. Banfield (2009), Geophysical monitoring of coupled microbial and geochemical processes during stimulated subsurface bioremediation, *Environ. Sci. & Technol.*, *43*(17), 6717–6723.

Willmann, M., J. Carrera, X. Sanchez-Vila, O. Silva, and M. Dentz (2010), Coupling of mass transfer and reactive transport for non-linear reactions in heterogeneous media, *Water Resour. Res.*, p. W07512. doi:10.1029/2009WR007739.

Yang, Z., A. Niemi, F. Fagerlund, and T. Illangasekare (2012a), Effects of single-fracture aperture statistics on entrapment, dissolution and source depletion behavior of dense non-aqueous phase liquids, *J. Contam. Hydrol.*, *133*, 1–16.

Yang, Z., A. Niemi, F. Fagerlund, and T. Illangasekare (2012b), A generalized approach for estimation of in-plane curvature in invasion percolation models for drainage in fractures, *Water Resour. Res.*, *48*(9).

Yang, Z., A. Niemi, F. Fagerlund, T. Illangasekare, and R. L. Detwiler (2013), Dissolution of dense non-aqueous phase liquids in vertical fractures: Effect of finger residuals and dead-end pools, *J. Contam. Hydrol.*, *149*, 88–99.

Yang, Z., I. Neuweiler, Y. Méheust, F. Fagerlund, and A. Niemi (2016), Fluid trapping during capillary displacement in fractures, *Adv. Water Resour.*, in press.

Zeng, J., Y. C. Yortsos, and D. Salin (2003), On the brinkman correction in unidirectional hele-shaw flows, *Phys. Fluids (1994-present)*, *15*(12), 3829–3836.

Zhdanov, S. A., A. Amiyan, L. M. Surguchev, L. M. Castanier, J. E. Hanssen, et al. (1996), Application of foam for gas and water shut-off: review of field experience, in *European Petroleum Conference*, Society of Petroleum Engineers.

Zhong, L., N. Qafoku, J. Szecsody, P. E. Dresel, and Z. F. Zhang (2009), Foam delivery of Calcium Polysulfide to the vadose zone for chromium(VI) immobilization: a laboratory evaluation, *Vadose Zone J.*, *8*, 976–985.

Zhong, L., J. Szecsody, F. Zhang, and S. M. Mattigod (2010), Foam delivery of amendments for vadose zone remediation: propagation performance in unsaturated sediments, *Vadose Zone J.*, *9*, 757–767.

Zhong, L., J. Szecsody, M. Oostrom, M. Truex, X. Shen, and X. Li (2011), Enhanced remedial amendment delivery to subsurface using shear thinning fluid and aqueous foam, *J. Hazard. Mater.*, *191*, 249–257.

Zitha, P., Q. Nguyen, P. Currie, and M. Buijse (2006), Coupling of foam drainage and viscous fingering in porous media revealed by x-ray computed tomography., *Trans. Por. Med.*, *64*, 301–313.

List of Figures

9 Key publications

The 7 articles below, which I consider key publications in my reference list, are appended to this thesis, starting on the next page:

- G. Løvoll, **Y. Méheust**, R. Toussaint, J. Schmittbuhl and K.-J. Måløy, Growth activity during fingering in a porous Hele Shaw cell, *Phys. Rev. E*, **70**(2), 026301 (2004).
- D. d. M. Fonseca, **Y. Méheust**, J. O. Fossum, K. D. Knudsen and K. J. Måløy, Phase diagram of polydisperse Na-fluorohectorite–water suspensions: A synchrotron small-angle x-ray scattering study, *Phys. Rev. E* **79**, 021402 (2009).
- J. Bouquain, **Y. Méheust**, D. Bolster, and P. Davy (2012), Impact of inertial effects on solute dispersion in channels with a periodically-varying aperture, *Phys. Fluids* **24**(8), 083602.
- J.-R. de Dreuzy, **Y. Méheust**, G Pichot (2012), Influence of fracture scale heterogeneity on the flow properties of three-dimensional Discrete Fracture Networks (DFN), *J. Geophys. Res.* **117**, B11207.
- P. de Anna, J. Jimenez-Martinez, H. Tabuteau, R. Turuban, T. Le Borgne, M. Derrien and **Y. Méheust** (2014), Mixing and reaction kinetics in porous media: an experimental pore scale quantification, *Environ. Sci. Tech.* **48**, 508-516.
- J. Jimenez-Martinez , P. de Anna , H. Tabuteau , R. Turuban , T. Le Borgne, and **Y. Méheust** (2015), Pore-scale mechanisms for the enhancement of mixing in unsaturated porous media and implications for chemical reactions, *Geophys. Rev. Lett.* **42**(13), 5316-5324.
- B. Géraud, S. A. Jones, I. Cantat, B. Dollet and **Y. Méheust** (2015), The flow of a foam in a two-dimensional porous medium, Water Resour. Res., in press.

Growth activity during fingering in a porous Hele-Shaw cell

Grunde Løvoll,[1,2] Yves Méheust,[3,2,1] Renaud Toussaint,[1,3] Jean Schmittbuhl,[2] and Knut Jørgen Måløy[1]
[1]*Department of Physics, University of Oslo, Norway*
[2]*Laboratoire de Géologie, École Normale Supérieure, Paris, France*
[3]*Department of Physics, NTNU Trondheim, Norway*
(Received 9 October 2003; revised manuscript received 10 February 2004; published 9 August 2004)

We present in this paper an experimental study of the invasion activity during unstable drainage in a two-dimensional random porous medium, when the (wetting) displaced fluid has a high viscosity with respect to that of the (nonwetting) displacing fluid, and for a range of almost two decades in capillary numbers corresponding to the transition between capillary and viscous fingering. We show that the invasion process takes place in an active zone within a characteristic screening length λ from the tip of the most advanced finger. The invasion probability density is found to only depend on the distance z to the latter tip and to be independent of the value for the capillary number Ca. The mass density along the flow direction is related analytically to the invasion probability density, and the scaling with respect to the capillary number is consistent with a power law. Other quantities characteristic of the displacement process, such as the speed of the most advanced finger tip or the characteristic finger width, are also consistent with power laws of the capillary number. The link between the growth probability and the pressure field is studied analytically and an expression for the pressure in the defending fluid along the cluster is derived. The measured pressure is then compared with the corresponding simulated pressure field using this expression for the boundary condition on the cluster.

DOI: 10.1103/PhysRevE.70.026301 PACS number(s): 47.20.Gv, 47.55.Mh, 47.54.+r, 47.55.−t

I. INTRODUCTION

Different types of unstable fluid displacements in porous media play an important role in many natural and commercial processes [1,2]. Development of a better understanding of these processes therefore has a broad scientific interest as well as potentially huge economical benefits. The complex patterns observed in such processes have been extensively studied and modeled over the last decades; see [1–7] and references therein.

The geometry of the displacement structures observed in immiscible two-phase flow is in general controlled by the competition between viscous forces, gravitational forces, and capillary forces; those various forces act on scales ranging from the pore scale to the system size. The relative wettabilities, viscosities, and densities of the fluids, as well as the heterogeneity of the underlying porous media, play an important role in the competition process. The relative magnitudes of viscous and capillary forces (on pore scale) are quantified through the dimensionless *capillary number* $\mathrm{Ca} = (\mu_w v_f a^2)/(\gamma \kappa)$ where μ_w is the viscosity in the wetting (displaced) fluid, v_f is the filtration speed, a is the characteristic pore size, γ is the interface tension, and κ is the permeability of the porous medium.

In this paper we address a drainage experiment in which nonwetting air displaces a high-viscous wetting glycerin/water solution in a horizontal two-dimensional porous medium; hence, gravity has no influence on the displacement. The porous medium consists of a Hele-Shaw cell filled with a random monolayer of monodisperse glass beads. We investigate the crossover regime between the regime of slow displacement for which capillary forces control the dynamics of the invasion process and the geometry of the resulting invasion structure (capillary fingering), and that of fast displacements where viscous forces are dominant (viscous fingering). We emphasize on the dependence of the invasion probability density ϕ, or activity, on the distance to the most advanced finger tip along the interface. The invasion probability density ϕ is the growth probability of the invasion structure; it is fundamental because both the structure and dynamics are controlled by this function. Growth probability has been discussed extensively in the past for diffusion limited aggregation (DLA) simulations [8–13] where it was found to be the multifractal distribution of the harmonic measure [11–14]. A strong analogy exists between the structures obtained by DLA and viscous fingering, as was first pointed by Paterson [15]. Both processes obey the Laplacian growth equation

$$\nabla^2 P = 0, \tag{1}$$

$$v \propto -\nabla P, \tag{2}$$

where P denotes the diffusing field—i.e., the probability density of random walkers in DLA or the pressure in viscous fingering—and v denotes the speed of the interface. However, both processes differ in that accreting particles of fixed size are added one by one in DLA, at a random location set by the growth probability proportional to $-\nabla P$, whereas in an empty Hele-Shaw cell, which is a regular porous medium of constant permeability, the growth process is deterministic and full layers are invaded along the whole interface, with a local velocity set by $-\nabla P$. In the absence of surface tension, Mullins-Sekerka instabilities develop in the deterministic Laplacian growth problem, leading to cusp singularities of the interface in a finite time [16]. This instability is regularized by the smallest scales accessible to the system, and another difference between DLA and viscous fingering in regular porous media is the nature of this so-called ultraviolet regularization, set by surface tension in viscous fingering or by the

particle size in DLA. The boundary value at the interface is given by surface tension γ for viscous fingering, $P \propto -\gamma/r$, where r is the local curvature of the boundary between both fluids, in contrast to DLA where it is set to constant P. These differences lead to very different structures in channel geometry—namely, stationary solutions corresponding to a Saffman-Taylor regular interface propagating at constant velocity in the case of viscous fingering in Hele-Shaw cells [7,17,18], as opposed to branched structures in the case of DLA [19,20]. In radial geometries however, solutions of both problems display branching and tip splitting, and some authors have argued that none of the above-mentioned differences affect the large scale structure and that viscous fingering patterns are identical to coarse grained DLA clusters [21]. Using the recently developed Hastings-Levitov formalism of iterated conformal maps [22], the relationship between DLA and deterministic Laplacian growth has been intensely investigated [22–28]. Although the issue for Laplacian growth is still controversial [24–26], it seems that DLA, Laplacian growth and viscous fingering in Hele-Shaw cells display indeed the same large-scale structure in radial geometry, with fractal dimensions respectively determined as $D=1.713\pm0.0003$ [29], $D=1.7$ [27], and $D=1.70\pm0.03$ [17].

The process of viscous fingering during drainage in a *random* porous medium, under study in the present paper, is *a priori* distinct from the above cases: although the pressure field satisfies the Laplace equation (1) at large scales, the presence of glass beads in the Hele-Shaw cell affects the viscous fingering process, modifying significantly the pressure boundary condition along the interface between the two fluids, with respect to the empty Hele-Shaw cell case. Fundamentally, the local interface curvature controlling the capillary pressure drop depends on the local pore geometry and is independent of the large-scale curvature, and distributed sizes of pore throats lead to a random distribution of capillary pressure thresholds inside the porous medium. These capillary pressure threshold values introduce a lower cutoff for the invasion probabilities, even for fast flows. In the slow displacement limit for which $v_f \simeq 0$, the invasion process is entirely controlled by the fluctuations of the capillary threshold distribution inside the porous medium [6,30]. For finite displacement velocities, as this study will show, the growth process is in this case intermediate between the one-by-one feature of DLA and the layer-by-layer characteristic of Laplacian growth: in the system studied here, several pores along the interface are invaded simultaneously, although not all of them—see Fig. 3—and it takes a finite time to invade a full pore. This pore-scale randomness in viscous fingering results in branched structure as well in channel geometry, as shown on Fig. 2, in contrast with the Saffman-Taylor fingers obtained in empty Hele-Shaw cells [7]. This might also be the reason why the measured fractal dimensions of viscous fingering patterns in radial geometry are reported slightly lower in random porous media similar to the one used here, $D=1.62$ [31], than in empty Hele-Shaw cells, $D=1.70$ [18].

Imbibition experiments (wetting fluid displacing a nonwetting fluid) were previously performed in a quasi-two-dimensional system [32,33], where the width of the viscous fingers was measured to scale with the capillary number as [32,33] $w_f \propto \mathrm{Ca}^{-0.5}$. This scaling relation was explained by a strong dynamic component of the capillary pressure [33]. We do not observe a strong dynamic component of the capillary pressure in our experiments (see below). The geometry of the invader for drainage is also significantly different from the invader structure of imbibition [32–35].

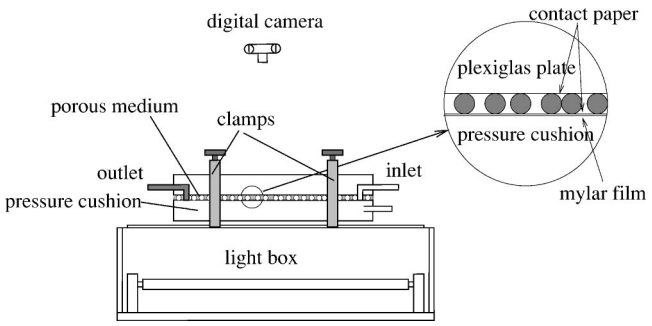

FIG. 1. Sketch of the experimental setup with the light box for illumination, the porous model, and the digital camera. The porous medium is sandwiched between two contact papers and kept together with a "pressure cushion."

In this study we study experimentally the growth probability density $\phi(z)$ as a function of the distance z (in the flow direction) from the most advanced finger tip and its dependence on the extraction speed (or capillary number). We also investigate experimentally the mass density $n(z)$ along the flow direction of the invader and confront the behavior of the measured $\phi(z)$ and $n(z)$ to what we expect from analytical arguments. A calculation of the z dependence of the pressure on the surface of the invader is presented, which yields the z dependence of the capillary pressure and shows a direct link with the measured growth probability density. Pressure measurements are performed in the model and compared with pressures simulated by solving the Laplace equation with this pressure boundary condition. Other features characteristic of the displacement, such as outermost tip velocity and the width of the invasion fingers, are also investigated.

The present article is organized as follows. We first present the experimental method (Sec. II). We then discuss the experimental results (Sec. III), and prospects (Sec. IV) before concluding (Sec. V).

II. EXPERIMENTAL METHOD

The experimental setup is shown in Fig. 1. The porous model consists of a monolayer of glass beads of diameter $a=1$ mm which is randomly spread between two contact papers [31,36]. The model is a transparent rectangular box of dimensions $L \times W$ and thickness a.

Two models of widths $W=430$ mm and $W=215$ mm have been used in the experiments; their other characteristics were identical. They are respectively referred to in the rest of the article as the "wide" and "narrow" models.

To prevent bending of the model a 2-cm-thick glass plate and a 2-cm-thick Plexiglas plate are placed on top of the model. To squeeze the beads and the contact paper together with the upper plate, a Mylar membrane mounted on a 2.5-cm-thick Plexiglas plate, below the model, is kept under a

3.5-m water pressure as a "pressure cushion." The upper and lower plates are kept together by clamps, and the side boundaries are sealed by a rectangular silicon rubber packing. Milled inlet and outlet channels are made in the upper Plexiglas plate. The distance between the inlet and outlet channels defines the length of the model, $L=840$ mm. One should also note that a few beads are removed from a small region near the center of the inlet channel, to initiate the invader in the center of the inlet. This is done to avoid edge effects appearing when the invader grows to the lateral boundaries of the model. The porosity of the models is measured to be 0.63 and the permeability is $\kappa=(0.0166\pm0.0017)\times10^{-3}$ cm^2 $=(1685\pm175)$ darcy.

The defending wetting fluid used in all our experiments is a 90%–10% by weight *glycerol-water* solution dyed with 0.1% Negrosine to increase the contrast between the colored fluid and the invader. *Air* is used as the invading nonwetting fluid. The *wetting* glycerol-water solution has a viscosity of $\mu_w\approx0.165$ Pa s and a density of $\rho_w=1235$ kg m^{-3} at room temperature. The corresponding parameters for the *nonwetting* air are $\mu_{nw}=1.9\times10^{-5}$ Pa s and $\rho_{nw}=116$ kg m^{-3}. The viscous ratio is thus $M=\mu_{nw}/\mu_w\sim10^{-4}$. The surface tension between these two liquids is $\gamma=6.4\times10^{-2}$ N m^{-1}. The temperature in the defending fluid is controlled and measured at the outlet of the model during each experiment, so as to accurately estimate the viscosity of the wetting fluid.

The absolute pressure in the wetting liquid is measured in the outlet channel and at a point at a distance of 280 mm (in the flow direction) from the inlet channel and 38 mm from the left boundary (looking in the flow direction) using Honeywell 26PCA Flow-Through pressure sensors.

The invader is visualized by illuminating the model from below with a light box and pictures are taken at regular intervals with a Kodak DCS 420 CCD camera, which is controlled by a computer over a SCSI connection. This computer records both the pictures and the pressure measurements. Each image contains 1536×1024 pixels, which corresponds to a spatial resolution of 0.55 mm per pixel or ~3.22 pixels per pore (1 mm^2); the color scale contains 256 gray levels. The gray level distribution of the image presents two peaks corresponding, respectively, to the white air-filled and dark gray glycerol-filled parts of the image. The image is filtered so as to obtain a clear boundary between the two phases, through a scheme that mainly consists in removing the background and thresholding at a gray level value between the two latter peaks. All further image treatments are performed on the resulting black and white image.

To check possible dynamic components of the capillary pressure we performed gravity stabilized experiments by keeping the experimental model vertical [36] and extracting the glycerol/water mixture from the bottom of the model. The capillary pressure was measured by recording the pressure in the model as the stabilized fluid front approaches the sensor. No systematic dynamic effect on the capillary pressure was found. For the low injection rates the width of the fronts was further used to estimate the minimum and width W_c of the capillary pressure threshold distribution.

Throughout the paper the following coordinate system is used: (x,z') is the orthonormal frame describing the porous medium plane, with z' the spatial coordinate in the direction of the flow (positive in flow direction). The position of the most advanced finger tip is denoted z'_{tip}; its speed along the z' axis is denoted $v_{tip}=\dot{z}'_{tip}$. The position along the z' axis computed with respect to that of the most advanced finger tip is $z=z'_{tip}-z'$. Those coordinates are indicated in Figs. 2 and 3.

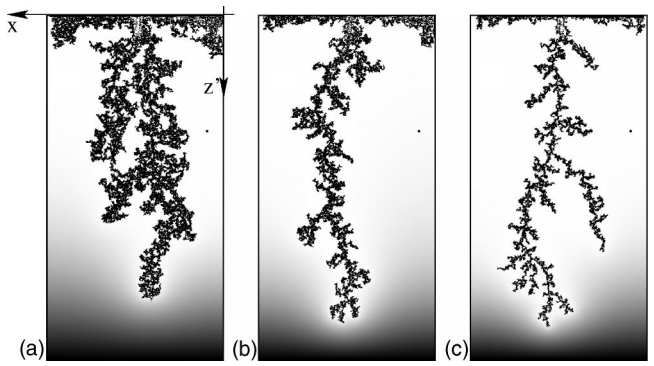

FIG. 2. Displacement structures obtained for different withdrawal rates: (a) Ca=0.027, (b) Ca=0.059, and (c) Ca=0.22. The images have been treated to separate the two phases. The black frame denotes the outer boundaries of the model, while the black spot close to the right edge of the model denotes the position of the pressure sensor. The simulated pressure field is shown superimposed on the image. Dark shadings correspond to low pressures while light shadings correspond to high pressure.

III. RESULTS

We present 12 experiments using the wide model for values of the capillary number Ca ranging from 1.4×10^{-2} to 3.6×10^{-1} and 5 experiments using the narrow model for capillary numbers ranging from 3.3×10^{-2} to 1.9×10^{-1}. The latter series was conducted to check system size dependences. For every experiment, we have carefully investigated the invasion process.

Figure 2 displays air clusters observed for the same porous medium, at three different flow rates. The complex structure of the air clusters is drawn in black. The particles of the porous medium are not shown. The defender—i.e., the glycerin/water solution—is drawn using a scale of grays ranging from white around the air cluster to black near the setup outlet; these shadings represent the intensity of the numerically estimated pressure field in the defending fluid (see Sec. III A). Figure 2(a) addresses an experiment carried out at a small rate (Ca=0.027). It displays a fat cluster where capillary forces dominate the dynamics of the invasion process, leading to a so-called *capillary fingering*. At larger displacement rates [Ca=0.22, Fig. 2(c)], the "fingers" appear thinner and less internal trapping of the defender is observed. This regime is dominated by viscous forces and is generally labeled as *viscous fingering*. For intermediate capillary numbers [Ca=0.059, Fig. 2(b)], the aspect of the cluster includes both geometries: capillary fingering at small scale and viscous fingering at large scale.

The pressure field around the clusters exhibits a fingerlike structure that has analogies to Saffman-Taylor fingers, as will

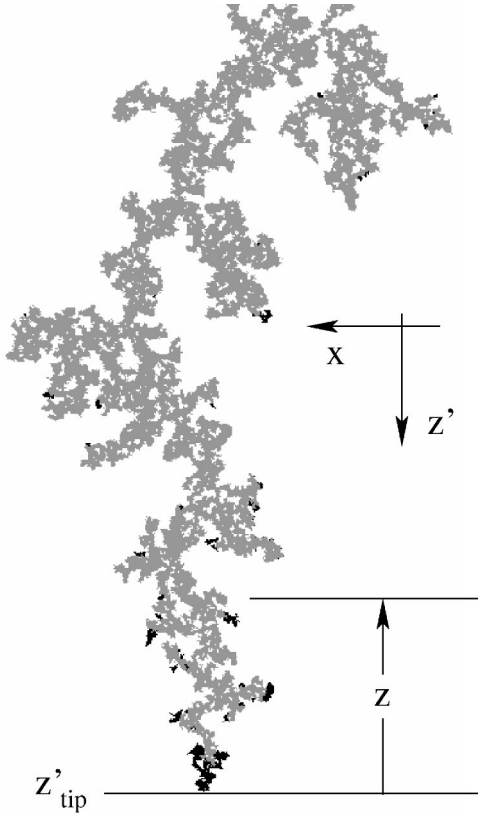

FIG. 3. Two consecutive images taken at a time interval $\Delta t \simeq 15$ during the experiment at Ca=0.059, drawn on top of each other. The invaded regions in the first image are painted light gray, the growth areas obtained by subtracting the first picture from the other one are painted black. The coordinate system used throughout the paper is also shown.

be discussed in Sec. IV. Accordingly, the displacement exhibits obvious capillary-number-dependent features, which are discussed in detail in Sec. III B below. In Sec. III A, we focus on the relation between the growth activity, the frozen structure left behind, and the pressure field in front of the fingers.

A. Relation between growth activity, frozen structure, and fluid pressures

The growth activity has been investigated by measuring the growth probability density $\phi(z)$ from series of images and performing pressure measurements.

1. Definition of growth probability density $\phi(z)$ and mass density $n(z)$

To investigate the growth process, images have been taken with constant time delay Δt between each image. The tip position of the longest finger is identified to find the coordinate system (x,z) and to be able to calculate the speed of the longest finger. The differential growth between two images is found by a direct image subtraction between two subsequent images. After the subtraction we typically have a collection of invaded pores representing the growth (see Fig. 3). The growth density $\phi^*(z)$ is defined as the average number of filled pores within $[z,z+\Delta z]$ divided with Δz. After an initial regime corresponding to the time needed for the longest finger to propagate a distance of the order of the width of the porous medium W, $\phi^*(z)$ is found to be fairly independent of time up to a few percents variations. In a given experiment with constant Ca, $\phi^*(z)$ is then averaged over all images excluding this initial regime, to obtain a good average of the stationary growth function. The growth probability density $\phi(z)=K\phi^*(z)$, where K is a normalization constant, is then found by normalizing $\phi^*(z)$ with respect to z so that

$$\int_0^L \phi(z)dz = 1. \tag{3}$$

Note that, in the remainder of the paper, z is in units of pore size ($a=1$ mm).

The mass density of the frozen structure $n(z)$ is defined as the average number of filled pores within $[z,z+\Delta z]$ divided with Δz. The average is taken over all images in a given experiment with constant Ca. Both $n(z)$ and $\phi(z)$ appeared to be fairly robust with respect to the width Δz of the analysis strips used to compute them.

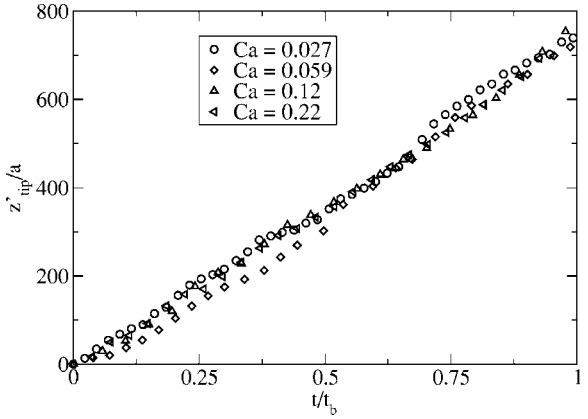

FIG. 4. Plot of the position of the most advanced finger tip, z'_{tip}, as a function of time. Data from the wide model. The time is rescaled by dividing with the break through time t_b, which is the time the most advanced finger reaches the outlet channel. The values of t_b are 5347 s, 1204 s, 476 s, and 256 s for capillary numbers Ca equal to 0.027, 0.059, 0.12, and 0.22, respectively.

2. Growth activity and the frozen structure left behind

For all experiments, the speed of the most advanced finger tip was observed to be fairly constant. Figure 4 shows the position of the most advanced finger tip, z'_{tip}, for different capillary numbers. After a short initial stage, the speed of the fingers saturates to a constant average value. Linear fits to the behavior z'_{tip} as a function of time outside the initiation stage provide an average finger tip speed v_{tip} for all experiments.

The measured invasion probability density function $\phi(z)$ is plotted in Fig. 5 as a function of the distance to the finger tip for the two system sizes on a linear-logarithmic plot. An exponential-like decay is seen for $z<W/2$ with a deviation

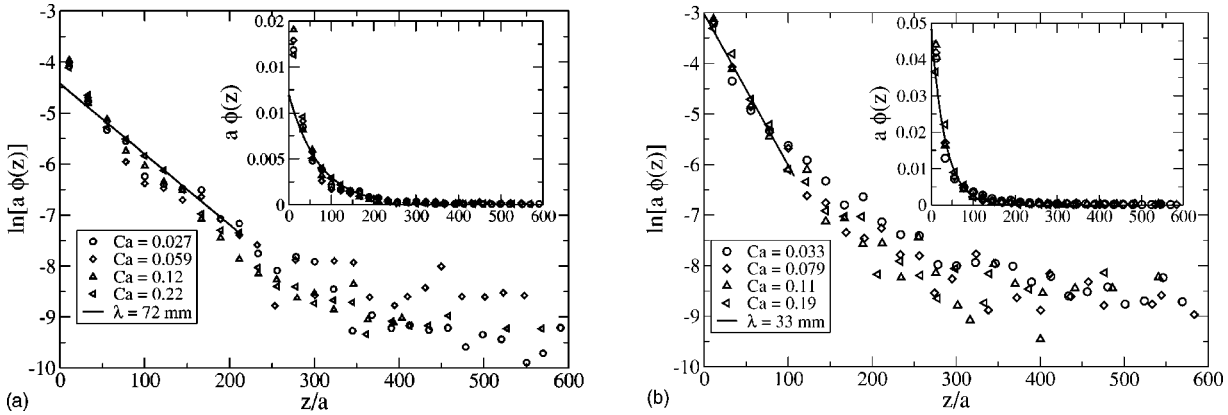

FIG. 5. Linear-logarithmic plot of the invasion probability density $\phi(z)$ as a function of the distance z to the finger tip (insets are double linear plots of the same invasion probability density). (a) Data from the wide experimental model and (b) from the narrow model. The solid lines in the curves correspond to the model function $\ln(Be^{-z/\lambda})$ obtained from linear regression over $\ln[a\cdot\phi(z)]$ for $z<W/2$, where $\phi(z)$ is the average measured invasion probability density. Note that $\phi(z)$ are averages of all the datasets and not only the sets shown in the graphs above. The average screening length λ is estimated from this fit.

from exponential behavior for larger lengths. A characteristic decay length or "screening length" λ is estimated from linear fits to the linear-logarithmic data for $z<W/2$ (see Fig. 5). As we can see from these plots a nice data collapse is obtained, indicating that the invasion probability density $\phi(z)$ and, thus, the screening length λ are independent of the capillary number for a given system. On the other hand, when comparing the two systems, the screening length λ depends on the system size: $\lambda=(72\pm10)$ mm for the wide model and $\lambda=(33\pm5)$ mm for the narrow model. The actual shape of function ϕ also seems to be weakly dependent on the system size.

Relating the mass of the frozen structure, $n(z)$, to the invasion probability density $\phi(z)$ and confronting the obtained relation to experimental results provides new insights into the displacement process. The total number of invaded pores in a time interval $[t,t+\Delta t]$ is $R\Delta t$, where R is the number of invaded pores per time unit. For a given flow rate Q, R is related to Q and to the characteristic pore volume V_{pore} by the relation $Q=RV_{\text{pore}}$, so that

$$R=\frac{W}{a^2}v_f, \tag{4}$$

where W is the width of the system, a is the characteristic pore size, and v_f is the Darcy or filtering velocity of the wetting fluid; for a given porous medium and fluid pair $v_f\propto \text{Ca}$. The number of invaded pores in the analysis strip defined by $z\in[z,z+\Delta z]$ during time interval $[t,t+\Delta t]$ is then $R\Delta t\phi(z)\Delta z$. The tip position z'_{tip} is further given by $z'_{\text{tip}}(t)=z'_0+v_{\text{tip}}t$ where v_{tip} is the speed of the finger tip (assumed to be constant) and $z'_0=z'_{\text{tip}}(t=0)$. This is a fairly good approximation after a short initial regime as seen in Fig. 4.

The total number of invaded pores in an analysis strip of width Δz at a distance z from the finger tip is thus given by

$$n(z)\Delta z=R\int_{t_0}^{t}\phi[z(t')]\Delta z dt', \tag{5}$$

where t_0 is the time at which $z'_{\text{tip}}=z'$. Taking advantage of the linear relation between the coordinate z and tip speed v_{tip}, $z(t)=z'_{\text{tip}}(t)-z'_{\text{tip}}(t_0)=(t-t_0)v_{\text{tip}}$, Eq. (5) becomes

$$n(z)=\frac{R}{v_{\text{tip}}}\int_0^z\phi(\tilde{z})d\tilde{z}\equiv\frac{R}{v_{\text{tip}}}\Phi(z). \tag{6}$$

Using Eq. (4) we finally obtain the relation between the linear density of invaded pores (or "cluster-mass" density), $n(z)$, to the cumulative invasion probability density distribution $\Phi(z)$:

$$n(z)=n_{\text{Ca}}\Phi(z), \tag{7}$$

where

$$n_{\text{Ca}}=\frac{W\gamma\kappa}{\mu_w a^4}\frac{\text{Ca}}{v_{\text{tip}}}. \tag{8}$$

The characteristic average mass density can also be related to the filtration velocity: $n_{\text{Ca}}=(W/a^2)(v_f/v_{\text{tip}})$. Equation (7) is confirmed by Fig. 6, where $n(z)/n_{\text{Ca}}$ is plotted as a function of z/a. All experimental plots collapse, confirming that there is one single cumulative probability distribution $\Phi(z)$ for the system for all experiments at different extraction speeds. The function $\Phi(z)$, computed as an average function from all cumulative probability functions for the various experiments, is plotted in Fig. 6 as a plain line. Note that n_{Ca} and consequently $n(z)$ are capillary number dependent, which is directly visible on Fig. 2. The explicit dependence of the saturation mass density on Ca will be plotted in Fig. 9(a). The inset of Fig. 6 shows $1-n(z)/n_{\text{Ca}}$ on a linear-logarithmic scale. The solid lines represents $1-\Phi(z)$ and the dashed lines $1-e^{-z/\lambda}$ which would be the model function for a pure exponential ϕ (λ is the screening length evaluated before).

From the results presented above we conclude that the active invasion zone is defined by a screening length λ which is constant for a given porous media and liquid pair and at a range of capillary numbers of two decades. However, we expect this result to be valid only for sufficiently high filtration speed v_f. Indeed, on the one hand, the capillary fingering regime ($\text{Ca}\simeq0$) corresponds to an invasion that is controlled by fluctuations in the capillary threshold pressures, so that

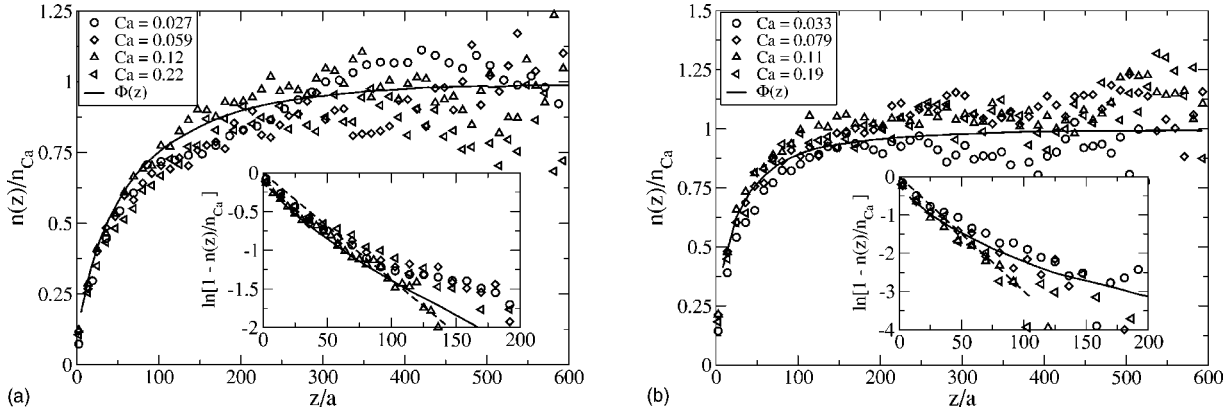

FIG. 6. Plot of the rescaled average mass density of nonwetting fluid $n(z)/n_{\mathrm{Ca}}$, where $n_{\mathrm{Ca}} \propto \mathrm{Ca}/v_{\mathrm{tip}}$, inside the model as a function of the distance to the tip of the most advanced finger z: (a) the wide model and (b) the narrow model. The average cumulative invasion probability function $\Phi(z)$ is plotted on top of the curves for comparison in the two cases. The insets of (a) and (b) show the plots $\ln[1-n(z)/n_{\mathrm{Ca}}]$ as a function of z. The solid lines in the insets correspond to $\ln[1-\Phi(z)]$, and the dashed lines have the slope $1/\lambda$ where λ is the screening length of $\phi(z)$ found from Fig. 5—i.e., respectively, $\lambda=(72\pm10)$ mm and (33 ± 5) mm for the wide model and narrow model.

invasion occurs along the whole front [6,30]. There is no well-defined finger tip or growth direction in that limit. The width of the capillary threshold pressure distribution W_c is larger than the viscous pressure drop over the whole system and defining a screening length or active zone is not meaningful.

When the length of the system is larger than its width, it is found from both pressure measurements and simulations that the decay in pressure into the structure from the longest finger occurs on a length scale of the order of the width of the system (see Fig. 2). We therefore expect W and not L to be the relevant length scale for the decay of the pressure field close to the tip. Viscous forces can therefore be considered to dominate capillary pressures if the following criteria are met:

$$W_c < \frac{W\mu v_f}{\kappa}, \tag{9}$$

or if we assume $W_c \sim \langle P_c \rangle \approx \gamma/a$, where $\langle P_c \rangle$ is the average capillary pressure (which is the case here):

$$\mathrm{Ca} > a/W. \tag{10}$$

For our system $a/W \sim 10^{-3}$, which is an order of magnitude smaller than our lowest capillary number.

On the other hand, for situations where the "pure viscous fingering" in a random porous media has been reached, there is no trapping of wetting liquid inside the fingers, which reached the lower one-pore width limit (at $\mathrm{Ca} \approx 0.2$ in our system). Whether the screening length or active zone has the same width or behaves identically as for lower capillary numbers is not clear. We believe that the screening by the most advanced finger is a viscous effect, which remains important as the displacement speed increases. In this one-pore limit, however, the tip speed dependence on the capillary number is modified, as will be further detailed in Sec. III B.

3. Relation between the growth probability density $\phi(z)$ and the fluid pressure

Figure 7 shows the dependence of the pressure difference $\Delta P(z)=P(z)-P(\infty)$ in the wetting liquid as a function of the distance z to the outermost tip for different capillary num-

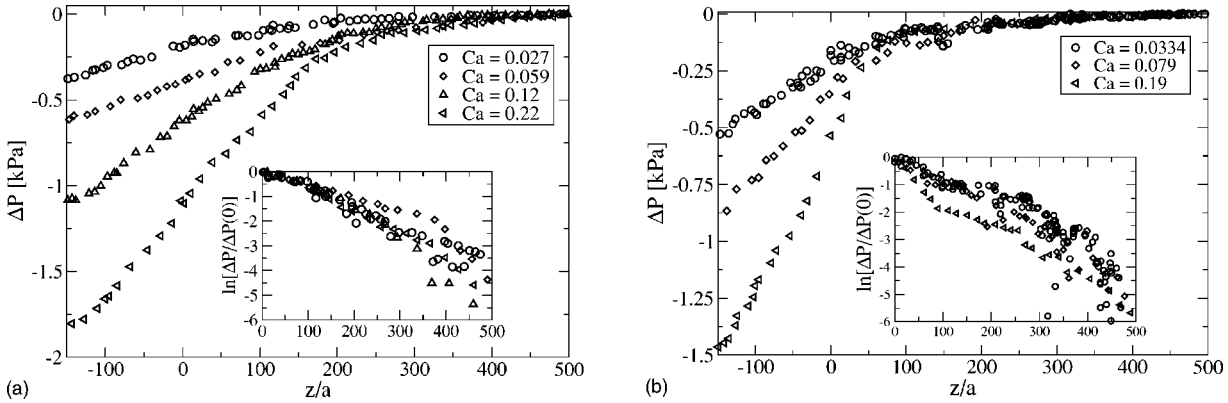

FIG. 7. Plot of the pressure difference $\Delta P(z)=P(z)-P(\infty)$ measured by the pressure sensor located in the position (x_s, z_s') $=(38\ \mathrm{mm}, 280\ \mathrm{mm})$. The inset is the same data plotted in a semilogarithmic plot where $P(z)$ is scaled with $\Delta P(0)=P(z=0)-P(\infty)$ to illustrate the decay of the pressure field. (a) is for the wide model and (b) is for the narrow model.

bers. Here $P(\infty) \equiv P_0 - P_c(\infty)$ is the liquid pressure along the interface far behind the finger tip, with P_0 the pressure in the nonwetting liquid and $P_c(\infty)$ the capillary pressure in this stagnant zone. It is important to note that the pressure $P(z)$ is measured on the side of the model (indicated in Fig. 2) while the fingers are propagating in the central part of the model (Fig. 2).

The pressure seems to be linearly dependent on the distance from the tip during a first stage before the tip reaches the sensor. In a second stage, after the finger tip has passed the sensor, pressure relaxes and reaches the value $P(\infty)$. A closer inspection of the pressure curves (see Fig. 7) shows that there is no clear systematic dependence of the pressure relaxation on the capillary number. The pressure difference $P(z) - P(\infty)$ decays with approximately the same length for the different capillary numbers (see inset of Fig. 7). This indicates that the details of the internal structure of the "fingers" do not have a strong influence on the pressure field on large scales.

The pressure measurements are related to the invasion activity by the following considerations. Let us consider the local speed of an interface located in an arbitrary pore throat between two pores, one filled with air and the other with the wetting liquid. Let $P(x,z)$ be the pore pressure in the wetting liquid and $P_t(x,z)$ be the capillary pressure threshold value to invade that pore. Note that this is different from the pressure $P(z)$ defined as the pressure measured on the side of the model at the sensor position. The pore throat at position (x,z) is passed under the condition that the pressure difference $P_c(x,z) = P_0 - P(x,z)$ is larger than the capillary threshold pressure $P_t(x,z)$ at this position. If invasion occurs, a characteristic value of the speed of the interface will be

$$v(x,z) = \frac{2\kappa}{\mu} \frac{P_0 - P(x,z) - P_t(x,z)}{a}. \tag{11}$$

In this equation we have used the permeability of the porous media κ as an approximation for the average single pore permeability to get the right order of magnitude. Let $N(P_t(x,z))$ be the capillary pressure distribution. For the sake of simplicity, we assume a flat capillary pressure distribution with lower limit $P_t^{\min}$, upper limit $P_t^{\max}$, and width W_c. Under the condition that the viscous pressure drop over a pore a does not exceed W_c (which we have checked by means of numerical simulations), the expectational value of the interface velocity (average value over the capillary threshold distribution), while the pore is getting invaded, will be

$$\begin{aligned}\langle v(x,z)\rangle &= \frac{1}{P_0 - P(x,z) - P_t^{\min}} \int_{P_t^{\min}}^{P_0 - P(x,z)} \frac{2\kappa}{a\mu} [P_0 - P(x,z) \\ &\quad - P_t(x,z)] dP_t \\ &= \frac{\kappa}{a\mu} [P_0 - P(x,z) - P_t^{\min}]. \end{aligned} \tag{12}$$

Here, $P_t^{\min}$ is the minimum of the distribution for capillary threshold; when $P_0 - P(x,z)$ goes to that minimum, the expectational value for the speed of the interface goes to zero. The growth probability density $\phi(x,z)$ for the invasion structure within a time $[t, t+\Delta t]$ at a position (x,z) is proportional to $\langle v(x,z)\rangle$ times the probability $p(x,z)$ that the throat gets invaded; hence,

$$\phi(x,z) = C \langle v(x,z)\rangle p(x,z), \tag{13}$$

where C is a normalization constant, which we can find by integrating the above equation along the invasion front:

$$\int_S \phi(x,z) dl = C \int_S \langle v(x,z)\rangle p(x,z) dl \tag{14}$$

$$1 = \frac{C}{a} \int_S a \langle v(x,z)\rangle p(x,z) dl = \frac{C}{a} Q, \tag{15}$$

where Q is the flow rate, and thus

$$C = \frac{a}{Q}. \tag{16}$$

Since we have assumed a flat capillary threshold distribution of width W_c, the probability that the pore at position (x,z) gets invaded is

$$p(x,y) = \frac{1}{W_c} [P_0 - P(x,z) - P_t^{\min}]. \tag{17}$$

From Eqs. (12)–(17) we obtain, for the growth probability density $\phi(x,z)$ in position (x,z),

$$\phi(x,z) = \frac{\kappa}{Q\mu W_c} [P_0 - P_t^{\min} - P(x,z)]^2. \tag{18}$$

Averaging this expression over x and introducing the number of interface sites at a distance z from the tip, $f(z)$, we obtain the invasion probability density $\phi(z)$ as

$$\phi(z) = f(z) \langle \phi(x,z)\rangle_x, \tag{19}$$

$$\phi(z) = f(z) \frac{\kappa}{Q\mu W_c} [P_0 - P_t^{\min} - \langle P(x,z)\rangle_x]^2, \tag{20}$$

for which we have assumed that $P(x,z)$ is a function of z only (lowest-order approximation). Equation (20) yields

$$\langle P(x,z)\rangle_x = P_0 - P_t^{\min} - \left(\frac{\phi(z)}{f(z)} \frac{Q W_c \mu}{\kappa} \right)^{1/2}, \tag{21}$$

which can be rewritten by introducing the relation between the flow rate and the capillary number. Accordingly the average pressure in the wetting fluid in the immediate vicinity of the interface and at position z is related to the activity $\phi(z)$ according to

$$\langle P(x,z)\rangle_x = P_0 - P_t^{\min} - \left(\mathrm{Ca}\, \gamma\, W_c \frac{W}{a} \frac{\phi(z)}{f(z)} \right)^{1/2}. \tag{22}$$

Let us now look closer at the "snapshots" of the experiments shown in Fig. 2. For $z=0$, the last correction term in Eq. (22) is 170 Pa for the fastest experiment (Ca=0.22) and 65 Pa for the slowest experiments (Ca=0.027). At the same moment, the imposed external pressures in the outlet channel are 3055 Pa for the fastest and 625 Pa for the slowest experi-

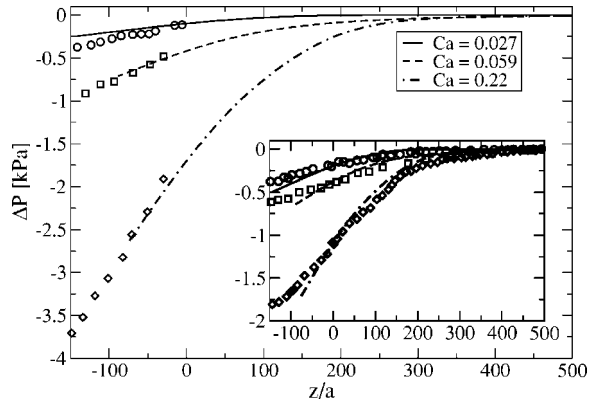

FIG. 8. The simulated pressure along the line with $x_s = 38$ mm (corresponding to the x coordinate of the pressure sensor) for the invasion structures in Fig. 2. The data points in the main graph show the corresponding pressures measured at the outlet sensor. In the inset we plot scaled simulation data with corresponding pressure data measured inside the model at $(x_s, z_s') = (38\ \text{mm},\ 280\ \text{mm})$.

ments. The minimum capillary pressure is estimated to 373 Pa and the width of the capillary distribution to 200 Pa. This indicates that the correction term in Eq. (22) should not be neglected. In Fig. 2 is shown the gray-scale map of the pressure field at a particular time, simulated from the displacement structures obtained experimentally. A very strong screening is seen for all injection rates. The large-scale structure of the pressure field in the vicinity of tip of the longest finger looks visually very similar even if the invader structure is quite different. In the simulations of the pressure field we have used Eq. (22) to set the proper boundary conditions. The pressure field has been calculated by solving the Laplace equation for the pressure using a conjugate gradient method [37]. We used the boundary condition given by Eq. (22) on the cluster and the inlet line. As boundary condition on the outlet we used the pressure $P(\infty) - \Delta P_{\text{tot}}$, where $-\Delta P_{\text{tot}}$ is the total viscous pressure drop imposed in the corresponding experiment at that moment. To obtain $P(\infty) = P_0 - P_c(\infty)$, the capillary pressure $P_c(\infty)$ was measured in the experiments for large values of z. Figure 8 shows the simulated pressure $\Delta P(x_s, z) = P(x_s, z) - P(\infty)$ as a function of the z coordinate relative to the tip position defined as previously, at a fixed lateral position x_s corresponding to the x coordinate of the pressure sensor. It is important to note that this is somewhat different from the experiments since the pressure is measured at different z' positions, but at the same time—i.e., with a fixed geometry of the invasion cluster—while in the experiments the pressure is measured at a fixed z' position, at different times corresponding to various stages of the invasion cluster. The length scale of the decay of the pressure for $z > 0$ is very similar in the experiments and the simulations (see comment below). However, the pressure difference $\Delta P(z)$ in the simulations is lower than the $\Delta P(z)$ measured by the sensor [at position $(x_s, z_s') = (38\ \text{mm},\ 280\ \text{mm})$] in the model (see Fig. 7). This is due to the strong boundary effects of the pressure close to the outlet channel: the tips in the simulations situations are very close to this boundary along which the pressure is fixed (see Fig. 2), while in the situations corresponding to the measurements at $z < 0$ plotted in Fig. 7, the outlet boundary was far ahead of the finger tip, and the pressure boundary condition was equivalent to an imposed gradient at infinite distance. To check the importance of this boundary effect on the magnitude of the pressure difference, the simulated pressure has been compared with the pressure difference $\Delta P(z)$ evaluated from measurements at the outlet channel, as the finger tip progressed further than the stage corresponding to the simulations. The agreement in Fig. 8 between the simulated pressure and the data points corresponding to the outlet channel measurements is then satisfactory.

To compare the length scale of the decay of the pressure for $z > 0$ between the simulations and the experiment, we then compare the pressure data measured inside the model at the sensor position to the simulation data scaled by a factor such as $\Delta P(x_s, z = 0)$, which would be equal in experiments and simulations. Such a rescaling of the simulation pressure profile simply corresponds to the result of an identical simulation still carried on the invasion clusters of Fig. 2, with identical boundary conditions derived from the growth density function for the pressure along the clusters, but where the imposed pressure along the bottom boundary is such that the pressure at point (x_s, z_{tip}') would coincide with the pressure measured in the experiments when the tip passed at the same height as the sensor—-i.e., when $z_{\text{tip}}' = z_s'$. This ensures that the pressure gradient and pressure value in the region around the tip of the invading cluster are of the same order in these rescaled simulations and in the experimental stages corresponding to $z \sim 0$ in Fig. 7, which is a first-order technique to correct for the strong boundary effect and compare with these experimental situations where the bottom boundary is much farther away. The pressure measured in the experiments at sensor position and this scaled simulation data are plotted in the inset of Fig. 8. This comparison shows that the decay in the pressure happens at comparable length scales in the simulations and experiments.

Eventually, the local structure of the finger and the lateral x distance from the invader to the pressure sensor will also have an important influence on the pressure field. The difference in the pressure field between the left and the right side of the finger (looking in the flow direction) in Fig. 2 illustrates this point. The deviation between the experimental data points and the simulations for the lowest capillary number of the main part of Fig. 8 may be explained by this effect. As the lateral position x_{tip} of the invading structure moves during the experiment and is importantly varying from an experiment to the next, this effect also explains the important dispersion of the scaled pressure drops $\Delta P(z)/\Delta P(0)$ observed in the inset of Fig. 7(b).

B. Capillary-number-dependent features

As stated in the introduction to Sec. III, Fig. 2 clearly shows that some features of the invading cluster depend on the capillary number. The mass $n(z)$ of the invasion cluster obviously decreases with increasing capillary number; in relation to this, the speed of the most advanced finger tip, v_{tip}, increases with the capillary number, and there is a systematic trend for fingers to become thinner as capillary number in-

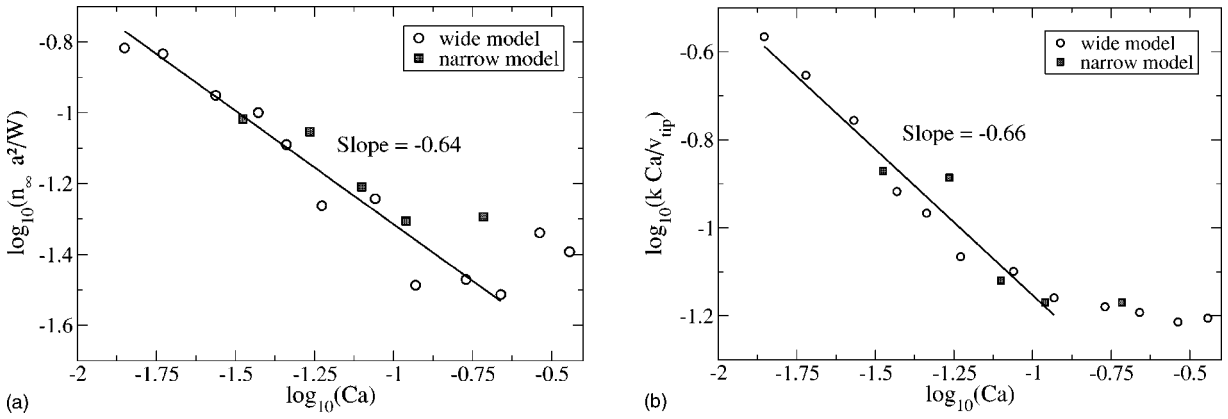

FIG. 9. Double logarithmic plots of (a) the saturated mass density n_∞ and (b) of the speed of the most advanced finger, v_{tip}, as a function of the capillary number, for the two sets of experiments. Both plots are consistent with a scaling in the form $n_\infty \propto \mathrm{Ca}/v_{\mathrm{tip}} \propto \mathrm{Ca}^{-\alpha}$, with $\alpha \approx 0.65$.

creases. In the following we first present results relative to the "mass density" in the stagnant zone, n_∞, and to the velocity of the most advanced finger tip, v_{tip}. In the end we discuss the results relative to measurements of the characteristic width of the fingerlike structures, the definition of which is not as straightforward and clear as those of n_∞ and v_{tip}.

The evolution of the average mass density in the stagnant zone n_∞ as a function of the capillary number is presented in Fig. 9(a) on a double-logarithmic scale. The data are consistent with a scaling law in the form $n_\infty \propto \mathrm{Ca}^{-\alpha}$, with a scaling exponent $\alpha \approx 0.65$ for both the wide and narrow models. Here n_∞ has been measured by fitting the function $n_\infty[1 - \exp(-z/\lambda)]$ with both parameters free to our measured $n(z)$ data. As a result of the dependence of the mass of the invasion cluster on the capillary number [Fig. 9(a)], the speed of the most advanced finger tip, v_{tip}, is expected to depend on the filtration speed or capillary number in a nonlinear way. The saturated mass density and the speed of the most advanced finger are related to each other through Eq. (7), according to

$$v_{\mathrm{tip}} \propto \frac{\mathrm{Ca}}{n_\infty}. \tag{23}$$

Based on that argument, $\mathrm{Ca}/v_{\mathrm{tip}}$ should therefore scale in the same way as n_∞ with respect to the capillary number. In Fig. 9(b), the quantity $k \cdot \mathrm{Ca}/v_{\mathrm{tip}}$ is plotted as a function of Ca on a double-logarithmic scale, where $k = 1$ m/s. The plot is consistent with the expected scaling (23) and the result for the mass density presented above.

The study of the dependence of the finger width on the capillary number is somewhat less straightforward, because our invading clusters structures exhibit extensive branching and display "fingers" both at small scales as "capillary fingers" and at large scales as "viscous fingers." Thus, a precise definition of a finger, and furthermore a finger width, is not an easy task for those structures. A possible method to determine the viscous finger width would consist in finding the characteristic crossover length between geometric features characteristic of viscous fingering and those characteristic of capillary fingering from the density-density correlation function of the structures. However, as a result of the small difference in fractal dimension between the two regimes, 1.83 ± 0.01 [6,30] for capillary fingering and 1.62 ± 0.04 [31,38] for viscous fingering, larger systems would be necessary for this method to be accurate enough. An experimental determination of the characteristic width w_f for viscous fingers was previously obtained for *imbibition* experiments [32], for which the characteristic finger width can be defined and found in a more straightforward manner. The obtained scaling was $w_f \propto \mathrm{Ca}^{-0.5}$. In those imbibition experiments, the finger width w_f was measured as the average length of cut segments perpendicular to the flow direction. This method can also be applied in our experiments, but due to the small scale fractal nature of the invasion front, trapping of wetting fluid inside the fingers and capillary fingering on small length scales, it is not obvious which length scales are being probed with this method. The results that we obtain are plotted as a function of the capillary number in Fig. 10. Clusters of wetting liquid trapped behind the displacement front have been removed from the picture prior to analysis. We then define the front width w_f as the average over z and time of

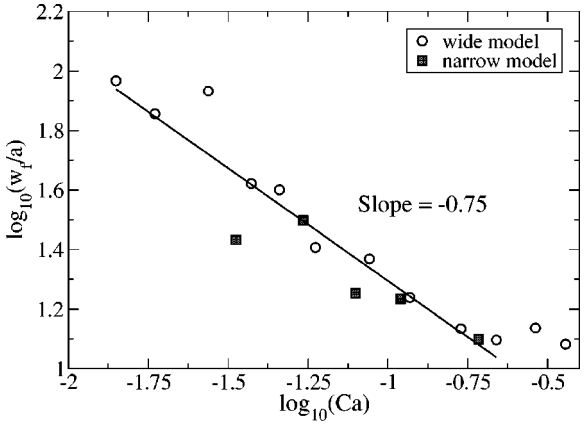

FIG. 10. Double-logarithmic plot of the measured characteristic width of the fingerlike structures as a function of the capillary number, for both the wide and narrow models. The data are consistent with a scaling of the finger width in the form $w_f \propto \mathrm{Ca}^{-\beta}$, with $\beta \approx 0.75$.

the length of the intersects between the invasion cluster emptied from these trapped regions and cuts perpendicular to the flow direction.

The measurements are consistent with a scaling law in the form $w_f \propto \mathrm{Ca}^{-\beta}$, with $\beta \approx 0.75$. This is significantly different from what was measured for imbibition. It also differs significantly from the scaling law expected from theoretical arguments for percolation in a destabilizing gradient [39,40] for two-dimensional systems: $w_f \propto \mathrm{Ca}^{-\beta}$ with $\beta = 0.57$. In our experiments, the destabilizing field (pressure) is highly inhomogeneous, which may explain why the behavior expected from the percolation in a gradient theory is not really observed.

From Figs. 9 and 10, the observed scalings appear to be valid for a limited range of capillary numbers. For high capillary numbers the observed scaling breaks down for Ca ≈ 0.2, which corresponds to situations where the characteristic finger width has reached the one pore limit. At the other limit, for small capillary numbers it is not clear if we reach the lower limit in capillary number. But we expect that the observed scaling breaks down for capillary numbers smaller than the criteria given in Eq. (10), $\mathrm{Ca} \sim 10^{-3}$. As a result of this, it should be noted that the measured exponents α and β only are meaningful for intermediate capillary numbers between the crossovers to the high- and low-capillary-number regimes and that the length scale for the low-capillary-number crossover is system size dependent. Our measured values should therefore be considered as lower bounds for the exponents rather than correct values since inclusion of data points in the crossover regimes will lead to underestimated values for the exponents. For more precise measurements of these exponents experiments on larger systems are needed.

IV. DISCUSSION AND PROSPECTS

Following a procedure similar to that used by Arneodo *et al.* [19] to study the statistical average properties of off-lattice DLA simulations in a linear channel, we introduce an average occupancy map $\pi(x,z)$. Let $g(x,z)$ be the invader occupation function equal to 1 when the local pore is air filled or 0 when it is liquid filled. For any position (x,z) (where z is relative to the tip position), $\pi(x,z)$ corresponds to the average over all times, of the invader occupation function. Points closer than W from the inlet are excluded from this average, since the geometry of the invading structure is expected to be strongly influenced by the central point injection technique in that zone. Similarly to the average DLA situation [19], this average occupancy map saturates to a maximum value $\pi_{\max}$ around the central line $x = W/2$, at distances z larger than W behind the tip position. For $z > W$, $\pi(x,z)$ fluctuates around an average saturated occupancy $\pi(x)$, which is independent of z. This average saturated occupancy is approximated for each experiment by averaging the invader occupation function over all times and all $z > W$. The quantity $\pi(x)$ depends on the capillary number, as expected since by definition $\int_0^W \pi(x)dx \simeq a^2 n_{\mathrm{Ca}}$.

However, the shape of this function, apart from a different $\pi_{\max}$, seems reasonably independent of the capillary number when $\mathrm{Ca} > 0.03$. This is demonstrated in Fig. 11, where the normalized saturated occupancy function for the thin model, $\rho(x/W) = W\pi(x)/\int_0^W \pi(x)dx$, is displayed for five experiments at $\mathrm{Ca} = 0.058$ and five experiments at $\mathrm{Ca} = 0.22$. The characteristic width of this function is obtained by using two definitions introduced by Arneodo *et al.* [19], $\int_0^W \pi(x)dx/\pi_{\max}$ or $(x^+ - x^-)$ where $\pi(x^+) = \pi(x^-) = 0.5\pi_{\max}$. Both definitions for both capillary numbers lead to a characteristic width around $0.4W$ (Fig. 11). The mean occupancy profile or average envelope, defined as the contour level $\pi(x,z) = 0.5\pi_{\max}$, presents some similarities to the shape of a Saffman-Taylor finger corresponding to the same saturation width [7]. Similar contour levels observed in off-lattice DLA simulations correspond to a characteristic selected width $0.62W$ [19,20] and present some similarities with the corresponding Saffman-Taylor finger, although the detailed shape differs [20]. The pressure field recorded at some distance exceeding $0.2W$ of the invader structure [41] is also consistently comparable to the pressure field around such a Saffman-Taylor finger, which arises from the fact that the Laplace equation controlling the pressure field is sensitive to the coarse external shape of the invader's boundary, rather than to the details of the branched structure inside this average envelope.

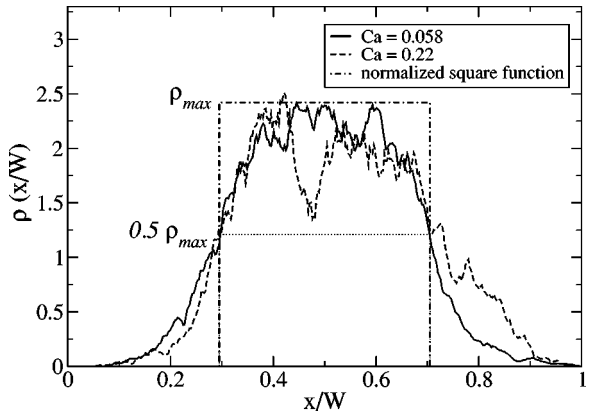

FIG. 11. Normalized average saturated occupation density for five experiments in the thin model at two different capillary numbers. Both functions present an effective width around $0.4W$.

Inside the average envelopes, at intermediate scales the structures correspond to "DLA-like" viscous fingers. On these length scales the viscous pressure differences in the fluid are significant compared to the width of the capillary pressure thresholds distribution W_c. The structure is fractal [41], with a fractal dimension identical to that previously measured in viscous fingering experiments in random porous media similar to ours 1.62 ± 0.04 [31]. On length scales smaller than characteristic finger width w_f, the viscous pressure drops are small compared to W_c. Inside the fingers the structures correspond to capillary fingering with a fractal dimension 1.83 ± 0.01 [30]. The cutoff length w_f between these two regimes is about the same size as the trapped wetting clusters. The saturation level of the envelope width seems insensitive to Ca when $\mathrm{Ca} > 0.03$ [41]. This implies that the saturated mass dependence Ca displayed in Fig. 9 results from the decrease of the characteristic finger width w_f with

the capillary number (Fig. 10). The structures therefore look more branched and thin at higher capillary numbers (Fig. 2), even if they still occupy the same characteristic zone in the linear cells.

The similarity between viscous fingering and DLA [8] was first proposed by Paterson [15] and is based on the equivalence between the probability field for DLA and the pressure field in the viscous fingering case. They both seem to obey Laplace's equation with similar boundary condition, Eqs. (1) and (2). However, the characteristic of the intermediate scales in our viscous fingering experiments displays fundamental differences from DLA growth models: the obtained saturation width $0.4W$ is significantly below the result $0.60W$ obtained from off-lattice DLA simulations [19,20] and also lower than the width $0.5W$ obtained for on-lattice DLA simulations [19] or for a Saffman-Taylor finger in a empty Hele-Shaw cell at high capillary numbers [7]. Average widths higher than $0.5W$ are reported in empty thin cells [18], depending on the capillary number and on the ratio of the cell thickness over width, which affects the role of a wetting oil film left behind the invasion front. The displacement regimes that we have studied correspond to what the authors of Ref. [18] would refer to with their notations as $1/B \sim 1000-10\,000$ and $w/b=200$, for which their experiments would display selected widths larger than $0.5W$ according to Fig. 3in their article [18]. The observed fractal dimension of the viscous fingering structures in a random porous medium similar to ours, 1.62 ± 0.04 [31], is also somewhat smaller than 1.7, the fractal dimension in radial viscous fingering in empty Hele-Shaw cells [17], in radial Laplacian growth [27], or in DLA [20,29]. This shows experimentally that there are some fundamental differences between these processes and viscous fingering in random porous media. Many works have recently focused on generalizations of Laplacian growth processes and DLA and put evidence on the fact that the fractal dimension or even the fractality of the grown structure depends on the precise boundary condition, growth rate, fraction of the perimeter growing simultaneously, and shot noise at the interface boundary [22–28]. The difference between these models shows the importance of the precise growth conditions along the interface. In the present experiments, the disordered porous material creates a nontrivial growth condition along the interface, dependent on the local pressure level, pressure gradient, and of a quenched disorder in the capillary pressure thresholds.

The fact that in these experiments the width of the mean occupancy profile and fractal dimension are below the DLA case make it more similar to another type of generalized DLA models—namely, dielectric breakdown models (DBM's). In the DBM the growth probability of the structures is proportional to a power higher than unity of the pressure gradient [20,42]. To better support the comparison to these various models, the precise determination of the average occupancy maps and fractal dimension(s) of the structure, as a function of capillary number and system size, is the subject of ongoing work [41].

V. CONCLUSION

We have studied the dynamics of the invasion process observed during drainage in a two-dimensional porous medium, for extraction speeds that result in an unstable fingering of the displacing nonwetting fluid into the displaced wetting fluid.

Our main finding is that for a given porous medium, the displacement is controlled by an invasion probability density that only depends on the distance of the point where it is measured to the tip of the most advanced finger tip and is independent of the capillary number. The decay of this invasion probability density, $\phi(z)$, defines an active zone for the invasion process, outside of which the viscous pressure field can be considered to be screened by the invasion structure. In particular, parts of the invasion structure lying outside this active zone are frozen and do not evolve in time any more. The size of the active zone, of characteristic screening length, λ, was found to be independent of the capillary number for a wide range of injection rates. In addition, experiments carried out on models with two different widths suggested that the invasion probability density appears to be capillary number independent, its actual shape being possibly fixed by the system size. While the invasion process is described by an invasion probability density that is independent of the capillary number, the invasion speed and displaced volume in the stagnant zone were found to scale on the capillary according to power laws, $n_\infty \propto \mathrm{Ca}/v_{\mathrm{tip}} \propto \mathrm{Ca}^{-0.65}$.

Current work [41] was also reported on the mean occupancy density behind the most advanced tip, which also seems to be a function of shape independent of the capillary number as soon as $\mathrm{Ca} > 0.03$, although its average value is capillary number dependent. The ratio of characteristic width of such density map over the system width was found around 0.4, which is significantly below the result corresponding to DLA simulations (0.6).

The link between the growth probability and the pressure field has been studied. An expression for the pressure boundary condition relating the pressure on the interface of the invader to the growth probability density function on the cluster, $\phi(z)$, has been calculated. The measured pressure has been compared to the corresponding simulated pressure by solving the Laplace equation for the pressure field using this expression for the boundary condition on the cluster. Good agreement is found between the simulations and the experiments.

System size dependences should be subject to further investigations, both experimentally and by means of computer simulations.

ACKNOWLEDGMENTS

This work was supported by NFR, the Norwegian Research Council, VISTA, the Norwegian academy of science and Letters' research program with Statoil, and the French/Norwegian collaboration PICS.

[1] J. Bear, *Dynamics of Fluids in Porous Media* (American Elsevier, New York, 1972).
[2] F. A. L. Dullien, *Porous Media Fluid Transport and Pore Structure*, 2nd ed. (Academic, San Diego, 1992).
[3] M. Sahimi, Rev. Mod. Phys. **65**, 1393 (1993).
[4] M. Sahimi, *Flow and Transport in Porous Media and Fractured Rock* (VCH Verlagsgesellschaft GmbH, Weinheim, Germany, 1995).
[5] R. Lenormand, E. Touboul, and C. Zarcone, J. Fluid Mech. **189**, 165 (1988).
[6] R. Lenormand and C. Zarcone, Transp. Porous Media **4**, 599 (1989).
[7] P. G. Saffman and G. Taylor, Proc. R. Soc. London, Ser. A **245**, 312 (1958).
[8] T. A. Witten and L. M. Sander, Phys. Rev. Lett. **47**, 1400 (1981).
[9] M. Plischke and Z. Racz, Phys. Rev. Lett. **53**, 415 (1984).
[10] M. Plischke and Z. Racz, Phys. Rev. Lett. **54**, 2054 (1985).
[11] P. Meakin, A. Coniglio, H. E. Stanley, and T. A. Witten, Phys. Rev. A **34**, 3325 (1986).
[12] T. C. Halsey, P. Meakin, and I. Procaccia, Phys. Rev. Lett. **56**, 854 (1986).
[13] C. Amitrano, A. Coniglio, and F. di Liberto, Phys. Rev. Lett. **57**, 1016 (1986).
[14] B. B. Mandelbrot, J. Fluid Mech. **62**, 331 (1974).
[15] L. Paterson, Phys. Rev. Lett. **52**, 1621 (1984).
[16] B. Shraiman and D. Bensimon, Phys. Rev. A **30**, 2840 (1984).
[17] E. Sharon, M. G. Moore, W. D. McCormick, and H. L. Swinney, Phys. Rev. Lett. **91**, 205504 (2003).
[18] M. G. Moore, A. Juel, J. M. Burgess, W. D. McCormick, and H. L. Swinney, Phys. Rev. E **65**, 030601 (2002).
[19] A. Arneodo, J. Elezgaray, M. Tabard, and F. Tallet, Phys. Rev. E **53**, 6200 (1996).
[20] E. Somfai, R. C. Ball, J. P. DeVita, and L. M. Sander, Phys. Rev. E **68**, 020401 (2003).
[21] L. M. Sander, P. Ramanlal, and E. Ben-Jacob, Phys. Rev. A **32**, 3160 (1985).
[22] M. B. Hastings and L. S. Levitov, Physica D **116**, 244 (1998).
[23] B. Davidovitch, H. G. E. Hentschel, Z. Olami, I. Procaccia, L. M. Sander, and E. Somfai, Phys. Rev. E **59**, 1368 (1999).
[24] F. Barra, B. Davidovitch, A. Levermann, and I. Procaccia, Phys. Rev. Lett. **87**, 134501 (2001).
[25] F. Barra, B. Davidovitch, and I. Procaccia, Phys. Rev. Lett. **65**, 046144 (2002).
[26] H. G. E. Hentschel, A. Levermann, and I. Procaccia, Phys. Rev. E **66**, 016308 (2002).
[27] A. Levermann and I. Procaccia, Phys. Rev. E **69**, 031401 (2004).
[28] M. G. Stepanov and L. S. Levitov, Phys. Rev. E **63**, 061102 (2001).
[29] B. Davidovitch, A. Levermann, and I. Procaccia, Phys. Rev. E **62**, R5919 (2000).
[30] R. Lenormand and C. Zarcone, Phys. Rev. Lett. **54**, 2226 (1985).
[31] K. J. Måløy, J. Feder, and T. Jøssang, Phys. Rev. Lett. **55**, 2688 (1985).
[32] J. P. Stokes, D. A. Weitz, J. P. Gollub, A. Dougherty, M. O. Robbins, P. M. Chaikin, and H. M. Lindsay, Phys. Rev. Lett. **57**, 1718 (1986).
[33] D. A. Weitz, J. P. Stokes, R. C. Ball, and A. P. Kushnick, Phys. Rev. Lett. **59**, 2967 (1987).
[34] R. Lenormand, C. Zarcone, and A. Sarr, J. Fluid Mech. **135**, 337 (1983).
[35] R. Lenormand, J. Phys.: Condens. Matter **2**, SA79 (1990).
[36] Y. Méheust, G. Løvoll, K. J. Måløy, and J. Schmittbuhl, Phys. Rev. E **66**, 051603 (2002).
[37] G. G. Batrouni and A. Hansen, J. Stat. Phys. **52**, 747 (1988).
[38] J.-D. Chen and D. Wilkinson, Phys. Rev. Lett. **55**, 1892 (1985).
[39] R. Lenormand, Proc. R. Soc. London, Ser. A **423**, 159 (1989).
[40] Y. C. Yortsos, B. Xu, and D. Salin, Comput. Geosci. **5**, 257 (2001).
[41] R. Toussaint, G. Løvoll, Y. Méheust, K. J. Måløy, and J. Schmittbuhl (unpublished).
[42] J. Mathiesen and M. H. Jensen, Phys. Rev. Lett. **88**, 235505 (2002).

Phase diagram of polydisperse Na-fluorohectorite–water suspensions: A synchrotron small-angle x-ray scattering study

D. M. Fonseca,[1,*] Y. Méheust,[1,2] J. O. Fossum,[1,†] K. D. Knudsen,[3] and K. P. S. Parmar[1,4]
[1]*Department of Physics, Norwegian University of Science and Technology (NTNU), Trondheim, Norway*
[2]*Geosciences Rennes, UMR CNRS 6118, Université de Rennes 1, Rennes, France*
[3]*Physics Department, Institute for Energy Technology (IFE), Kjeller, Norway*
[4]*Department of Chemical Engineering, Pohang University of Science and Technology, Pohang, South Korea*
(Received 6 August 2008; published 6 February 2009)

Systems of platelet-shaped nanostacks of the synthetic clay Na-fluorohectorite, suspended in saline solutions of various salt concentrations, exhibit a rich phase behavior with up to four phases coexisting in a single sample tube. They are studied here using small-angle x-ray scattering: the anisotropy of the obtained images is quantified, and, together with x-ray absorption measurements, this provides a precise determination of the phase boundaries, as well as a measure of the orientational ordering of the clay colloids in the various gel phases. The coexistence of different phases results from a sedimentation-induced vertical gradient in particle fraction. Quantitative relation of the vertical coordinate to the clay particle fraction in these samples allows determination of a phase diagram for these Na-fluorohectorite systems, as a function of the particle fraction and salt concentration.

DOI: 10.1103/PhysRevE.79.021402 PACS number(s): 82.70.Gg, 64.75.Xc, 61.05.cf

I. INTRODUCTION

Liquid suspensions of clays have received special attention during recent years. This is due among other factors to their role as model systems for nanoparticle assembly and ordering, including long-range ordering phenomena. These clay systems are interesting both for industrial applications and from a basic science point of view. Industrial applications for clay minerals range from petroleum-relevant areas to food and cosmetics. Fundamental studies of the complex physical phenomena in clay systems, and the resulting applications, are far from complete. Being "abundant, inexpensive, and environment friendly," clays are recognized by some authors as "the materials of the 21st century" [1].

The fluorohectorite studied here is a smectite clay, characterized by a layer structure with a layer thickness in the nanometer range. The smectite clay layer consists of one aluminum octahedral layer between two silicon tetrahedral layers (2:1 layer unit). Such layers stack together, but owing to their negatively charged surfaces, intercalated cations such as Na^+ or K^+ are needed to balance the charge and allow their stacking (see Fig. 1). Furthermore, these particle stacks can swell in the presence of water, i.e., water molecules may enter the interlayer space, increasing the distance between layers [2].

The basic colloidal particles that we will be discussing in the present paper are stacks of such layers with counterions between them, which we will call a platelet. The thickness, diameter, and surface charge of the platelets vary according to the type of smectite clay. The extensively studied laponite [3–5], for instance, has a platelet consisting of one single 2:1 layer unit with a diameter of around 30 nm and thickness of 1 nm [6].

In the present work we study sodium fluorohectorite (NaFHT) which is a synthetic 2:1 clay mineral where Na^+ is the counterion in the interlayer space. NaFHT is characterized by a high surface charge, $1.2e^-$ per unit cell (Si_8O_{20}), and by its high polydispersity in both particle size and aspect ratio [7]: the platelets display diameters varying from around 100 nm to 20 μm, and the observed thickness is in the 30–150 nm range [8]. NaFHT-NaCl-H_2O systems exhibit several coexisting phases which have been studied by x-ray diffraction [8], leading to the identification of three different gel phases characterized by differences in orientational order and/or size of the domains. Visual observations including the use of crossed polarizers [9] corroborated these wide-angle x-ray scattering measurements since a birefringent region was found coinciding with the oriented one. Recent studies include (i) magnetic resonance imaging (MRI) experiments of anisotropic water self-diffusion [10] which confirmed the isotropic-to-nematic transition and helped understand the orientation of the platelets; and (ii) small-angle x-ray scattering (SAXS) experiments [11] which attempted to obtain a fine characterization of the phase boundaries over a wide NaCl concentration range.

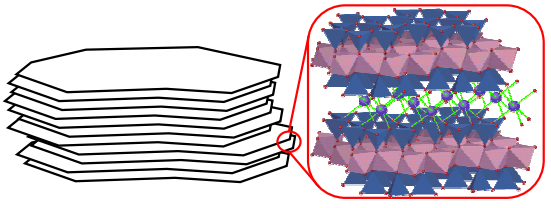

FIG. 1. (Color online) Simplified clay structure. The sodium fluorohectorite smectite clay particles are formed by stacked platelets with a thickness in the range 30–150 nm and a diameter in the range 100–20 000 nm. Detail: two platelets, each formed by an octahedral layer between two tetrahedral layers, and the counterions between them. For NaFHT the octahedra have Li and Mg and the tetrahedra are composed of Si; both structures have vertices of O and F, and the counterion is Na^+.

*fonseca@ntnu.no
†jon.fossum@ntnu.no

Saline solutions of NaFHT exhibit interesting phase behaviors owing to the competition between the van der Waals attraction and the electrostatic repulsion between the particles [12] and also due to the strong particle anisotropy. Since the electrostatic repulsion can be controlled by adding ions [13], systems of smectite clays in saline solutions are good systems for the study of self-assembly from platelet-shaped colloidal particles, including nematic self-assembly [3,5,14]. The particle anisotropy plays an important role as shown by Onsager [15], in his prediction that they undergo an isotropic-to-nematic transition at appropriate concentrations. Another interesting system is hard colloidal gibbsite platelets with an average diameter of 237 nm and thickness of 18 nm; this system was the first one shown to display isotropic, nematic, and columnar phases [16,17].

In this study, we employ the SAXS technique in order to study NaFHT dispersed in saline solutions. We attempt to obtain a proper phase diagram for the system, as determined by the volume fraction of clay and the concentration of sodium chloride. We also try to understand its organization from the profile of the SAXS patterns: at the selected range of x-ray scattering vectors, SAXS provides information on the arrangement regarding some of the dimensions of interest for our system, namely, the interparticle spacing and the thickness of the particles.

II. EXPERIMENT

Li-fluorohectorite clay was purchased in powder form from Corning Inc. (New York). It was cation-exchanged using NaCl, and then dialyzed in order to remove the excess Na^+ and Cl^- ions, and finally dried at 105 °C. The obtained clay crystallites have the nominal chemical formula $Na_{0.6}(Mg_{2.4}Li_{0.6})Si_4O_{10}F_2$. The samples were prepared though suspension of NaFHT in saline solutions at several concentrations; they are 3% NaFHT by mass and have the following NaCl concentrations: 0.1, 0.25, 0.5, 0.75, 1, 2.5, 5, 7.5, 10, and 25 m*M*. After their preparation they were left shaking for 12 h at 1000 rpm. Subsequently they were poured into 2 mm quartz capillaries until 7 cm of the capillaries were filled. The capillaries were then sealed with melted wax and left settling for 30 days. After a few days of settling, one can observe up to four phases in each capillary depending on the saline concentration [Figs. 2(a) and 2(b)]. The phase at the bottom is made of flocculated particles and is opaque; the one on top of it is translucent gel-like and is constituted of particles with a preferred direction of orientation; the next phase is transparent gel-like, created by particles without orientational ordering; and the phase at the top is transparent sol-like. In case the saline concentration is further increased—at some point—it will lead to total flocculation of the clay particles. It is worth mentioning that we here employ the word gel in a broad sense, since we could actually have a conventional gel, a glass, or both at different electrolyte and clay concentrations. Discrimination between gel and glass for the present system is beyond the scope of the present work.

When the samples are put between crossed polarizers, one can easily observe a birefringent phase. Figure 2(c) clearly displays the birefringency of the nematic phase.

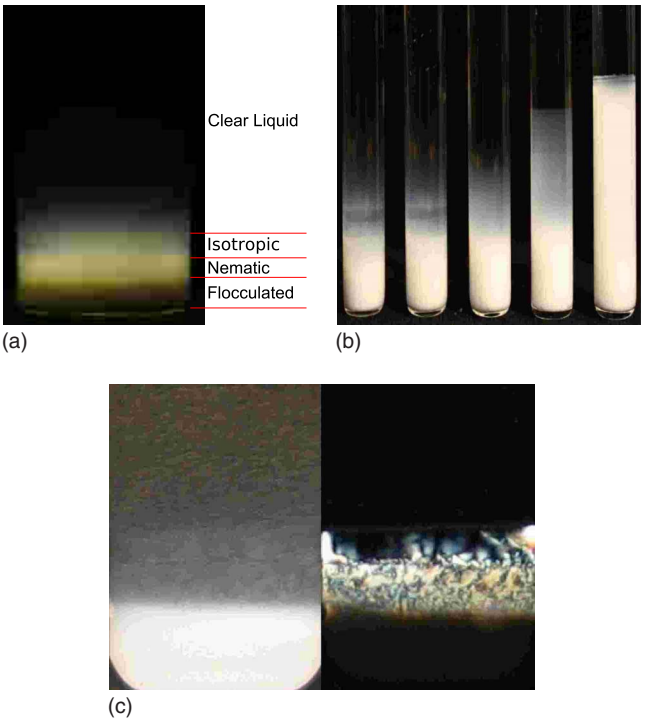

FIG. 2. (Color online) Samples: H_2O+NaCl+NaFHT after settling under action of gravity. All studied samples are 3% NaFHT by mass. (a) Four phases coexisting (different strata) in a single sample tube (circular ∅3 cm). 1 m*M* NaCl. (b) Effect of different salt concentrations (circular sample tube ∅1 cm). The amount of electrolyte has a significant effect on the system. NaCl concentrations from left to right: 0.1, 0.5, 1, 5, and 10 m*M*. (c) Birefringence of the nematic phase. Left: sample with black paper behind (its texture is seen). Right: sample between crossed polarizers. From bottom to top: opaque sediment, birefringent nematic, black isotropic with dendrites from nematic, and clear liquid separated by a thin line from isotropic (rectangular sample tube 1×10 mm^2).

The samples were brought to the Dutch-Belgian beamline (DUBBLE) at the European Synchrotron Radiation Facility (ESRF) 28 days before the date assigned for beam time, and they were left to rest there until the SAXS experiment was performed on site. The setup used covered the q range $0.015<q<0.33$ nm^{-1} [$q=|\mathbf{q}|=(4\pi/\lambda)\sin\theta$, where λ is the x-ray wavelength and 2θ is the scattering angle]; hence, the studied spatial resolution was approximately $2/q=10-130$ nm. Therefore, only the thickness of the aggregated particles and the expected interspacing can exhibit a signature in the data. The lateral size of these particles is generally too large to be seen here. By collecting two-dimensional (2D) data, we are able to distinguish standing aggregates from the ones that lie horizontally, and hence parallel arrangements from staggered ones.

Vertical transmission scans were performed for each sample, followed by data collection of SAXS patterns at different heights, from 1 up to 23 mm above the bottom of the sample. The clear liquid phase is located higher than that for all samples, and it was not studied here. Examples of patterns collected in the nematic and isotropic phases are displayed in Fig. 3; it is clear that the patterns are quite different

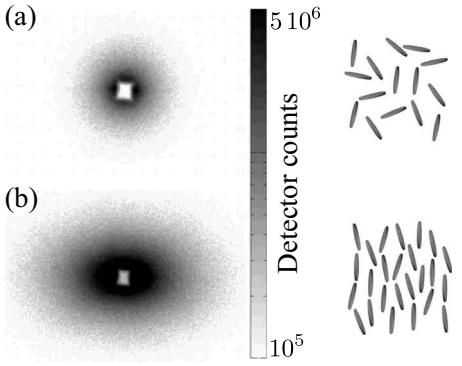

FIG. 3. Typical scattering patterns obtained in the experiment in (a) isotropic and (b) nematic phase. The sets of thin disks (viewed from the side) on the right exemplify possible arrangements responsible for creating the scattering patterns on the left.

from one phase to the other. In the isotropic gel the isointensity lines are circles; for the nematic gel they are ellipses with high eccentricity.

After the end of the experiment the patterns and the transmission data were carefully data reduced. The empty capillary scattering was not subtracted from the SAXS patterns since its scattering proved to be negligible compared to the scattering from the samples, but the empty tube absorption was taken into account in order to data-reduce the transmission data.

III. DATA ANALYSIS AND DISCUSSION

A. Phase diagram

In order to characterize the various phases, we determine isointensity lines of the SAXS patterns. For instance, if we select an intensity of around 2×10^6 detector counts, we have a circle in Fig. 3(a) and an ellipse for Fig. 3(b). In order to automate this analysis MATLAB was used to open each pattern, take a thin slice in intensity, and fit an ellipse to it. From this process, values for the semiaxes a and b of the ellipse and its angle of tilt were obtained; more details on this procedure can be found in Ref. [11]. Tables for the eccentricity ($e=\sqrt{1-b^2/a^2}$) and the angle of tilt were then built. However, since the saline concentrations used in the experiment form a nonregularly and nonmonotonically spaced grid, they were rebinned in order to create color maps from these tables [Figs. 4(a)–4(c)]. Owing to the fact that the angle of tilt has little significance for low-eccentricity patterns (i.e., ellipses close to circles), the low-eccentricity ($e<0.5$) regions of Fig. 4(b) were whitened. Also, since we are interested only in how much the particle orientations deviate from the horizontal and vertical, the angle data were remapped from the interval (0,360]° to (0,90]°.

From Figs. 4(a) and 4(b), we can easily identify the borders of the phases. The identification of the isotropic and nematic gels is rather straightforward since the former is characterized by low eccentricities (the ellipses are almost circles), while the latter is characterized by high eccentricities and low angles of tilt (the ellipses are horizontal). The sediment and flocculated phase display from low to average

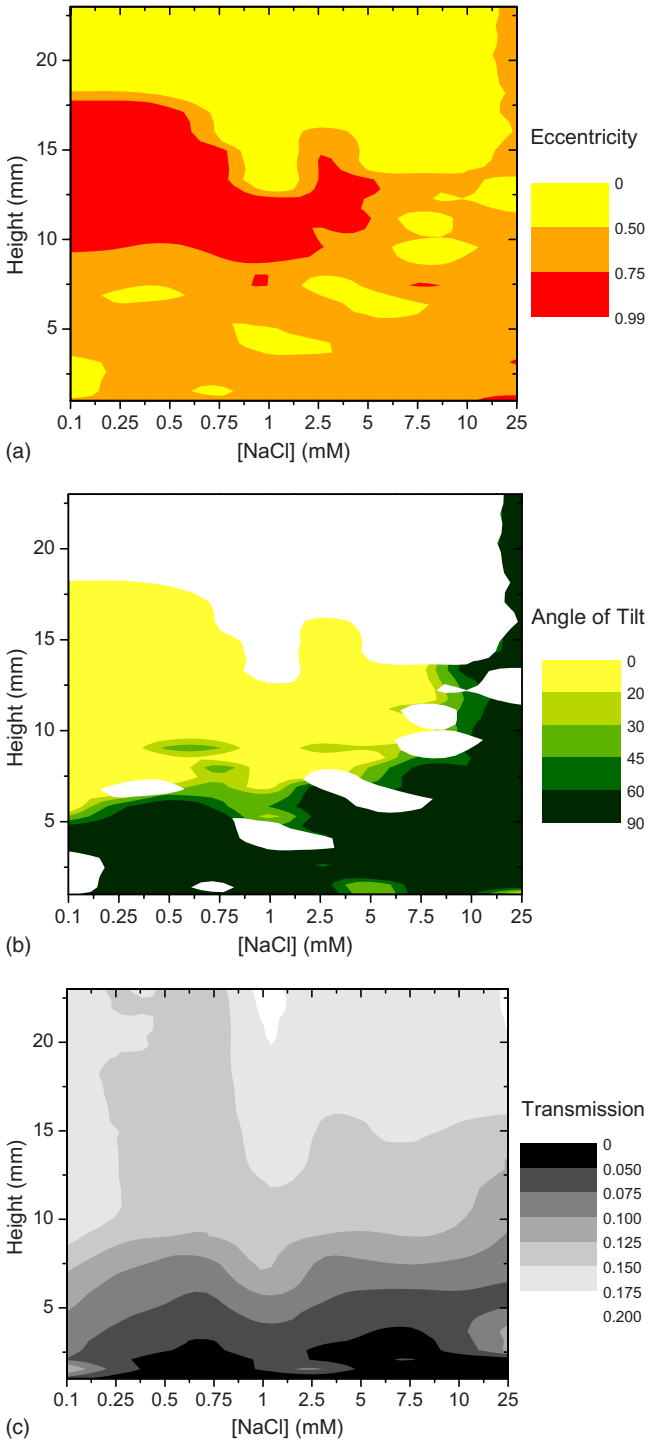

FIG. 4. (Color online) Color maps for the NaCl concentrations studied. The height above the bottom of the sample tube ranges from 1 up to 23 mm. (a) and (b) are constructed from analysis of the isointensity lines of the SAXS patterns. (a) Eccentricity. (b) Angle of tilt (low-eccentricity areas were whitened). (c) Transmission.

eccentricities and all possible angles of tilt, but on average they exhibit high angles of tilt (close to 90°). However, for higher saline concentrations, there is a change in behavior and, in the place where we would expect the nematic phase, higher angles of tilt are noticed; the eccentricities there are

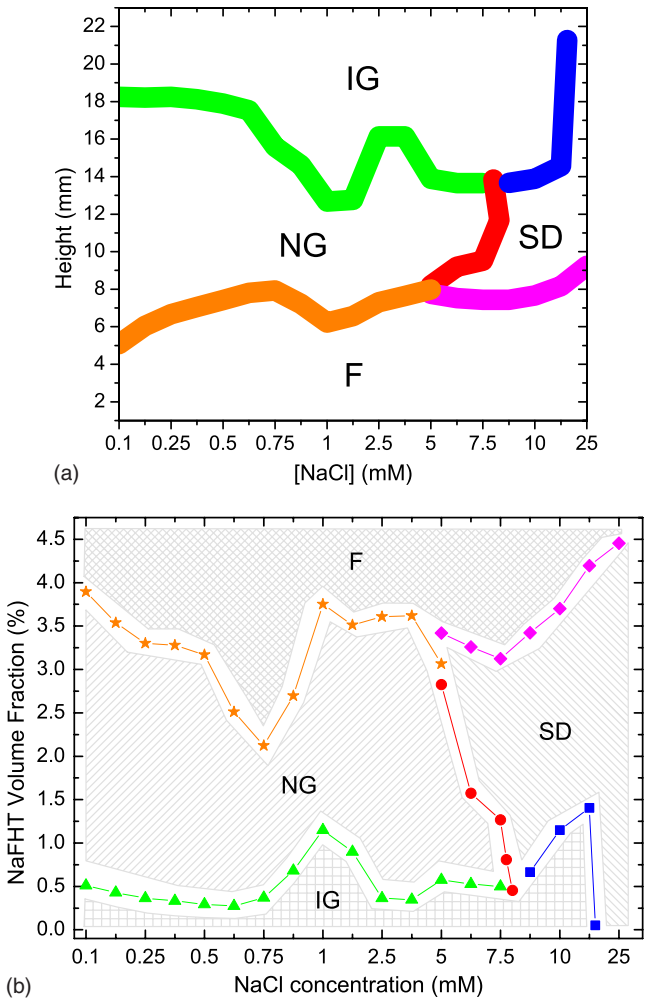

FIG. 5. (Color online) Phase borders for the samples. (a) Phase borders inferred from the eccentricity and angle of tilt color maps; see Figs. 4(a) and 4(b). (b) Phase diagram of the Na-fluorohectorite system, constructed from the phase borders of (a) and from the z (height) to Φ (clay volume fraction) relation inferred from the transmission color map.

lower than in the nematic but higher than in the isotropic phase. Also, some of the SAXS patterns in this region seem to be the superposition of ellipses at different angles of tilt (hence the final eccentricity—as computed here—is lower than for the individual ellipses). This agrees with a previous suggestion [8] of small domains (SDs) for those saline concentrations. Lastly, in order to separate the SDs from the sediment we assumed that the transmission values that separated sediment from nematic ($T \approx 0.1$) are still the threshold. The identified borders were put together in Fig. 5(a).

The next step is to go from the phase borders to a proper phase diagram, i.e., instead of using the height above the sample bottom z, we employ an intensive parameter, in the present case the clay volume fraction Φ, which is known from previous works on similar systems [18], and for nematically ordered systems in general from as early as the Onsager theory [15], to be a potential control parameter for the isotropic-nematic transition. In order to determine its values we used the transmission data, starting by assuring that the data were properly reduced, i.e., the transmission comes only from the sample (no glass). The transmission is given by

$$T = \exp(-\mu\rho d), \tag{1}$$

where μ is the mass absorption cross coefficient, ρ is the material density, and d is the thickness of the sample. Also, the linear absorption coefficient is defined as $\alpha \equiv \mu\rho$.

The x rays illuminate a volume $V=Ad$, where A is the section of the incoming beam, and d is the diameter of the tube (if the beam is well centered on the tube). In case the probed volume is much greater than the volume of the particles, as it is in the present case, we can write

$$\alpha = \frac{\alpha_c V_c + \alpha_s (V - V_c)}{V}, \tag{2}$$

where α_c and α_s are the absorption coefficients for the clay and the solution, respectively, and V_c is the total volume occupied by the clay particles in the probed volume. Using Eq. (1), Eq. (2) becomes

$$\frac{1}{d} \ln T = -\frac{\alpha_c V_c + \alpha_s (V - V_c)}{V}. \tag{3}$$

We now note that the volume fraction of clay is given by

$$\Phi = \frac{V_c}{V}. \tag{4}$$

Putting together Eqs. (3) and (4) we obtain

$$\Phi = -\frac{(1/d)\ln T + \alpha_s}{\alpha_c - \alpha_s}. \tag{5}$$

In Eq. (5), T was measured in the experiment, d is known, and the values for α_s and α_c can be determined theoretically as follows. Knowing the energy of the x rays (7.999 keV) one can evaluate the scattering cross section for each element [19]. From the knowledge of the chemical formula, the cross sections for the elements are weight averaged in order to obtain the cross section for the components of our samples (see Table I). Here the cross section is the sum of both photoabsorption and inelastic scattering cross sections, since we have light elements. Also, it is worth noting that the energy employed is far from absorption edges. Using the values from Table I and the mass density, one can find the corresponding linear absorption coefficients (see Table II).

The conversion from the $([\mathrm{NaCl}], z)$ to the $([\mathrm{NaCl}], \Phi)$ coordinate system is done in practice in the following way. From Eq. (5) and Tables I and II, a $\Phi([\mathrm{NaCl}], z)$ color map is plotted (not shown here), and the borders from Fig. 5(a) are superimposed on this plot. Then, the values of the clay volume fraction along the borders are collected. The phase diagram for the system is created by plotting these values versus salt concentration, as shown in Fig. 5(b). Note that the clear liquid phase was not studied and therefore its border is not presented here, and that for the highest saline concentration the isotropic phase starts higher than the studied range; thus it is not shown in the figure. Note that this approach is not completely sound for measurements performed too close to the bottom of the sample, since the diameter of the capillaries usually varies there.

TABLE I. Calculated cross sections.

Element	Atomic weight (g/mol)	Relative weight	Cross section (cm^2/g)	Weighted cross section (cm^2/g)
		NaCl		
$1\times$Na	22.99	0.39	28.42	11.178
$1\times$Cl	35.45	0.61	104.89	63.629
Total	58.44			74.807
		NaFHT		
$0.6\times$Na	13.79	0.04	28.42	1.014
$2.4\times$Mg	58.33	0.15	39.79	6.003
$0.6\times$Li	4.16	0.01	0.37	0.004
$4\times$Si	112.34	0.29	61.67	17.919
$10\times$O	159.99	0.41	11.35	4.696
$2\times$F	38	0.1	15.52	1.525
Total	386.62			31.160
		H_2O		
$2\times$H	2.02	0.11	0.35	0.040
$1\times$O	16	0.89	11.35	10.078
Total	18.02			10.118

First, it does not show a columnar phase owing to the high polydispersity of the system [16,17]; this was corroborated by thorough visual observations (shining visible light on the samples would produce bright reflections if there were columnar phases present). Second, we observe that in the low NaCl range (up to 0.75 m*M*), an increase in saline or particle concentration favors flocculation regarding the nematic gel (NG)-flocculated (F) transition; and favors the nematic phase in the isotropic gel (IG)–NG case. Both cases were expected since, as more particles are added, making them approach each other more closely, excluded volume effects tend to favor particle alignment (hence, the nematic phase); furthermore, an increased screening of their charges through addition of electrolyte leads to a decrease of the particles' electric diffuse layer volume, and therefore to the same result. As the particle or saline concentration is further increased it leads to flocculation of the particles.

From 1 to 2.5 m*M* there seems to be a discontinuity in the behavior at the left and at the right of this region. This is not unexpected since sudden changes in sample behavior have been seen to occur for saline concentrations around 1 m*M* for this system.

In the range from 2.5 m*M* and higher we notice that as the NaCl amount is increased the small-domain phase appears. At the highest saline concentration studied, i.e., 25 m*M*, the phase diagram shows that the flocculated and nematic phases seem to have merged into a single phase which goes higher in the sample tube. Visual observation of the sample does not

TABLE II. Cross sections for the compounds of interest at 20 °C and for a wavelength of 1.55 Å.

Compound material	ρ (g/cm^3)	μ (cm^2/g)	α (cm^{-1})
$Na_{0.6}(Mg_{2.4}Li_{0.6})\ Si_4O_{10}F_2$	2.75	31.160	85.69
H_2O	0.9982	10.118	10.100
NaCl	2.16	74.807	161.583
0.1 m*M* NaCl	0.99824	10.118	10.100
0.25 m*M* NaCl	0.99825	10.119	10.101
0.5 m*M* NaCl	0.99826	10.120	10.102
0.75 m*M* NaCl	0.99827	10.121	10.103
1 m*M* NaCl	0.99828	10.122	10.104
2.5 m*M* NaCl	0.99834	10.127	10.111
5 m*M* NaCl	0.99844	10.137	10.121
7.5 m*M* NaCl	0.99855	10.146	10.132
10 m*M* NaCl	0.99865	10.156	10.142
25 m*M* NaCl	0.99927	10.212	10.205

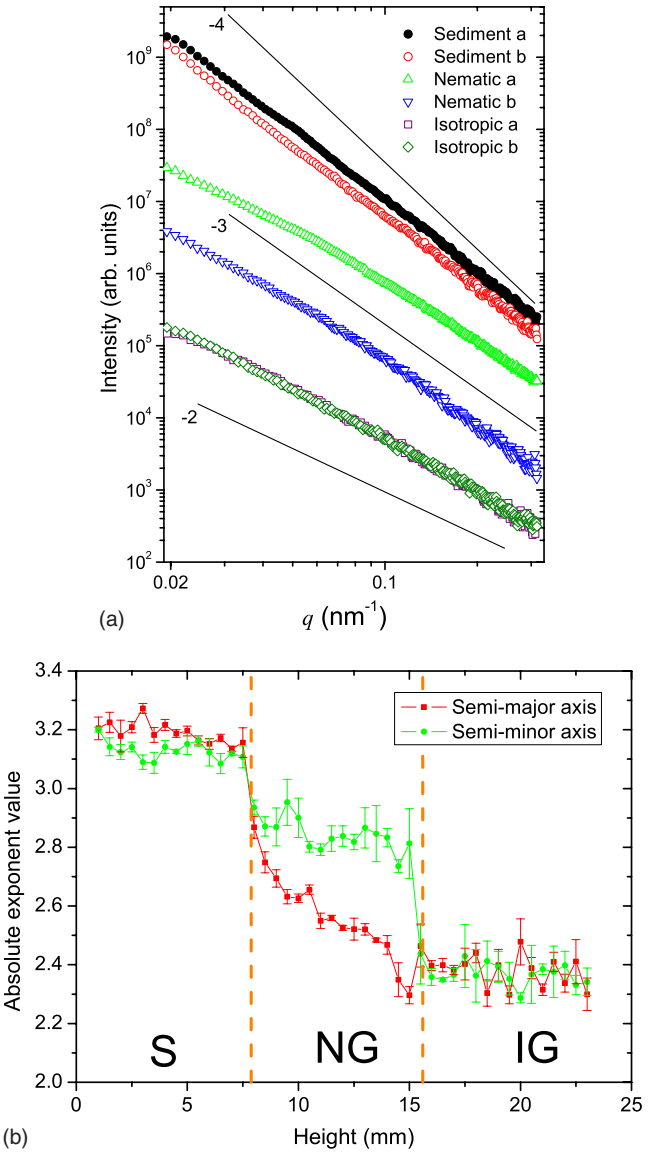

FIG. 6. (Color online) Scattering along the semimajor and semiminor axes for 0.75 mM NaCl sample. (a) Power-law behavior along the semiaxes a (major) and b (minor) in the sediment (vertically displaced by 10), nematic (no displacement), and isotropic (displaced by 10^{-1}) phases. (b) Exponent values in the high-q range versus height in sample. There is a clear split in values in the nematic phase and a small one in the sediment.

reveal a dividing line between the nematic and flocculated phases as the other samples do.

One possible interpretation for the observed behavior in the phase diagram is that we have both gel formation at lower saline concentrations (NG below 1 mM) and glass formation at higher concentrations (NG above 1 mM), similar to what was recently observed for laponite [20]. A comparison between gel and glass can be found in Ref. [21]. Hence, we suggest that the region around 1 mM could be a transition region between both arrested states of matter. In this picture, a further increase in saline concentration leads to glass formation at high NaCl concentration (around 25 mM).

In addition, our diagram displays a reentrant behavior reminiscent of that observed in laponite by Levitz *et al.* [22]:

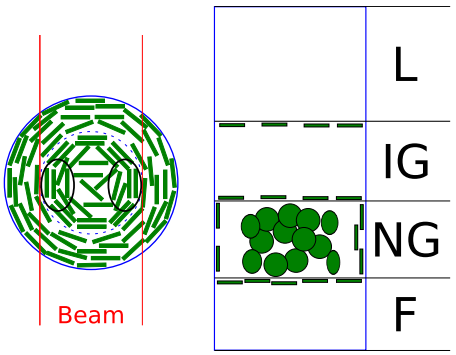

FIG. 7. (Color online) Organization of the platelets in the nematic phase and close to the phase borders. The disproportional image on the left is a section through the nematic phase. In the NG phase the particles contributing to the anisotropic scattering are mostly located between the particles close to the wall and those in the center (see the regions denoted by the two ellipses), and they must have their diameters along the beam path.

by following a line at constant particle volume fraction close to 1% in the phase diagram in Fig. 5(b), as the salt content is increased, one goes from the nematic gel to the isotropic gel and then back to the nematic gel; the same is observed between the nematic gel and the flocculated phase at particle volume fractions between 2% and 3.5%. In the study by Levitz *et al.*, the reentrant behavior involved two solidlike phases separated by the liquid phase, with a characteristic ionic strength of 0.1 mM separating a region of high ionic strength in which the Debye screening length was smaller than the diameter of laponite particles (approximately 30 nm), and another one in which their behavior was that of soft repulsive spheres due to the screening length being larger than the particle diameter. In our study, however, the screening length is always significantly smaller than the typical fluorohectorite particle diameter. Therefore, the reentrant behavior that we observe does not necessarily have the same origin as that mentioned in Ref. [22].

Further studies are needed to understand the phases present in the diagram. Cryofracture could possibly elucidate how the particles are organized in each phase, and provide additional information about the particle distribution size at each phase.

B. Radial intensity decays

When considering the radial decay of the scattering images, we notice that our system displays power-law behavior, i.e., $I(q) \propto q^{-\kappa}$. We have analyzed profiles of the scattering intensity $I(q)$ as a function of the magnitude of the scattering vector q along the semiaxes of the ellipse. Typical profiles for the three studied phases are exemplified in Fig. 6, where the plots regarding the sediment have been translated vertically by a factor of 10 whereas the ones for the isotropic phase have been displaced by a factor of 0.1. The profiles obtained do not present any peaks, indicating the lack of positional ordering within this q-range.

The scattering patterns displayed in Fig. 6 show shoulders around $q_c = 0.05 - 0.06$ nm^{-1}; thus for a value of $1/q_c$ around

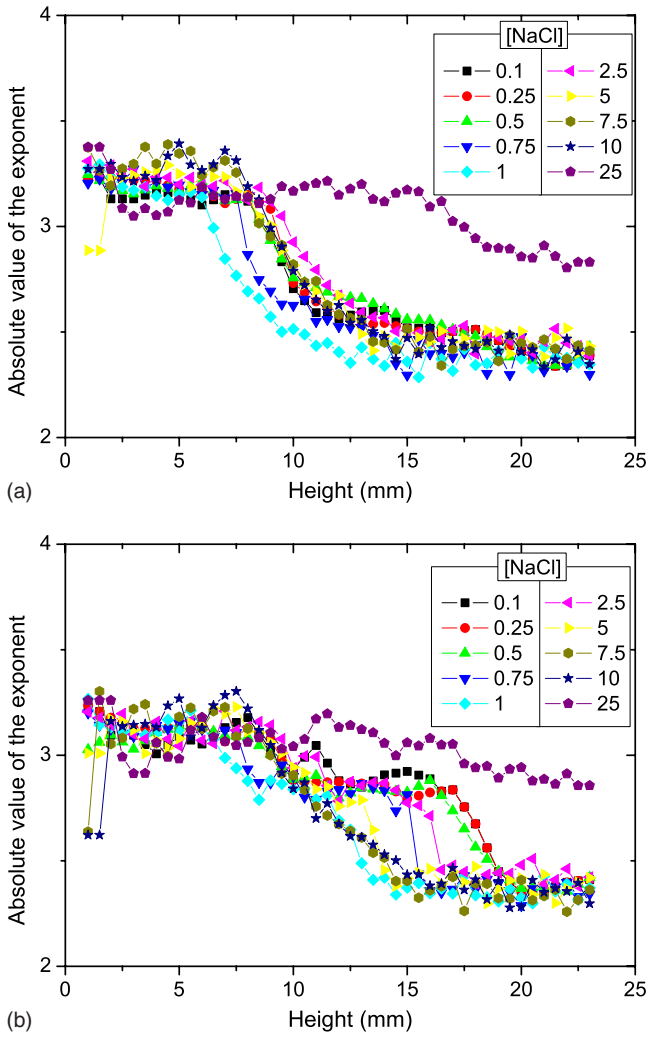

FIG. 8. (Color online) Absolute values of the exponents in the high-q range for the studied NaCl concentrations. The behavior at 25 mM NaCl is clearly different from that of the other saline concentrations. (a) Semimajor axis. For saline concentrations 0.1–10 mM all samples are similar with the exception of 0.75 and 1 mM, which are in a discontinuity region from the gel to the glass. (b) Semiminor axis. Some of the saline concentrations now exhibit a step.

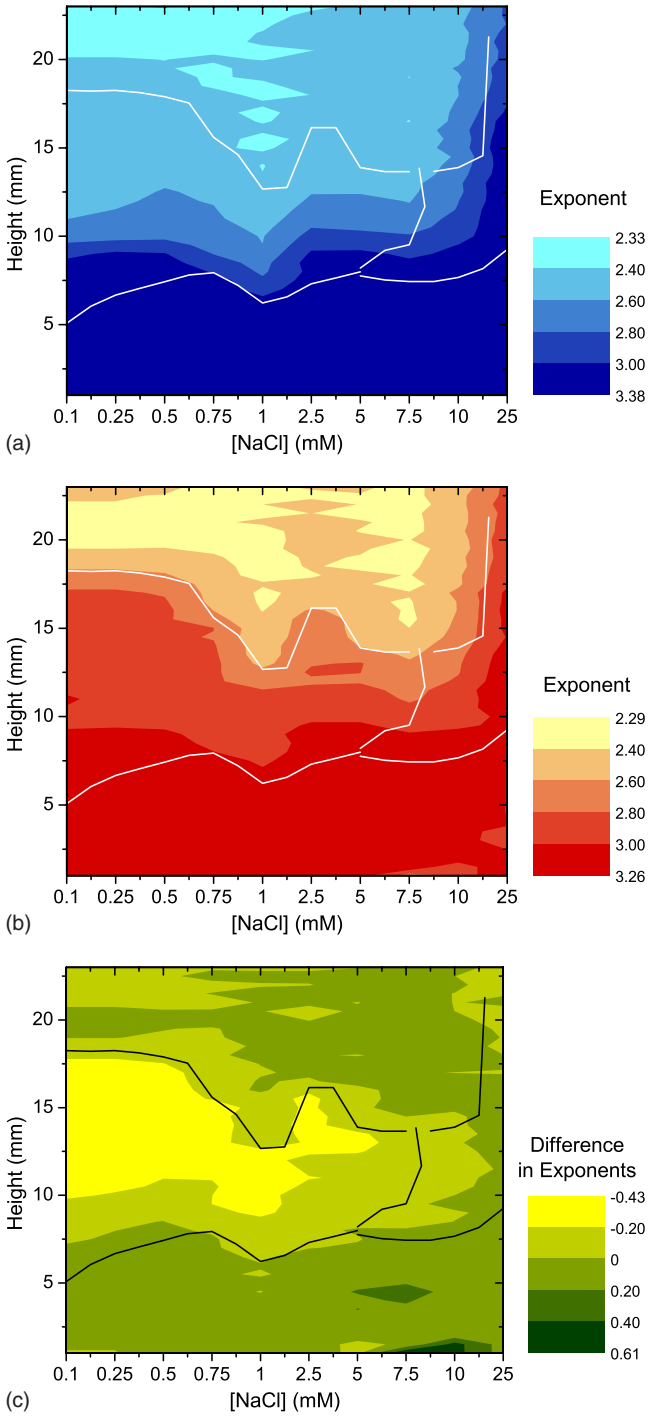

FIG. 9. (Color online) Color maps for the absolute values of the exponents in the high-q range. (a) Semimajor and (b) semiminor axis. (c) Difference between (a) and (b). The largest differences occur in the zone corresponding to the nematic phase. We observe that (a) displays steeper exponents in the sediment, whereas (b) displays steeper exponents in the nematic phase. The phase boundaries from Fig. 5(b) are superimposed onto the maps.

20 nm. However, in the present case, with a system of thin platelets, the relevant crossover length is $2/q_c$, as shown in Fig. 13(a) in the Appendix. Thus we observe a characteristic average dimension of about 36 nm for the particles in our system. The shoulder is seen most clearly for the nematic phase, but is present for all studied phases. It must therefore correspond to some dimension present in all phases; hence it is most likely related to the average platelet thickness in our system. We discuss now the exponents for the high-q range, defined here as those where $q > 0.06$ nm^{-1}.

In Fig. 6(b) we notice that the exponents drop from −3.2 in the sediment to −2.4 in the isotropic phase. It is interesting to note that the two axes change differently within the nematic phase. For the semiminor axis the slope just decreases in one step to −2.8. However, for the semimajor axis it initially drops to −2.8 and then linearly decreases to −2.4. Owing to the polydispersity of the system and also to the particle interactions we can only attempt a qualitative analysis. We know (see the Appendix) that for highly ordered disks the decay in scattered intensity corresponds to an exponent −3 for scattering vector perpendicular to the normal of the disk.

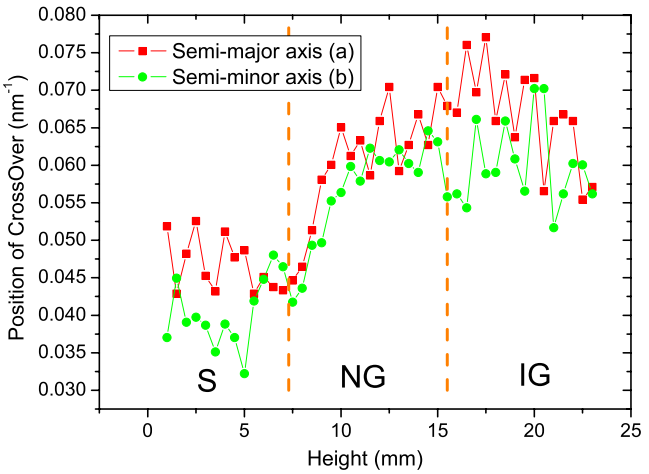

FIG. 10. (Color online) Crossover positions for the 2.5 mM NaCl sample.

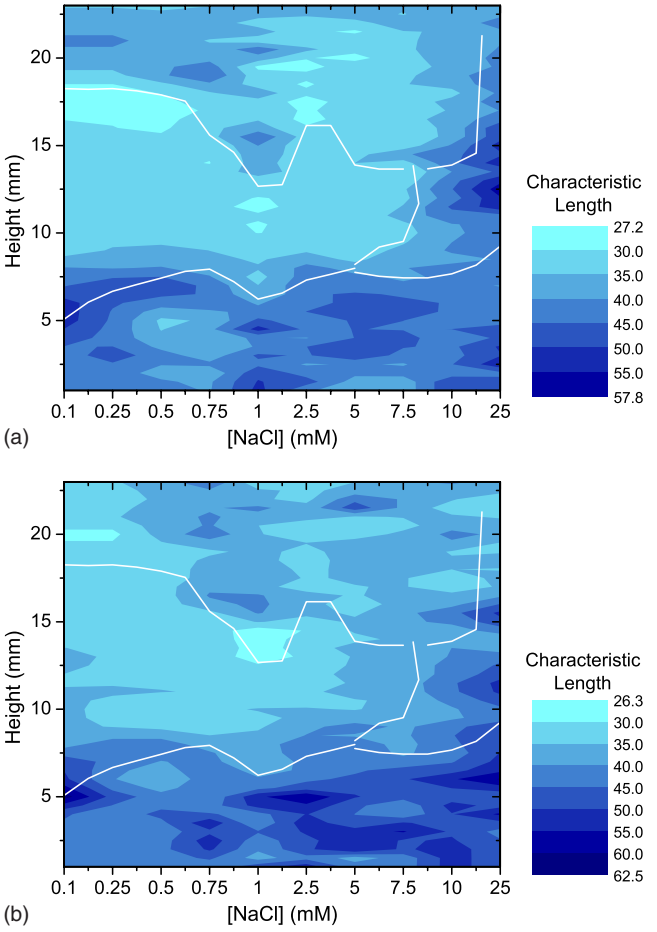

FIG. 11. (Color online) Color map for the corresponding characteristic lengths for the crossover positions. The phase boundaries from Fig. 5(b) are superimposed onto the map. (a) Semimajor axis and (b) semiminor axis.

On the other hand, for such systems, along the direction where the scattering vector is parallel to the normal the power law has an exponent of −2. Hence, from Fig. 6(b) we can infer qualitatively how the platelets are oriented in the nematic phase, since the ellipse tilt is 0° and since along the semiminor axis we observe an exponent close to −3 whereas for the semimajor axis it is around −2. This together with information from MRI results in Ref. [10] allows us to draw Fig. 7. From the MRI data one can also conclude that we should not expect values of exactly −3 and −2, since the particles with their normal parallel to the beam (like those close to the wall) contribute to decreasing the higher exponent and increasing the lower one. Note, however, that the sample cell used here has a diameter of 2 mm whereas for the one in Ref. [10] it is 10 mm. And in their case of wider cells, the authors of [10] observed that the orientational ordering occurs only close to the glass walls.

Here, since the sample tube is narrow, frustration occurs in its center, leading to a nematic phase with a line defect disclination of strength $m=+1$ [23–25] and if the diameter of the sample tube was increased the bulk would become isotropic, though the platelets close to the glass wall would still be oriented. A similar thought process regarding the moderate split in power-law exponents can be used for the sediment. In that case the populations of standing and lying particles are similar in number (the splitting is small), but the higher number of lying platelets is responsible for the observed eccentricity.

The orientation angles at the sediment (closer to 90°) are in agreement with those of Azevedo *et al.* [10], which concluded that at the transition from the nematic to the isotropic phase (isotropic in terms of water movement), the platelets below and above the boundary are edge to face. This observation is also in line with what was seen in Ref. [26].

In Fig. 8 we have plotted the evolution of the exponents along both semiaxes, for all samples. For the semimajor axis [Fig. 8(a)], all samples present the same behavior, with the exception of the highest saline concentration, namely, 25 mM, which behaves in a similar way along both axes, having a higher value than the others throughout. On the other hand, the semiminor axis [Fig. 8(b)] behaves differently. For the low saline concentrations, 0.1–2.5 mM, but not 1 mM, the decrease in exponent now exhibits a step, while for the rest of the concentrations the decrease now starts higher in the sample tube.

In Fig. 9, we have replotted the data from Fig. 8 as color maps. The difference between the two axes is plotted in Fig.

TABLE III. Expected power-law behavior.

Noninteracting monodisperse disks	Low q	Medium q	High q
Randomly oriented		q^{-2}	q^{-4}
Highly oriented ($\mathbf{q}\perp\hat{\mathbf{n}}$)		q^{-3}	q^{-3}
Highly oriented ($\mathbf{q}\parallel\hat{\mathbf{n}}$)			q^{-2}

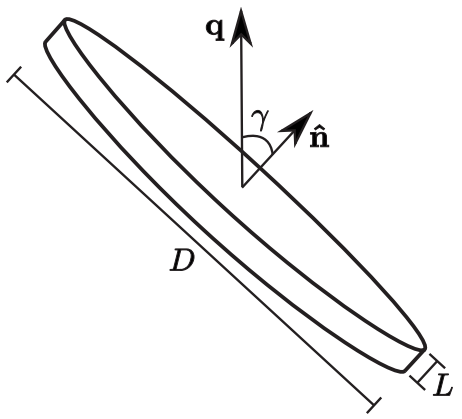

FIG. 12. Platelet geometry.

9(c), from which it is very clear that most of the difference in behavior occurs in the nematic phase, where the absolute value of the exponents is higher for the semiminor axis.

In Fig. 10, the position of the crossover in the SAXS data has been plotted. The characteristic length—inversely proportional to the position of the crossover—indicates thicker clay particles in the sediment (as expected). The behavior along both axes is very similar, indicating that the absence of ordering in the center of the tube makes the projection of the diameter of the platelets visible along both axes, though weaker for b. If we convert the shoulder position to the characteristic length $2/q_c$, we note that in the sediment it has a value of around 43 nm for the a axis and 50 nm for the b axis, whereas for the isotropic phase they are respectively equal to 30 and 33 nm. These values are within the range found in Ref. [8].

We have plotted the characteristic lengths for the crossover positions as color maps in Fig. 11. The plots suggest that particles are thicker in the floculated or sediment phase, but that they have similar thicknesses in both isotropic and nematic gels.

IV. CONCLUSION

We employed SAXS to determine the proper phase diagram for the NaFHT-NaCl-H_2O system, for which all gel or glass phases are visible simultaneously in each sample tube. The high polydispersity and the interaction of the particles did not allow us to fully understand the structural arrangement in the different phases. In particular, we believe that there are different arrested states (gel and glass phases) in the phase diagram, and further investigation is needed to corroborate that. However, we believe that the physical mechanism leading to the formation of these coexisting phases is to be understood as follows. It is driven by the sedimentation: after the flocculated phase has been formed by sedimentation of aggregates of clay particles and of the largest particles, further sedimentation of non-Brownian (large) clay particles occurs, leading to a vertical gradient in particle volume fraction. We have estimated this vertical volume fraction profile from x-ray absorption data. This eventually leads to nematic ordering in the lower (and denser) region above the flocculated phase, until the whole structure is "frozen" by gelation (or glass formation) over time. If the characteristic time for gelation were much smaller than that for the appearance of a nematic phase by sedimentation, we would see no appearance of a nematic gel phase within time scales of the order of our current observation time (i.e., some weeks).

The use of a 2D detector and analysis of the data along the two semiaxes proved useful in determining the orientational configuration of the platelets in the nematic phase and to some extent in the flocculated phase. However, the different particle configurations made it impossible to completely decouple the optical axes of the particles. A new experiment using narrow rectangular-section cells instead of circular ones will probably allow even more information to be extracted from the scattering intensity curves. However, by comparing the results from Ref. [10] to our observations, we were able to determine a plausible collective organization of the particles in the nematic phase. For future studies, we believe that a thorough cryofracture study of the phase diagram would determine the conformation of the particles in all phases, and would provide information on the particle-size distributions as a function of height in the sample tube.

In terms of particle typical sizes, we were able to draw the following conclusions. Particles in the nematic and isotropic phases were observed to have similar thickness, whereas the flocculated phase presents thicker particles. The particles in the nematic phase have their edges close to the glass walls of the tube and the platelets are standing (their normal is perpendicular to the tube axis). Particles in the flocculated phase have an almost isotropic distribution of orientations when compared to the nematic phase, but a slightly higher number of platelets lie horizontally.

ACKNOWLEDGMENTS

The authors acknowledge the European Synchrotron Radiation Facility for provision of synchrotron radiation facilities and we would like to thank Dr. Igor Dolbnya for assistance in using beamline BM26B. This work has received partial financial support from the Research Council of Norway (RCN) through the NANOMAT Program, RCN Projects No. 152426/431, No. 154059/420, and No. 148865/432, as well as through Projects No. 138368/V30 and No. SUP154059/420. Y.M. acknowledges travel support from the Egide organization under the Aurora project for French-Norwegian collaboration.

APPENDIX: POWER-LAW DECAY IN MODEL PLATELET SYSTEMS

The form factor $P(q)$ for a cylinder of diameter D and thickness L is given by [27]

$$P(q,\gamma) = \rho V \frac{\sin w}{w} \frac{2J_1(x)}{x}, \tag{A1}$$

where

$$w = qL \cos \gamma/2 \tag{A2}$$

and

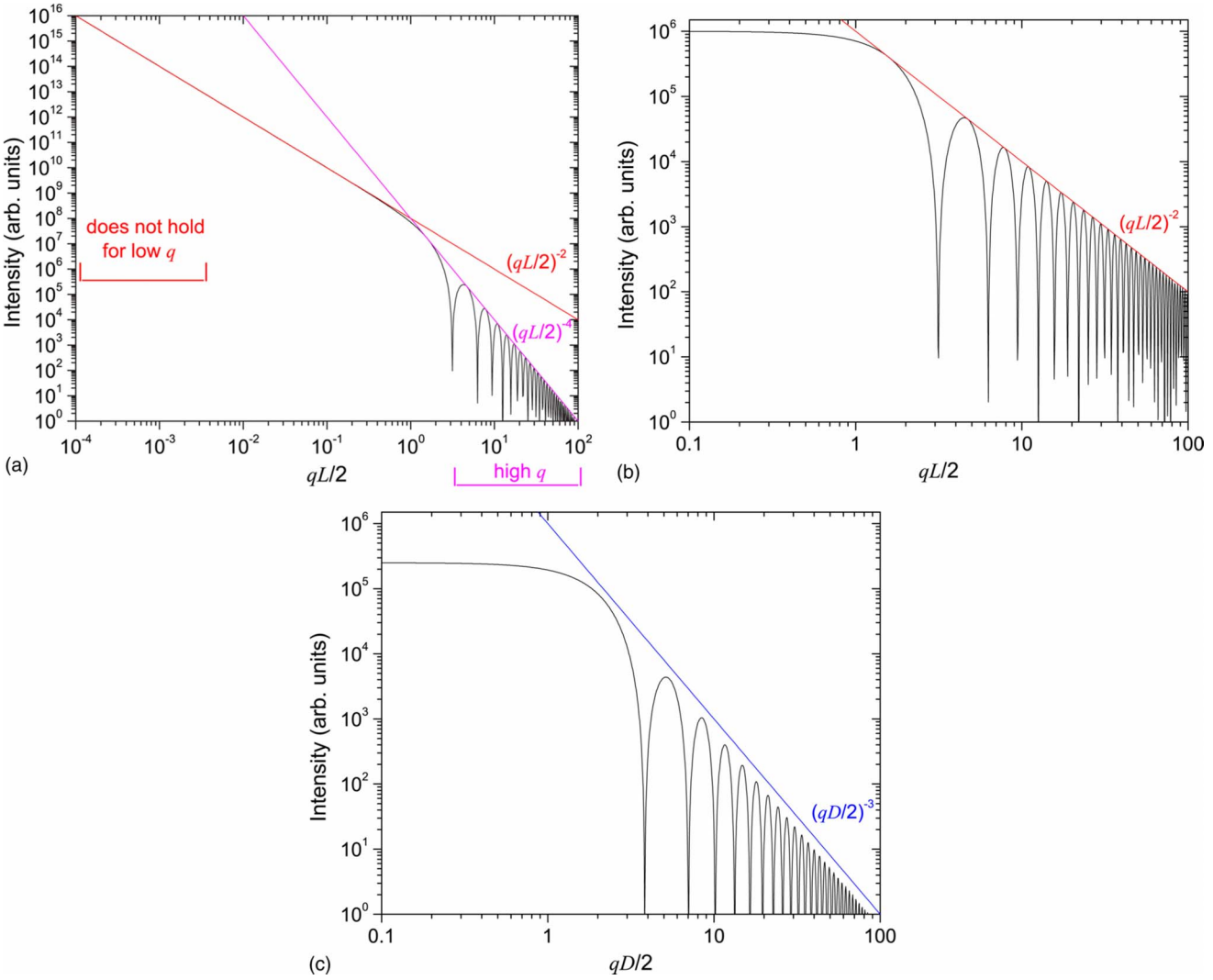

FIG. 13. (Color online) Expected power-law behavior for noninteracting monodisperse platelets. (a) Randomly oriented platelets case. A crossover is observed at $q \approx 2/L$. (b) Highly oriented platelets, parallel case ($\mathbf{q} \| \hat{\mathbf{n}}$). Note the shoulder at $q \approx 3/L$. (c) Highly oriented platelets, perpendicular case ($\mathbf{q} \perp \hat{\mathbf{n}}$). A shoulder occurs at $q \approx 4/D$.

$$x = q\frac{D}{2}\sin\gamma. \tag{A3}$$

Here γ is the angle between $\mathbf{q}$ and the normal of the disk, $\hat{\mathbf{n}}$ (see Fig. 12), V is its volume, ρ is the electronic density difference between the particle and the medium, and J_1 denotes the first-order Bessel function of the first kind.

For simplicity's sake we will assume that the particles do not interact; hence the structure factor will be neglected, i.e., $S(q)=1$. Also, we assume that the disks are monodisperse. In this case the scattered intensity for an isotropic system is

$$I(q) = K\langle |P(q)|^2 \rangle_\gamma, \tag{A4}$$

where K is an experimental constant and $\langle\ \rangle_\gamma$ should be understood as an average over all orientations.

Following the results obtained in Ref. [28] for isotropic and oriented systems of platelets, we note that for thin platelets ($D \gg L$) the term in x in Eq. (A1) falls off much faster than the one in w. Hence only small x values will contribute to the average, i.e., x values for which $\mathbf{q} \perp \hat{\mathbf{n}}$. Thus Eq. (A4) can be approximated to

$$I(q)_{\text{isotropic}} \approx KA\frac{2\pi}{q^2}\left(\frac{\sin(qL/2)}{qL/2}\right)^2. \tag{A5}$$

Thus, the scattering intensity obeys a q^{-2} power law, and in the limit of high q it changes to a q^{-4} power law. However, Eq. (A5) is not valid at low q since in that case x becomes significant.

On the other hand, for highly oriented systems we can divide the observed behavior into two cases, namely, transferred momentum along the normal of the platelet and perpendicular to it. In the former case, only the dependence on the thickness of the particle will survive; hence

$$I(q,\gamma=0)_{\text{oriented}} = K\left(\rho V \frac{\sin(qL/2)}{qL/2}\right)^2. \quad \text{(A6)}$$

For the latter case we note the opposite; thus only dependence on the particle diameter contributes,

$$I(q,\gamma=\pi/2)_{\text{oriented}} = K\left(2\rho V \frac{J_1(qD/2)}{qD/2}\right)^2. \quad \text{(A7)}$$

Equations (A5)–(A7) are plotted in Fig. 13, where the power-law behavior for this model platelet system can be seen. From them we note that a crossover for randomly oriented disks occurs at $q \approx 2/L$, and that for oriented platelets with normal perpendicular (parallel) to the scattering vector a shoulder appears at $q \approx 4/D$ ($q \approx 3/L$). Also, we observe the modulation arising from $J_1(x)$ and $\sin w$. The expected power-law behaviors are summarized in Table III.

[1] *Handbook of Clay Science*, edited by F. Bergaya, B. K. Theng, and G. Lagaly (Elsevier, Amsterdam, 2006).
[2] G. J. da Silva, J. O. Fossum, E. DiMasi, K. J. Måløy, and S. B. Lutnæs, Phys. Rev. E **66**, 011303 (2002).
[3] A. Mourchid, E. Lécolier, H. Van Damme, and P. Levitz, Langmuir **14**, 4718 (1998).
[4] D. Bonn, H. Tanaka, H. Kellay, G. Wegdam, and J. Meunier, Langmuir **15**, 7534 (1999).
[5] B. J. Lemaire, P. Panine, J. C. P. Gabriel, and P. Davidson, Europhys. Lett. **59**, 55 (2002).
[6] A. Mourchid, A. Delville, J. Lambard, E. Lécolier, and P. Levitz, Langmuir **11**, 1942 (1995).
[7] P. D. Kaviratna, T. J. Pinnavaia, and P. A. Schroeder, J. Phys. Chem. Solids **57**, 1897 (1996).
[8] E. DiMasi, J. O. Fossum, T. Gog, and C. Venkataraman, Phys. Rev. E **64**, 061704 (2001).
[9] J. O. Fossum, E. Gudding, D. d. M. Fonseca, Y. Meheust, E. DiMasi, T. Gog, and C. Venkataraman, Energy **30**, 873 (2005).
[10] E. N. de Azevedo, E. Engesberg, J. O. Fossum, and R. E. de Souza, Langmuir **23**, 5100 (2007).
[11] D. M. Fonseca, Y. Méheust, J. O. Fossum, K. D. Knudsen, K. J. Måløy, and K. P. S. Parmar, J. Appl. Crystallogr. **40**, s292 (2007).
[12] M. B. McBride and P. Baveye, Soil Sci. Soc. Am. J. **66**, 1207 (2002).
[13] J. N. Israelachvili, *Intermolecular and Surface Forces*, 2nd ed. (Academic Press, London, 1992).
[14] D. van der Beek, Ph.D. thesis, Utrecht University, 2005.
[15] L. Onsager, Ann. N.Y. Acad. Sci. **51**, 627 (1949).
[16] F. M. van der Kooij, K. Kassapidou, and H. N. W. Lekkerkerker, Nature (London) **406**, 868 (2000).
[17] D. van der Beek, P. Davidson, H. H. Wensink, G. J. Vroege, and H. N. W. Lekkerkerker, Phys. Rev. E **77**, 031708 (2008).
[18] P. Davidson and J.-C. P. Gabriel, *Nanocrystals Forming Mesoscopic Structures* (Wiley-VCH, Weinheim, 2005), Chap. 7, pp. 173–212.
[19] http://henke.lbl.gov/optical_constants/pert_form.html
[20] B. Ruzicka, L. Zulian, R. Angelini, M. Sztucki, A. Moussaïd, and G. Ruocco, Phys. Rev. E **77**, 020402(R) (2008).
[21] F. Sciortino, Eur. Phys. J. B **64**, 505 (2008).
[22] P. Levitz, E. Lecolier, A. Mourchid, A. Delville, and S. Lyonnard, Europhys. Lett. **49**, 672 (2000).
[23] N. D. Mermin, Rev. Mod. Phys. **51**, 591 (1979).
[24] R. Repnik, L. Mathelitsch, M. Svetec, and S. Kralj, Eur. J. Phys. **24**, 481 (2003).
[25] P. G. de Gennes and J. Prost, *The Physics of Liquid Crystals*, 2nd ed., International Series of Monographs on Physics No. 83 (Clarendon Press, Oxford, 1993).
[26] M. Dijkstra, J.-P. Hansen, and P. A. Madden, Phys. Rev. E **55**, 3044 (1997).
[27] A. Guinier and G. Fournet, *Small Angle Scattering of X-Rays* (Wiley, New York, 1955).
[28] J. D. F. Ramsay, S. W. Swanton, and J. Bunce, J. Chem. Soc., Faraday Trans. **86**, 3919 (1990).

AIP | Physics of Fluids

The impact of inertial effects on solute dispersion in a channel with periodically varying aperture

J. Bouquain, Y. Méheust, D. Bolster, and P. Davy

Citation: Phys. Fluids **24**, 083602 (2012); doi: 10.1063/1.4747458
View online: http://dx.doi.org/10.1063/1.4747458
View Table of Contents: http://pof.aip.org/resource/1/PHFLE6/v24/i8
Published by the American Institute of Physics.

The impact of inertial effects on solute dispersion in a channel with periodically varying aperture

J. Bouquain,[1,a)] Y. Méheust,[1,b)] D. Bolster,[2] and P. Davy[1]
[1]*Geosciences Rennes (UMR CNRS 6118), Université Rennes 1, Campus de Beaulieu, 35042 Rennes Cedex, France*
[2]*Department of Civil Engineering and Geological Sciences, University of Notre Dame, Notre Dame, Indiana 46556 USA*

(Received 9 May 2012; accepted 26 July 2012; published online 30 August 2012)

We investigate solute transport in channels with a periodically varying aperture, when the flow is still laminar but sufficiently fast for inertial effects to be non-negligible. The flow field is computed for a two-dimensional setup using a finite element analysis, while transport is modeled using a random walk particle tracking method. Recirculation zones are observed when the aspect ratio of the unit cell and the relative aperture fluctuations are sufficiently large; under non-Stokes flow conditions, the flow in non-reversible, which is clearly noticeable by the horizontal asymmetry in the recirculation zones. After characterizing the size and position of the recirculation zones as a function of the geometry and Reynolds number, we investigate the corresponding behavior of the longitudinal effective diffusion coefficient. We characterize its dependence on the molecular diffusion coefficient D_m, the Péclet number, the Reynolds number, and the geometry. The proposed relation is a generalization of the well-known Taylor-Aris relationship relating the longitudinal dispersion coefficient to D_m and the Péclet number for a channel of constant aperture at sufficiently low Reynolds number. Inertial effects impact the exponent of the Péclet number in this relationship; the exponent is controlled by the relative amplitude of aperture fluctuations. For the range of parameters investigated, the measured dispersion coefficient always exceeds that corresponding to the parallel plate geometry under Stokes conditions; in other words, boundary fluctuations always result in increased dispersion. The transient approach to the asymptotic regime is also studied and characterized quantitatively. We show that the measured characteristic time to attain asymptotic conditions is controlled by two competing effects: (i) the trapping of particles in the near-immobile zone and, (ii) the enhanced mixing in the central zone where most of the flow takes place (mainstream), due to its thinning. [http://dx.doi.org/10.1063/1.4747458]

I. INTRODUCTION

Ever since Taylor's seminal work[1] where he demonstrated that the transport of a solute in an axisymmetrical shear flow was effectively reduced to a one-dimensional dispersion process by using a longitudinal effective dispersion coefficient, the concept of effective dispersion has proven enormously useful and popular across a wide range of fields and applications. This includes, but is not limited to micro fluidic systems,[2,3] nutrient transport in bloodflow,[4,5] single and multiphase transport in porous media,[6–12] and transport in groundwater systems.[13–16]

The basic idea behind Taylor dispersion is simple. At "asymptotic" times, which are times when the solute has sampled by diffusion the full variability of the flow velocities, gradients of solute in the direction transverse to the flow direction can be considered negligible. At these times spreading of the

a)jeremy.bouquain@univ-rennes1.fr.
b)yves.meheust@univ-rennes1.fr.

plume occurs only in the longitudinal direction and can be described by a one-dimensional advection-diffusion model. The corresponding diffusive term features an effective dispersion coefficient that contains the longitudinal molecular diffusion but results mostly from the interaction between the transverse heterogeneity of the velocity field and the molecular diffusion in the transverse direction. The results of the earliest works, which addressed the axisymmetrical (cylindrical tube) geometry,[1,17] were later generalized to other geometries including the parallel plate,[18,19] and the principles hold for more complex systems. At times earlier than these "asymptotic" times, the behavior is more complicated as the rate of spreading of the plume and mixing are not the same.[14,20] A variety of works exist studying these pre-asymptotic times for the cylindrical- or parallel plate-configurations,[21–23] and also when density-driven coupling of flow and transport is present.[24] However, all these prior studies address advecting flows with no significant inertial effects (Stokes flow).

In many applications of practical interest, the relevant channels do not have constant aperture. However, using slightly more complicated approaches the notion of Taylor dispersion can still readily be applied using what has been coined generalized Taylor dispersion theory, which is based on the method of local moments.[6] Using such approaches, many authors have shown that deviation from parallel smooth boundaries can significantly alter behavior,[25] leading to relative increases,[26–29] or even decreases[7,30,31] in the effective dispersion.

In most studies for flow through porous media it is reasonable to assume small Reynolds numbers $Re \leq \mathrm{o}(1)$. Thus it is common practice to assume that flow is governed by the Stokes equations where inertial effects are neglected. While this is very often a reasonable assumption,[32] a variety of practical situations exist where the Reynolds number can become of order unity and larger, so that inertial effects are no longer negligible. Practical examples include flow through fractures with large aperture[33–36] and flows where the viscosity can be small such as carbon sequestration where the viscosity of supercritical CO_2 can be one or two orders of magnitude smaller than that of water.[37]

Increased inertial effects play an interesting role on the structure of the flow.[38,39] In particular. they lead to the presence of recirculation zones.[33] Such recirculation zones can actually also occur in Stokes flow (see examples in Refs. 7, 16, 40, and 41 as well as Ref. 42 for an account of why it occurs), but under increased inertial effects they develop under much weaker geometrical constraints and also exhibit less symmetry than in Stokes flows. These recirculation zones represent low velocity regions that can have a significant impact on effective solute transport and, in particular, on the asymptotic dispersion, both for reactive[32] and inert solute transport,[7] depending on typical mass transfer time scales.[43–45]

In this work, considering an idealized pore geometry, we focus on flow regimes at Reynolds numbers larger than 1, where inertial effects become significant. However, we do not consider situations where the Reynolds number becomes sufficiently large for the flow to become turbulent. We consider the evolution in size of the recirculation zones with increasing Reynolds number and investigate what effect this has on the pre-asymptotic transport and ultimately on asymptotic longitudinal dispersion. We compute the two-dimensional flow field using a finite-element model and the solute transport based on a random walk method. We first characterize the flow and transport from a phenomenological point of view and then examine quantitatively how the time derivative of the second centered moment of the solute concentration field evolves in time, in particular, how its asymptotic value scales with the Reynolds and Péclet numbers, and how that scaling depends on the geometry.

The paper is organized as follows: we describe the geometry, the mathematical basis and the numerical implementation of our simulations in Sec. II; the results are presented in Sec. III, and discussed in Sec. IV.

II. METHODS

A. Geometry definition

We define a two-dimensional geometry with a sinusoidal wall boundary, as described in Refs. 7 and 16:

$$h(x) = \bar{h} - h' \cos\left(\frac{2\pi x}{L}\right), \tag{1}$$

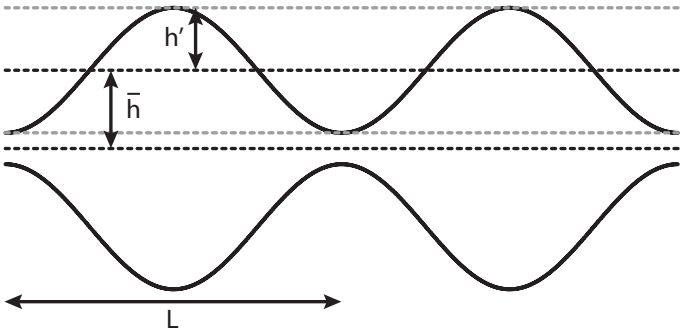

FIG. 1. Geometry of two consecutive unit cells. $\bar{h}$ is the average half-aperture, h' define the aperture fluctuation, and L is the length of the unit cell, or wavelength of the sinusoidally varying channel.

where h is the half-aperture at horizontal position x, $\bar{h}$ is the average half-aperture, $h\prime$ is the amplitude of the aperture fluctuation, and L is the length of the "unit" cell (see Fig. 1). The fluid flows from left to right.

This geometry can be fully characterized by two dimensionless numbers, namely, the aspect ratio of the cell ϵ,

$$\epsilon = \frac{2\bar{h}}{L}, \tag{2}$$

and the relative amplitude of the aperture fluctuations, a,

$$a = \frac{h'}{2\bar{h}}. \tag{3}$$

When a equals its maximum value of 1/2, the channel is closed and pores are disconnected from the network. When a goes to 0, the channel is smooth and goes to the parallel plate geometry.

While this is obviously a simplified model for a real porous medium, Edwards *et al.*[11] illustrated that it is likely relevant for representing flow and transport in a cylindrically packed porous medium. It has also sometimes been considered as an idealized model for the geometry of a geological fracture,[46] although realistic fracture geometries are known to be even more complicated.[47] A recent study demonstrated that many of the qualitative and quantitative features regarding velocity distributions and influence on solute transport of a more complex porous medium are well represented by such a simple geometry.[48]

The channel half mean aperture $\bar{h}$, the mean fluid velocity $\bar{u}$, defined in two dimensions as the ratio of the constant volumetric flow rate to $\bar{h}$, and the fluid cinematic viscosity ν control the Reynolds number

$$Re = \frac{2\bar{h}\,\bar{u}}{\nu}. \tag{4}$$

On a typical pore scale, Reynolds numbers are usually small,[16,49] of the order of 10^{-4} to 10^{-1}. For such Reynolds numbers, flow is described by the linear Stokes equation. For a slowly varying boundary, i.e., $\epsilon \ll 1$ and small Reynolds number, Kitanidis and Dykaar[16] derived an analytical solution for the flow velocity using a perturbation expansion in ϵ. However, at larger Reynolds numbers when inertial terms cannot be neglected, this semi-analytical approach is no longer valid; to the best of our knowledge no obvious analytical approach exists to solving the nonlinear governing Navier-Stokes equations.

B. Basic equations and numerical simulations

1. Flow

Direct numerical simulations of the steady state flow through the geometry described in Sec. II A were conducted. The flow is assumed to be incompressible. The conservation of mass

therefore reads as

$$\nabla . \boldsymbol{u} = 0, \tag{5}$$

where $\boldsymbol{u}$ is the velocity field. The conservation of momentum equation is expressed by the Navier-Stokes equation

$$\rho \left(\frac{\partial \boldsymbol{u}}{\partial t} + (\boldsymbol{u} \cdot \nabla)\boldsymbol{u} \right) = \rho\, \boldsymbol{g} - \nabla p + \eta\, \nabla^2 \boldsymbol{u}, \tag{6}$$

where ρ is the density of the fluid, $\boldsymbol{g}$ is the gravity field, and η is the dynamic viscosity of the fluid.

The system of joint equations (5) and (6) are solved using a finite element method. The finite element numerical simulation is conducted with the commercially available software COMSOL MULTIPHYSICS, in two dimensions and using Lagrange-quadratic elements. The flow is solved on a mesh consisting of triangular elements (up to 100 000) with a maximum side length fixed to $L/280$. At larger scales, there is no anisotropy induced by the meshing. The solver computes the transient flow iteratively until a stationary solution has been obtained.

The left and right in- and outflow boundaries are treated as periodic, that is, the flow velocity $\boldsymbol{u}$ across the cross section is the same at the inlet and at the outlet. A mean flow is imposed on the inlet boundary. The outlet is set to a constant pressure, which allows the solver to adjust the pressure in the geometry to suit the globally imposed volumetric flow. The details of the numerical method for flow, applied to a different but similar geometry, is described in detail in Ref. 24.

2. Transport

We neglect any possible density-driven retroaction of transport on flow, i.e., we assume that the presence of the solute plays a negligible role in changing the density of the fluid. The transport problem is therefore treated once the flow field has been solved for. It is solved numerically using Lagrangian particle tracking random walk simulations based on the Langevin equation. This approach is chosen for two reasons: (i) because of the periodic domain considered here, one does not have to *a priori* impose the size of the domain and one can allow transport to occur over as a large a distance/computational domain as desired and (ii) because Lagrangian methods do not suffer from problems associated with numerical diffusion in the same way that Eulerian methods can; as we are trying to quantify a dispersive effect we wish to minimize uncertainties on the results as much as possible. The initial condition that we choose is a line uniformly distributed across the width of the channel, i.e.,

$$c(x, z) = \delta(x). \tag{7}$$

In discrete time, the equation of motion of the nth solute particle, located at position $\boldsymbol{x}'$ at initial time, is given by the Langevin equation

$$\begin{aligned} x^{(n)}(t + \Delta t\,|\boldsymbol{x}') &= y^{(n)}(t\,|\boldsymbol{x}') + u^{(n)}(t\,|\boldsymbol{x}')\Delta t + \eta_1 \sqrt{2D_{\mathrm{m}}\Delta t}, \\ y^{(n)}(t + \Delta t\,|\boldsymbol{x}') &= y^{(n)}(t\,|\boldsymbol{x}') + v^{(n)}(t\,|\boldsymbol{x}')\Delta t + \eta_2 \sqrt{2D_{\mathrm{m}}\Delta t}, \end{aligned} \tag{8}$$

where $\boldsymbol{x}^{(n)} = (x^{(n)}, y^{(n)})$ denotes the position of the particle and $\boldsymbol{u}^{(n)} = (u^{(n)}, v^{(n)})$ its velocity. The η_i $(i = 1, \ldots, d)$ are independently distributed Gaussian random variables with zero mean and unit variance. This Langevin equation is equivalent to the Fokker-Planck equation; it is identical to the advection-diffusion equation, which describes the time evolution of the solute concentration field inside the system. Solid boundaries are modeled as elastic reflection boundaries in order to account for their impermeability.

The mean half aperture $\bar{h}$, the mean fluid velocity $\bar{u}$, and molecular diffusion coefficient D_{m} control the Péclet number

$$Pe = \frac{2\bar{h}\,\bar{u}}{D_{\mathrm{m}}}. \tag{9}$$

The average position of the solute plume is that of its center of mass

$$x_{\mathrm{G}}(t) = \frac{1}{N}\sum_{n=1}^{N}\left[x^{(n)}(t)\right]. \tag{10}$$

The velocity of the center of mass is the mean horizontal velocity of the solute plume. We normalize it by the mean advection velocity

$$\tilde{u}_{\mathrm{G}}(t) = \frac{1}{\bar{u}}\frac{dx_{\mathrm{G}}}{dt}. \tag{11}$$

The cross-sectionally integrated mass is

$$M(x,t) = \int_{-h(x)}^{h(x)} C(x,y,t)\,dy, \tag{12}$$

resulting in a mean cross-sectional concentration $\bar{C}(x,t)$ with the form

$$\bar{C}(x,t) = \frac{1}{2h(x)}M(x,t). \tag{13}$$

We quantify longitudinal dispersion in this system from calculations of the horizontal spatial moments of the plume as it evolves in time. The *i*th local moment is given by averaging over the *i*th power of the positions of all N simulated particles originating from a single $\mathbf{x}'$,

$$\mu^{(i)}(t \mid \mathbf{x}') = \lim_{J\to\infty}\frac{1}{N}\sum_{j=1}^{N}\left[x^{(j)}(t)\right]^{i}. \tag{14}$$

The global moments are obtained by summation over all initial positions $\mathbf{x}'$,

$$m^{(i)}(t) = \lim_{M\to\infty}\frac{1}{M}\sum_{m=1}^{M}\mu^{(i)}(t \mid \mathbf{x}'^{(m)}). \tag{15}$$

The apparent dispersion coefficient is then given by

$$D_{\mathrm{a}}(t) = \frac{1}{2}\frac{d}{dt}\left[m^{(2)}(t) - m^{(1)}(t)^2\right]. \tag{16}$$

When particles have had sufficient time to sample all the flow lines by diffusion, the asymptotic apparent dispersion coefficient is typically attained. It is defined as

$$D_{\mathrm{a}}^{\infty} = \lim_{t\to\infty} D_{\mathrm{a}}(t). \tag{17}$$

The transport process can then be considered a one-dimensional longitudinal advection-diffusion process with an effective diffusion coefficient equal to D_{a}^{∞}.

The Taylor-Aris dispersion occurring in a channel of uniform aperture is a well-known limit case for the configuration studied here. In this study, we wish to compare only the term induced by the coupling of diffusion and advection processes and remove the longitudinal diffusion term alone. We do so by subtracting D_{m} from both our dispersion coefficients and the Taylor-Aris dispersion coefficient $D_{\mathrm{T.A.}}$,[1,17] thereby defining a normalized dispersion coefficient as

$$\tilde{D}_{\mathrm{a}}(t) = \frac{D_{\mathrm{a}}(t) - D_{\mathrm{m}}}{D_{\mathrm{T.A.}} - D_{\mathrm{m}}}, \tag{18}$$

which for the particular asymptotic dispersion coefficient is

$$\tilde{D}_{\mathrm{a}}^{\infty} = \frac{D_{\mathrm{a}}^{\infty} - D_{\mathrm{m}}}{D_{\mathrm{T.A.}} - D_{\mathrm{m}}}. \tag{19}$$

Here, $D_{\text{T.A.}}$ is defined for a parallel plate fracture with identical mean aperture and is given by (Wooding[18])

$$D_{\text{T.A.}} = D_{\text{m}} + \frac{2}{105}\frac{\left(\bar{u}\bar{h}\right)^2}{D_{\text{m}}}. \tag{20}$$

In terms of Peclet number it can be written as

$$D_{\text{T.A.}} = D_{\text{m}}\left[1 + \frac{2}{105}Pe^2\right]. \tag{21}$$

The simulations release N particles distributed evenly along the cross section of the channel at horizontal position $x = 0$. This means that $\boldsymbol{x}'$ in Eqs. (14) and (15) is $(0, y)$, the vertical position y being distributed uniformly between $-\bar{h} + h'$ and $\bar{h} - h'$. For all the time dependent studies, we normalize time by τ, a characteristic advection time defined as the time needed for a particle moving at the mean velocity $\bar{u}$ to cross a single unit cell

$$\tau = \frac{t\,\bar{u}}{L}. \tag{22}$$

Additionally, for convenience, $\bar{u}$ is set to 1 for all the simulations and the total mass injected is equal to 1.

III. RESULTS

In Secs. III A and III B below we first describe the observed flow and transport, respectively, qualitatively. We then study the longitudinal effective dispersion coefficient quantitatively.

A. Flow phenomenology

The presence of recirculation zones depends on the geometry (ϵ and a) and on the Reynolds number. Examples are given in Fig. 2. At very small Reynolds numbers, Stokes flow conditions are

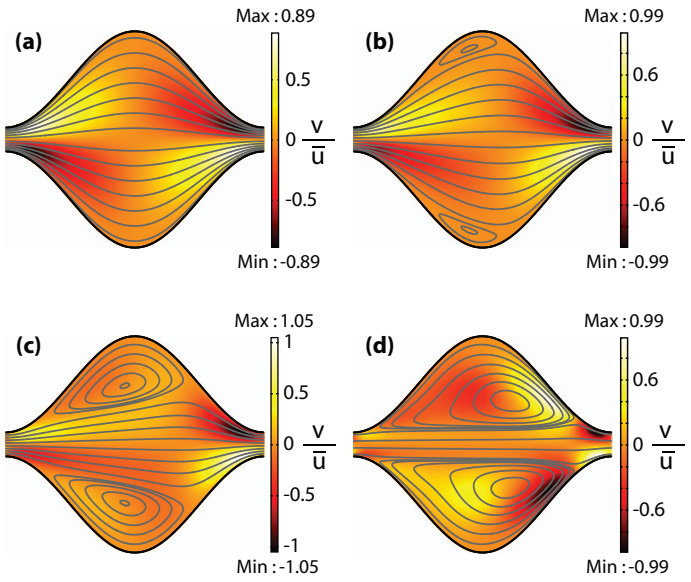

FIG. 2. The shade/color maps show the vertical component of the velocity field, v, normalized by the mean horizontal velocity $\bar{u}$. Flow lines are superimposed. The cell geometry is ($\epsilon = 0.47$, $a = 0.4$), and four Reynolds numbers are considered: In (a), $Re = 0.1$ and the ratio between the volume of the recirculation zone and the volume of the cell ϕ is 0%; in (b), $Re = 10$ and $\phi = 10\%$; in (c), $Re = 20$ and $\phi = 47\%$; in (d), $Re = 100$ and $\phi = 75\%$. Fluid flows from left to right.

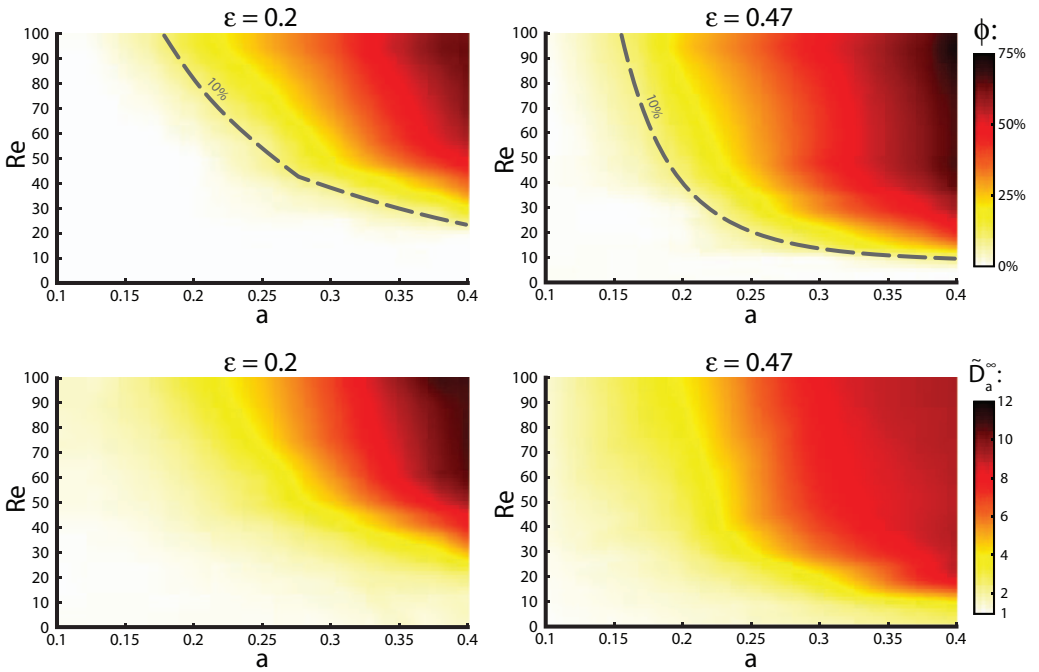

FIG. 3. Volume of the recirculation zone (first row) and normalized asymptotic dispersion coefficient (second row) as a function of the Reynolds number and the relative aperture fluctuation a, for two values of the cell aspect ratio ϵ and $Pe = 100$. The dashed line represents the 10% threshold below which the transport is slightly to not impacted by the presence of a recirculation zone. The data are interpolated using a trilinear interpolation.

fulfilled and the flow is reversible when changing the direction of time, which results in its geometry being symmetric with respect to the vertical line $x = L/2$, as shown in Fig. 2(a). In this figure, no recirculation zones are to be seen: each streamline is homothetic to one of the walls (Fig. 2(a)); note that this homothecy between the walls and streamlines is not enforced by the flow equations and thus not always true: when ϵ and a are both sufficiently large, recirculation zones are visible even in Stokes flow conditions.[7,16] At larger Re values inertial effects become evident and the flow lines and vertical velocity maps become asymmetric with respect to the vertical line $x = L/2$ (Fig. 2(b)), showing that the flow is no longer reversible. The recirculation zones appear in the widest part of the cell in Fig. 2(c), and their size grows monotonically with Re (see Fig. 2(c) for which $\epsilon = 0.47$, $a = 0.4$, and $Re = 20$). The growth is asymmetric but ultimately leads to a flow shape similar to that seen with a single fracture with perpendicular lateral dead ends such as the geometry studied by Lucas.[33]

We define the volume fraction of the recirculation zone ϕ as the ratio of the volume of the recirculation zone to that of the cell, V_{RZ}/V. It provides a measure of what fraction of the pore space corresponds to a flow that is bounded in the longitudinal direction and, therefore, will not contribute to advecting particles from one unit cell to the next one.

ϕ is a function of the geometry and the Reynolds number (see Fig. 3). Maps of ϕ as a function of the relative aperture fluctuation a and the Reynolds number are shown in the top row of Fig. 3 for two values of the cell aspect ratio ϵ. The isoline $\phi = 10\%$ is chosen as the threshold at which we consider that the presence of these recirculation zones begins to have a significant impact on asymptotic transport (i.e., on the asymptotic dispersion coefficient). Depending on the geometry, the 10% limit can be reached at a quite low Reynolds numbers. For example, for $a = 0.25$, i.e., when the aperture at the x position at which the fracture is the widest is equal to 3 times the aperture in the channel throat, Reynolds number values as low as 20 are sufficient for recirculation zones to significantly impact transport. But we shall see in Sec. III D that for $a = 0.166$ (i.e., the max/min aperture ratio being 2), transport is unaffected by recirculation zones for $Re \lesssim 100$.

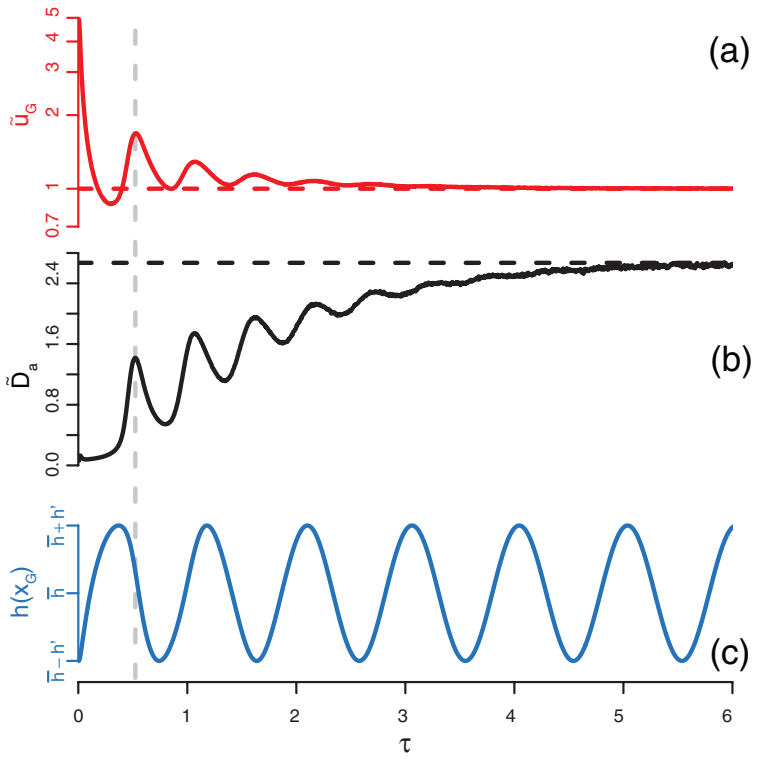

FIG. 4. Evolution of (a) the normalized mean horizontal velocity $\tilde{u}_G$, (b) the normalized dispersion coefficient $\tilde{D}_a$, and (c) the aperture at the position of the center of mass, $h(x_G)$, as a function of the reduced time $\tau = t\,\bar{u}/L$. The geometry is defined by $\epsilon = 0.47$ and $a = 0.4$, flow and transport by $Pe = 100$ and $Re = 1$.

B. Transport phenomenology

Figure 4 shows a representative analysis of the observables for the transport in a case where $Pe = 100$, $Re = 1$, $\epsilon = 0.47$, and $a = 0.4$. The flow configuration is very similar to the one shown in Fig. 2(a), without any recirculation zone. We expect that once all the particles have experienced all velocities in the domain, the horizontal velocity of the center of mass should converge to the mean flow velocity. This behavior is confirmed in Fig. 4(a). The normalized dispersion coefficient $\tilde{D}_a$ also tends to an asymptotic value, which is larger than 1. It means that the effective diffusion coefficient value is larger than the one predicted for the uniform aperture case of identical mean aperture.

The early time oscillations of the dispersion coefficient are directly related to the oscillation of the velocity of the center of mass due to the spatial variability in aperture, flow incompressibility, and imposed constant flow rate. The shape of the time evolution of the solute mean velocity is directly related to the geometry parameters (ϵ and a), Reynolds number (Re) and Péclet number (Pe). When a increases, the velocity difference between the widest and thinnest zone becomes larger and the oscillation amplitudes increase. When ϵ increases, the length of the cells is smaller and thus the frequency of the oscillation increases. The effect of an increase of Re alone is a widening of the recirculation zones such that the longitudinal flow appears similar to the parallel plate case (the oscillation amplitude decreasing dramatically) but with a smaller effective mean aperture. Consequently, the velocity of the plume center of mass also increases as most of the solute is in the mainstream (that is outside of the recirculation zone), leading to a higher oscillation frequency. When Pe decreases, the higher diffusion coefficient contributes to reaching the asymptotic regime sooner, which means that the oscillations are dampened more quickly.

The first peak of the dispersion coefficient in Fig. 4 occurs at $\tau \approx 0.5$ (shown with a dashed gray line) and nearly coincides with the first peak of the horizontal velocity. A snapshot of the spatial solute distribution at this moment is shown in Fig. 5. A significant part of the solute mass is in the

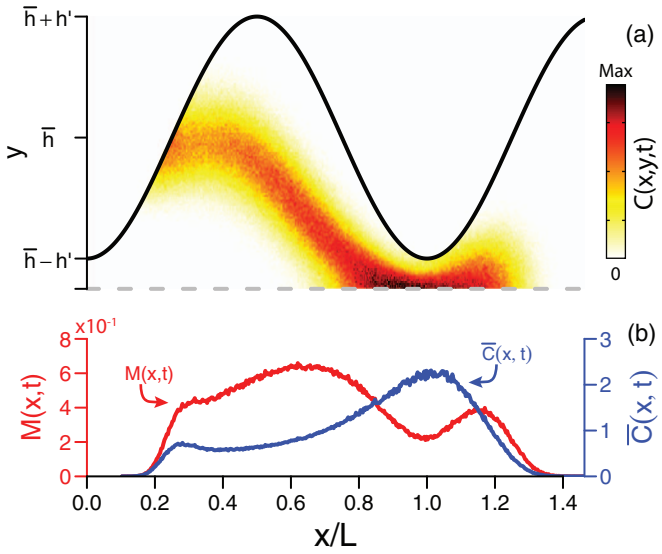

FIG. 5. Snapshot of (a) the concentration field and (b) the vertically summed mass $M(x,t)$ and vertically averaged concentration $\bar{C}(x,t)$ at the first peak time in the longitudinal dispersion coefficient evolution shown by the gray dashed line in Fig. 4 (i.e., at $\tau \approx 0.5$) . The geometry is defined by $\epsilon = 0.47$ and $a = 0.4$, flow and transport by $Pe = 100$ and $Re = 1$.

cell throat where the velocity is at a maximum, while the rest of the solute is in a relatively slow zone. In this configuration, the plume is highly stretched, leading to a large dispersion coefficient value.

Figures 6 and 7 provide a comparison of the spatial distribution of the concentration at a time $\tau \approx 1.25$ for two opposite cases; a highly diffusive one with smaller Péclet number ($Pe = 50$) (Fig. 6) and a highly advective one with large Péclet number ($Pe = 500$) (Fig. 7). The Reynolds number is high in both cases ($Re = 200$), with fully developed recirculation zones, as seen in Fig. 2(d). Note that the maximum concentration values are different and so are the color scales. In the first cell, vertically averaged solute concentration is very similar in both cases. In Fig. 7, solute barely enters the recirculation zones and most of the mass is in the center of the cells, moving

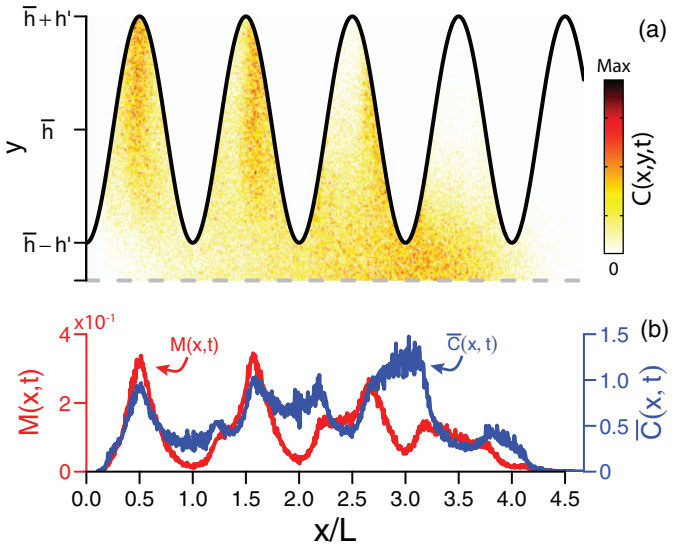

FIG. 6. Snapshot of (a) the concentration field and (b) the vertically summed mass $M(x,t)$ and vertically averaged concentration $\bar{C}(x,t)$ in a geometry with $\epsilon = 0.19$ and $a = 0.38$ at time $\tau \approx 1.25$. The configuration is highly diffusive ($Pe = 50$, $Re = 200$).

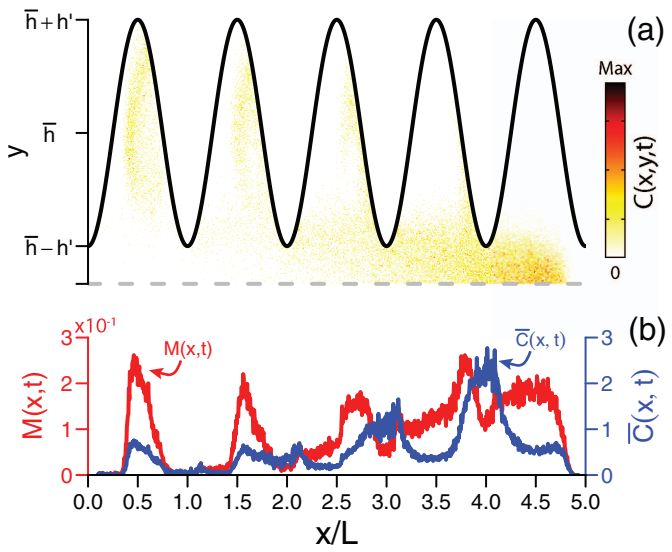

FIG. 7. Snapshot of (a) the concentration field and (b) the vertically summed mass $M(x,t)$ and vertically averaged concentration $\bar{C}(x,t)$ in a geometry with $\epsilon = 0.19$ and $a = 0.38$ at time $\tau \approx 1.25$. The configuration is highly diffusive ($Pe = 500$, $Re = 200$).

quickly. Particles can jump by diffusion on to a line on the edge of the recirculation zone and then enter more deeply into the zone by advection. As such, they are observed to be advected deeper into the recirculation zone by the right side of the unit cell. As the diffusion coefficient is small while the probability to enter the recirculation zone is low, the probability to exit it again is also low. On the contrary, in Fig. 6 a significant amount of the total mass has been able to enter the recirculation by diffusion. In Fig. 6(b), the particles are nearly equally distributed in the three first cells and begin to enter the fourth cell. The concentration values are mostly in the range [0.3,1] and three throat zones are not empty. In Fig. 7(b), most of the particles are at the front of the plume, even if a significant amount is trapped in the recirculation zones. The concentration is already very low in the first throats but high at the front of the plume. The concentration values are mostly in the range [0,2].

C. Time evolution of the apparent dispersion coefficient

For most of the simulations, as illustrated in Fig. 4 for $\epsilon = 0.47$ and $a = 0.4$, the dispersion coefficient oscillates in time before reaching an asymptotic value (see Figure 8). These early time oscillations are directly related to the shape of the geometry and to the evolution of the velocity of the center of mass; in particular, the oscillations of the dispersion coefficient and those of $\tilde{u}_G$ seem to be in phase. The oscillations dampen over time, and their oscillation amplitude increases when Re decreases or a increases. The oscillations also tend to dampen more quickly with a lower Pe, due to more rapid diffusive smearing. The oscillation frequency is directly related to a mean velocity calculated only in the zone outside of the recirculation zones. Thus, it increases when Re or ϵ increases.

It turns out that, once normalized by a proper $\tilde{u}_G^{\lambda}$ law, the longitudinal dispersion data exhibit next to no fluctuations reminiscent of the sinusoidal boundary conditions (see inset in Fig. 8); additionally, we note that it is well described by a stretched exponential behavior. In other words, the D_a data have excellent fitted a law of the form (Fig. 8),

$$D_a(\tau) = D_a^{\infty}\left(1 - \exp\left[-\left(\frac{\tau}{\tau_c}\right)^{\gamma}\right]\right)\tilde{u}^{\lambda}, \tag{23}$$

where D_a^{∞} is the asymptotic dispersion coefficient, τ_c is a characteristic time, $\tilde{u}_G$ is the rescaled velocity of the solute center of mass as defined by Eq. (11), and γ is the exponent inside the stretched

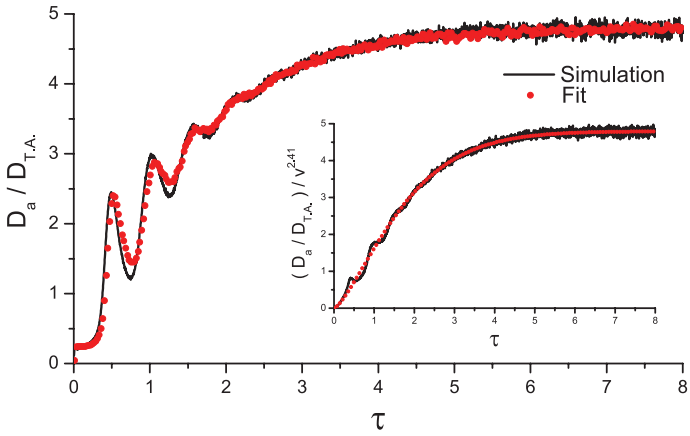

FIG. 8. Time evolution of the normalized dispersion coefficient and fit comparison using Eq. (23). In this case, $Pe = 50$, $Re = 10$, $\epsilon = 0.47$, and $a = 0.4$. The characteristic time to the asymptote is $\tau_c = 4.10$, the asymptotic dispersion coefficient is $D_a^\infty / D_{T.A.} = 4.80$ and the power coefficients are $\gamma = 1.36$ and $\lambda = 2.41$.

exponential. The fitting parameters D_a^∞, τ_c , γ, and λ correspond to distinct geometric properties of the curve, and are therefore obtained with only a small degree of uncertainty.

In addition to properly describing the whole time evolution of the longitudinal dispersion, the fit provides us with a robust estimate of the asymptotic value for the dispersion coefficient. We will focus on this observable hereafter.

D. Asymptotic dispersion coefficient as a function of flow and geometry parameters

1. Dependence on the Reynolds and Péclet numbers

For each geometry, the asymptotic dispersion coefficient $\tilde{D}_a^\infty$ is computed from the fit of the apparent longitudinal dispersion coefficient with time. In Fig. 9(a), we show how it varies as a function of *Re* and *Pe*. Under conditions of lower Reynolds number, $\tilde{D}_a^\infty$ is controlled by the Péclet number. When the Reynolds number increases, $\tilde{D}_a^\infty$ increases and then reaches an asymptotic value at a large Reynolds number. Indeed, when a sufficiently high Reynolds number is reached, the recirculation zone ceases to grow further (or at least grows very slowly). The numerical model is only valid when the flow remains stationary, which requires that no transition to turbulence occurs in any part of the system, so we never perform simulation with Reynolds greater than 250. With this limit, we can observe the plateau for only a few geometries that have large values of a. For most of them, only the low Reynolds plateau and the beginning of the dispersion coefficient increase are observed. Note that the inset in Fig. 9(a) shows the same data as a function of the Péclet number, for the various Reynolds numbers investigated; obviously the behavior as a function of *Pe* is a power law whose exponent hardly depends on *Re*.

Our goal is to find an empirical relation for $\tilde{D}_a^\infty$ as a function of *Re* and *Pe*. For a given geometry and for $Pe > 50$, all the curves of $\tilde{D}_a^\infty$ as a function of *Re* collapse in one by applying a scaling coefficient κ (Fig. 9(b)). For a given geometry, this scaling coefficient only depends on *Pe*. As shown in the inset of Fig. 9(b), κ scales as a power law of the Péclet

$$\kappa = \alpha\, Pe^{\beta}. \tag{24}$$

This scaling simply derivates from the power law behavior shown in the inset of Fig. 9(a).

2. Global scaling

The asymptotic dispersion coefficient values can be described by

$$\tilde{D}_a^\infty(Pe, Re) = \left[\alpha\, Pe^{\beta}\right]\ f(Re), \tag{25}$$

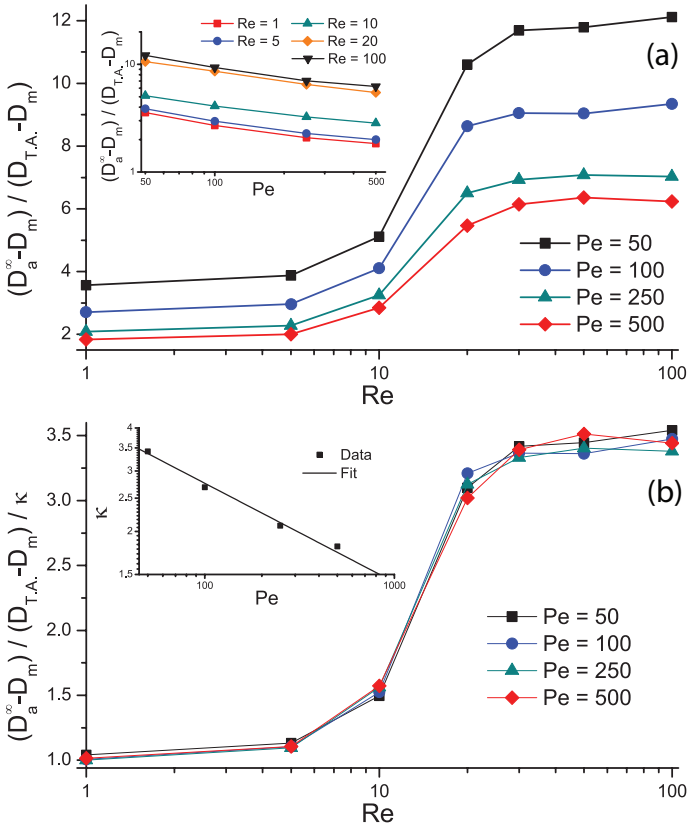

FIG. 9. (a) Normalized asymptotic dispersion coefficient as a function of *Re* for several *Pe* values; the inset shows the same data plotted as a function of the Péclet, for all values of *Re*. (b) shows the same data once scaled and the inset in (b) shows the fit of the scaling coefficient κ as a function of *Pe*. The geometry parameters are $\epsilon = 0.47$ and $a = 0.4$.

that is,

$$D_{\mathrm{a}}^{\infty}(Pe, Re) = D_{\mathrm{m}}\left[1 + \frac{2}{105}\left(\alpha\, Pe^{\beta+2}\right)\ f(Re)\right], \tag{26}$$

where α and β are coefficients that only depend on the geometry and $f(Re)$ is a function of *Re* with small and large asymptotic values at small and large *Re*, respectively. A linear combination of the error function and the $y = 1$ constant function seems suitable. As the second plateau is never reached for most of the geometries, it is difficult to infer a precise functional shape for the fit.

Equation (26) can be compared directly with Eq. (21). The asymptotic dispersion coefficient description and the Taylor-Aris dispersion coefficient share similarities. The latter classic form is complemented with a correction β to the power of *Pe* and with an additional factor that only depends on the Reynolds number.

Figure 10 shows the relation between the parameters α and β and the relative amplitude of the aperture fluctuations, a. Several geometries corresponding to the same a but to different cell aspect ratios ϵ share an identical α: this figure suggests that there is no significant dependence of the prefactor α of Eq. (26) on ϵ. In contrast, α increases monotonically with a. Similarly, the exponent parameter β appears to depend weakly on ϵ, but exhibits a marked decreasing trend as a function of a. When a tends to 0, α tends to 1, β to 0, and thus κ tends to 1. This is consistent with the fact that very small values of a correspond to geometries that approach the parallel plate geometry, for which $D_{\mathrm{a}}^{\infty} = D_{\mathrm{T.A.}}$.

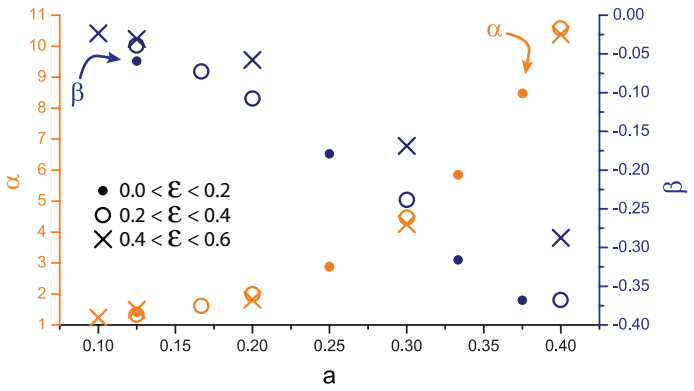

FIG. 10. Fitting parameters α (orange online symbols) and β (blue online symbols) as a function of a. The three types of symbols denote three different ranges of values for the cell aspect ratio ϵ.

3. Relation between the size of the recirculation zones and the asymptotic dispersion coefficient

In the bottom row of Fig. 3, we plot maps of the normalized asymptotic dispersion coefficient as a function of the relative amplitude of the aperture fluctuations, a, and the Reynolds number, for the same two values of the cell aspect ratio ϵ as chosen to illustrate the size of the recirculation zones in the top row of the same figure. These maps of $\tilde{D}_{\mathrm{a}}^{\infty}$ have been obtained by interpolating all available $\tilde{D}_{\mathrm{a}}^{\infty}$ data, measured for various Reynolds numbers and a variety of values of a. For example, the curve in Fig. 9(a) for $Pe = 100$ is a vertical slice of Fig. 3 at $a = 0.4$. Accordingly, the topography of the $\tilde{D}_{\mathrm{a}}^{\infty}$ maps in Fig. 3 is consistent with the plots discussed in Sec. III D 1. In particular, Fig. 3 illustrates that when a goes to 0, $\tilde{D}_{a}^{\infty}$ goes to 1, and thus $f(Re)$ to 1.

A comparison of the two rows of Fig. 3 shows that for a given Péclet number value, the dispersion coefficient evolution is tightly correlated to the volume of the recirculation zones, ϕ. This is a direct consequence of the phenomenology of transport as discussed in Sec. III B, and of solute trapping in recirculation zones at the back of the solute cloud. In this respect, the asymptotic dispersion is also expected to be related to the variance of the velocity fluctuations, and indeed maps (not shown here) of this variance as a function of a and the Reynolds appear very similar to those of ϕ shown in the first row of Fig. 3.

E. Characteristic time to reach the asymptotic regime as a function of flow and geometry parameters

For each geometry, the characteristic time τ_c necessary to reach the asymptotic regime is obtained from the fit of the time evolution of the apparent longitudinal dispersion coefficient. Figure 11 shows its evolution as a function of Re for various Pe values. Figure 11(a) is obtained with a geometry defined by $\epsilon = 0.47$ and $a = 0.4$, while Fig. 11(b) corresponds to a geometry defined by $\epsilon = 0.19$ and $a = 0.38$. In others words, the values of a are similar in the two configurations, but the ϵ values differ by a factor of two. The characteristic time is likely related to the minimum duration needed for a particle to experience the whole cross-sectional profile of velocities by diffusion, and therefore controlled both by the actual value of the diffusion coefficient and by the characteristic transverse distance particles have to cover by diffusion. This latter aspect is confirmed in Fig. 11. For a given Pe value, the asymptotic regime is clearly reached sooner when the cell aspect ratio ϵ is smaller ((b) case). Also, for a given geometry, the higher the Péclet number, the shorter the characteristic time, reflecting a slower sampling of the velocity heterogeneity as diffusion is weaker.

At intermediate Re values (i.e., when the recirculation zones are growing), the trapping of particles delays the asymptotic regime. The curves are shifted toward larger Re values as the Péclet number decreases: when Pe is small, the recirculation zone has to grow significantly (and

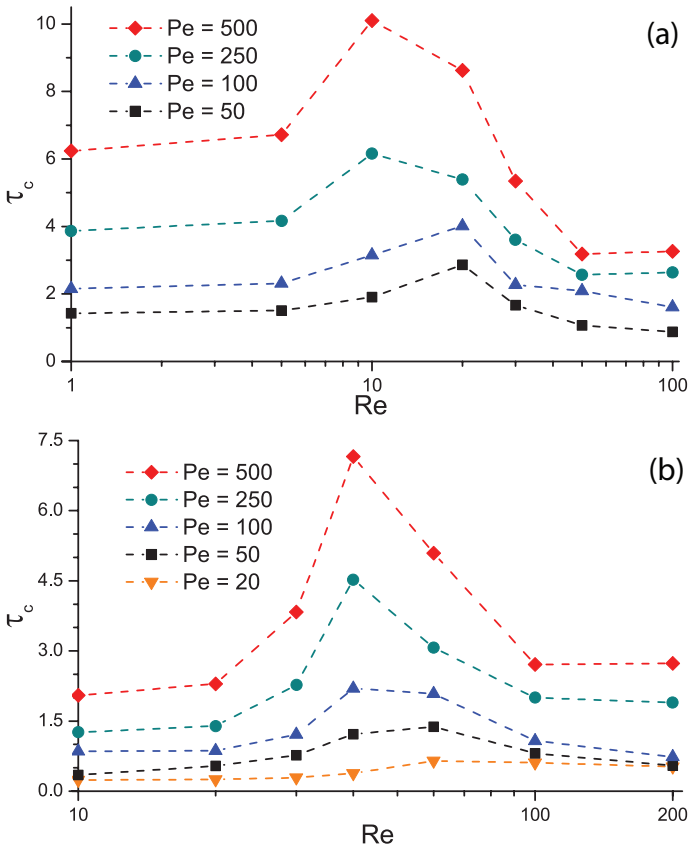

FIG. 11. Characteristic time of the asymptotic regime as a function of *Re* for several *Pe* values. In (a), geometry parameters are $\epsilon = 0.47$ and $a = 0.4$; in (b), geometry parameters are $\epsilon = 0.19$ and $a = 0.38$.

thus, the *Re* must increase significantly) before the characteristic time rises. The growth of the recirculation zones (and thus the thinning of the mainstream) induces rapid homogenization in the central zone. This phenomenon tends to decrease the characteristic time against the delaying effect of trapping. Thus, trapping in the recirculation zones and faster mixing in the central zone compete in controlling the characteristic time τ_c. Depending on the geometry, the Péclet number and the Reynolds number, one of those two phenomena dominates. When the value of ϵ is large (Fig. 11(a)), the asymptotic regime is reached faster for larger *Re* conditions than for lower *Re* conditions because of the enhanced mixing in the mainstream, which dominates over trapping. On the contrary, when ϵ is smaller (Fig. 11(b)), trapping is predominant and the characteristic time τ_c is lower under large *Re* conditions than under low *Re* conditions.

F. Breakthrough curves

Sample breakthrough curves are given in Fig. 12. The concentration is measured at position $x = 50L$, well after the dispersion coefficient has reached its asymptotic value.

The first arrival time is controlled predominantly by the advection and diffusion of a particle traveling at or close to the center of the cell where the longitudinal velocities are largest. As the recirculation zones grow, the bulk of the longitudinal flow occurs in an increasingly smaller volume of the cell, thus resulting in larger maximum velocities. Thus, the larger the Reynolds number, the smaller the time needed for the fastest particles to travel through the cells.

Lower *Pe* values lead to smaller asymptotic dispersion coefficient values, which manifests itself as higher, but narrower peaks in the breakthrough curves. For the parallel plates geometry case, the asymptotic dispersion coefficient is smallest.

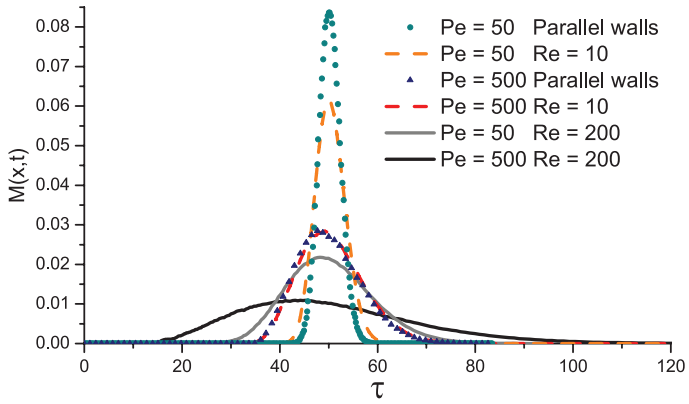

FIG. 12. Breakthrough curves after 50 unit cells have been travelled (i.e., at $x = 50L$), for configurations of low and high diffusion ($Pe = 50$ and $Pe = 500$) and for low and high Reynolds numbers ($Re = 10$ and $Re = 200$) in a geometry with $\epsilon = 0.19$ and $a = 0.38$. Additionally, two breakthrough curves for a parallel plate geometry with the same mean aperture (i.e., $a = 0$) at $Pe = 50$ and $Pe = 500$ are shown.

IV. CONCLUSION

We have studied numerically the impact of inertial effects on flow and transport in channels of periodically varying aperture. In particular, we investigated the conditions under which recirculation zones appear and monitored the volume fraction occupied by these "transport-delaying" zones as a function of the geometrical parameters (i.e., the aspect ratio of a cell and the relative amplitude of the aperture fluctuations). Recirculation zones grow when the aperture fluctuation, the aspect ratio of the cell or the Reynolds number increase. A range of geometry parameters and Reynolds number values exists for which the volume of the recirculation zones is very sensitive to these parameters. For a number of geometries, Reynolds number values as low as 20 are sufficient to create recirculation zones that impact transport significantly. In such geometries, the recirculation zones can be sufficiently large to occupy up to 75% of the pore volume even when the Reynolds numbers are less than 50. It is important to emphasize that the flow is laminar and not turbulent; recirculation zones that arise from inertial effects are characterized by their asymmetry relative to the longitudinal reflection plane.

As anticipated from the generalized Taylor dispersion theory, the longitudinal apparent dispersion coefficient reaches in time an asymptotic value corresponding to an effective diffusion coefficient for longitudinal transport. The deviation of this asymptotic dispersion coefficient from the equivalent Taylor-Aris value (which corresponds to a parallel plate channel with the same cell aspect ratio and no fluctuation on the boundary) accounts for the impact of the flow complexity on longitudinal transport along the system. We propose an expression for that asymptotic dispersion coefficient (Eq. (26)) that is a generalization of the well-known expression by Taylor and Aris,[1,17] and that takes molecular diffusion, the Reynolds number, the Péclet number, and the cell geometry into account. The dependence of $D_a^\infty/D_m - 1$ on the Reynolds number, at least for the range of parameters investigated here, is found to be uncorrelated to the other parameters; that is, its influence appears as a separate factor with a given functional form $f(Re)$. The dependence of $D_a^\infty/D_m - 1$ on the Péclet is found to deviate from its form in the well-known Taylor-Aris expression, where it scales as Pe^2, to a related, but different power law $Pe^{2+\beta}$. The exponent β is controlled by the cell geometry. Another effect of the cell geometry is an additional geometry-controlled prefactor α in $D_a^\infty/D_m - 1$. Both geometric parameters α and $-\beta$ were found not to depend (or only very weakly) on the cell aspect ratio; they are positive increasing functions of the relative amplitude of aperture fluctuations, a. One can expect the asymptotic dispersion coefficient to deviate all the more from the Taylor-Aris dispersion coefficient as the relative amplitude of the aperture fluctuations and the Reynolds number increase, and as the Péclet number decreases. For realistic scenarios, the asymptotic dispersion coefficient value could be up to an order of magnitude (or more specifically 12 times) larger than the Taylor-Aris dispersion coefficient. The evolution of the asymptotic disper-

sion coefficient as a function of the geometry parameters and of the Reynolds number is closely tied to the volume of the recirculation zones, which illustrates in a stunning manner their role in the deviation from the behavior under uniform aperture.

We were also able to infer a functional form for the pre-asymptotic evolution of the dispersion coefficient. Short period initial oscillations of the signal were, in particular, shown to be mostly due to oscillations of the average solute velocity as it passes "pores" and "throats" of the medium. The approach to the asymptotic regime occurs over a characteristic time that is typically much larger than the characteristic advection time (for Peclet number of practical interest $Pe > O(1)$), and is also impacted by the presence of recirculation zones. The evolution of that characteristic time as a function of the geometrical parameters, the Reynolds number and the Péclet number is controlled by two oppositely competing phenomena. When the recirculation zones are sufficiently large, the trapping of particles inside them delays the establishment of the asymptotic regime. But when the recirculation zone is even larger, the enhanced mixing in the mainstream due to the thinning of that zone leads to faster homogenization and thus a decrease in the characteristic time. Depending on the specific parameter values, one phenomenon dominates and the characteristic time can be either larger or smaller than the one measured under low Reynolds number (Stokes) conditions.

In addition to generalizing the theoretical Taylor-Aris dispersion relation to inertial laminar flows, the current study could also be useful to predict longitudinal dispersion in flows at sufficiently large Reynolds and in systems for which the sinusoidal geometry, albeit not exactly describing the actual geometry, is a decent approximation of the real system. It is, for example, the case for tracer tests under pumping conditions in homogeneous rocks with sufficiently large and well sorted grains.

[1] G. I. Taylor, "Dispersion of soluble matter in solvent flowing slowly through a tube," Proc. R. Soc. London **219**(1137), 186 (1953).
[2] L. E. Locascio, "Microfluidic mixing," Anal. Bioanal. Chem. **379**(3), 325–327 (2004).
[3] A. Tripathi, O. Bozkurt, and A. Chauhan, "Dispersion in microchannels with temporal temperature variations," Phys. Fluids **17**(10), 103607 (2005).
[4] J. H. Forrester and D. F. Young, "Flow through a converging-diverging tube and its implications in occlusive vascular disease – II," J. Biomech. **3**(3), 307–316 (1970).
[5] H. Ye, D. B. Das, J. T. Triffitt, and Z. Cui, "Modelling nutrient transport in hollow fibre membrane bioreactors for growing three-dimensional bone tissue," J. Membr. Sci. **272**(1–2), 169–178 (2006).
[6] H. Brenner, "Dispersion resulting from flow through spatially periodic porous media," Philos. Trans. R. Soc. London **297**(1430), 81–133 (1980).
[7] D. Bolster, M. Dentz, and T. Le Borgne, "Solute dispersion in channels with periodically varying apertures," Phys. Fluids **21**(5), 056601 (2009).
[8] D. L. Koch and J. F. Brady, "The symmetry properties of the effective diffusivity tensor in anisotropic porous media," Phys. Fluids **30**(3), 642 (1987).
[9] D. Koch and J. Brady, "A non-local description of advection-diffusion with application to dispersion in porous media," J. Fluid Mech. **180**(1), 387–403 (1987).
[10] J. Salles, J.-F. Thovert, R. Delannay, L. Prevors, J.-L. Auriault, and P. M. Adler, "Taylor dispersion in porous media: Determination of the dispersion tensor," Phys. Fluids A **5**(10), 2348 (1993).
[11] D. A. Edwards, M. Shapiro, H. Brenner, and M. Shapira, "Dispersion of inert solutes in spatially periodic, two-dimensional model porous media," Transp. Porous Media **6**(4), 337–358 (1991).
[12] D. Bolster, M. Dentz, and J. Carrera, "Effective two-phase flow in heterogeneous media under temporal pressure fluctuations," Water Resour. Res. **45**(5), 1–14, doi:10.1029/2008WR007460 (2009).
[13] G. Dagan and A. Fiori, "The influence of pore-scale dispersion on concentration statistical moments in transport through heterogeneous aquifers," Water Resour. Res. **33**(7), 1595, doi:10.1029/97WR00803 (1997).
[14] M. Dentz and J. Carrera, "Mixing and spreading in stratified flow," Phys. Fluids **19**(1), 017107 (2007).
[15] A. Fiori, "On the influence of pore-scale dispersion in nonergodic transport in heterogeneous formations," Transp. Porous Media **30**(1), 57–73 (1998).
[16] P. K. Kitanidis and B. B. Dykaar, "Stokes flow in a slowly varying two-dimensional periodic pore," Transp. Porous Media **26**(1), 89–98 (1997).
[17] R. Aris, "On the dispersion of a solute in a fluid flowing through a tube," Proc. R. Soc. London **235**(1200), 67–77 (1956).
[18] R. Wooding, "Instability of a viscous liquid of variable density in a vertical Hele-Shaw cell," J. Fluid Mech. **7**(04), 501 (1960).
[19] B. Berkowitz and J. Zhou, "Reactive solute transport in a single fracture," Water Resour. Res. **32**(4), 901–913, doi:10.1029/95WR03615 (1996).
[20] V. Zavala-Sanchez, M. Dentz, and X. Sanchez-Vila, "Characterization of mixing and spreading in a bounded stratified medium," Adv. Water Resour. **32**(5), 635–648 (2009).
[21] W. N. Gill and R. Sankarasubramanian, "Exact analysis of unsteady convective diffusion," Proc. R. Soc. London **316**(1526), 341–350 (1970).
[22] M. Latini and A. Bernoff, "Transient anomalous diffusion in Poiseuille flow," J. Fluid Mech. **441**, 399–411 (2001).

[23] D. Bolster, F. J. Valdés-Parada, T. Le Borgne, M. Dentz, and J. Carrera, "Mixing in confined stratified aquifers," J. Contam. Hydrol. **120–121**, 198–212 (2011).
[24] J. Bouquain, Y. Meheust, and P. Davy, "Horizontal pre-asymptotic solute transport in a plane fracture with significant density contrasts," J. Contam. Hydrol. **120–121**, 184–97 (2011).
[25] M. E. Erdogan and P. C. Chatwin, "The effects of curvature and buoyancy on the laminar dispersion of solute in a horizontal tube," J. Fluid Mech. **29**, 465–484 (1967).
[26] D. A. Hoagland and R. K. Prud'Homme, "Taylor-aris dispersion arising from flow in a sinusoidal tube," AIChE J. **31**(2), 236–244 (1985).
[27] D. M. Tartakovsky and D. Xiu, "Stochastic analysis of transport in tubes with rough walls," J. Comput. Phys. **217**(1), 248–259 (2006).
[28] D. Xiu and D. M. Tartakovsky, "Numerical methods for differential equations in random domains," SIAM J. Sci. Comput. (USA) **28**(3), 1167 (2006).
[29] L. W. Gelhar, "Stochastic subsurface hydrology from theory to applications," Water Resour. Res. **22**(9S), 135S, doi:10.1029/WR022i09Sp0135S (1986).
[30] G. Drazer, H. Auradou, J. Koplik, and J. P. Hulin, "Self-affine fronts in self-affine fractures: Large and small-scale structure," Phys. Rev. Lett. **92**(1), 014501 (2004).
[31] S. Rosencrans, "Taylor dispersion in curved channels," SIAM J. Appl. Math. **57**(5), 1216 (1997).
[32] B. B. Dykaar and P. K. Kitanidis, "Macrotransport of a biologically reacting solute through porous media," Water Resour. Res. **32**(2), 307, doi:10.1029/95WR03241 (1996).
[33] Y. Lucas, M. Panfilov, and M. Bues, "High velocity flow through fractured and porous media: The role of flow non-periodicity," Eur. J. Mech. B/Fluids **26**(2), 295–303 (2007).
[34] K. Chaudhary, M. B. Cardenas, W. Deng, and P. C. Bennett, "The role of eddies inside pores in the transition from Darcy to Forchheimer flows," Geophys. Res. Lett. **38**(24), L24405, doi:10.1029/2011GL050214 (2011).
[35] M. B. Cardenas, D. T. Slottke, R. A. Ketcham, and J. M. Sharp, "Effects of inertia and directionality on flow and transport in a rough asymmetric fracture," J. Geophys. Res. **114**(B6), B06204, doi:10.1029/2009JB006336 (2009).
[36] M. B. Cardenas, "Direct simulation of pore level Fickian dispersion scale for transport through dense cubic packed spheres with vortices," Geochem., Geophys., Geosyst. **10**(12), Q12014, doi:10.1029/2009GC002593 (2009).
[37] J. E. Garcia and K. Pruess, "Flow instabilities during injection of CO2 into saline aquifers," in *Proceedings of Tough Symposium 2003* (Lawrence Berkeley National Laboratory, 2003).
[38] J. G. I. Hellström, P. J. P. Jonsson, and T. S. Lundström, "Laminar and turbulent flow through an array of cylinders," J. Porous Media **13**(12), 1073–1085 (2010).
[39] T. Masuoka, Y. Takatsu, and T. Inoue, "Chaotic behavior and transition to turbulence in porous media," Nanoscale Microscale Thermophys. Eng. **6**(4), 347–357 (2002).
[40] C. Pozrikidis, "Creeping flow in two-dimensional channels," J. Fluid Mech. **180**, 495–514 (1987).
[41] A. E. Malevich, V. V. Mityushev, and P. M. Adler, "Stokes flow through a channel with wavy walls," Acta Mech. **182**(3–4), 151–182 (2006).
[42] H. K. Moffatt, "Viscous and resistive eddies near a sharp corner," J. Fluid Mech. **18**, 1–18 (1963).
[43] R. Haggerty and S. M. Gorelick, "Multiple-rate mass transfer for modeling diffusion and surface reactions in media with pore-scale heterogeneity," Water Resour. Res. **31**(10), 2383, doi:10.1029/95WR10583 (1995).
[44] J. Carrera, X. Sánchez-Vila, I. Benet, A. Medina, G. Galarza, and J. Guimerà, "On matrix diffusion: Formulations, solution methods and qualitative effects," Hydrogeol. J. **6**(1), 178–190 (1998).
[45] L. D. Donado, X. Sanchez-Vila, M. Dentz, J. Carrera, and D. Bolster, "Multicomponent reactive transport in multicontinuum media," Water Resour. Res. **45**(11), W11402, doi:10.1029/2008WR006823 (2009).
[46] R. Zimmerman, S. Kumar, and G. Bodvarsson, "Lubrication theory analysis of the permeability of rough-walled fractures," Int. J. Rock Mech. Min. Sci. Geomech. Abstr. **28**(4), 325–331 (1991).
[47] S. R. Brown, "Simple mathematical model of a rough fracture," J. Geophys. Res. **100**(B4), 5941–5952, doi:10.1029/94JB03262 (1995).
[48] T. Le Borgne, D. Bolster, M. Dentz, P. de Anna, and A. Tartakovsky, "Effective pore-scale dispersion upscaling with a correlated continuous time random walk approach," Water Resour. Res. **47**(12), 1–10, doi:10.1029/2011WR010457 (2011).
[49] J. Bear, *Dynamics of Fluids in Porous Media*, Elsevier ed. (Dover, New York, 1972).

Influence of fracture scale heterogeneity on the flow properties of three-dimensional discrete fracture networks (DFN)

J.-R. de Dreuzy,[1,2] Y. Méheust,[2] and G. Pichot[3]

Received 18 May 2012; revised 28 August 2012; accepted 10 September 2012; published 16 November 2012.

[1] While permeability scaling of fractured media has been so far studied independently at the fracture- and network- scales, we propose a numerical analysis of the combined effect of fracture-scale heterogeneities and the network-scale topology. The analysis is based on $2 \cdot 10^6$ discrete fracture network (DFNs) simulations performed with highly robust numerical methods. Fracture local apertures are distributed according to a truncated Gaussian law, and exhibit self-affine spatial correlations up to a cutoff scale L_c. Network structures range widely over sparse and dense systems of short, long or widely distributed fracture sizes and display a large variety of fracture interconnections, flow bottlenecks and dead-ends. At the fracture scale, accounting for aperture heterogeneities leads to a reduction of the equivalent fracture transmissivity of up to a factor of 6 as compared to the parallel plate of identical mean aperture. At the network scale, a significant coupling is observed in most cases between flow heterogeneities at the fracture and at the network scale. The upscaling from the fracture to the network scale modifies the impact of fracture roughness on the measured permeability. This change can be quantified by the measure α_2, which is analogous to the more classical power-averaging exponent used with heterogeneous porous media, and whose magnitude results from the competition of two effects: (i) the permeability is enhanced by the highly transmissive zones within the fractures that can bridge fracture intersections within a fracture plane; (ii) it is reduced by the closed and low transmissive areas that break up connectivity and flow paths.

Citation: de Dreuzy, J.-R., Y. Méheust, and G. Pichot (2012), Influence of fracture scale heterogeneity on the flow properties of three-dimensional discrete fracture networks (DFN), *J. Geophys. Res.*, *117*, B11207, doi:10.1029/2012JB009461.

1. Introduction

[2] Natural fractured media display a strong hydraulic complexity coming from the fractures' internal topography, from their arrangement in complex networks, and from the interaction of the fractures with the environing rock matrix [*Bear et al.*, 1993; *National Research Council*, 1996]. As a result, flows are generally localized in complex structures and the bulk hydraulic properties display a large variability both inside a given medium and between different media. [*Clauser*, 1992; *Hsieh*, 1998; *Tsang and Neretnieks*, 1998]. Only few of these flow structures can be identified deterministically by geophysical and hydraulic methods [*Rubin and Hubbard*, 2006; *Yeh and Liu*, 2000]; most of them can only be modeled statistically. Such an approximated statistical representation is sufficient for a large range of purposes. For example the knowledge of the detailed flow structure is not crucial to estimate an effective permeability. With this in mind, a prerequisite of modeling consists in determining which fracture properties are essential for hydraulic and transport properties. This has been the original goal of the Discrete Fracture Network approach (DFN). DFNs mimic natural fractured media by representing each fracture individually. They have first been designed toward homogenizing fractured media [*Long et al.*, 1982], and further applied to understanding the flow structures of complex fracture networks [*Davy et al.*, 2006a; *de Dreuzy et al.*, 2001b, 2001c, 2002, 2004a; *Le Goc et al.*, 2010; *Leung and Zimmerman*, 2010], permeability and dispersivity upscaling [*Baghbanan and Jing*, 2007; *Charlaix et al.*, 1987; *de Dreuzy et al.*, 2001a, 2010; *Frampton and Cvetkovic*, 2007, 2009; *Mettier et al.*, 2006; *Park et al.*, 2001; *Snow*, 1969] and, more generally, the definition of the right modeling approach [*Cello et al.*, 2009; *Davy et al.*, 2006a; *Ji et al.*, 2011; *Jourde et al.*, 2007; *Long and Witherspoon*, 1985; *Painter and Cvetkovic*, 2005; *Sahimi*, 1993]. As a further interest, DFNs can extract key information on flow properties from the large geological and geophysical data available on fracture media [*Bonnet et al.*, 2001; *Davy et al.*, 2010]. In this sense

[1]Institute of Environmental Analysis and Water Studies, CSIC, Barcelona, Spain.
[2]Géosciences Rennes, UMR CNRS 6118, Université de Rennes 1, Rennes, France.
[3]IRISA, INRIA, Université de Rennes 1, Rennes, France.

Corresponding author: J.-R. de Dreuzy, Géosciences Rennes, UMR CNRS 6118, Université de Rennes 1, Campus de Beaulieu, FR-35042 Rennes CEDEX, France. (jean-raynald.de-dreuzy@univ-rennes1.fr)

0148-0227/12/2012JB009461

the DFN approach is used to "precondition" equivalent continuum heterogeneous approaches, to which it becomes complementary rather than competitive [*Hsieh*, 1998; *Neuman*, 2005]. It is according to this logic that the generalized radial flow model has been developed [*Barker*, 1988], used [*Cappa et al.*, 2006; *Le Borgne et al.*, 2004], justified [*de Dreuzy and Davy*, 2007; *de Dreuzy et al.*, 2004b] and extended [*Acuna and Yortsos*, 1995; *Cello et al.*, 2009].

[3] So far, hydraulic DFN studies have been performed mostly in 2D. The three-dimensional (3D) flow simulation models have been developed essentially either as a proof of concept [*Dershowitz and Fidelibus*, 1999; *Lenti and Fidelibus*, 2003; *Long et al.*, 1985; *Maryka et al.*, 2004] or for specific site studies [*Cacas et al.*, 1990a, 1990b; *Kalbacher et al.*, 2007]. The only existing 3D stochastic DFN simulations have demonstrated first the broad range of transport transit times within a given fracture networks, as well as between average travel times measured from different simulation runs [*Nordqvist et al.*, 1996], and second the possibility of removing smaller fractures from fracture networks dominated by the longest fractures [*Wellman et al.*, 2009]. 3D stochastic DFN modeling has been hindered because of the difficulty of generating meshes of good quality with classical mesh generation algorithms [*Kalbacher et al.*, 2007; *Maryka et al.*, 2004; *Vohralik et al.*, 2007]. Flow simulations in complex 3D fracture networks require either modifications of the geometrical configurations that are detrimental to the mesh generation on the whole 3D structure [*Erhel et al.*, 2009a], or the decoupling of the mesh generation between fractures using Mortar-like methods [*Pichot et al.*, 2010].

[4] In the fracture network models mentioned above, the basic geometric and hydraulic object is the single fracture. Its hydraulic behavior is classically described by a scalar transmissivity: independently of the flow conditions, the ratio of the overall volumetric flow through the fracture to the norm of the corresponding pressure gradient (computed between the fracture's inlet and outlet) is equal to the ratio of the transmissivity to the fluid's absolute viscosity, the transmissivity being solely dependent on the fracture geometry. The first approximation model for a fracture is the parallel plate, for which the transmissivity is proportional to the plate separation distance to the power of 3 (see, among many others, *Zimmerman and Bodvarsson* [1996b]). In reality, the distribution of local apertures within a geological fracture is nonuniform, due to the roughness of the two facing rock walls. Early experiments [*Cook*, 1992; *Durham and Bonner*, 1995; *Durham*, 1997; *Witherspoon et al.*, 1979] demonstrated that the resulting transmissivity is different from that of a parallel plate model of identical mean aperture [*Cook*, 1992; *Durham and Bonner*, 1995; *Durham*, 1997; *Witherspoon et al.*, 1979]. Numerical modeling of the flow has shown how the deviation from the parallel plate model increases with fracture closure and how it results from aperture heterogeneities-induced flow channeling within the fracture plane. Indeed, the rough walls of a rock joint exhibit peculiar statistical properties: their topographies are scale-invariant over a broad range of length scales [*Brown and Scholz*, 1985; *Power and Durham*, 1997; *Schmittbuhl et al.*, 1993] and are matched over a characteristic "correlation" scale [*Brown et al.*, 1986; *Isakov et al.*, 2001], so that the aperture distribution is also scale invariant from at least the scale of the rock grain up to the latter correlation length [*Brown et al.*, 1986; *Glover et al.*, 1998]. This scale invariance is controlled in first approximation by a scalar parameter usually denoted Hurst exponent; over a broad range of length scales and material types (including geological fracture walls), rough surfaces resulting from brittle fracturing have been measured to exhibit a Hurst exponent very close to 0.8 [*Bouchaud et al.*, 1990]. The spatially correlated fluctuations of the aperture field allow for the existence of correlated large aperture "channels" and low aperture "barriers" within the aperture plane; numerical simulations based on the Reynolds equation [*Brown*, 1987] have shown that these channels and barriers are responsible for a channeling of the flow [*Brown*, 1987], which impacts the permeability of a given fracture, for a given direction of the macroscopic flow. That permeability may also be estimated through a generalized critical path analysis from a critical barrier defined as the smallest permeability line orthogonal to flow [*Talon et al.*, 2010a, 2010b]. Numerical simulations show that, depending on how the channels and barriers are oriented with respect to the macroscropic flow, they can either ease the flow through the fracture and make it more permeable than a parallel plate model of identical mean aperture [*Méheust and Schmittbuhl*, 2000], or hinder the flow with respect to that through a parallel plate model [*Brown*, 1987; *Méheust and Schmittbuhl*, 2000, 2001]. However, if one considers a population of statistically identical fractures, favorable configurations are less frequent than unfavorable ones, so that the mean behavior corresponds to a transmissivity lower than that of the parallel plate of identical mean aperture [*Méheust and Schmittbuhl*, 2001]. In addition, the variability over the statistics increases with the fracture closure, defined as the ratio of the aperture spatial variability to its mean value. Another puzzling finding by *Méheust and Schmittbuhl* [2001] is that a given rough fracture does not have an intrinsic transmissivity: it depends in particular on the flow orientation with respect to the fracture at least at scales smaller than the correlation length. The role played by the correlation length has however been little studied. *Méheust and Schmittbuhl* [2003] have shown that as soon as the correlation length is significantly smaller than the distance between the inlet and outlet, the fracture behaves as a parallel plate. Note also that the average behavior of a statistically homogeneous population of fractures depends only weakly on the spatial correlations [*Méheust and Schmittbuhl*, 2001]: it is mostly identical to that of a population of uncorrelated fractures.

[5] Up to now little has been tempted to model the hydraulic effects of the fracture-scale aperture heterogeneity and of the network-scale intricate structure simultaneously. A first intuitive approximation would consist in replacing the internally heterogeneous fractures by parallel plates having the same equivalent transmissivity T or equivalently a distance between the plates equal to $(12T)^{1/3}$. It is however both practically difficult and theoretically questionable. First, as explained above, a rough fracture does not have an intrinsic permeability independent of the boundary conditions, which makes this approximation both wrong from a theoretical point of view and arbitrary from a practical point of view. Second, the organization of flow potentially exploits the 2D aperture heterogeneity within the fracture plane and 3D high transmissivity shortcuts at the network scale simultaneously: the inlets and outlets for flow in a fracture are intersections with other fractures, and therefore depend on the network structure. In the most dramatic configurations, local fracture

closure may lead to the disconnection of some hydraulic paths and consequently induce an extended flow reorganization at the network scale.

[6] Such effects can only be addressed using a three-dimensional model that accounts both for (i) interior fracture geometrical heterogeneities and (ii) the fracture arrangements in networks of complex topology. Due to previous technical limitations of 3D simulation methods, the flow localization effects at the fracture- and at the network- scale have so far been analyzed separately, with the exception of one article [*Hamzehpour et al.*, 2009] that presented a model based on very restrictive assumptions. First, the fractures had a binary aperture distribution, that is, the apertures within a fracture plane could be either null or have a nonzero value given once for all, for all open regions in all fractures in the DFN. Second, all fractures had the same size. Third, the fracture density was much larger than that corresponding to the percolation threshold. In what follows, thanks to recently developed 3D simulation methods [*Erhel et al.*, 2009a], we analyze the combined effects of fracture-scale heterogeneity and network-scale structure on the permeability of the bulk fractured media, investigating DFNs in which individual fractures (i) have a realistic aperture distribution that is self-affine up to the correlation length in open regions of the fracture plane, and (ii) have sizes that can be as large as the medium size L and as small as $L/10$. We investigate different types of network structures, including networks with a power law size distribution of the fracture sizes, and vary the fracture density from configurations far above the percolation threshold, for which mean field approximations are likely to be relevant, down to the vicinity of the percolation threshold, for which only extensive Monte-Carlo numerical experiments can give insight into the systems' hydraulic behavior.

[7] In what follows, we describe the studied model at the fracture and network scales successively, as well as the flow models (section 2) and their numerical implementation (section 3). Because of a lack of reference results at the fracture scale for the range of closures considered, we first study the mean fracture-scale permeability (section 4), which we then use when discussing the network scale equivalent permeability (section 5). We finally discuss the hydraulic interaction between the network topology and the fracture scale heterogeneity, in section 6.

2. Discrete Fracture Network Model

[8] Among the large range of possible Discrete Fracture Network models (DFNs), we have chosen a classical design and added complexities at the fracture scale. The rock matrix is assumed to be almost impervious in comparison to the fractures so that flow only occurs inside fractures. At the fracture scale, the flow complexity consists in a channeling that arises from the self-affine aperture distribution of the individual fracture. At the network scale, the flow complexity arises from the fracture size distribution and depends on the density of the fractures in the network. Other assumptions have been taken as simple and standard as possible. The originality of this study lies in that the stochastic DFN flow simulations are performed with a resolution high enough for the flow complexity to be solved inside the smallest fractures.

[9] We successively present the network structure, the geometrical characteristics both of a single fracture and of the ensemble of fractures, and the flow models at the fracture and network scales.

2.1. Fracture Network Structure

[10] For the sake of simplicity, fractures are modeled as disks. The fracture size thus corresponds to the diameter of the disk. No location or position is favored, meaning that the fracture orientation and position distributions are uniform within the system. Under these simplifications, the two geometrical features that control hydraulic properties at the network scale are the uniform scalar density of fractures and the fracture size-distribution. In fact, both these features have a dramatic impact on the connection and homogenization scales of the medium. The connection scale is the scale above which networks become connected on average. The homogenization scale is characteristic of flow channeling; it is defined as the characteristic distance between two adjacent flow channels carrying equally large flow rates [*de Dreuzy et al.*, 2001b].

[11] Let us first discuss the size distribution. Observations of geological fractured media have shown that the density function for their fracture size is broad-ranged and exhibits no characteristic length scale; it is well modeled by a power law in the form:

$$f(L_f) = \frac{a_{3D} - 1}{L_{fmin}^{-a_{3D}+1}} L_f^{-a_{3D}} \text{ for } L_f \in \left[L_{fmin}; L_{fmax}\right] \quad (1)$$

where $-a_{3D}$ is the characteristic exponent for the probability density, and $[L_{fmin}; L_{fmax}]$ is the range of modeled fracture sizes [*Bonnet et al.*, 2001; *Davy et al.*, 2010; *Segall and Pollard*, 1983]. The exponent a_{3D} controls the relative proportion of longer and shorter fractures. Field data, in particular from outcrops, provide essentially the 2D exponent a_{2D}, which ranges between 1 and 3.5 [*Bonnet et al.*, 2001]. For uncorrelated fractures, the 3D and 2D exponents are related according to $a_{3D} = a_{2D} + 1$ [*Darcel et al.*, 2003b; *Piggot*, 1997]; the exponent a_{3D} thus ranges in the interval [2; 4.5].

[12] While the observed fracture size distribution extends over several orders of magnitude, 3D flow simulations cannot account for such a scale dynamics and remain technically limited to a narrower scale interval, covering around one order of magnitude. Because of this limitation, three types of size distribution are considered in what follows. In the first type, fractures are all much longer than the system size (Figure 1, left). This type of 3D system has been widely used since the pioneering work of *Snow* [1969]. From the hydraulic point of view it corresponds to a power law distribution with $a_{3D} = 2$ [*Bour and Davy*, 1998] because in power law distributed systems with $a_{3D} = 2$ all fractures that contribute to flow extend across the whole medium. In the second type, all fractures have the same size L_{fmin} significantly smaller than the system size L (Figure 1, middle). This case corresponds to the classical percolation theory scheme [*Stauffer and Aharony*, 1992] and is obtained when a_{3D} goes to infinity (Figure 1, left). In the third type, fracture sizes effectively follow a power law distribution with an exponent $a_{3D} = 3.5$ on a scale range extending from L_{fmin} to the system size L (Figure 1, right). As the impact of a given fracture on percolation is rated by the cube of its size because of excluded volume arguments [*Balberg et al.*, 1984; *de Dreuzy et al.*, 2000], both smaller and longer fractures effectively contribute to network connectivity for $a_{3D} = 3.5$ [*Bour and*

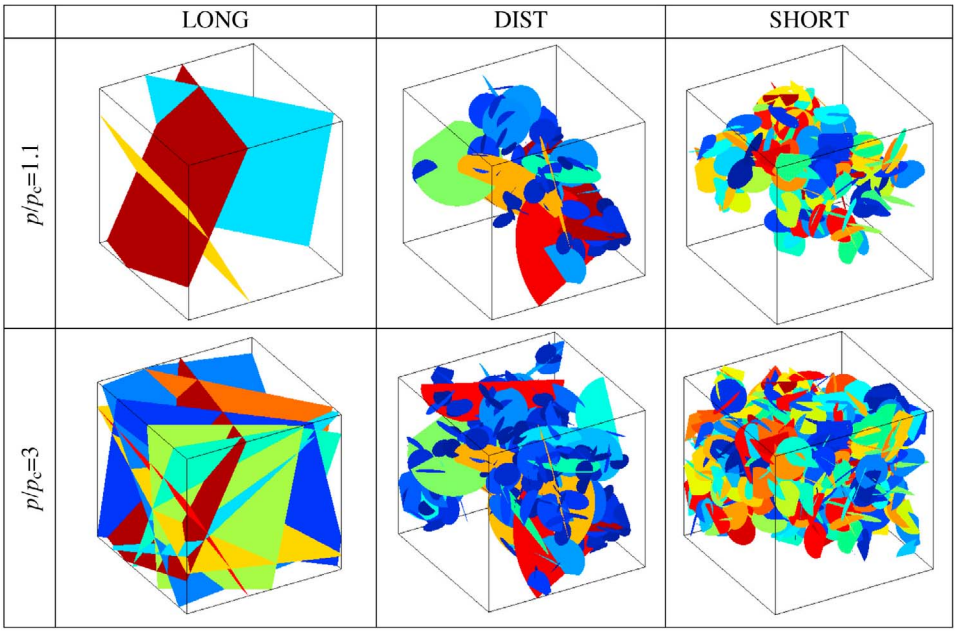

Figure 1. Examples of discrete fracture networks: (left) with long fractures (LONG) and L/L_{fmin} = 10, (middle) with a power law fracture size distribution (DIST) and L/L_{fmin} = 10, and (right) with uniform fracture sizes and L/L_{fmin} = 5 (SHORT). (top) Two networks that are close to the percolation threshold (p/p_c = 1.1) and (bottom) those that are significantly above it (p/p_c = 3). Note that colors do not have any further meaning than identifying the different fractures.

Davy, 1998; *de Dreuzy et al.*, 2000]. We shall denote those three types of network as SHORT, LONG and DIST (Table 1), respectively.

[13] As mentioned above, the other key characteristic parameter of the fracture network is the fracture density. We consider the two extreme cases of sparse and dense fracture networks. Below the percolation threshold, hydraulic properties are determined neither by the network structure nor by the fracture internal characteristics but rather by rock matrix properties [*Hsieh et al.*, 1993]. The sparsest networks of interest in our framework are thus networks at the percolation threshold. We denote as dense networks those with a fracture density much larger than the threshold density. Whatever the configuration, density is always defined by reference to the percolation threshold. We choose the percolation parameter p as the measure of density; it is defined from the truncated third moment of the fracture size distribution, according to

$$p = \frac{N}{L^2} \int_{L_{fmin}}^{L_{fmax}} (\min(L_f, \alpha L))^3 \; f(L_f) dL_f \qquad (2)$$

where N is the fracture number and αL is the mean size of a fracture truncated by the boundaries of the cubic domain of linear size L [*de Dreuzy et al.*, 2000]. The percolation parameter is less classical than other measures like the fracture number per unit length P_{30} or the total fracture surface per unit volume P_{32} [*Davy et al.*, 2006b]. The advantage of the percolation parameter over other measures is that it provides the same rating of the position of the fracture network with respect to the percolation threshold whatever the fracture size distribution. In what follows, the sparse network case corresponds to $p = p_c$, while the dense network case will be taken as $p = 3p_c$ for the LONG and DIST configurations. Because of numerical limitations, the fracture density is bounded toward larger values by time constraints imposed on running the flow simulations.

2.2. Aperture Distribution of Individual Fractures

[14] As described at length in the introduction, geological fractures are defined by two facing rock surfaces, which are rough but can be approximated at large scales as two parallel planes. If the fracture walls do not touch each other, the

Table 1. Common Characteristics of the Discrete Fracture Networks[a]

Parameter	Notation	Value
	Network Scale	
Domain size	[L, L, L]	DIST: L/L_{fmin} = 10 SHORT: L/L_{fmin} = 5
Orientation distribution		Uniform
Position distribution		Poissonian
Length distribution	SHORT	$L_f = L_{fmin}$
	DIST	$L_{fmin} \le L_f \le L_{fmax}$
	LONG	$L_f = L_{fmax}$
Fracture density	p/p_c	$1.05 \le p/p_c \le 3$
	Fracture Scale	
Roughness exponent	H	0.8
Cutoff length	L_c	$0.5 \le L_c/L_{fmin} \le 3$
Fracture closure	c_{frac}	$0.5 \le c_{frac} \le 3$

[a]Density is defined by the percolation parameter p with p_c its value at percolation threshold. The maximum fracture length L_{fmax} is not equal but close to the system size L as the truncation of the largest fractures by the cubic system generates a complex object, the typical size of which may be somewhat larger than the system size L.

distribution of local apertures, a, is simply the difference between the two facing topographies, and its mean value $\bar{a}$ is equal to the separation between the two average planes, traditionally denoted mechanical aperture, a_m. When the wall topographies are brought sufficiently close to each other, they touch at one point, at which a goes to zero. In our model, we allow further closure of the fracture by "melting" the overlapping rock masses into each other. In other words we put all negative local values of the aperture to zero. The motivation for this procedure is mostly simplicity, and its mechanical validation may be considered doubtful; it is however common practice in the field [*Brown*, 1987; *Thompson and Brown*, 1991; *Thompson*, 1991]. A fracture with closed zones has a mean aperture that is larger than its mechanical aperture: $\bar{a} > a_m$.

[15] As the two fracture walls of a natural fracture exhibit Gaussian height distributions of identical amplitudes, and due to the closure rule presented above, the aperture field is distributed according to a Gaussian law truncated so that a values always be nonnegative:

$$p(a) = \begin{cases} \frac{1}{\sigma_a\sqrt{2\pi}} e^{-\frac{(a-a_m)^2}{2\sigma_a^2}} & \text{if } a \geq 0 \\ 0 & \text{if } a \leq 0 \end{cases} \quad (3)$$

where $\sigma_a = \sigma_a(L_f)$ is the standard deviation of the overall distribution prior to the truncation of negative values. Furthermore, the spatial organization of this distribution obeys the following constraints: wall topographies are (i) self-affine and (ii) matched above a characteristic scale L_c, which we denote correlation length. Note that the meaning of that correlation length is unusual, since the two surfaces are uncorrelated with each other at scales smaller than L_c, and identical above. Consequently, prior to the truncation of negative aperture values, the aperture field is self-affine up to the correlation length L_c and exhibits no spatial correlations at scales larger than L_c [*Brown*, 1995; *Méheust and Schmittbuhl*, 2003]. In other words, the standard deviation of a computed on a window of size l, $\sigma_a(l)$, and prior to its truncation to only positive values, scales as [*Schmittbuhl et al.*, 1995]:

$$\begin{cases} \sigma_a(l) \propto l^H & \text{for } 0 \leq l \leq L_c \\ \sigma_a(l) \propto L_c^H & \text{for } L_c \leq l \leq L_f \end{cases}; \quad (4)$$

where H is the Hurst exponent (or roughness exponent) that is characteristic of the self-affinity. Note that after truncation of the negative values, the effective standard deviation of a computed on a window of size l, $\sigma_a^*(l)$, is smaller than $\sigma_a(l)$.

[16] The above scale-invariance property corresponds to a power spectral density $S = |\tilde{a}|^2$ (where the $\tilde{a}$ denotes the Fourier transform of a) of the aperture field prior to truncation in the form [*Méheust and Schmittbuhl*, 2003]:

$$\begin{cases} S(\mathbf{k}) = |\tilde{a}|^2(k_c) & \text{for } k \leq k_c \\ S(\mathbf{k}) = |\tilde{a}|^2(k_c)\left(\frac{k}{k_c}\right)^{-2(1+H)} & \text{for } k \geq k_c \end{cases} \quad (5)$$

where $\mathbf{k}$ is the two-dimensional Fourier vector along the fracture plane, k is its Euclidian norm, and k_c is the wave number corresponding to the correlation length. This description in the Fourier space is completely equivalent to that in terms of spatial correlations.

[17] Provided that the Hurst exponent be set to 0.8 [*Bouchaud et al.*, 1990], our statistical model of rough fracture is based on three parameters: the ratio of the fracture length to the correlation length, L_f/L_c; the root mean square amplitude of the aperture field, which we can choose to define at the scale of the fracture, $\sigma_a = \sigma_a(L_f)$; and the mechanical aperture a_m. We introduce the *a priori fracture closure* as the ratio of σ_a to the mechanical aperture:

$$c_{frac} = \frac{\sigma_a}{a_m}. \quad (6)$$

c_{frac} represents the magnitude of the roughness relative to the distance between the two mean planes of the fracture walls. It is important to keep in mind that $\bar{a}$ and σ_a^*, differ all the more from a_m and σ_a, respectively, as c_{frac}, and therefore the proportion of closed regions within the fracture plane, are larger. Consequently, the *effective fracture closure*

$$c_{frac}^* = \frac{\sigma_a^*}{\bar{a}}$$

differs all the more from c_{frac} as the closure is larger (Figure 2a). From equation (3) it follows that

$$p(a/a_m) = \begin{cases} \frac{1}{c_{frac}\sqrt{2\pi}} e^{-\frac{(a/a_m - 1)^2}{2c_{frac}^2}} & \text{if } a \geq 0 \\ 0 & \text{if } a \leq 0 \end{cases}$$

and the proportion of closed regions within the fracture plane is simply

$$g(c_{frac}) = p(a = 0) = \frac{1}{2}\left[1 - \text{erf}\left(\frac{1}{\sqrt{2}c_{frac}}\right)\right]. \quad (7)$$

Figure 2b illustrates the dependency of g on c_{frac}. Note that the distribution of the local fracture transmissivities, $p(T)$, can be derived directly from the $p(a)$ *by* assuming locally the validity of the cubic law:

$$p(T) = \frac{1}{\sigma_a\sqrt{2\pi}} \frac{1}{3\beta^{1/3}T^{2/3}} \exp\left(-\frac{\left((T/\beta)^{1/3} - \sigma_a/c_{frac}\right)^2}{2\sigma_a^2}\right) \quad (8)$$

for $T > 0$, with $\beta = 1/12$. The aperture and transmissivity distributions are illustrated in Appendix A.

[18] In conclusion, the aperture distribution of a rough fracture is fully described by the set of parameters (c, σ_a, L_f/L_c).

2.3. Variability Among the Fractures of a Network

[19] A given DFN consists of rough fractures all described by the same statistical model. The variability within the population of fractures arises from two effects: first, the variability among the values chosen for c, σ_a, and L_f/L_c; and second, through the stochastic nature of the aperture field generation for individual fractures. We have chosen to consider a fractured medium that is homogeneous to some extent, in that the correlation length of its fractures, L_c, and the fluctuations of their roughness, if measured at the same given scale for all, are

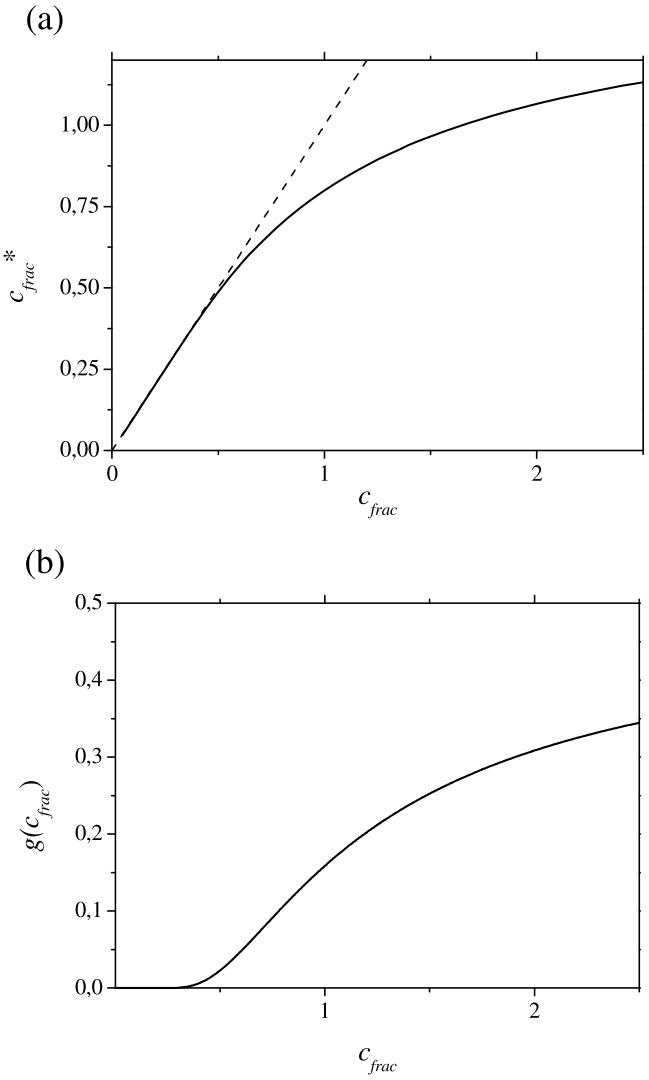

Figure 2. Evolution of (a) the effective fracture closure c^*_{frac} and (b) the proportion of closed regions of a fracture as a function of the imposed a priori fracture closure, c_{frac}.

both uniform across the medium; consequently, $\sigma_a(L_c)$ is uniform. Furthermore, we assume that the mechanical load per surface unit, F_N/L_f^2, that is imposed on each fracture plane, and which is responsible for its partial closure, is uniform across the medium as well, and independent of the fracture orientation: in other words, the stress tensor within the medium is uniform and isotropic. These are reasonable simple assumptions if all fractures in the network arise from the same fracturing process. Another more subtle assumption, which we have not addressed here, would consist in correlating the mechanical load and the fracture orientations.

[20] Let us now relate the assumption of uniform load per surface unit and the variability of the fracture closures in the DFN. *Persson* [2001] developed a theory of contact mechanics between randomly rough surfaces. If the contact is elastic, it is well known [see, e.g., *Johnson*, 1985] that the contact between two surfaces is equivalent to that between a flat plane and a rough surface corresponding to the negated aperture field. *Persson* [2001] addressed in particular the case of a rough topography that is self-affine up to a given cutoff scale. This corresponds exactly to the closure of our synthetic rough fractures, the system size being our fracture size L_f and the cutoff scale being our correlation length L_c. These theoretical results by *Persson* [2001], later verified by numerical simulations [*Persson et al.*, 2002], showed that the total contact surface is always proportional to the mechanical load (computed by considering asperities defined down to the smallest meaningful scale), that is, that closure occurs under constant stress on contact points. Furthermore, if L_c is independent of the system size L_f, the contact surface S_c is also independent of L_f, but if L_c is equal to L_f, then S_c is proportional to L_f^H. Expressed for the fractures in our DFNs, it means that the ratio of the closed area of a given fracture's plane to its total area is

$$\frac{S_c}{L_f^2} = F \cdot \frac{F_N}{L_f^2} \cdot \min\left(L_c^H, L_f^H\right) \tag{9}$$

where both the stress factor F_N/L_f^2, the cutoff scale L_c and the prefactor F are uniform over the medium. The mechanical properties of the bulk material (elastic modulus and Poisson ratio) are here hidden inside the prefactor F, which also features the geometric parameters that are characteristic of the rough surfaces: typical size of the smallest asperities, cutoff length L_c, and Hurst exponent H [*Persson*, 2001]. As the relation between the a priori closure c_{frac} of a fracture and S_c/L_f^2 is the one to one function g defined by equation (7), identical for all fractures in the medium (at least if $\sqrt{S_c} \le L_c$), one can define a global *medium closure*, c, as

$$c = g^{-1}\left(F \cdot \frac{F_N}{L_f^2} \cdot L_c^H\right) \tag{10}$$

such that each individual a priori fracture closure can be written as

$$\begin{aligned} c_{\mathrm{frac}} &= c && \text{if } L_f \ge L_c \\ c_{\mathrm{frac}} &= g^{-1}\left(g(c) \cdot \left(\frac{L_f}{L_c}\right)^H\right) && \text{if } L_f \le L_c \end{aligned} . \tag{11}$$

[21] Let us examine what this means for the different types of DFNs. In SHORT systems, all fractures have the same size L_f and thus the same fracture closure. In LONG systems, all fractures have a length larger than L_c and thus a constant fracture closure c_{frac} equal to c. For DIST systems with L_c from 0.5 to 3 and $L = 10$, the a priori closure of a fracture depends on its length. For these systems we make the approximation that the a priori individual fracture closures are all equal to the medium closure c. This is not true for the majority of fractures that have length smaller than L_c, but holds for the large fractures that contribute most significantly to the overall flow.

[22] In conclusion, assuming a uniform and isotropic stress tensor within the medium results in all fractures having the same a priori closure in SHORT and LONG systems. We make the approximation that this property also holds for DIST systems. The a priori fracture closure c_{frac} is then a scalar quantity that is uniform over the whole medium: for DFNs of types LONG and DIST, it is equal to the medium closure c, while for DFNs of type SHORT, it is related to c according to equation (11). Note that in contrast to c_{frac}, the individual effective fracture closures c^*_{frac} can exhibit a

dispersion around a mean value due to the stochastic nature of the topographies. In what follows, we shall study the permeability of the medium as a function of the a priori fracture closure c_{frac}.

2.4. Flow Model in Individual Fractures

[23] The flow in fractures is modeled according to the lubrication approximation, i.e., assuming a creeping flow (no inertial effects) and a gradient of the aperture field topography much smaller than 1 [*Méheust and Schmittbuhl*, 2001; *Zimmerman and Bodvarsson*, 1996a, 1996c]. It implies that (i) the pressure field can be considered to only depend on the two-dimensional position along the mean fracture plane, and (ii) that the local flux $\boldsymbol{q}$ field, defined as the integral along the fracture aperture of the flow velocity field, is related at each point of the mean fracture plane to the local pressure gradient, $\boldsymbol{\nabla} P$, according to a local cubic law in the form:

$$\mathbf{q} = -\frac{a^3}{12\eta}\boldsymbol{\nabla} P \tag{12}$$

where a is the local aperture as defined above and η is the viscosity of water. Note that equation (12) is identical to the well-known cubic law relating the volumetric flow through a parallel plate fracture to the macroscopic gradient defined at the fracture scale. By definition [see *Johnson*, 1985] the local flux is a conservative quantity, which yields the well-known Reynolds equation:

$$\boldsymbol{\nabla}\cdot\left(a^3\boldsymbol{\nabla} P\right) = 0. \tag{13}$$

To our knowledge, this equation was first utilized to study the flow through a geological rough fracture by *Brown* [1987]. Inverting this equation provides the pressure field in the fracture plane from the knowledge of the aperture field and of the pressure conditions on the fracture domain boundaries; the local fluxes are then computed through equation (12), and the total volumetric flux Q through the fracture as the integral of local fluxes through an appropriate section of the fracture.

[24] Models based on the Reynolds equation suffer from the limitations mentioned above. However, the assumption of the slowly varying aperture field is valid at sufficiently large length scales, due to its self-affine nature: its gradient goes to 0 at very large scales, and to infinity at infinitely small scales; since it is mostly the few larger Fourier modes of the aperture field that control the transmissivity of the fracture [*Méheust and Schmittbuhl*, 2003], the limitations of the Reynolds equation are mostly those inherent to the Stokes flow approximation [*Brown et al.*, 1995; *Witherspoon et al.*, 1980]. In other words, our study is only valid for Reynolds numbers smaller than 1 in all fractures of the network. This is not a very severe limitation under hydrogeological conditions.

2.5. Flow Model at Network Scale

[25] In order to define a bounded open domain, the network is embedded into a cube of edge size L, orientated along the directions of a x, y, z coordinate system with the origin at the center of the cube. The matrix is considered impervious, thus the flow domain is the union of the N_{F} fractures Ω_{f} ($f = 1..N_{\mathrm{F}}$), with N_{I} intersection S_{k} ($k = 1..N_{\mathrm{I}}$) between the fractures. The flow model of the previous section (at the fracture scale) is complemented with continuity conditions on fracture intersections S_{k}, which are written:

$$\begin{aligned} &h_{k,f} = h_k, \forall f \in F_k \\ &\sum_{f\in F_k} \mathbf{q}_{k,f}\cdot\mathbf{n}_{k,f} = 0 \end{aligned} \tag{14}$$

where F_{k} is the set of fractures intersecting on S_{k}, h_{k} the head on the intersection S_{k}, $h_{k,f}$ the trace of the head on S_{k} in fracture f, $\mathbf{q}_{k,f}$ the flow through the intersection in the fracture f, and $\boldsymbol{n}_{k,f}$ the normal to the intersection S_{k} in the fracture Ω_{f} [*Erhel et al.*, 2009a; *Noetinger and Jarrige*, 2012; *Vohralik et al.*, 2007]. The chosen boundary conditions are classical permeameter boundary conditions: two opposite faces of the cube have fixed heads (Dirichlet type boundary conditions) and the four orthogonal faces are impervious (Neumann type boundary conditions). Boundary conditions on the fracture f are summarized as:

$$\begin{aligned} &h = h_+ \text{ on } \Gamma_f \cap \Gamma_{y+} \\ &h = h_- \text{ on } \Gamma_f \cap \Gamma_{y-} \\ &\mathbf{q}\cdot\mathbf{n} = 0 \text{ on } \Gamma_f \backslash \left(\Gamma_{y+} \cup \Gamma_{y-}\right) \end{aligned} \tag{15}$$

where Γ_{x-}, Γ_{x+}, Γ_{y-}, Γ_{y+}, Γ_{z-}, Γ_{z+} are the six faces of the cube and Γ_{f} is the border of the fracture f. The direction of the head gradient along y will be referred to as the main flow direction.

3. Numerical Methods

[26] We have developed a complete software suite, called MP_FRAC, which generates a random DFN and simulates a steady state flow in this network, with various boundary conditions [*Erhel et al.*, 2009a]. This software is integrated in the platform H2OLab [*Erhel et al.*, 2009b]. The generation methods for the networks and for the fracture-scale aperture distributions are classical and are recalled in Appendices B and C for completeness. The flow solution method for single fractures is classical but features an original measurement of the connectivity prior to the solving of the flow, while the flow solution method for full fracture networks is less classical and applied for the first time to a geophysical study. They are both described below.

3.1. Independent Resolution of the Flow Inside a Single Fracture

[27] In section 4 below, we compute the transmissivity of individual rough fractures inside a DFN and investigate the statistics of the fracture transmissivities, independently of their position in the DFN. With this procedure, we aim at measuring the typical impact of fracture wall roughness on the hydraulic behavior of a given fracture within the network. This impact will be utilized for the interpretation of the full network-scale simulation, which are described in section 3.2 and interpreted in section 5.

[28] The transmissivity of each individual rough fracture is obtained by computing the pressure field directly on the square grid on which the aperture field is generated (see section 2.2), and with simple boundary conditions: a constant pressure head in-between two of the facing boundaries (denoted inlet and outlet), and periodic boundary conditions on the two lateral boundaries. The resolution consists in the inversion of equation (13) using a conjugate gradient method

and a dual grid in order for pressure gradients to be computed in a symmetrical manner at the proper grid nodes. See *Méheust and Schmittbuhl* [2001, 2003] for a detailed description of the numerical method.

[29] For these flow simulations at the fracture scale, the connectivity of the fracture is checked prior to computing the flow, in the following manner. The aperture field is thresholded into a mask that only takes two values: 0 for closed areas of the fracture plane, 1 otherwise. The clusters corresponding to a mask value of 1 are then labeled using the Hoshen-Kopelman algorithm [*Hoshen*, 1997]; if at least one of these clusters extends throughout the fracture size, parallel to the macroscopic pressure head, there exists one connected path of nonzero apertures from the inlet to the outlet of the fracture. If not the fracture is considered non-connected, and we do not compute the flow through it. Note that in this manner we also discard a very small proportion of fractures for which the flow would be possible thanks to the periodic boundary conditions, along a direction that is very oblique with respect to that of the macroscopic pressure gradient; for these fractures, the flow (and, consequently, the transmissivity) computed using periodic lateral boundary conditions is very different from what it would be using impermeable lateral boundary conditions, which is why we choose to consider more realistic to define them as non-connected hydraulically.

[30] For connected networks, we compute the equivalent fracture permeability, K_F, using Darcy's law at the fracture scale

$$K_F = \frac{Q}{L\Delta h} \tag{16}$$

where Q is the total volumetric flow through the inlet face of the domain, Δh is the head difference between the domain inlet and outlet, and L is the characteristic fracture size. We focus on the dimensionless ratio of the fracture permeability K_F to the permeability K_0 of a parallel plate fracture with an aperture $a = \sigma_a(L_f)/c_{frac}$ identical to the mechanical aperture of the rough fracture. We recall that $\sigma_a(L_f)$ is the standard deviation of the overall distribution and c_{frac} is the medium fracture closure. Whatever the fracture size distribution, K_0 is defined unequivocally. Averages will be performed on 500 simulations of individual fractures discretized on 512 × 512 grids.

3.2. Flow Modeling and Simulation in the 3D Fracture Network

[31] The numerical model of the flow in the entire network, resolved at the fracture scale, is based on the Mixed Finite Element method, mainly for two reasons: it ensures both local and global mass conservation and it provides an accurate velocity field, which can be used in subsequent transport simulations. We implemented the so-called RT0 scheme [*Brezzi and Fortin*, 1991; *Raviart and Thomas*, 1977]. The networks considered have a very specific geometry: it is a 3D intricate structure of 2D domains. Since the matrix is impervious, the mesh is 2D inside each fracture, 1D at the intersections between fractures, and a 3D set of 2D intersecting domains at the network scale. A first difficulty is to generate this mesh, since it cannot be handled directly by a mesh generator. A second difficulty is to ensure head and flow continuity at the intersections of the fractures and a third challenge is to solve the resulting linear system.

[32] To generate the mesh, a first approach is to first discretize the boundaries and the intersections, then the 2D fractures. However, this method induces very small angles because of the intricate geometry and may fail for some networks [*Mustapha*, 2005]. Therefore, we designed a new method, introducing a pre-processing step where intersections are discretized with a regular grid. Moreover, local adjustments are necessary to guarantee geometrical properties. We developed this approach in both a conforming and a non-conforming setting [*Erhel et al.*, 2009a; *Pichot et al.*, 2010, 2012]. Local modifications and a non conforming method are also used in *Vohralik et al.* [2007]. With a hybrid method and a conforming mesh, it is finally quite easy to ensure the continuity conditions at the intersections, because of the choice of the main unknowns (the head at each edge of the mesh) [*Erhel et al.*, 2009a]. With a non-conforming mesh, we used the Mortar framework to write the discrete problem [*Pichot et al.*, 2010]. However, the pre-processing step induces particular cases where some parts of intersections are common to three fractures or more. Thus, we had to generalize the Mortar method to deal with these configurations [*Pichot et al.*, 2012]. The conforming mesh method has been validated with the non-conforming mesh method [*de Dreuzy et al.*, 2012] and is used throughout this paper.

[33] Linear equations written at each edge of the mesh express local mass conservation. The resulting linear system $Ax = b$, where x is the trace of hydraulic unknowns on edges and b accounts for boundary conditions, is large. It has as many unknowns as edges in the mesh but is sparse, with roughly five nonzero coefficients per line for a mesh with triangles [*Erhel et al.*, 2009a]. The matrix A of the system is SPD (symmetric positive definite), also for the non-conforming case. Thus several solving algorithms can be used: a direct method, based on the Cholesky factorization; an algebraic multigrid method; a preconditioned conjugate gradient method, with various preconditioners; a domain decomposition method [*Poirriez*, 2011]. High performance computing is required to handle very large systems. Once the system is solved, it is easy to compute the head inside each triangle and the transverse flux at each edge, using the RT0 scheme.

[34] An example of the resulting flows is shown in Figure 3. It addresses the sparse DIST network of Figure 1 for the two configurations of smooth (parallel plate) and rough fractures, and for a fracture closure c_{frac} of 1. The two configurations exhibit a strong channeling both at the network scale and at the fracture scale and a wide variety of flow values. Comparison between the two demonstrates the strong influence of the fracture aperture distribution on the volume occupied by the flow: it is heavily channelized within the fracture planes in the rough fracture configuration, appearing more 1D than 2D. The focus of the present article is to determine to which extent these differences in flow structures impact the equivalent permeability of the medium.

3.3. Network Connection and Equivalent Permeability

[35] Local closure of fractures may induce network disconnection at larger scales. It occurs when closed areas prevent flow through a fracture plane that the network structure would otherwise (i.e., at moderate fracture closure) direct a

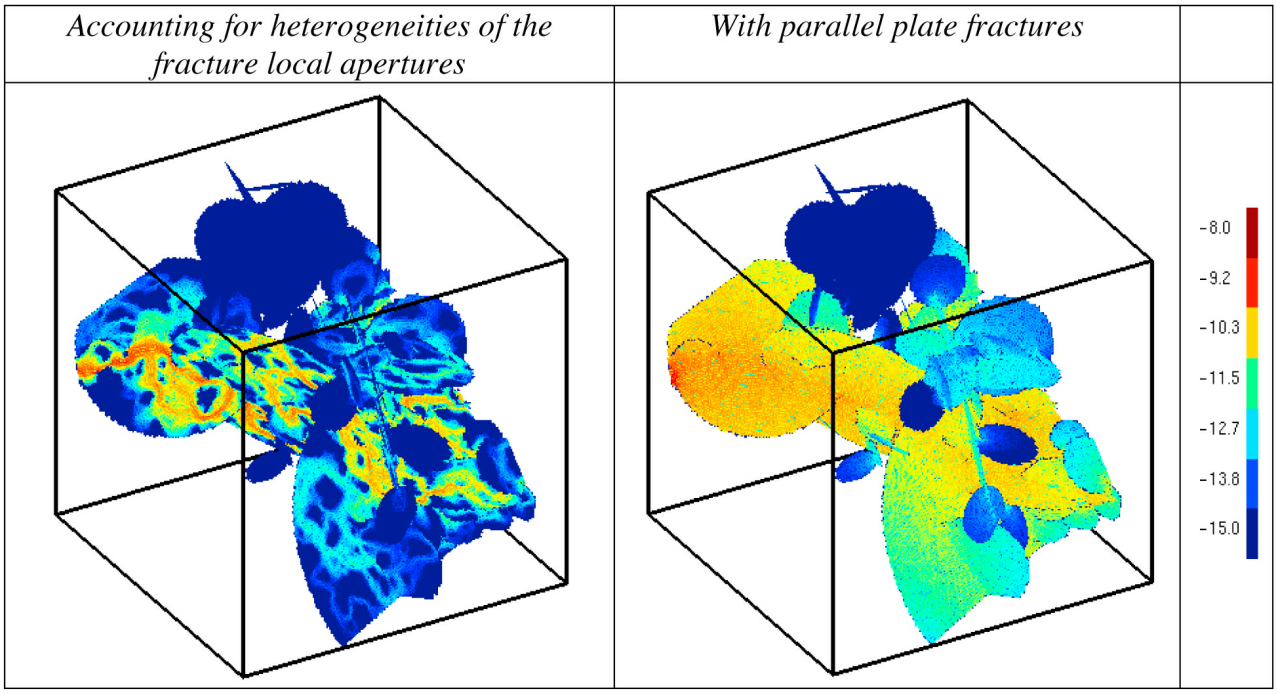

Figure 3. Flow field within the sparse DIST network shown in Figure 1 (top middle), (left) when heterogeneities of the fracture local apertures are taken into account ($c_{\mathrm{frac}} = 1$) and (right) when fractures are modeled as parallel plates. Scale on the right displays the logarithm of the mean flow value within a mesh cell.

significant volumetric flow to. A particular case occurs when an intersection between two fractures that is an essential hydraulic link at moderate fracture closures falls entirely inside a closed zone of one of these fractures. In the most critical configuration, one particular fracture acts as a global bottleneck, focusing all the flow through the network; it is sufficient that the closure of that fracture create a closed zone that renders its transmissivity null for the full network to be hydraulically disconnected. Less radical configurations feature the closure of more than one bottleneck on several parallel major flow paths. The identification of the disconnected networks is performed during flow simulation using the following method. Closed zones within a given fracture are allocated an aperture four orders of magnitude smaller than the mean aperture of the fracture in question. According to the cubic law (12), their local transmissivity is then twelve orders of magnitude smaller than the mean fracture transmissivity. By imposing that the precision for the numerical flow resolution be much larger (10^{-9} in practice) than the latter local transmissivity ratio, we ensure that the flow solver fails to solve the linear system for disconnected networks. In consistency with the percolation theory, the probability for a network to be connected (or connection probability) is denoted Π. The disconnection probability $1\text{-}\Pi$ is expected to increase with fracture closure.

[36] For connected networks, we compute the equivalent network permeability according to equation (16) where L is the medium linear size. As we focus here on the influence of fracture scale heterogeneities on the hydraulics at the network scale, we compare the behaviors of two networks with the same topology: one with rough fractures, the other one with parallel plate fractures. More precisely: for each studied network topology, we first simulate the flow in a configuration where heterogeneities of the local fracture apertures are taken into account, and compute the DFN's equivalent permeability K_{N+F} (the lower subscript "$N+F$" stands for "*Network+Fracture*" meaning that complexities are accounted both at the network and at the fracture scales). Equivalent permeability using Darcy's law at the network scale is computed according to:

$$K_{N+F} = \frac{Q}{L\Delta h} \tag{17}$$

where Q is the total volumetric flow through the inlet face of the domain, Δh is the head difference between the domain inlet and outlet, and L is the characteristic network size. We then simulate the flow through a network with the same topology and using the same computational mesh, but where each (rough) fracture has been replaced by a parallel plate fracture with the same (arithmetic) mean aperture. We denote K_N the corresponding equivalent permeability (the subscript "N" stands for "*Network*" meaning that complexity only comes from the network scale while apertures are uniform within fractures). Let us underline here that, while in the latter case the fracture local aperture fields are uniform within each fracture, so that one can assign one scalar aperture for each of them, they are not homogeneous over the population of fractures. Indeed, the fracture aperture standard deviation at scale L_c, Γ, is uniform over the medium, and so is the fracture closure $c_{\mathrm{frac}} = \sigma_a(L_f)/a_m$, where the overall standard deviation of a fracture's local aperture field $\sigma_a(L_f)$ depends on the fracture size distribution according to equation (4); thus, the

relation $a_m = \sigma_a(L_f)/c_{frac}$ imposes the variability of the mechanical apertures a_m among fractures in the DFN.

[37] We then compute the ratio of the permeabilities K_{N+F} and K_N for each DFN realization and investigate how this ratio is distributed over a large population of statistically equivalent DFNs. In this manner we filter as much as possible the first order influence of the network topology on the medium permeability, and account for the interaction between that topology and the flow localization within fracture planes. In what follows we determine the mean value for the permeability ratio over N_{SC} connected Monte-Carlo simulations as

$$\left\langle \frac{K_{N+F}}{K_N} \right\rangle = \frac{1}{N_{SC}} \sum_{t=1}^{N_{SC}} \left(\frac{K_{N+F}}{K_N} \right)_i \tag{18}$$

Note that we study the effect of fracture closure on (i) network connectivity and (ii) equivalent permeability for connected networks separately, excluding the non-connected fracture networks from the statistics of the equivalent permeability, in a manner similar to what was done in the study at the fracture scale (see section 3.1). In this study, we limit our investigations to the mean permeability ratios to obtain the general tendencies of the coupling between the fracture- and network-scale flow complexities. The variability of the permeability ratios is also of interest and deserves in itself a full study that should account for the dependence of the variability on the different fracture sizes. This could be done for example by fixing the larger fractures to focus solely on the variability of the fracture-to-network flow correlations.

3.4. Model Parameters

[38] Table 1 summarizes the model assumptions and parameters. We have chosen to normalize all dimensions by the minimal fracture size L_{fmin}. The normalization by L_{fmin} takes different meanings depending on the nature of the fracture size distribution. For networks of "infinite" fractures (LONG), the sole characteristic scale is the system size ($L_{fmin} \gg L$ and $L_{fmax} \gg L$). In the other cases (DIST and SHORT), the significant parameter is L/L_{fmin}. For fracture networks having a non-trivial fracture size distribution (DIST), enlarging the system is exactly equivalent to enhancing the fracture resolution, that is keeping L constant and lowering L_{fmin}.

[39] The choice of the size range L/L_{fmin} and of the number of Monte-Carlo simulations N_{SC} derives from a balance between the two necessities of (i) describing a reasonably large network topological complexity and (ii) sampling the permeability variability over a sufficiently large number of DFN realizations. A large number of Monte-Carlo simulations is mandatory due to the strong variability of the network topology over different realizations, especially for large distributions of the fracture sizes (DIST). The topological variability fundamentally arises from the numerous respective positions of the middle-sized fractures, which are found in limited numbers because of the power law size distribution and because the number of fractures in the network that can be handled by the simulation is also limited. To ease off this necessary trade-off between, on the one side, the number of fractures in the DFNs and the range of the described length scales, and on the other side, the number of DFN realization that are computed, we have looked for the most adapted flow numerical solvers to make it possible to solve systems of the order of 10^5 to 10^6 mesh cells in a few seconds to a few minutes at most [*Erhel et al.*, 2009a]. For these sizes of systems, the most efficient system solvers are based on the multifrontal method [*Davis and Duff*, 1999]. Thanks to this optimization, we fix $L/L_{fmin} = 10$ for LONG and DIST networks, and $L/L_{fmin} = 5$ for SHORT networks. The reason why we can afford less realizations and smaller systems in the SHORT case is that the cumulated fracture surface is much larger with more dead ends and fractures that do not effectively take part to connectivity. Thus, SHORT systems require more CPU time for the same relative density measured with respect to the percolation threshold. Let us here underline that the model studied is quite complex as it involves structures at the fracture and at the network scale that are both handled stochastically. The number of Monte-Carlo simulations ranges from 10^2 to 10^3 simulations for the denser and the sparser networks, respectively. The smaller number of simulations for the denser structures is justified by the less critical nature of the flow structure in those cases. The number of simulations was fixed by a preliminary convergence analysis that showed that results were not changed by more than 5% when doubling the number of simulations. We explore the parameter space densely and report in what follows the characteristic tendencies obtained for a subset of the simulations performed. Overall the numerical simulations performed for this study amounts to around $2\ 10^6$.

4. Results for Individual Fractures Within a DFN

[40] The case of individual fractures needed to be revisited in order to get a reference behavior at the fracture scale in the exact conditions modeled in complete "N+F" systems. Former studies have either handled different fracture aperture models or the same model on a much more restricted range of closures [*Méheust and Schmittbuhl*, 2003] or not accounted for the distribution of fracture sizes. For poly disperse systems (DIST), since the correlation length L_c is identical for all fractures, the ratio L_f/L_c depends on a particular fracture's length. This does modify the averaged connectivity and hydraulic properties of the medium. We examine the disconnection probability 1-Π and permeability ratio as defined by section 3.1 for 500 single fractures that follow the length distribution of the three fracture network types SHORT, DIST and LONG. Results are displayed in Figure 4a for $L_c = 1$ and $L_c = 3$ in the DIST case.

[41] The disconnection probabilities 1-Π (Figure 4a) logically increases while increasing the fracture closure c and/or the aperture correlation scale L_c, as both effects result in extending the area of the closed regions of the fracture plane 1-Π follows the average proportion of closed regions in a fracture's plane.

[42] Disconnection occurs preferentially in the fractures of size smaller or around the correlation scale L_c because, for these fractures, correlations exist in the aperture field up to the scale of the fracture length, so that a single closed region of the fracture plane extending throughout the fracture may by itself disconnects it. Fracture disconnection might thus occur either by reducing the fracture lengths (shift from DIST to SHORT type of fracture length distribution) or by enlarging L_c, which is in effect the cut-off length controlling the size of the closed regions.

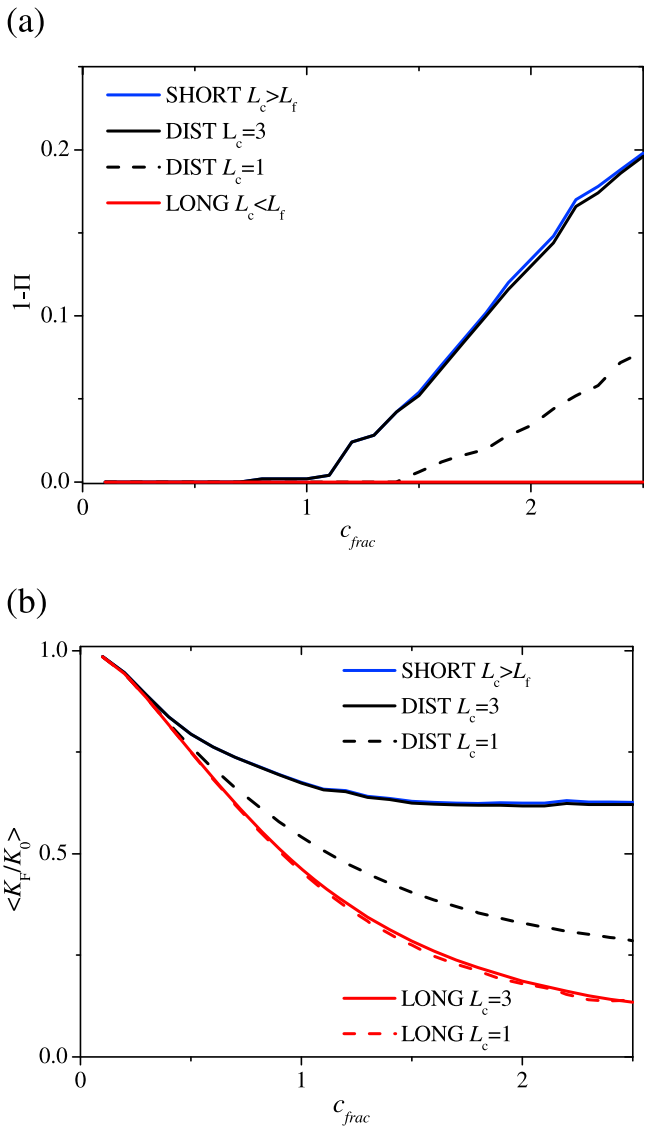

Figure 4. (a) Fracture-scale disconnection probability 1-Π and (b) average permeability ratio $\langle K_F/K_0 \rangle$. When not indicated, values are valid for all values of L_c larger than 1.

[43] $\langle K_F/K_0 \rangle$ varies consistently with 1-Π (Figure 4b). It goes to 1 at infinitely small closure c_{frac} (i.e., when the local transmissivity distribution vanishes) and decreases monotonically with the fracture closure, while the variability steadily increases. As $\langle K_F/K_0 \rangle$ is always smaller than 1, distributed apertures always reduce the equivalent permeability compared to the parallel plate behavior. This effect results from the variability of the flow channeling inside the fracture plane. It is in particular controlled by the orientation toward the average flow of the channels with the largest local transmissivities [*Méheust and Schmittbuhl*, 2001]. Configurations detrimental to flow being more numerous than those enhancing flow, permeability is reduced on average. Flow reduction is enhanced by larger L_c values. These results are consistent with the ones previously acquired by *Méheust and Schmittbuhl* [2001, 2003], complement them on a fuller range of closure values. For the DIST case, they also quantitatively differ because of the L_f/L_c variability induced by the fracture size distribution.

5. Results for Full Fracture Networks

[44] We are reporting the effect of both fracture aperture and fracture network properties by systematically varying the fracture closure c, the cutoff length L_c, the type of fracture size distribution (SHORT, DIST, LONG) and the density of fractures in the network, p/p_c. Beyond the systematic characterization of connectivity and effective permeability, we seek a better understanding of the interactions between fracture-scale heterogeneities and network-scale topology by comparing the fracture-scale and network-scale results.

5.1. Disconnection Probability

[45] Disconnection at the network scale (Figure 5) follows the same tendency as at the fracture scale (Figure 4a). Disconnection grows monotonously with the closure c_{frac}. The disconnection probability is a more pronounced phenomenon at the network scale, because closed areas do not have to extend across whole fracture planes for the network to lose its connectivity, but it is sufficient for them to just close the bottle necks of the connectivity structure. Consequently, the disconnection probability 1-Π is significant for DFNs that are close to the percolation threshold, and sharply decreases as the density of fractures is increased (Figure 5, squares compared to disks), since a larger number of potential paths are then made available. For DFNs with a larger density, the disconnection rate becomes even lower at the network scale than at the fracture scale because of the existence of parallel connected paths that cannot be all disconnected by closed areas. This phenomenon is even more marked for SHORT than for DIST networks (Figure 6b compared to Figure 6a) as the number of connected paths increases faster with density for smaller fractures (with the measure of density given by equation (2)).

[46] Because of the finite size of the systems studied, the latter analysis will likely hold for DIST networks but is incomplete for SHORT networks at threshold. In fact, for DIST networks, fractures forming the connected structures range over a limited size interval [*de Dreuzy et al.*, 2001c; *Wellman et al.*, 2009]. Increasing the system size or equivalently enhancing the system resolution will not issue dramatic changes in the system connectivity, but rather add smaller fractures to the existing main connected paths. On the contrary, for SHORT networks at the percolation threshold, increasing the system size results in enlarging the number of fractures that are essential to network connectivity; indeed, the number of these links scales as L^{d_R} with $d_R = 1.14$ in 3D systems [*Stauffer and Aharony*, 1992]. As the system size is increased more and more, the probability that breaking just one of these links might disconnect the whole network increases to 1. For SHORT networks that are lying above the percolation threshold, this situation is not to be encountered as long as the typical distance between two independent paths, also called the correlation length in the percolation theory terminology (but not to be confused with the our correlation length L_c), is smaller than the system size.

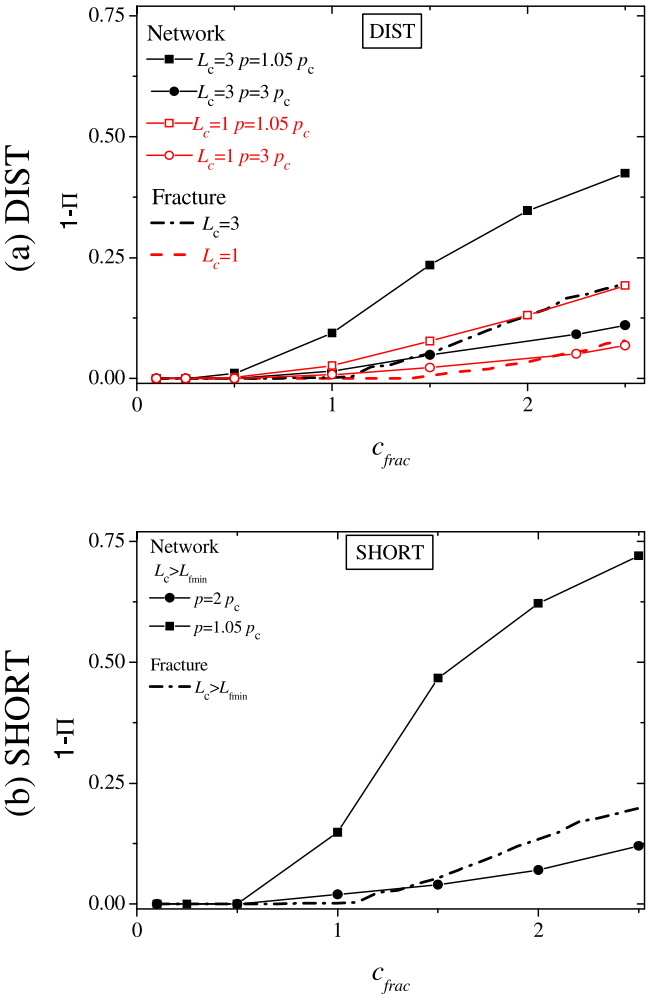

Figure 5. Network-scale disconnection probability for SHORT and DIST networks. LONG networks never become disconnected. Note that the vertical scale has been chosen to be equal in both graphs.

5.2. Mean Permeability Ratio $\langle K_{N+F}/K_N \rangle$

[47] The behavior of the mean permeability ratio $\langle K_{N+F}/K_N \rangle$ as a function of the medium closure is illustrated in Figure 6. Larger values close to 1 indicate a restricted effect of heterogeneous fracture aperture distributions, while values deviating from 1 indicate on the contrary that taking heterogeneities below the fracture scale into account in the model changes the DFN's hydraulic behavior significantly. $\langle K_{N+F}/K_N \rangle$ is also always smaller than 1, at least in the density range studied here. It means that the local fracture aperture distribution reduces the equivalent network permeability systematically. In addition, $\langle K_{N+F}/K_N \rangle$ ranges between 0 and 1 covering almost all possible values, and systematically decreases as a function of the closure c_{frac}. This effect first comes from the influence of the aperture distribution at the fracture scale itself, measured by $\langle K_F/K_0 \rangle$ (see section 4). $\langle K_{N+F}/K_N \rangle$ and $\langle K_F/K_0 \rangle$ do in fact display very similar tendencies as functions of the fracture closure c_{frac} (Figure 6, thick lines compared to line and symbols plots of the same color). However, they differ quantitatively, except in few cases like for the distributed fracture length networks DIST with L_c = 1 at p/p_c = 3, and the long fracture networks LONG with L_c = 1 at p/p_c = 1.05.

[48] These two specific cases occur at highly different fracture densities. In the second case (long fractures), the equality is expected because, networks that are close to the percolation threshold consist of almost a unique fracture.

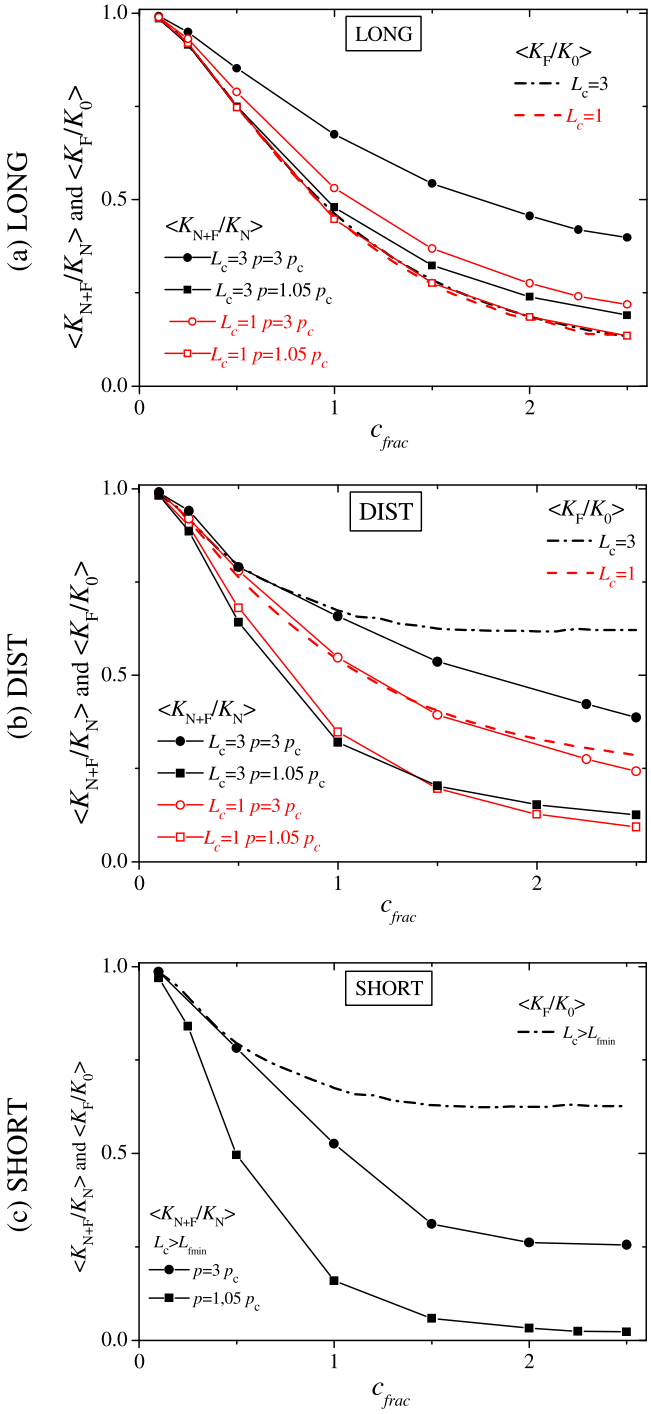

Figure 6. Network- and fracture-scale permeability ratios. Each point represents an average over 10^2 and 10^3 simulations for the denser and sparser cases respectively.

A small difference between the network scale and the fracture scale occurs because of the possible connection by 2 to 3 diagonal fractures in series rather than 1 fracture in some configurations. These differences are negligible for system sizes L much larger than the cut-off length L_c.

[49] In most cases, the fracture and network scale permeability ratios differ significantly. There exists both configurations for which the network scale permeability ratio is smaller than its fracture scale counterpart, and configurations for which it is larger. When $\langle K_{N+F}/K_N\rangle > \langle K_F/K_0\rangle$, two effects compete: aperture heterogeneities below the fracture scale tend to decrease the medium permeability, while the network topology tends to increase it by allowing the fluid to select a path through the most transmissive fractures. For example in the LONG case above percolation threshold (Figure 6a), networks are made up of a superposition of long fractures, each of them almost extending through the whole domain. Taken individually, they would lead to a permeability ratio identical to that at the fracture scale. Taken together, they intersect themselves and offer additional larger transmissivity shortcuts and deviations, enhancing thus the equivalent network permeability.

[50] On the contrary, for the SHORT networks made up of small fractures (Figure 6c), the effect of the network is to reduce the equivalent permeability ($\langle K_{N+F}/K_N\rangle < \langle K_F/K_0\rangle$) in complete consistency with the previously reported effect on the disconnection rate (see section 5.1). These connected networks made up of small fractures have the most complex topology. Close to the percolation threshold, they display a large number of bottle necks, which are expected to be highly sensitive to local apertures within fracture planes. A small reduction of the aperture around these bottle necks will strongly reduce the full network permeability, while a large enhancement of the permeability of the same zones will only slightly increase the network permeability. The permeability ratio reduction can be quite large around the percolation threshold where $\langle K_F/K_0\rangle$ tends to 0.5 while $\langle K_{N+F}/K_N\rangle$ tends to 0. If that reduction is less marked above the threshold, for which bottle necks are rarer, it is still very well marked and can be explained within the framework of critical path analysis [*Ambegaokar et al.*, 1971; *Charlaix et al.*, 1987; *Hunt and Gee*, 2002]. Above the percolation threshold, small apertures acting as bottle necks lower the permeability of the whole path to which they belong. Increasing the fracture density means increasing the number of alternative paths and progressively removing the limitations induced by smaller fracture apertures by allowing them to be bypassed.

[51] The length-distributed configurations (DIST) display a richer range of behaviors, with network-scale permeability ratios smaller than their fracture-scale counterpart around the percolation threshold ($p/p_c = 1.05$), as for the SHORT case (Figure 6b, squares), but of same magnitude for higher densities $p/p_c = 3$ and $L_c = 1$, as for the LONG case (Figure 6b, red circles). Around the percolation threshold, $\langle K_{N+F}/K_N\rangle$ is not affected by L_c and tends to be controlled essentially by the fracture network topology and the fracture closure c_{frac} and not by the repartition of apertures within the fractures (L_c), once the network has proven to be connected. In other words, for DFNs at the percolation threshold, L_c mostly influences the disconnection rate 1-Π but not the permeability ratio of the connected networks. If closed areas do not cover the network bottle necks, their relative extension within the fracture does not influence the network transmissivity. Flow equally bypasses these closed zones whatever their extension as long as they do not disconnect the network. While the equivalent permeability is not much altered, flow structures within the network vary consequently as shown by Figure 3. These variations concern both the fracture scale and the network scale. Aperture-scale heterogeneity tend to modify the circulation pattern within the fracture because of constraints imposed by the neighboring fractures. This is shown in Figure 7, which compares flows in a given fracture at two different fracture closures c_{frac} equal to 0.25 (Figure 7, left) and 1 (Figure 7, right) within the network displayed in Figure 3. The thick black segments identify the intersections of the fracture plane with the neighboring fractures. The comparison of the flow and head fields (Figures 7 (middle) and 7 (bottom)) shows that when aperture heterogeneity is present in the fracture, the flow is partly re-directed to the top left side of the fracture (from left to right in Figure 7) and that this re-direction cannot be explained by the local transmissivity structure (Figure 7, top). In fact the right side of the fracture remains hydraulically well connected.

[52] Above the percolation threshold, percolation is less critical, and the effective permeability becomes sensitive to the mean medium permeability, and consequently to the cut-off scale of the aperture correlation pattern (Figure 6b, red circles compared to black disks).

5.3. Permeability Correction Factor

[53] As shown in the previous section, $\langle K_{N+F}/K_N\rangle$ and $\langle K_F/K_0\rangle$ display similar tendencies as a function of fracture closure c_{frac}. The same kind of similarity is displayed both for aperture cutoff scales L_c and network topologies (density and length distribution). Based on this similarity, and depending on whether the network permeability is reduced or enhanced by the fracture aperture distribution, we define the correction factor α:

$$\begin{aligned} \text{if } \frac{\left\langle \frac{K_{N+F}}{K_N} \right\rangle}{\left\langle \frac{K_F}{K_0} \right\rangle} > 1 \quad &\text{then} \quad \alpha = \frac{\left\langle \frac{K_{N+F}}{K_N} \right\rangle}{\left\langle \frac{K_F}{K_0} \right\rangle} - 1 \\ &\text{otherwise} \quad \alpha = 1 - \frac{\left\langle \frac{K_F}{K_0} \right\rangle}{\left\langle \frac{K_{N+F}}{K_N} \right\rangle} \end{aligned} . \tag{19}$$

The absolute value of α is a measure of how much the typical ratio of the permeability of the full fracture network to that of the corresponding parallel plate fracture network differs from the typical permeability ratio of a single rough fracture within the network to the corresponding parallel plate fracture; $\alpha < 0$ when the network structure induces a reduction of the permeability compared to the equivalent fracture transmissivity. Conversely $\alpha > 0$ when permeability is enhanced. Note that equation (19) defines $\langle K_{N+F}/K_N\rangle/\langle K_F/K_0\rangle$ as continuous for $\langle K_{N+F}/K_N\rangle = \langle K_F/K_0\rangle$. The correction factor α can take all possible negative values as $\langle K_{N+F}/K_N\rangle$ can tend to zero for hardly connected networks. α is however bounded above by the ratio of the maximum local transmissivity to the minimum one, minus 1. Although not providing any new information with respect to $\langle K_{N+F}/K_N\rangle$ and $\langle K_F/K_0\rangle$, α demonstrates

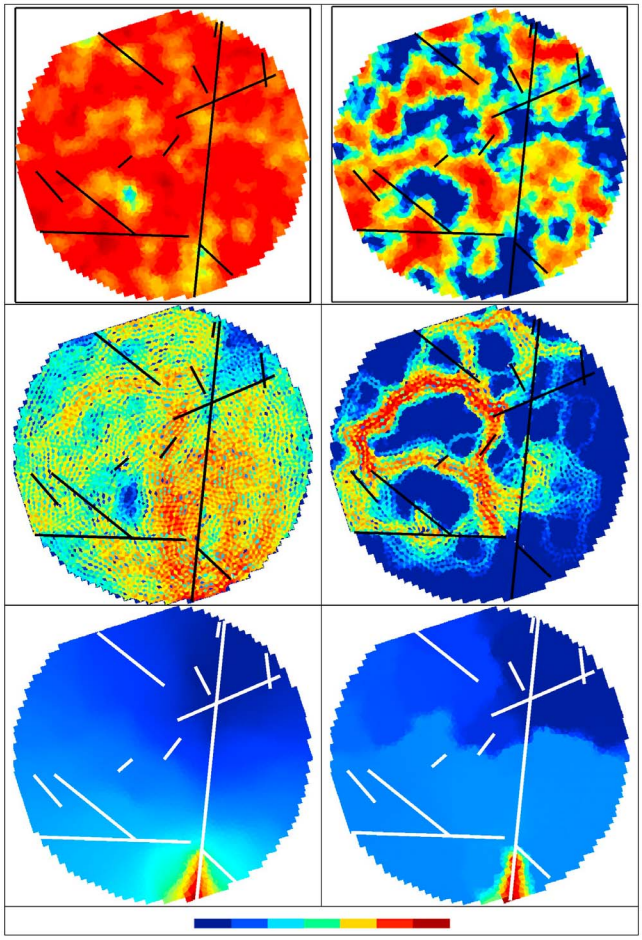

Figure 7. (top) Log-permeability fields, (middle) logarithm of the flow fields, and (bottom) head fields in one of the large fractures of the DIST network shown in Figure 1 at fracture closures (left) $c_{\mathrm{frac}} = 0.25$ and (right) $c_{\mathrm{frac}} = 1$; the correlation length is $L_c = 1$. The traces of the intersections with the other fractures are represented as black linear segments superimposed on the permeability and flow fields. Color scales are all relative to the minimum ($x_{\min}$) and maximum ($x_{\max}$) of the quantity (x) represented. Colors are matched to the corresponding quantity on a continuous scale where the discrete values $x_{\min} + k/6\,(x_{\max} - x_{\min})$, for $0 \le k \le 6$, correspond respectively to the following colors: navy ($k = 0$), blue ($k = 1$), cyan ($k = 2$), green ($k = 3$), orange ($k = 4$), red ($k = 5$), and purple ($k = 6$), shown at the very bottom of the figure. Note that the small-scale color variability of the flow field (Figure 7, middle) comes from the representation of the norm of the flow field averaged over the edges of each mesh cell.

several essential features of the effect of the network structure on the upscaling of local transmissivity distributions. First, α ranges over a wide interval between -31 and $+2$ (Figure 8). Except for networks of long fractures or very dense networks, the network topology generally induces a reduction of permeability rather than an increase. Second, α is monotonic as a function of the fracture closure c_{frac}. For given assumptions for the fracture and network structures (fixed length distribution, L_c and p/p_c), α is either monotonically increasing, monotonically decreasing or steadily zero. Third, the variations of α are rather quadratic than linear, which implies a strong impact of fracture closure on the reduction and enhancement factors. The systematic similarity between fracture- and network-scales variations previously evoked

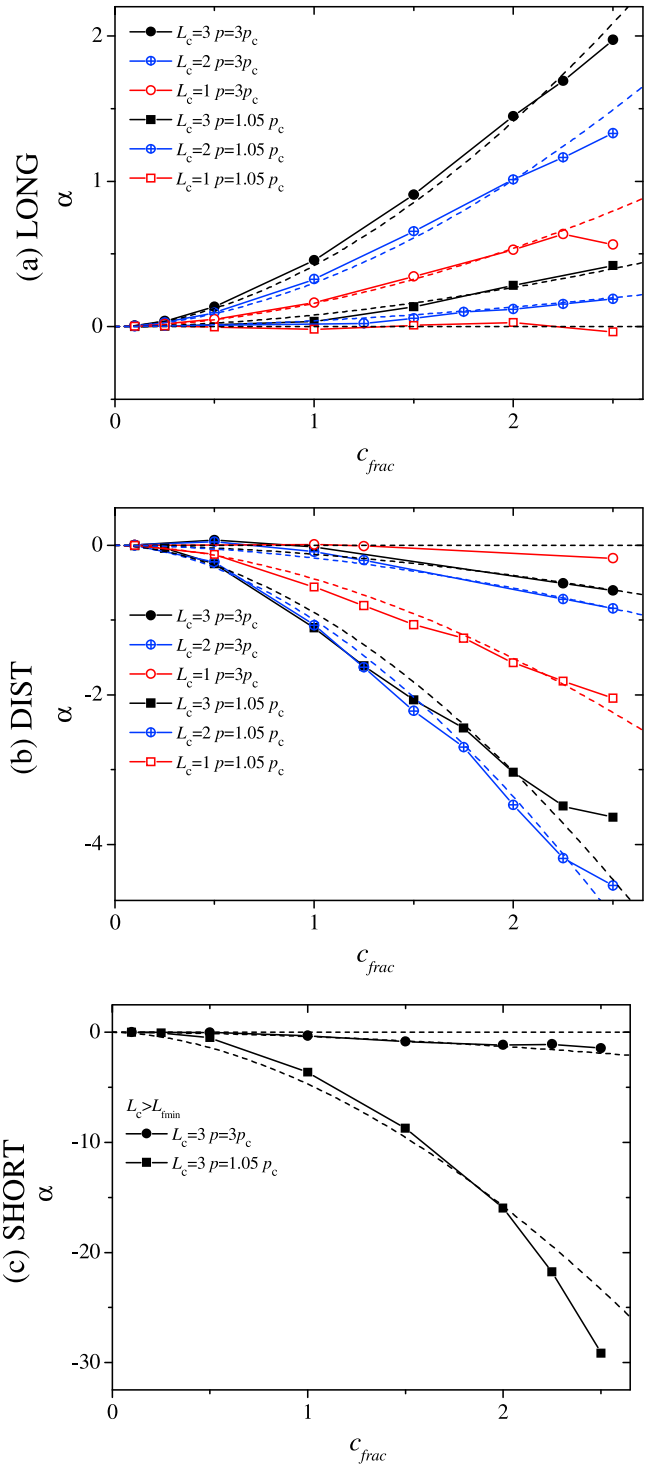

Figure 8. Permeability enhancement and reduction factors $\alpha+$ and $\alpha-$ as functions of fracture closure c for different values of fracture density p/p_c and cut-off scale L_c. The dashed line next to the data plot represents the closest power law tendency: $c_{\mathrm{frac}}^{1.75}$.

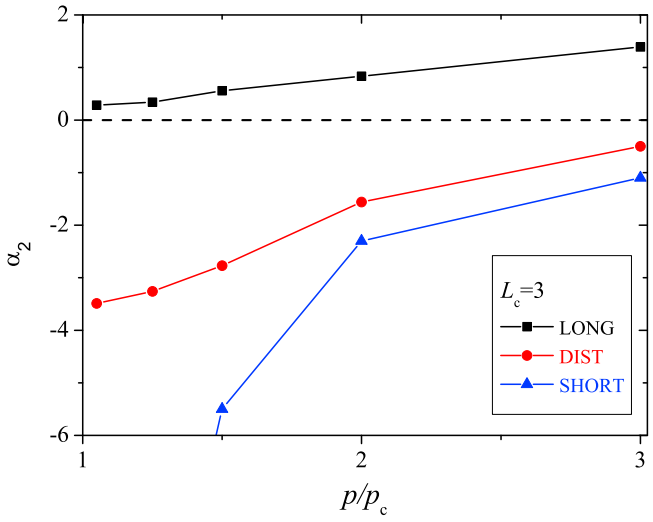

Figure 9. Characteristic permeability correction factor α_2 as a function of the fracture density relative to the percolation threshold.

translates to the variations of α as a function of the fracture closure c_{frac}. Moreover the scaling tendency appears to be very close to $c_{\text{frac}}^{1.75}$ (dashed line compared to data point). Deviations are generally less than 5% and do not go over 10%, which is quite remarkable given the simplicity of the power law model. The case relevant to percolation theory at threshold should be set aside as already discussed in section 5.1. Thus α may be approximated by:

$$\alpha(c_{\text{frac}}) \approx \alpha_2 \left(\frac{c_{\text{frac}}}{2}\right)^{1.75} \tag{20}$$

where we have chosen to relate the characteristic amplitude of α to its value $\alpha_2 = \alpha(c_{\text{frac}} = 2)$.

6. Discussion

[54] The correction factor α may be interpreted as the correction that should be applied to the network permeability by using equations (19) and (20), to account for aperture distributions within fracture planes, without modeling them explicitly:

$$\begin{aligned} &\text{if } \alpha > 0 \text{ then} && \langle K_{N+F}\rangle = \langle K_N\rangle \left\langle \frac{K_F}{K_0}\right\rangle \left(1 + \alpha_2 (c_{\text{frac}}/2)^{1.75}\right) \\ &\text{otherwise} && \langle K_{N+F}\rangle = \langle K_N\rangle \left\langle \frac{K_F}{K_0}\right\rangle \frac{1}{\left(1 - \alpha_2 (c_{\text{frac}}/2)^{1.75}\right)} \end{aligned} . \tag{21}$$

α_2 can be considered to fully characterize the interaction between fracture and network scale heterogeneities. When $\alpha_2 = 0$, the full medium permeability can be directly written as the network permeability times the mean equivalent fracture permeability ratio $\langle K_{N+F}\rangle = \langle K_N\rangle\langle K_F/K_0\rangle$. In other word, fracture-scale and network-scale effects on the equivalent permeability are completely decoupled in this case. Such a situation occurs for example when networks are made up of a small number of long fractures (LONG) with a cut-off scale sufficiently small compared to the system scale. This is typically a situation where homogenization is expected to be closely verified. When density increases, α_2 becomes positive as the network structure can offer bypasses to some of the smallest permeability areas. In most cases, the correction (21) should be applied to the simple decomposition into network-scale and fracture-scale permeabilities.

[55] We interpret α_2 as the upscaling parameter characterizing the effect of the network topology on the upscaling of permeability, from its fracture scale measure and up to the DFN's equivalent permeability in the same spirit as the power-averaging exponent ω [*de Dreuzy et al.*, 2010; *Desbarats*, 1992; *Renard and de Marsily*, 1997; *Ronayne and Gorelick*, 2006]. ω was initially defined to describe in a compact way the upscaling law for a lognormal distribution of local permeabilities as a function of the Euclidean dimension of the embedding space [*Desbarats*, 1992; *Matheron*, 1967]. ω ranges between -1 (harmonic average) and 1 (arithmetic average), corresponding respectively to a purely system in series and a purely parallel system. Upscaling in 1D is performed by the harmonic mean ($\omega = -1$), in 2D by the geometrical mean ($\omega = 0$), and in 3D it is very close to $\omega = 1/3$. A non integer value like 1/3 indicates that the organization of the flow paths occurs more in parallel than in series and that the upscaling can be straightforwardly expressed as a well-defined composition of the arithmetic and geometric average. α_2 and ω operate on different types of local permeability distributions, which are the lognormal distribution for ω and a truncated Gaussian for α_2, as well as by their range of variations: while ω is limited in the interval $[-1, 1]$, α_2 can take a much larger range of values. But one can draw a formal analogy between them along the two following lines: (i) They both express upscaling laws in a compact way. When ω and α_2 are negative, upscaling results in permeability decrease, and conversely when ω and α_2 are positive. (ii) Most importantly, they do not depend on the magnitude of the local permeability distribution (c_{frac} here, for α_2), but only on the structural properties of the system such as the Euclidean dimension for ω and the topological structure of the fracture network for α_2. (iii) When $\langle K_{N+F}/K_N\rangle > \langle K_F/K_0\rangle$, α_2 is positive and the organization of fluxes among various fractures is more in parallel than in series, as when ω is positive, so that on the one hand the network structure enhances the effective permeability from fracture to network scale, and on the other hand the system permeability will typically be sensitive to the mean medium properties (fracture density, cut-off scale). Conversely, when $\langle K_{N+F}/K_N\rangle < \langle K_F/K_0\rangle$, α_2 is negative and the organization of fluxes is more in series than in parallel, as is the case when ω is negative. Consequently, the network structure then reduces the effective permeability from the fracture scale to the network scale, and the system permeability will be more sensitive to local values of permeabilities and especially to those around connectivity constrictions. In summary, α_2 is a quantitative measure of how the two competing effects previously observed in section 5.2 balance each other; it offers an alternative to ω for these types of local permeability distributions that are properly described neither by harmonic averages, nor by geometric averages.

[56] Going more into details, we relate the variations of α_2 to key geometrical characteristics of the fracture and network structures. First, when α_2 is positive, it increases monotonically with the fracture density whatever the type of fracture length distribution (Figure 9). Higher fracture densities offer

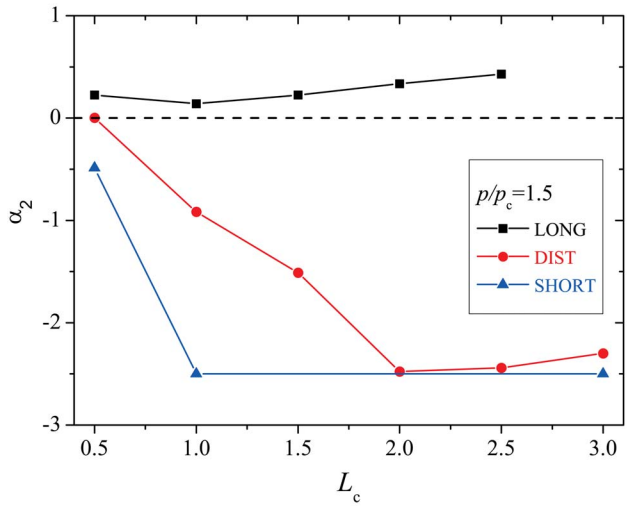

Figure 10. Characteristic permeability modification factor α_2 as a function of the cutoff scale L_c.

more parallel paths that can act as alternatives to paths that necessarily contain small local permeabilities. At the fracture scale, high transmissive areas of typical size L_c may fully bridge the characteristic flow distance within the fracture. We shall denote this scale d_I. On the flow structure presented in the right middle row of Figure 7, d_I would be taken as the mean distance between fracture intersections (thick black segments) along the main flow channels. If this definition is conceptually intuitive, a proper derivation of d_I would be difficult. It is however straightforward that d_I is inversely proportional to the fracture density and that the bridging effect previously described depends on the ratio L_c/d_I. The increase of L_c/d_I promotes the development of highly permeable paths that exploit only the high permeability zones of the fractures. This is a typically a positive correlation effect on the global flow between the fracture- and network-scales.

[57] Sections 5.1 and 5.2 have revealed the existence of another effect linked to the lengths of the fracture intersection. Fracture intersections falling into closed areas have a major effect on the connection probability at the percolation threshold. If this effect is minor on the permeability of DFNs that are at the percolation threshold, it becomes more important for those that are above threshold, because it induces hydraulic disconnection of otherwise geometrically connected paths. The induced permeability reduction depends on the ratio of the mean fracture intersection length l_I to the cutoff-scale L_c. Both effects cumulate in the DIST case while only the second one is active in the LONG case, which explains the stronger impact of the fracture density on α_2 in the DIST case (Figure 9).

[58] Both effects may however lead to different sensitivity of the correction factor α_2 to the cutoff length L_c, as evidenced in Figure 10. For DFNs of type SHORT (blue triangles), the sharp reduction of permeability when the fracture length becomes larger than the cut-off length L_c comes from the second disconnecting effect (decrease of l_I/L_c). It also dominates in DFNs of type DIST for $L_c < 2 = L/5$ (Figure 10, red disks). In this case, which is the most realistic with respect to modeling a geological medium, α_2 decreases regularly to nearly 0 as L_c is decreased to 0.5 = L/20. This means that if the medium size is 20 times larger than the correlation length, the coupling between fracture-scale and network-scale flow heterogeneities is weak. For these DIST configurations and for $L_c > 2$, in contrast, variations are reversed with a slight but genuine increase of α_2 that is likely to be due to the first bridging gap effect controlled by L_c/d_I. For DFNs of type LONG, α_2 mostly increases, also as a consequence of the "bridging gap" effect (Figure 10, black squares).

[59] The disconnecting effect highlights the importance of the correlation between the aperture field and the position of the fracture intersections within the corresponding fracture plane. Larger apertures at fracture intersections might sharply enhance network permeability and should be investigated using the available experimental means [e.g., *Detwiler et al.*, 1999; *Pyrak-Nolte and Morris*, 2000]. The bridging gap effect highlights the importance of the fracture network structure, and in particular of its correlation pattern. The spatial distribution of the fracture centers is not Poissonian [*Bour and Davy*, 1999; *Darcel et al.*, 2003a]. The mechanical constraints imposed externally on and induced internally by fracture intersections generate more complex correlation structures that result in relatively dense but poorly connected networks [*Davy et al.*, 2010]. Under those assumptions, which are more complex than the ones upon which we have based the present study, the flow distribution is expected to be broader and the hydraulically active scale between fracture intersections, d_I, to be strongly influenced accordingly.

7. Conclusions

[60] We have developed a model to study the combined effect of fracture scale heterogeneity and network topology on the equivalent permeability of a fractured medium. At the fracture scale, local apertures are distributed according to a truncated Gaussian distribution and spatially correlated according to a self-affine pattern with an upper cutoff scale L_c. The ratio of the local aperture variance to its mean, denoted as the fracture closure c_{frac}, is the key parameter that controls the heterogeneity of local permeabilities at the fracture scale. At the network scale, the network topology is described both by a fracture length distribution and by a fracture density. We have considered a wide range of densities, ranging from sparse networks close to the percolation threshold to dense networks well above the threshold, and various networks with highly differing topologies, consisting either of fractures much smaller than the network scale L, much longer than L or of a full distribution of fracture sizes between $L/10$ and L. Flow simulations were performed first on single fractures to obtain a reference for permeability upscaling and second at the network scale using numerical methods that account for complex three-dimensional network geometries. Because of the numerous sources of complexity, we performed an extensive sampling of the parameter space with 100 to 1000 Monte-Carlo replicas for each parameter set, which amounts to around two million simulations altogether. We have also set up a methodology that optimizes the analysis of the combined effect of the fracture- and network-scale complexity by systematically comparing the same network structures with and without heterogeneity in the local fracture apertures (i.e., fracture wall roughness).

[61] At the fracture scale, we have shown that the distribution of local apertures systematically induces a reduction

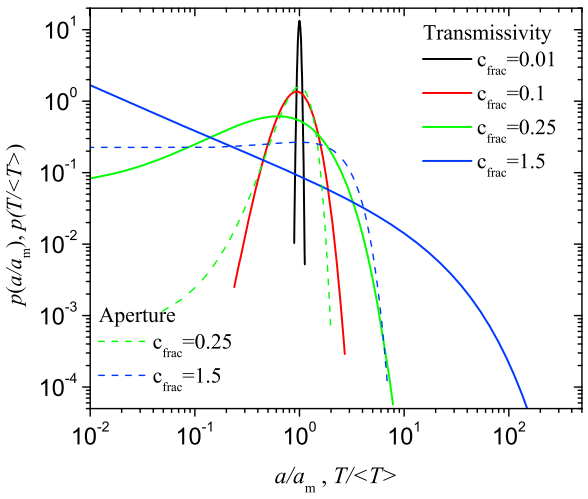

Figure A1. Aperture- and transmissivity- distributions within a fracture shown as dashed and solid lines, respectively, for various levels of fracture closure.

of the mean equivalent permeability because of the higher probability of generating obstacles than channels, in full consistency with previous studies performed for narrower ranges of heterogeneities [*Méheust and Schmittbuhl*, 2000, 2003]. The maximum reduction of the mean equivalent permeability remains limited to a factor of 2 to 6, depending mostly on the ratio of the fracture scale to the self-affinity cutoff scale, while the local transmissivity distribution spans several orders of magnitude. The restricted range covered by the reduction of equivalent permeability compared to the widely distributed local transmissivities is a remarkable property of the fracture transmissivity field.

[62] At the network scale, the equivalent permeability was found to be either larger or smaller than its fracture scale counterpart. By systematically studying the network-scale permeability with reference to the permeability of the corresponding network of parallel plate fractures, we investigated the cumulative effect of fracture heterogeneity and network topology. For most of the configurations studied, the permeability of a network consisting of rough fractures cannot be simply obtained as the product of (i) the permeability of a network consisting of the same fractures but without any wall roughness and (ii) a correction factor accounting for the typical permeability reduction of a single fracture when taking its local aperture heterogeneities into account. In other words, there is a significant coupling between flow heterogeneities at the fracture scale and flow heterogeneities at the network scales. A consequence of that coupling is that for a given network topology, in many cases, the DFN's equivalent permeability will not be properly predicted by a simulation where each fracture is modeled as a parallel plate with a given permeability. However, when the system size is larger than about 20 times the correlation length L_c, this coupling is found to be weak; for a correlation length given as a property of the rough fractures, this fixes the range of system sizes for which it is important to take fracture scale heterogeneities into account: at very large scales, DFNs of parallel plates with the proper hydraulic aperture distribution are a proper hydraulic description of the fractured medium.

[63] The enhancement or reduction of the impact of fracture wall roughness on permeability when upscaling from the fracture scale toward the network scale is measured by the correction factor α, which means that α quantifies the above mentioned coupling. Enhancement is found to occur for dense systems and for network of long fractures. Reduction occurs for networks that are closer to the percolation threshold and for network of small fractures. The correction (either enhancement or reduction) factor α appears to depend on the fracture closure c_{frac} according to a power law dependence of exponent close to 1.75. Thanks to this simple dependence, flow upscaling from the fracture-scale up to the network scale can be fully characterized by the correction factor α_2, defined as the enhancement or reduction factor α at $c_{\text{frac}} = 2$. α_2 is a quantitative measure that is analogous to the more classical power-averaging exponent ω in this case, for which the local transmissivity distribution neither has a harmonic average nor a geometric average. A systematic analysis of α_2 as a function of the model parameters showed that the flow upscaling is governed by two competing effects. On the one hand, the network permeability is lowered by the disconnection effect that consists in fracture intersections falling inside closed or low transmissive areas. The permeability reduction increases with the ratio of the characteristic distance between intersections within the flow structure to the aperture cutoff scale. On the other hand, the network permeability is enhanced by the existence of high permeability zones within the fractures that can bridge the portion of a fracture plane between intersections with hydraulically active fractures. The permeability enhancement then increases with the ratio of the cutoff scale L_c to the characteristic distance between fracture intersections.

[64] In further studies, we plan to extend our investigations to other controlling factors including shear displacement of the fractures, which results in a fracture-scale permeability anisotropy that is potentially correlated to the fracture orientation; more generally we shall study how an anisotropic mechanical load impacts the permeability of the entire medium through its effect on fracture-scale heterogeneity.

Appendix A: Illustration of Local Aperture and Transmissivity Distributions

[65] Figure A1 displays the distribution of aperture normalized by its mechanical aperture, $a_m = \sigma_a/c_{\text{frac}}$, and the distribution of local transmissivities T, normalized by its characteristic value $\langle T\rangle = \beta a_m = \beta(\sigma_a/c_{\text{frac}})^3$. It appears that the relative transmissivity distribution (solid lines) is much wider than the aperture distribution (dashed lines) for not too small values of c. For c approximately larger than 1, the transmissivity distribution is a power law of exponent $-2/3$ truncated by a fast decreasing exponential as shown by equation (8). Because the power law exponent is larger than -1, the mean and standard deviation of the relative positive permeability values $\mu(T/\langle T\rangle)$ and $\sigma(T/\langle T\rangle)$ are dominated by the larger normalized permeability values (Figure A2), where $\langle T\rangle$ is the average value of the truncated transmissivity distribution. It explains the strong increase of the transmissivity distribution's width with c_{frac} (Figure A1). The standard deviation of the aperture distribution becomes larger than its mean when c_{frac} becomes larger than about 0.35. The mean

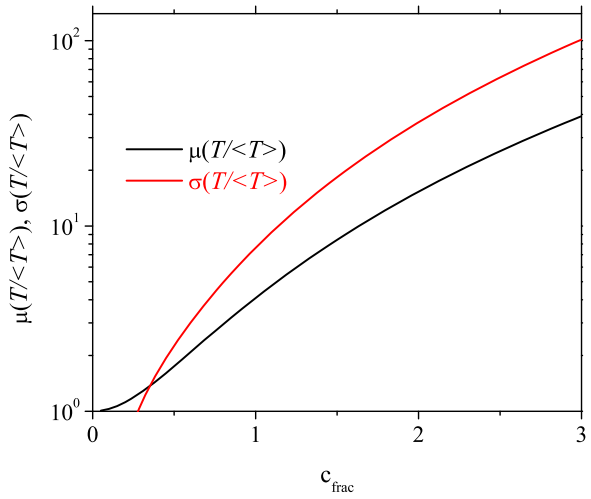

Figure A2. Mean and standard deviation of the local truncated fracture transmissivity distribution as a function of the a priori fracture closure c_{frac}.

and standard deviation increase by one and a half to two orders of magnitude for c_{frac} ranging from 0.35 to 2.5.

Appendix B: Fracture Network Generation

[66] In order to generate random DFNs, with various probability laws modeling the geometry and the physical properties, we developed a specific tool [*Erhel et al.*, 2009b, 2011], with streams of random numbers generated by the RngStream package [*L'Ecuyer et al.*, 2002], and input and output parameters described in XML files. This generic tool allows also running multiparametric simulations with a large number of samples. It provides simulation results for each sample as well as statistical results. The software MP_FRAC uses this tool extensively, whereas computational geometry is handled by the CGAL package (CGAL, Computational Geometry Algorithms Library, http://www.cgal.org). Currently, MP_FRAC can simulate steady state flow with various types of boundary conditions.

[67] The simulation domain has been set to a cube of edge length L. Fracture centers are generated within the domain uniformly by imposing uniform distributions of their coordinates in the three directions. The power law fracture length distribution is sampled by the inverse probability integral transform, which consists in sampling and then inverting the cumulative probability distribution. The orientation distribution of fracture normal vectors is generated by the rejection sampling method. Points are uniformly generated in a unit cube, accepted if within the unit sphere and then projected on the sphere to give the direction normal to the fracture plane [*de Dreuzy et al.*, 2000].

Appendix C: Fracture Aperture Distributions

[68] The aperture field for each fracture is generated on a square grid, in the Fourier domain: its Fourier transform is defined as $\tilde{a}(\mathbf{k}) = \sqrt{S(k)}\,\exp(i\varphi(\mathbf{k}))$, where $S(k)$ is a power spectrum in the form expressed by equation (5) and $\varphi(\boldsymbol{k})$ is a phase that is drawn randomly from a uniform distribution on the $[0; 2\pi]$ interval for all wave vectors pertaining to one half of the Fourier space, and set to $\varphi(\mathbf{k}) = -\varphi(-\mathbf{k})$ on the other half. The random phase definition ensures that the inverse Fourier transform, a, of the complex function $\tilde{a}$ be real in the space domain.

[69] At this point, the mean value of the aperture field is subtracted from it, and the whole field is scaled so as to ensure an overall standard deviation as defined by equation (4). It is then added a constant shift corresponding to the desired mechanical aperture $a_m = \sigma_a/c_{frac}$. Finally, all negative values of the local apertures are set to a very small value. That very

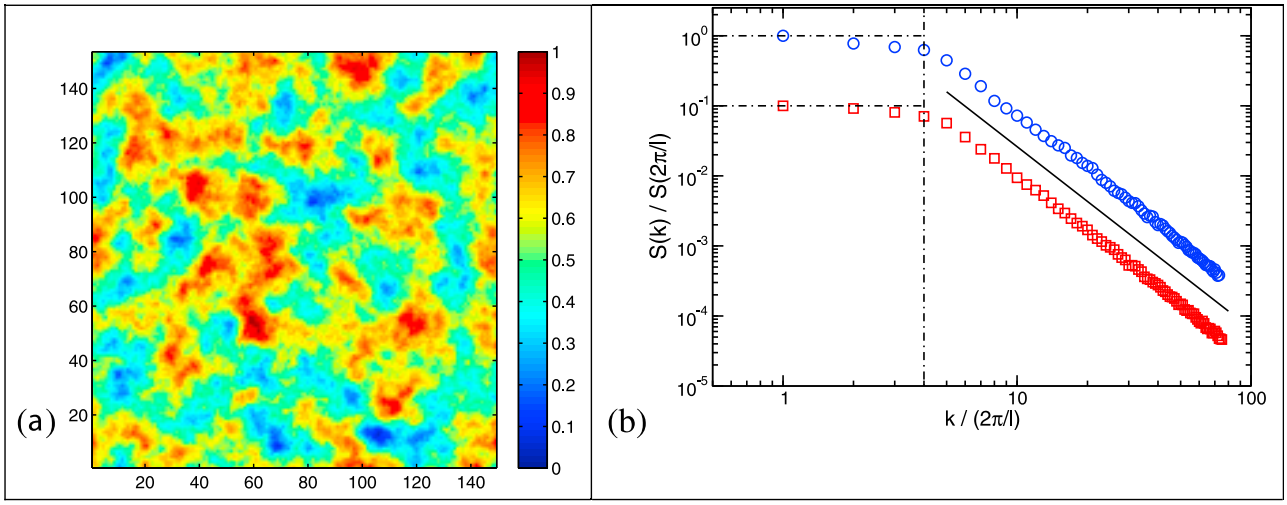

Figure C1. (a) Local aperture field within a large fracture for which the correlation length L_c is a fourth of the fracture size L_f. The relative closure is $c_{frac} = 1/4$ so that no closed region exists in the fracture plane; the aperture field has been normalized by its largest local maximum value. (b) Corresponding average power spectral densities of horizontal (in blue) and vertical (in red) topographic profiles; the red plot has been scaled by a factor 1/10 for clarity; the black solid line represents a power law behavior of exponent −2.60, corresponding to a Hurst exponent $H = 0.80$.

small value is chosen differently depending on the type of simulations that are performed: in the study of the permeability at the fracture scale (section 4 below) the aperture of the closed zones is set to the mean aperture divided by 10^{10}; for the flow simulation in the full DFN network (section 5), it is set to the mean aperture divided by 10^4. Figure C1a provides a representation of such an aperture field ($L_c = L_f/4$ and $a_m = 4\sigma_a$), in which the colormap is mapped to local apertures: there is hardly any closed region in that case (c_{frac} = 0.25) of the fracture plane appear in dark blue while the largest local aperture appears in bright red. It appears clearly on the topographic map that correlated low- or high- aperture regions do not extend along the fracture plane over lengths larger than L_c. The corresponding spectral densities for horizontal and vertical profiles of the topography, averaged over all profiles, are shown in Figure C1b; they agree well with equation (5), which validates the generation scheme.

[70] In the network simulations, the aperture field of a given fracture is first generated on a fine square grid and then interpolated on the triangular unstructured mesh of the fracture within the network. The square grid step is chosen twice finer than the triangle characteristic scale, and averaging of apertures is performed over the grid cells of the regular grid embedded within each triangle.

[71] **Acknowledgments.** J.-R. de Dreuzy acknowledges the European Union for its additional funding through the IEF Marie-Curie fellowship (PIEF-GA-2009-251710). Additional funding was provided by the French National Research Agency ANR through the H2MNO4 project for the development of simulation methods (ANR-MN-2012-).

References

Acuna, J. A., and Y. C. Yortsos (1995), Application of fractal geometry to the study of networks of fractures and their pressure transient, *Water Resour. Res.*, *31*(3), 527–540, doi:10.1029/94WR02260.

Ambegaokar, V., et al. (1971), Hopping conductivity in disordered systems, *Phys. Rev., B, Solid State*, *4*(8), 2612–2620, doi:10.1103/PhysRevB.4.2612.

Baghbanan, A., and L. R. Jing (2007), Hydraulic properties of fractured rock masses with correlated fracture length and aperture, *Int. J. Rock Mech. Min. Sci.*, *44*(5), 704–719, doi:10.1016/j.ijrmms.2006.11.001.

Balberg, I., et al. (1984), Excluded volume and its relation to the onset of percolation, *Phys. Rev. B*, *30*(7), 3933–3943, doi:10.1103/PhysRevB.30.3933.

Barker, J. A. (1988), A generalized radial flow model for hydraulic test in fractured rock, *Water Resour. Res.*, *24*(10), 1796–1804, doi:10.1029/WR024i010p01796.

Bear, J., et al. (1993), *Flow and Contaminant Transport in Fractured Rock*, Academic, San Diego, Calif.

Bonnet, E., et al. (2001), Scaling of fracture systems in geological media, *Rev. Geophys.*, *39*(3), 347–383, doi:10.1029/1999RG000074.

Bouchaud, E., et al. (1990), Fractal dimension of fractured surfaces: A universal value?, *Europhys. Lett.*, *13*, 73–79, doi:10.1209/0295-5075/13/1/013.

Bour, O., and P. Davy (1998), On the connectivity of three dimensional fault networks, *Water Resour. Res.*, *34*(10), 2611–2622, doi:10.1029/98WR01861.

Bour, O., and P. Davy (1999), Clustering and size distributions of fault patterns: Theory and measurements, *Geophys. Res. Lett.*, *26*(13), 2001–2004, doi:10.1029/1999GL900419.

Brezzi, F., and M. Fortin (1991), *Mixed and Hybrid Finite Element Methods*, Springer, Berlin, doi:10.1007/978-1-4612-3172-1.

Brown, S. (1987), Fluid flow through rock joints: The effect of surface roughness, *J. Geophys. Res.*, *92*(B2), 1337–1347, doi:10.1029/JB092iB02p01337.

Brown, S. R. (1995), Simple mathematical model of rough fracture, *J. Geophys. Res.*, *100*(B4), 5941–5952, doi:10.1029/94JB03262.

Brown, S. R., and C. H. Scholz (1985), Broad bandwidth study of the topography of natural rock surfaces, *J. Geophys. Res.*, *90*, 12,575–12,582, doi:10.1029/JB090iB14p12575.

Brown, S. R., et al. (1986), Correlation between the surfaces of natural rock joints, *Geophys. Res. Lett.*, *13*(13), 1430–1433, doi:10.1029/GL013i013p01430.

Brown, S. R., et al. (1995), Applicability of the Reynolds equation for modeling fluid flow between rough surfaces, *Geophys. Res. Lett.*, *22*(18), 2537–2540, doi:10.1029/95GL02666.

Cacas, M. C., et al. (1990a), Modeling fracture flow with a stochastic discrete fracture network: Calibration and validation: 1. The flow model, *Water Resour. Res.*, *26*(3), 479–489.

Cacas, M. C., et al. (1990b), Modeling fracture flow with a stochastic discrete fracture network: Calibration and validation: 2. The transport model, *Water Resour. Res.*, *26*(3), 491–500.

Cappa, F., et al. (2006), Hydromechanical modelling of pulse tests that measure fluid pressure and fracture normal displacement at the Coaraze Laboratory site, France, *Int. J. Rock Mech. Min. Sci.*, *43*(7), 1062–1082, doi:10.1016/j.ijrmms.2006.03.006.

Cello, P. A., et al. (2009), Flow dimension and anomalous diffusion of aquifer tests in fracture networks, *Vadose Zone J.*, *8*(1), 258–268, doi:10.2136/vzj2008.0040.

Charlaix, E., et al. (1987), Permeability of a random array of fractures of widely varying apertures, *Transp. Porous Media*, *2*, 31–43, doi:10.1007/BF00208535.

Clauser, C. (1992), Permeability of crystalline rock, *Eos Trans. AGU*, *73*(21), 233, doi:10.1029/91EO00190.

Cook, N. G. W. (1992), Natural joints in rock: Mechanical, hydraulic and seismic behavior and properties under normal stress, *Int. J. Mech. Min. Sci. Geomech. Abstr.*, *29*(3), 198–223, doi:10.1016/0148-9062(92)93656-5.

Darcel, C., et al. (2003a), Cross-correlation between length and position in real fracture networks, *Geophys. Res. Lett.*, *30*(12), 1650, doi:10.1029/2003GL017174.

Darcel, C., et al. (2003b), Stereological analysis of fractal fracture networks, *J. Geophys. Res.*, *108*(B9), 2451, doi:10.1029/2002JB002091.

Davis, T. A., and I. S. Duff (1999), A combined unifrontal multifrontal method for unsymmetric sparse matrices, *Trans. Math. Software*, *25*(1), 1–20, doi:10.1145/305658.287640.

Davy, P., et al. (2006a), Flow in multiscale fractal fracture networks, *Geol. Soc. Spec. Publ.*, *261*, 31–45.

Davy, P., et al. (2006b), A note on the angular correction applied to fracture intensity profiles along drill core, *J. Geophys. Res.*, *111*, B11408, doi:10.1029/2005JB004121.

Davy, P., et al. (2010), A likely universal model of fracture scaling and its consequence for crustal hydromechanics, *J. Geophys. Res.*, *115*, B10411, doi:10.1029/2009JB007043.

de Dreuzy, J.-R., and P. Davy (2007), Relation between fractional flow models and fractal or long-range 2-D permeability fields, *Water Resour. Res.*, *43*, W04431, doi:10.1029/2006WR005236.

de Dreuzy, J. R., et al. (2000), Percolation threshold of 3D random ellipses with widely scattered distributions of eccentricity and size, *Phys. Rev. E*, *62*(5), 5948–5952, doi:10.1103/PhysRevE.62.5948.

de Dreuzy, J. R., et al. (2001a), Advective transport in the percolation backbone in two dimensions, *Phys. Rev. E*, *64*, 056305.

de Dreuzy, J. R., et al. (2001b), Hydraulic properties of two-dimensional random fracture networks following a power law length distribution: 2. Permeability of networks based on log-normal distribution of apertures, *Water Resour. Res.*, *37*(8), 2079–2095, doi:10.1029/2001WR900010.

de Dreuzy, J. R., et al. (2001c), Hydraulic properties of two-dimensional random fracture networks following a power law length distribution: 1. Effective connectivity, *Water Resour. Res.*, *37*(8), 2065–2078.

de Dreuzy, J. R., et al. (2002), Permeability of 2D fracture networks with power-law distributions of length and aperture, *Water Resour. Res.*, *38*(12), 1276, doi:10.1029/2001WR001009.

de Dreuzy, J.-R., et al. (2004a), Influence of spatial correlation of fracture centers on the permeability of two-dimensional fracture networks following a power law length distribution, *Water Resour. Res.*, *40*, W01502, doi:10.1029/2003WR002260.

de Dreuzy, J. R., et al. (2004b), Anomalous diffusion exponents in continuous two-dimensional multifractal media, *Phys. Rev. E*, *70*(1), 016306, doi:10.1103/PhysRevE.70.016306.

de Dreuzy, J.-R., et al. (2010), Use of power-averaging for quantifying the influence of structure organization on permeability upscaling, *Water Resour. Res.*, *46*, W08519, doi:10.1029/2009WR008769.

de Dreuzy, J.-R., et al. (2012), Synthetic benchmark for modeling flow in 3D fractured media, *Comput. Geosci.*, doi:10.1016/j.cageo.2012.07.025, in press.

Dershowitz, W. S., and C. Fidelibus (1999), Derivation of equivalent pipe networks analogues for three-dimensional discrete fracture networks by the boundary element method, *Water Resour. Res.*, *35*(9), 2685–2691, doi:10.1029/1999WR900118.

Desbarats, A. J. (1992), Spatial averaging of transmissivity in heterogeneous fields with flow toward a well, *Water Resour. Res.*, *28*(3), 757–767, doi:10.1029/91WR03099.

Detwiler, R. L., et al. (1999), Measurement of fracture aperture fields using transmitted light: An evaluation of measurement errors and their influence on simulations of flow and transport through a single fracture, *Water Resour. Res.*, *35*(9), 2605–2617, doi:10.1029/1999WR900164.

Durham, W. B. (1997), Laboratory observations of the hydraulic behavior of a permeable fracture from 3800 m depth in the KTB pilot hole, *J. Geophys. Res.*, *102*(B8), 18,405–18,416, doi:10.1029/96JB02813.

Durham, W. B., and B. P. Bonner (1995), Closure and fluid flow in discrete fractures, in *Fractured and Jointed Rock Masses*, edited by L. R. Myer et al., pp. 441–446, A. A. Balkema, Rotterdam, Netherlands.

Erhel, J., et al. (2009a), Flow simulation in three-dimensional discrete fracture networks, *SIAM J. Sci. Comput.*, *31*(4), 2688–2705, doi:10.1137/080729244.

Erhel, J., et al. (2009b), A parallel scientific software for heterogeneous hydrogeology, in *Parallel Computational Fluid Dynamics 2007*, *Lect. Notes in Comput. Sci. and Eng.*, vol. 67, pp. 39–48, Springer, Berlin.

Erhel, J., et al. (2011), Multi-parametric intensive stochastic simulations for hydrogeology on a computational grid, in *Parallel Computational Fluid Dynamics*, *Lect. Notes in Comput. Sci. and Eng.*, vol. 74, pp. 389–397, Springer, Berlin.

Frampton, A., and V. Cvetkovic (2007), Upscaling particle transport in discrete fracture networks: 1. Nonreactive tracers, *Water Resour. Res.*, *43*, W10428, doi:10.1029/2006WR005334.

Frampton, A., and V. Cvetkovic (2009), Significance of injection modes and heterogeneity on spatial and temporal dispersion of advecting particles in two-dimensional discrete fracture networks, *Adv. Water Resour.*, *32*(5), 649–658, doi:10.1016/j.advwatres.2008.07.010.

Glover, P. W. J., et al. (1998), Synthetic rough fractures in rocks, *J. Geophys. Res.*, *103*(B5), 9609–9620, doi:10.1029/97JB02836.

Hamzehpour, H., et al. (2009), Percolation and permeability of networks of heterogeneous fractures, *Phys. Rev. E*, *79*(3), 036302.

Hoshen, J. (1997), Percolation and cluster structure parameters: The enhanced Hoshen-Kopelman algorithm, *Phys. Rev. E*, *56*(2), 1455–1460, doi:10.1103/PhysRevE.56.1455.

Hsieh, P. A. (1998), Scale effects in fluid flow through fractured geological media, in *Scale Dependence and Scale Invariance in Hydrology*, pp. 335–353, Cambridge Univ. Press, Cambridge, U. K., doi:10.1017/CBO9780511551864.013.

Hsieh, P. A., et al. (1993), Methods of characterizing fluid movement and chemical transport in fractured rock, in *Field Trip Guidebook for Northeastern United States*, edited by J. T. Cheney and J. C. Hepburn, pp. R1–R30, Geol. Soc. of Am., Boulder, Colo.

Hunt, A. G., and G. W. Gee (2002), Application of critical path analysis to fractal porous media: Comparison with examples from the Hanford site, *Adv. Water Resour.*, *25*(2), 129–146, doi:10.1016/S0309-1708(01)00057-4.

Isakov, E., et al. (2001), Fluid flow through rough fractures in rocks I: High resolution aperture determinations, *Earth Planet. Sci. Lett.*, *191*(3–4), 267–282, doi:10.1016/S0012-821X(01)00424-1.

Ji, S. H., et al. (2011), Influence of fracture connectivity and characterization level on the uncertainty of the equivalent permeability in statistically conceptualized fracture networks, *Transp. Porous Media*, *87*(2), 385–395, doi:10.1007/s11242-010-9690-9.

Johnson, K. L. (1985), *Contact Mechanics*, Cambridge Univ. Press, Cambridge, U. K.

Jourde, H., et al. (2007), Relationship between the geometrical and structural properties of layered fractured rocks and their effective permeability tensor. A simulation study, *J. Hydrol.*, *337*(1–2), 117–132, doi:10.1016/j.jhydrol.2007.01.027.

Kalbacher, T., et al. (2007), Geometric modelling and object-oriented software concepts applied to a heterogeneous fractured network from the Grimsel rock laboratory, *Computat. Geosci.*, *11*(1), 9–26, doi:10.1007/s10596-006-9032-8.

Le Borgne, T., et al. (2004), Equivalent mean flow models for fractured aquifers: Insights from a pumping tests scaling interpretation, *Water Resour. Res.*, *40*, W03512, doi:10.1029/2003WR002436.

L'Ecuyer, P., et al. (2002), An object-oriented random-number package with many long streams and substreams, *Oper. Res.*, *50*(6), 1073–1075, doi:10.1287/opre.50.6.1073.358.

Le Goc, R., et al. (2010), Statistical characteristics of flow as indicators of channeling in heterogeneous porous and fractured media, *Adv. Water Resour.*, *33*(3), 257–269, doi:10.1016/j.advwatres.2009.12.002.

Lenti, V., and C. Fidelibus (2003), A BEM solution of steady-state flow problems in discrete fracture networks with minimization of core storage, *Comput. Geosci.*, *29*(9), 1183–1190, doi:10.1016/S0098-3004(03)00140-7.

Leung, C. T. O., and R. W. Zimmerman (2010), Estimating the hydraulic conductivity of two-dimensional fracture networks using effective medium theory and power-law averaging, in *Rock Mechanics in Civil and Environmental Engineering*, pp. 243–246, CRC Press, Boca Raton, Fla.

Long, J. C. S., and P. A. Witherspoon (1985), The relationship of the degree of interconnection to permeability in fracture networks, *J. Geophys. Res.*, *90*(B4), 3087–3098, doi:10.1029/JB090iB04p03087.

Long, J. C. S., et al. (1982), Porous media equivalents for networks of discontinuous fractures, *Water Resour. Res.*, *18*(3), 645–658, doi:10.1029/WR018i003p00645.

Long, J. C. S., et al. (1985), A model for steady fluid flow in random three-dimensional networks of disc-shaped fractures, *Water Resour. Res.*, *21*(8), 1105–1115, doi:10.1029/WR021i008p01105.

Maryka, J., et al. (2004), Numerical simulation of fracture flow with a mixed-hybrid FEM stochastic discrete fracture network model, *Comput. Geosci.*, *8*(3), 217–234.

Matheron, G. (1967), *Eléments Pour une Théorie des milieux Poreux*, Masson, Paris.

Méheust, Y., and J. Schmittbuhl (2000), Flow enhancement of a rough fracture, *Geophys. Res. Lett.*, *27*(18), 2989–2992, doi:10.1029/1999GL008464.

Méheust, Y., and J. Schmittbuhl (2001), Geometrical heterogeneities and permeability anisotropy of rough fractures, *J. Geophys. Res.*, *106*(B2), 2089–2102, doi:10.1029/2000JB900306.

Méheust, Y., and J. Schmittbuhl (2003), Scale effects related to flow in rough fractures, *Pure Appl. Geophys.*, *160*(5–6), 1023–1050, doi:10.1007/PL00012559.

Mettier, R., et al. (2006), Influence of small-scale heterogeneities on contaminant transport in fractured crystalline rock, *Ground Water*, *44*(5), 687–696, doi:10.1111/j.1745-6584.2006.00236.x.

Mustapha, H. (2005), Simulation numérique de l'écoulement dans des milieux fracturés tridimensionnels, PhD thesis, Univ. of Rennes 1, Rennes, France.

National Research Council (1996), *Rock Fractures and Fluid Flow*, Natl. Acad. Press, Washington, D. C.

Neuman, S. P. (2005), Trends, prospects and challenges in quantifying flow and transport through fractured rocks, *Hydrogeol. J.*, *13*(1), 124–147, doi:10.1007/s10040-004-0397-2.

Noetinger, B., and N. Jarrige (2012), A quasi steady state method for solving transient Darcy flow in complex 3D fractured networks, *J. Comput. Phys.*, *231*(1), 23–38, doi:10.1016/j.jcp.2011.08.015.

Nordqvist, A. W., et al. (1996), Effects of high variance of fracture transmissivity on transport and sorption at different scales in a discrete model for fractured rocks, *J. Contam. Hydrol.*, *22*(1–2), 39–66, doi:10.1016/0169-7722(95)00064-X.

Painter, S., and V. Cvetkovic (2005 Upscaling discrete fracture network simulations: An alternative to continuum transport models, *Water Resour. Res.*, *41*, W02002, doi:10.1029/2004WR003682.

Park, Y.-J., et al. (2001), Transport and intersection mixing in random fracture networks with power law length distributions, *Water Resour. Res.*, *37*(10), 2493–2501, doi:10.1029/2000WR000131.

Persson, B. N. J. (2001), Elastoplastic contact between randomly rough surfaces, *Phys. Rev. Lett.*, *87*(11), 116101, doi:10.1103/PhysRevLett.87.116101.

Persson, B. N. J., F. Bucher, and B. Chiaia (2002), Elastic contact between randomly rough surfaces: Comparison of theory with numerical results, *Phys. Rev. B*, *65*(18), 184106, doi:10.1103/PhysRevB.65.184106.

Pichot, G., et al. (2010), A mixed hybrid mortar method for solving flow in discrete fracture networks, *Appl. Anal.*, *89*(10), 1629–1643, doi:10.1080/00036811.2010.495333.

Pichot, G., et al. (2012), Flow simulation in 3D multi-scale fractured networks using non-matching meshes, *SIAM J. Sci. Comput.*, *34*(1), B86–B105.

Piggot, A. R. (1997), Fractal relations for the diameter and trace length of disc-shaped fractures, *J. Geophys. Res.*, *102*(B8), 18,121–18,125.

Poirriez, B. (2011), Étude et mise en oeuvre d'une méthode de sous-domaines pour la modélisation de l'écoulement dans des réseaux de fractures en 3D, PhD thesis, Univ. of Rennes 1, Rennes, France.

Power, W. L., and W. B. Durham (1997), Topography of natural and artificial fractures in granitic rocks: Implications for studies of rock friction and fluid migration, *Int. J. Rock Mech. Min. Sci.*, *34*(6), 979–989, doi:10.1016/S1365-1609(97)80007-X.

Pyrak-Nolte, L. J., and J. P. Morris (2000), Single fractures under normal stress: The relation between fracture specific stiffness and fluid flow, *Int. J. Rock Mech. Min. Sci.*, *37*(1–2), 245–262.

Raviart, P. A., and J. M. Thomas (1977), A mixed finite element method for second order elliptic problems, in *Mathematical Aspects of the Finite Element Method*, *Lect. Notes in Math.*, vol. 606, pp. 292–315, Springer, New York, doi:10.1007/BFb0064470.

Renard, P., and G. de Marsily (1997), Calculating equivalent permeability: A review, *Adv. Water Resour.*, *20*(5–6), 253–278, doi:10.1016/S0309-1708(96)00050-4.

Ronayne, M. J., and S. M. Gorelick (2006), Effective permeability of porous media containing branching channel networks, *Phys. Rev. E*, *73*(2), 026305, doi:10.1103/PhysRevE.73.026305.

Rubin, Y., and S. Hubbard (2006), *Hydrogeophysics*, Springer, Dordrecht, Netherlands.

Sahimi, M. (1993), Flow phenomena in rocks: From continuum models to fractals, percolation, cellular automata, and simulated annealing, *Rev. Mod. Phys.*, *65*(4), 1393–1534, doi:10.1103/RevModPhys.65.1393.

Schmittbuhl, J., et al. (1993), Field-measurements of the roughness of fault surfaces, *Geophys. Res. Lett.*, *20*(8), 639–641, doi:10.1029/93GL00170.

Schmittbuhl, J., et al. (1995), Scaling invariance of crack surfaces, *J. Geophys. Res.*, *100*(B4), 5953–5973, doi:10.1029/94JB02885.

Segall, P., and D. D. Pollard (1983), Joint formation in granitic rock of the Sierra-Nevada, *Geol. Soc. Am. Bull.*, *94*(5), 563–575, doi:10.1130/0016-7606(1983)94<563:JFIGRO>2.0.CO;2.

Snow, D. T. (1969), Anisotropic permeability of fractured media, *Water Resour. Res.*, *6*, 1273–1289, doi:10.1029/WR005i006p01273.

Stauffer, D., and A. Aharony (1992), *Introduction to Percolation Theory*, 2nd ed., Taylor and Francis, Bristol, U. K.

Talon, L., et al. (2010a), Permeability estimates of self-affine fracture faults based on generalization of the bottleneck concept, *Water Resour. Res.*, *46*, W07601, doi:10.1029/2009WR008404.

Talon, L., et al. (2010b), Permeability of self-affine aperture fields, *Phys. Rev. E*, *82*(4), 046108, doi:10.1103/PhysRevE.82.046108.

Thompson, M. E. (1991), Numerical simulation of solute transport in rough fractures, *J. Geophys. Res.*, *96*(B3), 4157–4166, doi:10.1029/90JB02385.

Thompson, M., and S. Brown (1991), The effect of anisotropic surface-roughness on flow and transport in fractures, *J. Geophys. Res.*, *96*(B13), 21,923–21,932, doi:10.1029/91JB02252.

Tsang, C.-F., and I. Neretnieks (1998), Flow channeling in heterogeneous fractured rocks, *Rev. Geophys.*, *36*(2), 275–298, doi:10.1029/97RG03319.

Vohralik, M., et al. (2007), Mixed and nonconforming finite element methods on a system of polygons, *Appl. Numer. Math.*, *57*(2), 176–193, doi:10.1016/j.apnum.2006.02.005.

Wellman, T. P., et al. (2009), Effects of simplifying fracture network representation on inert chemical migration in fracture-controlled aquifers, *Water Resour. Res.*, *45*, W01416, doi:10.1029/2008WR007025.

Witherspoon, P., et al. (1979), Observations of a potential size effect in experimental determination of the hydraulic properties of fractures, *Water Resour. Res.*, *15*(5), 1142–1146, doi:10.1029/WR015i005p01142.

Witherspoon, P. A., et al. (1980), Validity of cubic law for fluid-flow in a deformable rock fracture, *Water Resour. Res.*, *16*(6), 1016–1024, doi:10.1029/WR016i006p01016.

Yeh, T. C. J., and S. Y. Liu (2000), Hydraulic tomography: Development of a new aquifer test method, *Water Resour. Res.*, *36*(8), 2095–2105, doi:10.1029/2000WR900114.

Zimmerman, R. W., and G. S. Bodvarsson (1996a), Hydraulic conductivity of rock fractures, *Transp. Porous Media*, *23*(1), 1–30, doi:10.1007/BF00145263.

Zimmerman, R. W., and G. S. Bodvarsson (1996b), Hydraulic conductivity of rock fractures, *Transp. Porous Media*, *23*, 1–30.

Zimmerman, R. W., and G. S. Bodvarsson (1996c), Effective transmissivity of two-dimensional fracture networks, *Int. J. Mech. Min. Sci. Geomech. Abstr.*, *33*(4), 433–438, doi:10.1016/0148-9062(95)00067-4.

Environmental Science & Technology

Article

pubs.acs.org/est

Mixing and Reaction Kinetics in Porous Media: An Experimental Pore Scale Quantification

Pietro de Anna,[†,‡] Joaquin Jimenez-Martinez,[†] Hervé Tabuteau,[§] Regis Turuban,[†] Tanguy Le Borgne,[†] Morgane Derrien,[†] and Yves Méheust*[,†]

[†]Géosciences Rennes, UMR 6118, CNRS, Université de Rennes 1, Rennes, France

[‡]Massachusetts Institute of Technology, Boston, Massachusetts, United States

[§]IPR, Université Rennes 1 - CNRS, UMR 6251, Campus Beaulieu, F-35042 Rennes, France

Supporting Information

ABSTRACT: We propose a new experimental set up to characterize mixing and reactive transport in porous media with a high spatial resolution at the pore scale. The analogous porous medium consists of a Hele-Shaw cell containing a single layer of cylindrical solid grains built by soft lithography. On the one hand, the measurement of the local, intrapore, conservative concentration field is done using a fluorescent tracer. On the other hand, considering a fast bimolecular reaction $A + B \rightarrow C$ occurring as A displaces B, we quantify the rate of product formation from the spatially resolved measurement of the pore scale reaction rate, using a chemiluminescent reaction. The setup provides a dynamical measurement of the local concentration field over 3 orders of magnitude and allows investigating a wide range of Péclet and Damköhler numbers by varying the flow rate within the cell and the local reaction rate. We use it to study the kinetics of the reaction front between A and B. While the advection-dispersion (Fickian) theory, applied at the continuum scale, predicts a scaling of the cumulative mass of product C as $M_C \propto \sqrt{t}$, the experiments exhibit two distinct regimes in which the produced mass M_C evolves faster than the Fickian behavior. In both regimes the front rate of product formation is controlled by the geometry of the mixing interface between the reactants. Initially, the invading solute is organized in stretched lamellae and the reaction is limited by mass transfer across the lamella boundaries. At longer times the front evolves into a second regime where lamellae coalesce and form a mixing zone whose temporal evolution controls the rate of product formation. In this second regime, the produced mass of C is directly proportional to the volume of the mixing zone defined from conservative species. This interesting property is indeed verified from a comparison of the reactive and conservative data. Hence, for both regimes, the direct measurement of the spatial distribution of the pore scale reaction rate and conservative component concentration is shown to be crucial to understanding the departure from the Fickian scaling as well as quantifying the basic mechanisms that govern the mixing and reaction dynamics at the pore scale.

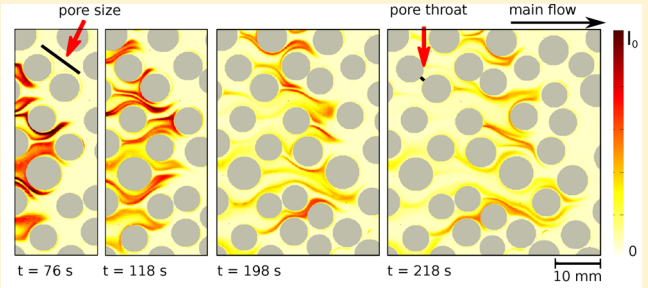

field of light intensity produced by cheminoluminescent reactions between reactants

1. INTRODUCTION

Chemical reactions govern various systems, and play a central role in to many medical and industrial applications (e.g., reactive transport in the subsurface and biological activity in living tissues[1,2]). While in well mixed reactors the kinetics are fully controlled by chemical processes, in many real situations spatial heterogeneities lead to a complex temporal evolution of the system kinetics, which depend on the transport and mixing mechanisms.[3,4] Mixing is the ensemble of processes by which substances originally segregated into different volumes of space tend to occupy the same common volume.[5] The physical processes responsible for mixing at the hydrodynamical scale are advection and molecular diffusion. In porous media, heterogeneous advection acts to spread the solutes in the local direction of the flow while diffusion tends to homogenize their spatial distribution (e.g., refs 6−10).

At the continuum scale classical descriptions of transport and mixing in porous media consist in modeling effective transport by the same theoretical framework as pore scale (diffusive) transport. The interaction between heterogeneous advection and diffusion at the pore scale are lumped in a dispersion coefficient. That dispersion coefficient describes the effective mixing processes of the solute (e.g., refs 7,11, and 12), and is obtained by upscaling of the pore scale information to the Darcy scale, for example using volume averaging (e.g., refs 13 and 14) or homogenization (e.g., ref 15) techniques. However, medium heterogeneities lead to a distortion of the solute plume that, for times smaller than the typical transport time over a

Received: July 21, 2013
Revised: November 18, 2013
Accepted: November 25, 2013
Published: November 25, 2013

typical heterogeneity scale, increases the solute's spreading but not its degree of mixing. Thus, in general, these coupled processes of spreading and mixing need to be studied in a different manner.[10,16,17,42,43] The kinetics of reactive systems resulting from mixing in heterogeneous media can then be very different from the one derived from Fickian theories, as observed not only for porous media,[7,18−24,47] but also for a wide range of disordered and fractal systems,[25] Rayleigh-Taylor systems,[26] turbulent and chaotic flows,[1,3] homogeneous systems with the presence of stochastic fluctuations[27,28] and planar fractures.[29] Nevertheless, the impact of incomplete mixing processes and non Fickian dispersion on the effective reaction kinetics is still an open issue (e.g., ref 10).

Quantification of the degree of local mixing is a key to understanding and predicting the fate of chemical reactions whose kinetics are fast enough to be limited by mixing processes. For those systems, it is necessary to assess the local concentration fields within the porous space, at the hydrodynamic (or local) scale.[7,43] Dynamical visualization techniques have been developed to study mixing in continuous media (e.g., turbulence[30] or population dynamics of plankton in oceanic flows[1]). For porous media, that are discontinuous and characterized by the no-slip boundary conditions at solid−liquid interface, averaged concentration fields have been often evaluated experimentally through the Beer−Lambert law and colorimetry techniques applied to the light that has traveled through a bead pack representing an analogous porous medium (e.g., refs 7 and 31). The concentration of transported fluorescent colloids has also been inferred from their measured fluorescence (e.g., ref 18). Those techniques quantify the local concentration fields averaging over several pore size and, thus, cannot capture the incomplete mixing eventually present within the pores. Few experimental techniques have been developed to measure the local concentration fields and mass of reaction product (e.g., ref 19) in steady state conditions within the pores.[42] The main goal of the present work is to develop a method to perform dynamical pore scale measurements of local concentration fields and reaction rates. We thus measure the kinetics of an irreversible fast bimolecular reaction $A + B \rightarrow C$ taking place at the front between the reactants, one displacing the other, in a ($2d$) porous medium.

The analogous porous medium consists of a Hele-Shaw cell containing a single layer of cylindrical solid grains. The radii and positions of the grains along the plates are fully controlled: by using a technique common in microfluidics, we reproduce a numerical model defined at will. To assess the local concentration field of a passive scalar we consider a fluorescent tracer and we relate the local concentration to the measure of the light emitted by the stimulated tracer via a calibration process with known concentrations. To quantify the local kinetics of a mixing-limited bimolecular irreversible reaction $A + B \rightarrow C$, we resort to the fast chemiluminescent reaction described by Jonsson and Irgum:[32] for each reaction of a molecule of A with a molecule of B, a photon is emitted. The amount of light detected per unit time is, thus, proportional to the amount of reactions that have taken place. We show the relationship between the rate of product formation and the local mixing properties of the reactants, which are controlled by transport within the pores of the considered heterogeneous medium. The assessments of (i) local mixing and (ii) rate of product formation are done in two independent experiments. The findings from the two experiments, which are respectively the time evolution of the mixing volume and that of global rate of product formation, are successfully related to each other. Note that the extrapolation of the results obtained from micromodel experiments to the field is not direct in general. However, this represents a first modeling step in the development of a theoretical framework that shall quantify the impact of incomplete mixing conditions on reaction kinetics. This will provide scaling laws linking the microscale processes to the Darcy scale behavior, which is relevant to large scale modeling and applications (e.g., ref 10).

2. THEORETICAL FRAMEWORK FOR MIXING AND REACTION AT THE PORE SCALE

We consider a $2d$ medium composed of a polydispersed population of n_g randomly distributed circular grains with mean porosity ϕ. Its geometry is characterized by two length scales, the average pore throat h and the average pore size ξ (see figure in the first page). The former represents the smaller gap where a solute plume is forced to pass, while the latter is the average distance between two consecutive pore throats connected by the flow.

The flow of an incompressible fluid is described by its local velocity field $\mathbf{v}$, which is given by the continuity equation (mass conservation), $\nabla \cdot \boldsymbol{v} = \mathbf{0}$ and the momentum conservation, that is, the Navier−Stokes equation. We assume that the $2d$ porous medium is horizontal: the flow velocities are parallel to the horizontal plane and, thus, gravity does not impact them. We define the Reynolds number as $Re = \overline{v}h/\nu$, where ν is the kinematic viscosity of the fluid and $\overline{v}$ is the average flow velocity. It compares the characteristic ratio of the inertial forces in the longitudinal direction (within the pores) to the viscous forces that tend to homogenize momentum in the transverse direction (within the pore throats), for the flow of a Newtonian fluid. At low Reynolds numbers, typical of porous media, the momentum conservation for stationary conditions leads to the Stokes (laminar) flow. As a consequence of the no-slip boundary conditions at the grain walls, the velocity field of a liquid flowing through a porous medium is typically characterized by the existence of a braided network of preferential flow paths in channels, as well as low velocity or stagnation zones (e.g., ref 22).

The medium of volume V is initially saturated with a solution B, with a spatially homogeneous concentration c_0. At time $t = 0$, another solution A, also of uniform concentration c_0, starts to be injected continuously through the inlet boundary ($x = 0$). The two solutions A and B are fully miscible, and their contact front coincides initially with the inlet boundary (grains excluded), of length l_0. As solutions are transported in the medium, at the front between A and B, solution mixing takes place. The reaction between the chemicals A and B is considered bimolecular and irreversible.

We define the Péclet number by $Pe = \overline{v}(h/2)^2/(2D\xi)$. It is the ratio of the characteristic diffusion time over half a pore throat $\tau_D = (h/2)^2/(2D)$ to the characteristic advection time over a typical pore length $\tau_a = \xi/\overline{v}$. The reaction time scale is defined by the kinetics in well-mixed conditions $\tau_r = 1/(c_0 k)$.[33] The ratio of advection to reaction time scales is the Damköhler number $Da = \tau_a/\tau_r$. We consider the case of a reaction that is quasi-instantaneous with respect to advective mechanisms: $Da \gg 1$. In other words, once the reactants are locally mixed, they are chemically depleted in a very short time and reactions stop: only the occurrence of further mixing will allow reactions to take place again.

dx.doi.org/10.1021/es403105b | Environ. Sci. Technol. 2014, 48, 508−516

A global measure of the chemical kinetics can be given in terms of the temporal scaling of the total mass of C present in the system at instant t:

$$M_C(t) = \int_V \mathrm{d}\boldsymbol{x} c_C \tag{1}$$

Well Mixed Reactant. Classical approaches consider A and B well mixed within the pores and consequently describe transport at the continuum scale as one-dimensional along the main flow direction (x).[34] In this framework the solute dispersion is described in terms of concentration fields $\overline{c}_i$ that are averaged over the elementary representative volume, larger than a single pore. The time evolution of these locally averaged concentrations undergoing reactions and transport is then described by a unidimensional advection-dispersion-reaction equation.[14] The average concentration is then advected by the constant Darcy velocity (that is, the fluid velocity defined at the continuum scale) and follows a Fickian spreading described in terms of an effective dispersion coefficient D^* that is the sum of the molecular diffusion coefficient and of the longitudinal hydrodynamic dispersion coefficient. Assuming that the support volume, larger than the single pore, is well mixed, the reaction rates are given by the mass action law $r_i^* = -k\overline{c}_A\overline{c}_B$ for $i = A, B$ and $r_C^* = -k\overline{c}_A\overline{c}_B$.[7,9,10] In this framework, the total mass of C present at instant t in the system is [7]

$$M_C(t) = c_0\sqrt{\frac{2\sigma^2}{\pi}} = c_0\sqrt{\frac{4D^*t}{\pi}} \tag{2}$$

where $\sigma^2 = 2D^*t$ is the spatial variance of a solute plume undergoing Fickian conservative transport. The nature of such a Fickian scaling law is intimately related to the complete mixing condition assumed at the pore scale. To capture, describe and predict the deviation of real systems from the model of eq 2, we shall assume that the support scale at which the transported chemicals are well mixed is much smaller than the pore scale.

Imperfectly Mixed Reactants. As discussed in ref 38 and summarized in the following, the global kinetics of the system is determined by the evolution of the mixing interface between the two chemicals. This interface Ξ between A and B is stretched by the flow field heterogeneity and develops a lamella-like topology[5,35−37] (see also the case of a conservative tracer transported in a heterogeneous porous medium as in Figure 2). A recent numerical study on pore scale mixing has shown that until those lamellae start interacting with each other, the length Σ of Ξ evolves linearly in time as $l_0(1 + \gamma t)$, where l_0 is its initial length and γ the so-called stretching rate.[38] Since the considered reaction is fast compared to transport mechanisms, the mass of A that by diffusion crosses the interface instantaneously reacts to form C, whose kinetics follows

$$\frac{\mathrm{d}M_C(t)}{\mathrm{d}t} = D\int_\Xi |\nabla c_A|\mathrm{d}\Sigma \approx Dl_0c_0\frac{(1+\gamma t)}{s(t)} \tag{3}$$

where $\Sigma = l_0(1+\gamma t)$ is the length of the interface Ξ, s its width and $|\overline{\nabla c}| \sim c_0/s$ is the average gradient across the reactants interface. The dynamics of s is controlled by the competition between stretching and diffusion:

$$s = s_0\sqrt{\frac{3\beta - 2 + 2(1+\gamma t)^3}{3\beta(1+\gamma t)^2}} \tag{4}$$

with $\beta = (s_0^2\gamma)/D$ and $s_0 = s(0)$, as discussed in refs 39 and 38. The lamellae width s decreases until compression and diffusive growth equilibrate: afterwards, the width s grows diffusively as $s \propto \sqrt{t}$.

The behavior described by eqs 3 and 4 is in fact valid until the time t^* at which the lamellae of the interface Ξ begin to interact with each other by diffusion. Their coalescence process leads to the formation of aggregate lamellae bundles,[37] so that the evolution of the interface length Σ is no longer linear in time. In this coalescence regime, the role of individual lamella is no longer dominant and the rate of product formation is simply controlled by the growth of the mixing volume V_m, defined as the portion of the system where a conservative component $c_R = c_A + c_C$ transported by the flow varies between the injected value and zero:[38]

$$M_C(t) \propto V_m \tag{5}$$

3. MATERIALS AND METHODS

3.1. Porous Medium Design: Use of the Soft Lithography Technique. We have prepared a synthetic $2d$ porous medium containing $n_g = 244$ grains, of size $S = 160$ mm in the longitudinal (main flow) direction and 100 mm in the transverse one, and characterized by a porosity $\phi = 0.55$ (see inset of Figure 1a). The device used to model the described porous medium is a Hele-Shaw cell consisting of two parallel transparent plates separated by cylindrical impermeable pillars, representing the grains of the porous medium. To build this device, we use the lithographic technique described in references 40 and 41 where two rectangular glass plates of the same size are superposed and positioned with a uniform separation distance a. Note that techniques aimed at building a $2d$ porous medium with precise given geometric characteristics have been used earlier,[44,45] but soft lithography, developed in the last 10 years mostly in the field of microfluidics, is of much easier use since it does not require a laser nor the motors to drive the photochemical reactor with high accuracy. A mask with the negative image of the chosen geometry is printed at a high resolution, here 128 000 dots per inch (DPI), on a transparent film (photomask). The porous space is represented by a single black cluster containing transparent disks that correspond to the grains. This film is placed on top of the two glass plates, the space between which is filled with a UV-sensitive glue. This glue, Norland Optical Adhesive 81, is sensitive to the entire range of long wavelength from 320 to 400 nm, with a peak sensitivity around 365 nm. A collimated light source (ThorLabs M365L2) that emits a UV beam of wavelengths limited to a sharp window peaked at 365 nm at 1 mW, is placed at a distance of 23 cm from the two glass plates and along a direction perpendicular to the mask (see Figure 1a inset). Irradiating the glue in between the glass plates through the photomask for a controlled time results in photo-polymerization of the glue in the regions where the UV light has been allowed to pass, as shown in Figure 1a. After flooding out the liquid glue remaining in the porous space, we obtain solid cylindrical grains consisting of a hard polymer. This technique provides full control on the geometry of the produced medium (here, the position and size of the cylinders).

Placing the UV source at a distance of 23 cm from the target, we measured a homogeneous power per unit surface of 0.6 ± 0.1 mW/cm^2 over an area of 15×15 cm^2. In order to obtain cylinders with sharp boundaries, the UV-light exposure time τ_{exp} was optimized: for the thickness $a = 1$ mm exposed to a UV

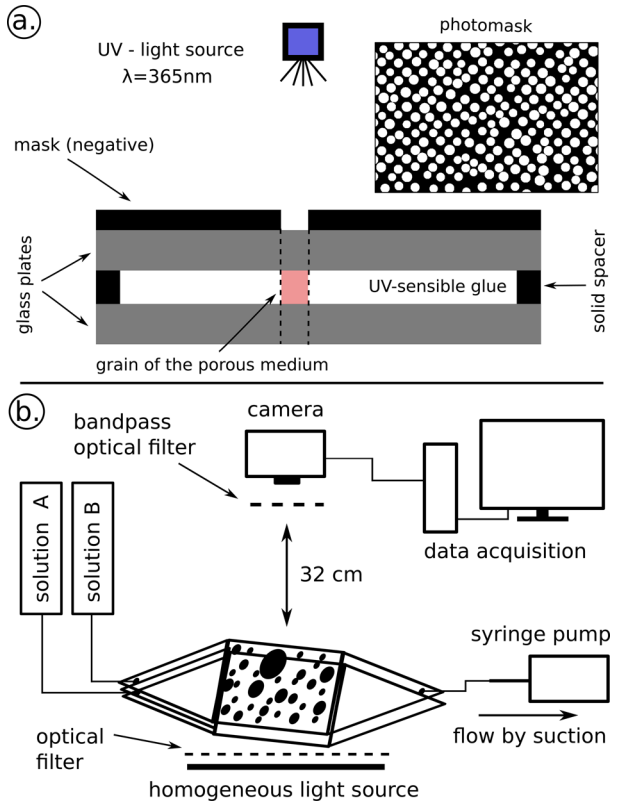

Figure 1. a. Principle of the soft lithography technique. The two glass plates are separated by a distance a = 1 mm. The photomask (inset) is placed on top of the two plates. The space between them is filled with a liquid UV-sensitive glue. The light coming from the collimated 365 nm UV source passes through the transparent disks in the mask, polymerizing the glue and giving rise to solid grains. b. A scheme of the experimental setup. A solution A is continuously injected in the porous medium saturated with a solution B through suction by a syringe pump. A homogeneous radiation of light excites the fluorescent tracer transported within the pores. A first filter in between the light source and the cell removes all wavelengths that are typical of the fluorescent emission. A second filter in front of the camera selects only the light emitted by the tracer. For the quantification of rate of product formation we use the same setup, removing the light source and the optical filters.

radiation dose of 0.6 ± 0.1 mW/cm^2, we obtained τ_{exp} = 95 s. The cure time τ_{exp} is dependent on the needed dose of radiation and thus on the light intensity and the thickness of the glue, which in our case coincides with the distance a between the glass plates. The cure time is also slightly dependent on the age of the glue. Thus, for every lithography process that was carried out, τ_{exp} was reoptimized.

Once the grains are produced in between the glass plates, two opposite sides of the chamber are sealed using the same glue as above. The other two opposite sides will constitute the inlet and the outlet of the set up. The injection system is shown schematically in Figure 1b: via two inlet points on two separate superposed prisms (one for each injected substance), the flow is carried out homogeneously in the chamber. In this way the two different injected solutions will mix only inside the porous medium. The flow velocities within such a chamber placed horizontally are not impacted by body forces, and are consequently parallel to the plane of the chamber. They are controlled locally, due to the no-slip boundary conditions, by the smallest distance between neighboring solid walls. In this case, the wall to wall distances that control the flow are the thickness of the Hele-Shaw cell (distance between the horizontal glass plates), a, and the widths of the pore throats, the average value of which is $h \sim 1$ mm. If the cell is very thin compared to the average pore throat, $a \ll h$, then the vertical profile of the flow will be parabolic, while in the other direction it will correspond to a plug flow[46] and the flow field heterogeneity in most of the porous volume will remain moderate. In particular, for Hele-Shaw flow the fluid shear will mostly occur in the vertical direction, except in narrow limit layers close to the cylinders' walls, so that hydrodynamic dispersion will be less efficient in the medium. To avoid this condition, we set the cell thickness to $a \simeq h$, a = 1 mm.

3.2. Characterization of Passive Scalar Transport. We impose a controlled flow rate Q between the inlet and outlet boundaries of the cell using a syringe pump (*Harvard Apparatus PHD 2000*), by suction. We use a glass syringe of 50 mL (Tomopal Inc.). Once the cell, the injection system and all the pipes have been fully saturated with clear water, a solution of Fluorescein (Fluorescein sodium salt) of concentration c_0 = 255 mg/L is injected. The injection system is schematically shown in Figure 1 b. A point injection is homogeneously transferred to the inlet opening of the chamber via two superposed prisms: one dedicated to the injection of clear water and the other to the fluorescent solution. In this way the two different injected solutions will mix only inside the porous medium.

A panel source that produces a spatially homogeneous intensity of light illuminates the porous medium from below. An optical filter (LEE 126 Mauve), positioned between the light panel and the cell, prevents wavelengths in the window $\lambda \in [505-580]$ nm from passing through. The fluorescent tracer, excited by the radiation received at λ = 494 nm, emits photons with a wavelength λ = 521 nm while relaxing to its ground state. The amount of emitted photons is proportional to the number of excited tracer molecules and, thus, to the local tracer concentration. A second filter (Edmund Optics 520 nm CWL, 10 nm Bandwidth), placed in front of a high resolution camera (an actively cooled Princeton Instruments, MegaPlus EP11000), allows only wavelengths in a sharp window with peak at λ = 520 nm ±10 nm to pass.

The camera is placed on top of the porous medium at a distance of 32 cm. We focus the optics onto the cell median horizontal plane, which is located at half the thickness of the porous medium. In the configuration used, the size of a pixel corresponds to 0.043 mm on the porous medium. In absence of fluorescent tracer no light is emitted and the associated value of the intensity detected by the camera, stored in an image, represents the background noise of our measurement. When Fluorescein is present, photons are emitted and some of them detected by the camera: the associated value is in between 0 (or the noise) and $2^{12} - 1$, since the camera has a 12-bit pixel depth. The measurement of the light intensity detected by the camera in each pixel, during the exposure time τ_{exp}, is stored in gray scale images. We take pictures every two seconds while injecting the fluorescent tracer: all images are processed and converted to images of local concentration field (averaged over the pixel size), via the calibration procedure described in detail in the Supporting Information (SI). The calibration procedure is associated to an exposure time value that remained unchanged during the experiment. With this set up the background noise in the intensity measurement is 0.66% of the maximum pixel depth (the average pixel value in the background image is 26 over 4096 channels, 12-bit). This

dx.doi.org/10.1021/es403105b | *Environ. Sci. Technol.* 2014, 48, 508−516

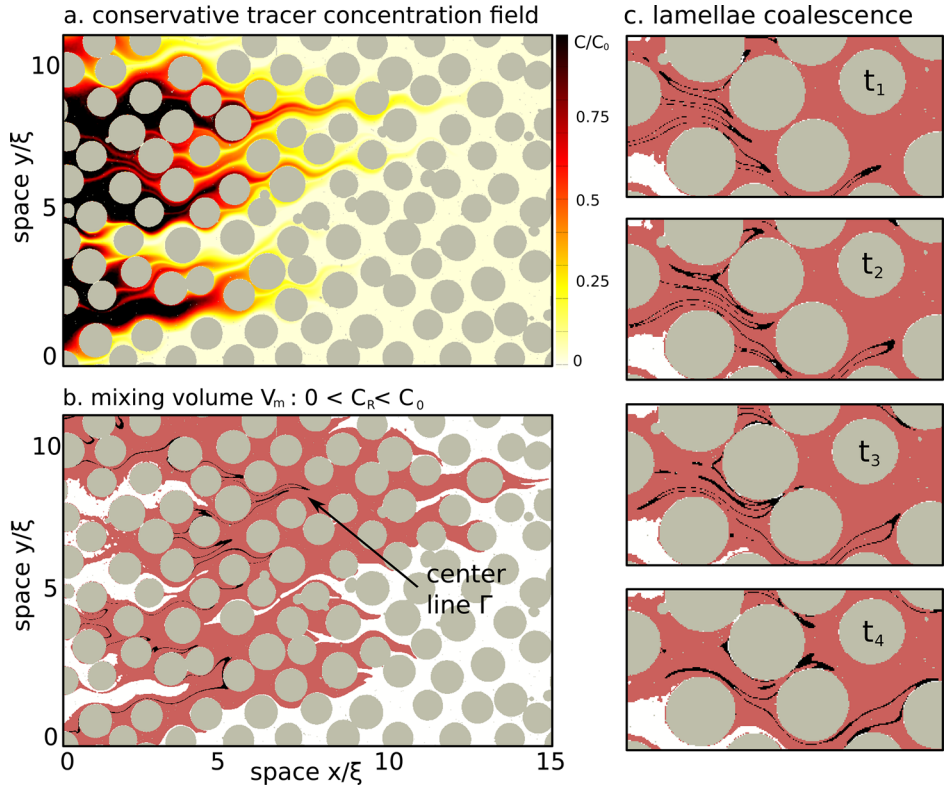

Figure 2. a. the concentration field of the conservative tracer; b. the mixing volume V_m (red area) defined as the volume of the system where $99\%c_0 > c_R > 1\%c_0$. Within the mixing volume, its center line Γ, defined as the points where $49\%c_0 > c_R > 51\%c_0$, is plotted in black. *c*. The coalescence of lamellae is represented by the merging of the centerline in four consecutive snapshots at times t_1 = 290 s, t_2 = 373 s, t_3 = 455 s, and t_4 = 538 s.

implies that the minimum concentration that can be detected, after calibration, is 0.43 mg/L, that is 0.17% of the injected concentration c_0 = 255 mg/L. Thus, this technique provides a spatially resolved detection and quantification of concentrations down to 0.2% of the injected concentration value.

3.3. Characterization of a Reactive Front from the Spatial Distribution of Local Reaction Rates. To quantify the kinetics of the front between two chemicals *A* and *B* we choose two reactants that, when mixed, produce light proportionally to the amount of reactions that take place, a property that is called cheminoluminescence. Each reaction produces a photon. To this end, we use the very fast peroxyoxalate chemiluminescence described in reference 32 where the best combination of reaction speed and intensity of the emitted light is discussed. We use bis(2,4,6-trichlorophenyl)oxalate (TCPO) under the catalytic influence of 1,8-diazabicyclo-[5,4,0]-undec-7-ene (DBU) and 1,2,4-Triazole that when combined with the fluorescent dye 3-aminofluoranthene (3−AFA) and hydrogen peroxide (H_2O_2), will start a chemiluminescent reaction and glow a fluorescent color. In order to reproduce the kinetics $A + B \rightarrow C$ we use the same molar concentration of TCPO and H_2O_2, which are the limiting species of the reaction. Following,[32] we prepare two solutions *A* and *B*. We define *A* as a mixture of a molar concentration of 0.5 mM of DBU, 5 mM of Triazole, 50 nM of 3 − AFA and 1 mM of H_2O_2. We define *B* as a solution of 1 mM of TCPO. The solvent is the same for both solutions, Acetonitrile; at 25 °C it has a dynamic viscosity $\mu = 3.4 \times 10^{-4}$ kg/(m·s), a density ρ = 0.787 kg/m^3 and thus a kinematic viscosity $\nu = 0.45 \times 10^{-4}$ m^2/s. We have successfully tested the resistance of the glue used to produce the cell to this strong solvent for more than 24 h. We assume that the diffusion coefficients of solutions *A* and *B* are identical. Since the molar masses of TCPO (448.90) and Fluorescein (376.28) are of the same order of magnitude, as well as their densities, we assume that the diffusion coefficient of TCPO is the same as the one of Fluorescein in a fluid with the same viscosity as Acetonitrile, $D = 1.6 \times 10^{-3}$ mm^2/s.

The kinetics of the considered reaction can be tuned as described in ref 32 by changing the proportion of the catalysts in the solutions *A* and *B* in order to obtain faster or slower reactions. We define t_r as the characteristic time for the reaction to reduce the emitted light by a factor 10 in a well mixed volume. As discussed in ref 32 for the chemicals chosen and the adopted molar concentrations, t_r is around 2s. In order to study a mixing limited reaction we want to impose that the Damköhler, $Da = \tau_a/\tau_r$, be much larger than 1, thus we will impose a flow rate such that the average velocity $\overline{v}$ over the average pore size ξ = 12 mm be smaller than ξ/τ_r = 6 mm/s.

For the quantification of the rate of product formation we use a sCMOS camera (the Hamamatsu ORCA flash 4.0) that is very sensible to light and has pixel resolution of 16−bit, but a smaller spatial resolution (4 megapixel) compared with the CCD camera used for the conservative tracer concentration measurements. The spatial light distribution recorded in one such picture provides a measurement of the derivative in time of the concentration of the reaction product *C*, that is, dc_C/dt. In addition, at a given time, the overall activity of the reaction can be quantified from the total light intensity detected per unit time, as

$$I(k) = \sum_{ij} P_{i,j}^{(k)}/\tau_k^{\exp} \qquad (6)$$

dx.doi.org/10.1021/es403105b | *Environ. Sci. Technol.* 2014, 48, 508−516

where $P_{i,j}^{(k)}$ is the value of the pixel of coordinate indices (i,j) in the kth image taken and τ_k^{exp} is the exposure time of the camera for that image. This total intensity is proportional to the derivative in time of the total produced mass of the product C.

4. RESULTS AND DISCUSSION

4.1. Solute Tracer Mixing and Dispersion. We measure the evolution of the local concentration field $c_R(x,t)$ of a fluorescent tracer inside the synthetic porous medium. An example of the concentration field measured at a given time is shown in Figure 2.a, and the longitudinal projections of the concentration field are shown in inset of Figure 3 at four

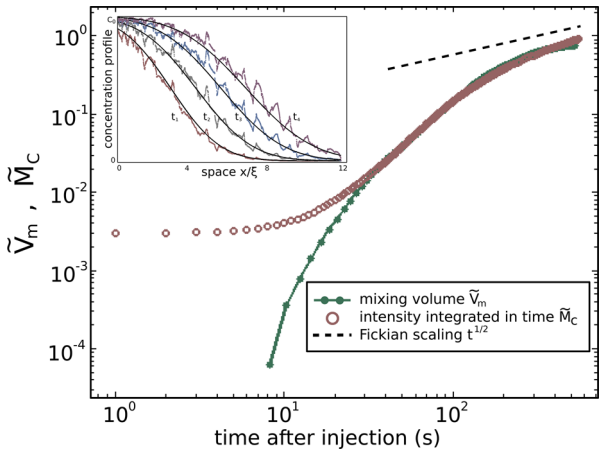

Figure 3. The solid line connecting the dots represents the temporal scaling of the mixing volume $\tilde{V}m = \varepsilon V_m$ that has been rescaled by the arbitrary constant ε, for an imposed flow rate Q = 8.3 mm^3/s. In the coalescence regime it scales as the temporal evolution of the total mass produced by the reaction, rescaled by its value at the end of the experiment: $\tilde{M}_C$, shown as circles. This quantity is given by the temporal integration of eq 6. Note that the mixing volume is rescaled by an arbitrary constant to match the two curves. In the inset: longitudinal projections of the concentration field of the injected conservative tracer (Fluorescein) at four times: t_1 = 290 s, t_2 = 373 s, t_3 = 455 s and t_4 = 538 s. The smooth solid lines represent the analytical solution of eq 7 at the same times.

equispaced times. The data can be fitted well with the analytical solution of a unidimensional advection-dispersion equation (e.g., ref 34):

$$c_R(x,t) = \frac{c_0}{2}\mathrm{erfc}\left(\frac{x-\overline{v}t}{\sqrt{2D^*t}}\right) \quad (7)$$

where the measured average velocity of the front, corresponding to the Darcy velocity, is $\overline{v}$ = 0.21 mm/s, and the dispersion coefficient has been fitted to D^* = 2.15 mm^2/s. A similar result was obtained in ref 7 for conservative transport.

We then measure the mixing volume V_m defined as the ensemble of pixels where the associated value of the concentration field is in between 1% and 99% of c_0. The mixing volume associated to the concentration field snapshot of Figure 2.a is shown in Figure 2.b. The temporal evolution of the mixing volume rescaled by an arbitrary constant, $\tilde{V}_m = \varepsilon V_m$, is shown as a solid line connecting dots in Figure 3. A comparison with the Fickian behavior $t^{1/2}$ shows that mixing is clearly non Fickian over the range of time scales investigated. Thus, the mixing volume cannot be predicted from the knowledge of dispersive spreading alone, as previously observed by the authors of refs 7 and 31 with measurements performed at the Darcy scale. This can be also observed qualitatively from the images of the concentration field in Figure 2.a, which shows that the pores are far from being well mixed.

Superimposed on the image of V_m in Figure 2.b, we have represented by a solid curve the center line Γ of V_m, defined as the ensemble of points at which the concentration field c_R has values between 49% and 51% of c_0. In the right column of Figure 2, we have represented four zoomed snapshots of V_m and its center line Γ. The evolution of this line illustrates the deformation induced by the flow heterogeneity, which creates stretched lamellae that are initially well-defined and separated. As time increases, lamellae undergo a coalescence process to form a larger lamellae bundle. This process is qualitatively similar to that observed in heterogeneous Darcy scale permeability fields.[37] In the following we quantify the impact of these phenomena (lamella stretching and coalescence) in the case where a reaction takes place at the front between two displacing chemicals.

4.2. Control of a Reaction Front by the Dynamics of Mixing. We now present the results obtained from the reactive transport experiments that we performed in the two-dimensional porous medium described in Section 3.1. To test and validate the technique, we have assessed the kinetics of the aforementioned chemicals A and B in a configuration for which the advection-dispersion-reaction equation and eq 2 are a valid description: a cell of thikness a = 1 mm without obstacles, representing a simple planar fracture (see Figure 4). The details of this validation can be found in the SI.

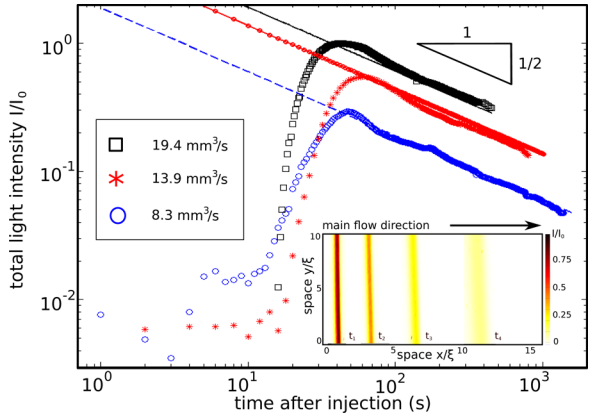

Figure 4. Temporal evolution of the total light intensity as defined in eq 6. The characteristic diffusion time over the half cell aperture, $t_T = (a/2)^2/(2D)$ = 83.3 s, defines the beginning of the Taylor dispersion regime (the impact of vertical gradients on longitudinal dispersion are becoming negligible): it is independent of the imposed flow rate. In the inset: four snapshots of the light intensity detected by the camera at four consecutive times (t_1 = 130s, t_2 = 230s, t_3 = 430s and t_4 = 737s) for flow Q = 8.3 mm^3/s during the reactive front displacement along the planar fracture. See also the SI.

The main physical quantities that characterize these reactive transport experiments performed in the analogous porous medium are summarized in Table 1.

Initially, fingers of the invading chemical penetrate channels between grains. The reaction takes place at the interface Ξ between the two chemicals, whose perimeter is represented in the inset of Figure 6, that is, at the boundaries of the fingers. The interface Ξ is stretched by the flow field heterogeneity, and develops a lamella-like topology. As mentioned previously, this

dx.doi.org/10.1021/es403105b | Environ. Sci. Technol. 2014, 48, 508−516

Table 1. Experimental Conditions of the Conservative and Reactive Experiments, for the Three Investigated Flow Rates: Flow Q, Mean Velocity $\overline{v}$, the Reynolds (c conservative and r reactive case), Péclet, and Damköhler Numbers

Q [mm^3/s]	$\overline{v}$ [mm/s]	Re_c [-]	Re_r [-]	Pe [-]	Da [-]
8.3	0.08	0.08	0.0002	0.54	72
27.8	0.28	0.28	0.0006	1.8	21.6
83.3	0.83	0.83	0.002	5.4	7.2

type of mixing process is known to occur under advection by heterogeneous flows.[5,35−37] At larger times, the lamellae coalesce by diffusion and the reaction occurs over a more dispersed area of the porous space. We quantify the rate of product formation at the heterogeneous front between the two chemicals by measuring the total intensity I, as defined by eq 6, of the light detected per unit time.

The temporal scaling of the light intensity I is shown in Figure 5 (symbols) for three imposed flow rates Q_1 = 8.3 mm^3/s, Q_2 = 27.8 mm^3/s and Q_3 = 83.3 mm^3/s. At all times the temporal scaling of the measured total intensity I is significantly different from the $t^{-1/2}$ behavior predicted by the model of ref 7, which has been validated for the Taylor dispersion case (Hele-Shaw cell without solid grains inside). As suggested by eq 3, in the lamellae stretching regime the reaction rate is directly related to the length Σ_i of the interface Ξ between the two chemicals. We measure the temporal evolution of Σ_i by computing, for each recording time, the perimeter of the area where the reaction takes place, that is, where light is detected, as shown in the inset of Figure 6. This has been done for each investigated flow rate Q_i (i = 1, 2, 3). When lamellae are separated and independent, the interface length Σ grows approximately linearly: $\Sigma_i = l_0(1 + \gamma_i t)$. Figure 6 shows the temporal scaling of the measured $\Sigma_i - \Sigma_i(0)$ for the three flow rates; its temporal behavior is well fitted by $l_0\gamma_i t$, where the stretching rate is fitted for the flow rate Q_2 (γ_2 = 0.6 s^{-1}) and the stretching rates for the two other flow rates are inferred according to $\gamma_1 = (Q_1/Q_2)\gamma_2$ and $\gamma_3 = (Q_3/Q_2)\gamma_2$. The transition

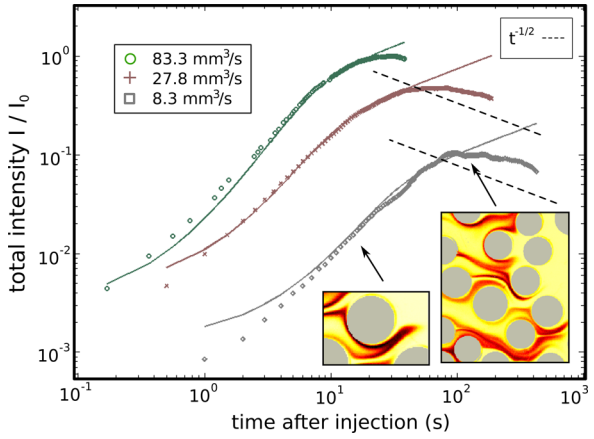

Figure 5. Temporal evolution of the global rate of product formation for three imposed flows. Before the diffusive coalescence of lamellae takes place, the model described by eq 3 predicts the experimental data well. At larger times the rate of product formation decays slower than the Fickian scaling $t^{-1/2}$. In this regime the temporal evolution of M_C is well predicted by the scaling of the mixing volume V_m of a conservative solute, measured independently (see Figure 3).

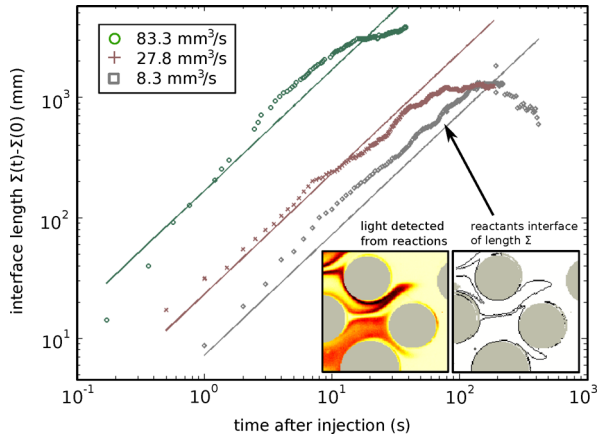

Figure 6. The dots represent the temporal evolution of $\Sigma - \Sigma(0)$, where Σ is the length of the interface between the chemicals A and B, measured as the perimeter of the image portion where light is detected. For each investigated flow rate Q_i (i = 1,2,3) and for times smaller than t^* = 105, 38, and 17 s, respectively, $\Sigma_i - \Sigma(0)$ scales as $l_0\gamma_i t$ (lines). In the inset we show a zoomed-in snapshot of the light detected at the front between the two injected chemicals and of the corresponding perimeter of the zone where reactions take place.

times between the linear and non linear regime for Σ_i are t_1^* = 105 s, t_2^* = 38s and t_3^* = 17s. In this linear stretching regime, the kinetics of the front (symbols in Figure 5) is fully controlled by line stretching and the lamellae width evolution, as described by eq 3 (the solid lines in Figure 5). Note that the value of c_0 is fitted from our measure for the flow 8.3 mm^3/s and used for all the other experiments (without any other fitting parameter). Note also that when replicating an experiment in the same flow conditions, we obtain slightly different spatial configurations of the detected light due to the fact that our control on the initial conditions is not perfect. However, the overall behavior (as quantified by the temporal evolution of the global rate of product formation) results to be the same.

At later times ($t > t^*$), the interface length Σ stops growing linearly and the rate of product formation slows down. Note that in this coalescence regime the temporal scaling of the kinetics decays more slowly than the $t^{-1/2}$ behavior observed in the Taylor-dispersion case. As stated by eq 5, the scaling of the mass production by the reaction in this coalescence regime can be well predicted by the temporal scaling of the mixing volume V_m, which is measured from independent conservative transport experiments (see Figure 3).

In summary, we have considered a situation in which two chemicals, one displacing the other, are mixed within a heterogeneous porous medium and cannot be considered well mixed at the pore scale. The kinetics of the reaction is controlled by the geometry of the interface front between the two chemicals. This geometry has a lamellae-like topology and is controlled by the dynamic competition between advective stretching and molecular diffusion. In a first regime, stretching is dominant and results in a linear growth of the interface length; in a second regime, molecular diffusion promotes the coalescence of lamellae. The global reaction rate measured with our experimental setup is in agreement with the prediction of the model described by eqs 3 and 5 for the stretching and coalescence regime,[38] respectively, that accounts for incomplete mixing at the pore scale. Particularly, in the second (coalescence) regime, the scaling is expected to be directly related to the evolution in time of the mixing volume of a

conservative solute, $V_m(t)$. This is confirmed by a comparison with the $V_m(t)$ measured from an independent experiment addressing conservative transport in the same porous medium. Note that while this conservative transport experiment exhibits Fickian longitudinal dispersion, the rate of product formation shows a non-Fickian behavior characteristic of incomplete mixing at the pore scale.

The experimental technique proposed here allows for the quantification of the local rate of product formation and for the measurement of passive concentration fields at the pore scale. It can be applied to many configurations of mixing and reactive transport in porous media. The more complex three-dimensional case would lead to different reaction front geometries. However, the basic mechanisms that determine the dynamics of the chemical reaction in two dimensions, are the same basic mechanisms that control the reaction dynamics in three dimensions, where the invasion front of the displacing solute is not a diffuse line but a surface, which is stretched and compressed according to the kinematics of the local flow field. In this work we have considered the extreme case of a kinetics that can be considered instantaneous with respect to the mixing mechanisms, but the same technique can be used to study configurations where kinetics and mixing compete. In fact, using a different combination of the catalysts of the chemoluminescent reaction, it is possible to obtain a controlled slower kinetics, as described in ref 32.

■ ASSOCIATED CONTENT

Supporting Information

The Supporting Information details the calibration procedure used in this study to obtain measurement of the concentration field of the considered fluorescent tracer and the validation of the rate of product formation assessment. This material is available free of charge via the Internet at http://pubs.acs.org.

■ AUTHOR INFORMATION

Corresponding Author

*(Y.M.) E-mail: yves.meheust@univ-rennes1.fr.

Notes

The authors declare no competing financial interest.

■ ACKNOWLEDGMENTS

P.d.A. and T.L.B. acknowledge the financial support of the European Commission through FP7 ITN project IMVUL (Grant Agreement 212298) and Marie Curie ERG grant Reactive Flows (Grant Agreement Number 230947). J.J.-M. expresses his gratitude to Fondation Rennes 1 (Chaire Environment et Innovation). Y.M. gratefully acknowledges support from Rennes-Métropole through an A.I.S grant for equipment and from CNRS/INSU under grant number 786971 of the EC2CO program. Jean-Jacques Kermarrec, Pascal Rolland and Alain Faisant are gratefully acknowledged for their contribution in the design of the experiment.

■ REFERENCES

(1) Tel, T.; Demoura, A.; Grebogi, C.; Karolyi, G. Chemical and biological activity in open flows: A dynamical system approach. *Phys. Rep.* **2005**, *413*, 91−196.

(2) Seymour, J. D.; Gage, J. P.; Codd, S. L.; Gerlach, R. Anomalous fluid transport in porous media induced by biofilm growth. *Phys. Rev. Lett.* **2004**, *93*, 198103.

(3) Neufeld, Z.; Hernandez-Garica, E. *Chemical and Biological Processes in Fluid Flows: A dynamical System Approach*; Imperial College Press: London, 2010.

(4) Horsthemke, W.; Fedotov, S.; Mendez, V. *Reaction-Transport Systems*, 1st ed.; Springer: Berlin, 2010.

(5) Ottino, J. *The Kinematics of Mixing: Stretching, Chaos, And Transport*; Cambridge University Press, 1989.

(6) Jha, B.; Cueto-Felgueroso, L.; Juanes, R. Fluid mixing from viscous fingering. *Phys. Rev. Lett.* **2011**, *106*, 194502.

(7) Gramling, C. M.; Harvey, C. F.; Meigs, L. C. Reactive transport in porous media: A comparison of model prediction with laboratory visualization. *Environ. Sci. Technol.* **2002**, *36*, 2508−2514.

(8) De Wit, A. Fingering of chemical fronts in porous media. *Phys. Rev. Lett.* **2001**, *87*, 054502.

(9) Tartakovsky, A. Langevin model for reactive transport in porous media. *Phys. Rev. E* **2010**, *82*, 026302.

(10) Dentz, M.; Le Borgne, T.; Englert, A.; Bijeljic, B. Mixing, spreading and reaction in heterogeneous media: A brief review. *J. Contam. Hydrol.* **2011**, *120*−*121*, 1−17.

(11) Taylor, G. Dispersion of Soluble Matter in Solvent Flowing Slowly through a Tube. *Proc. R. Soc. A* **1953**, *219*, 186−203.

(12) Aris, R. On the dispersion of a solute in a fluid flowing through a tube. *Proc. R. Soc. A* **1956**, *253*, 67−77.

(13) Quintard, M.; Whitaker, S. Convection, dispersion, and interfacial transport of contaminants: Homogeneous porous media. *Adv. Water Resour.* **1994**, *17*, 221−239.

(14) Whitaker, S. *The Method of Volume Averaging*; Springer, 1999; Vol. *1*.

(15) Hornung, U. *Homogeneization and Porous Media*; Springer-Verlag: New York, 1997.

(16) Kitanidis, P. K. The concept of the dilution Index. *Water Resour. Res.* **1994**, *30*, 2011.

(17) Le Borgne, T.; Dentz, M.; Davy, P.; Bolster, D.; Carrera, J.; de Dreuzy, J.; Bour, O. Persistence of incomplete mixing: A key to anomalous transport. *Phys. Rev. E* **2011**, *84*, 015301.

(18) Weisbrod, N.; Niemet, M.; Selker, J. Light transmission technique for the evaluation of colloidal transport and dynamics in porous media. *Environ. Sci. Technol.* **2003**, *37*, 3694−3700.

(19) Willingham, T.; Werth, C.; Valocchi, A. Evaluation of the effects of porous media structure on mixing-controlled reactions using pore-scale modeling and micromodel experiments. *Environ. Sci. Technol.* **2008**, *42*, 3185−3193.

(20) Berkowitz, B.; Scher, H. Theory of anomalous chemical transport in random fracture networks. *Phys. Rev. E* **1998**, *57*, 5858−5869.

(21) Le Borgne, T.; Bolster, D.; Dentz, M.; de Anna, P.; Tartakovsky, A. M. Effective pore-scale dispersion upscaling with a correlated continuous time random walk approach. *Water Resour. Res.* **2011**, *47*, W12538.

(22) de Anna, P.; Le Borgne, T.; Dentz, M.; Tartakovsky, A.; Bolster, D.; Davy, P. Flow Intermittency, Dispersion and Correlated Continuous Time Random Walks in Porous Media. *Phys. Rev. Lett.* **2013**, *101*, 184502.

(23) Bijeljic, B.; Mostaghimi, P.; Blunt, M. Signature of Non-Fickian Solute Transport in Complex Heterogeneous Porous Media. *Phys. Rev. Lett.* **2011**, *107*, 204502.

(24) Sahimi, M. *Flow and Transport in Porous Media and Fractured Rock*; Wiley-VCH, 2011.

(25) Havlin, S.; Ben-Avraham, D. Diffusion in disordered media. *Adv. Phys.* **2002**, *51*, 187−292.

(26) Scagliarini, A.; Biferale, L.; Mantovani, F.; Pivanti, M.; Pozzati, F.; Sbragaglia, M.; Schifano, S. F.; Toschi, F.; Tripiccione, R. Front propagation in Rayleigh-Taylor systems with reaction. *J. Phys.: Conference Series* **2011**, *318*, 092024−1/10.

(27) Kang, K.; Redner, S. Fluctuation-dominated kinetics in diffusion-controlled reactions. *Phys. Rev. A* **1985**, *32*, 435−447.

(28) de Anna, P.; Le Borgne, T.; Dentz, M.; Bolster, D.; Davy, P. Anomalous Kinetics in Diffusion Limited Reactions Linked to Non-Gaussian Concentration PDF. *J. Chem. Phys.* **2011**, *135*, 174104.

(29) Porta, G. M.; Thovert, J. F.; Riva, M.; Guadagnini, A.; Alder, P. Microscale simulation and numerical upscaling of a reactive flow in a plane channel. *Phys. Rev. E* **2012**, *86*, 036102.
(30) Villermaux, E.; Duplat, J. Mixing is an aggregation process. *Compt. Rend. Mec.* **2003**, *91*, 18450.
(31) Oates, P. M.; Harvey, C. F. A colorimetric reaction to quantify fluid mixing. *Exp. Fluids* **2006**, *41*, 673−683.
(32) Jonsson, T.; Irgum, K. Very fast peroxyoxalate chemiluminescence. *Anal. Chim. Acta* **1999**, *400*, 257−264.
(33) Connor, K. *Chemical Kinetics*; VCH publishers, 1990.
(34) Bear, J. *Dynamics of Fluids in Porous Media*; American Elsevier, New York, 1972.
(35) Kleinfelter, N.; Moroni, M.; Cushman, J. H. Application of the finite-size Lyapunov exponent to particle tracking velocimetry in fluid mechanics experiments. *Phys. Rev. E* **2005**, *72*, 056306.
(36) Duplat, J.; Villermaux, E. Mixing by random stirring in confined mixtures. *J. Fluid Mech.* **2008**, *617*, 51−86.
(37) Le Borgne, T.; Dentz, M.; Villermaux, E. Stretching, coalescence and mixing in porous media. *Phys. Rev. Lett.* **2013**, *110*, 204501.
(38) de Anna, P.; Le Borgne, T.; Dentz, M.; Tartakovsky, A. M. Kinetics of reactive fronts in porous media. *under review* **2013**.
(39) Villermaux, E. Mixing by porous media. *Compt. Rend. Mec.* **2012**, *340*, 933−943.
(40) Harrison, C.; Cabral, J. a. T.; Stafford, C. M.; Karim, A.; Amis, E. J. A rapid prototyping technique for the fabrication of solvent-resistant structures. *Journal of Micromechanics and Microengineering* **2004**, *14*, 153−158.
(41) Cabral, J. a. T.; Hudson, S. D.; Harrison, C.; Douglas, J. F. Frontal photopolymerization for microfluidic applications. *Langmuir: the ACS journal of surfaces and colloids* **2004**, *20*, 10020−9.
(42) Rolle, M.; Eberhardt, C.; Chiogna, G.; Cirpka, O. A.; Grathwohl, P. Enhancement of dilution and transverse reactive mixing in porous media: Experiments and model-based interpretation. *Journal of Contaminant Hydrology* **2009**, *47*.
(43) Chiogna, G.; Cirpka, O. A.; Grathwohl, P.; and Massimo Rolle. Transverse mixing of conservative and reactive tracers in porous media: Quantification through the concepts of flux-related and critical dilution indices. *Water Resour. Res.*, **2011**, *47*.
(44) Bonnet, J.; Lenormand, R. Constructing micromodels for study of multiphase flow in porous-media. *Exp. Fluids* **1977**, *32*, 477−480.
(45) Didierjean, S.; Souto, H. P. A.; Delannay, R.; Moyne, C. Dispersion in periodic porous media. Experience versus theory for two-dimensional systems. *Chem. Eng. Sci.* **1997**, *52*, 1861−187.
(46) Hele-Shaw, H. S. S. author. *Trans. Instn. Nav. Archit.* **1898**, *40*, 21.
(47) Raje, D. S.; Kapoor, V. Experimental study of bimolecular reaction kinetics in porous media. *Environ. Sci. Technol.* **2000**, *34*, 1234−1239.

■ NOTE ADDED AFTER ASAP PUBLICATION

This paper was modified from the original version published on December 6, 2013 to include an additional reference and to fix a typo in Figure 2. The corrected version was published on December 10, 2013.

AGU PUBLICATIONS

Geophysical Research Letters

RESEARCH LETTER
10.1002/2015GL064513

Key Points:
- Enhancement of solutes mixing in unsaturated porous media
- Mixing-induced reactivity in unsaturated porous media
- Vadose zone and gas-oil reservoir

Supporting Information:
- Texts S1 and S2 and Figures S1 and S2
- Figure S1
- Figure S2
- Data S1
- Texts S1 and S2 and Figure S1

Correspondence to:
J. Jiménez-Martínez and Y. Méheust,
jjimenez@lanl.gov;
yves.meheust@univ-rennes1.fr

Citation:
JimÉnez-MartÍnez, J., P. de Anna, H. Tabuteau, R. Turuban, T. Le Borgne, and Y. Méheust (2015), Pore-scale mechanisms for the enhancement of mixing in unsaturated porous media and implications for chemical reactions, *Geophys. Res. Lett.*, *42*, 5316–5324, doi:10.1002/2015GL064513.

Received 11 MAY 2015
Accepted 16 JUN 2015
Accepted article online 22 JUN 2015
Published online 14 JUL 2015

Pore-scale mechanisms for the enhancement of mixing in unsaturated porous media and implications for chemical reactions

Joaquín Jiménez-Martínez[1,2], Pietro de Anna[3], Hervé Tabuteau[4], Régis Turuban[1], Tanguy Le Borgne[1], and Yves Méheust[1]

[1]Geosciences Rennes, UMR 6118, CNRS, Université de Rennes 1, Rennes, France, [2]Now at Los Alamos National Laboratory, Los Alamos, New Mexico, United States, [3]Department of Civil and Environmental Engineering, Massachusetts Institute of Technology, Cambridge, Massachusetts, USA, [4]IPR, Université de Rennes 1-CNRS, UMR 6251, Rennes, France

Abstract Porous media in which different fluid phases coexist are common in nature (e.g., vadose zone and gas-oil reservoirs). In partially saturated porous media, the intricate spatial distributions of the wetting and nonwetting phases causes their flow to be focused onto preferential paths. Using a novel 2-D experimental setup allowing pore-scale measurement of concentration fields in a controlled unsaturated flow, we highlight mechanisms by which mixing of an invading fluid with the resident fluid is significantly enhanced when decreasing saturation. The mean scalar dissipation rate is observed to decrease slowly in time, while under saturated conditions it decays rapidly. This slow decrease is due to sustained longitudinal solute fingering, which causes concentration gradients to remain predominantly transverse to the average flow. Consequently, the effective reactivity is found to be much larger than under saturated conditions. These results provide new insights into the role that multiphase flows play on mixing/reaction in porous media.

1. Introduction

The mixing of solutes in unsaturated porous media flows (i.e., when at least two immiscible fluids or phases coexist) is a common process controlling solute concentrations and the associated reactivity in natural processes and industrial systems. This includes for instance rainwater infiltration in soils and related migration and dilution of diffuse or point source contaminants, artificial recharge and unconventional irrigation, enhanced oil recovery, geological storage of CO_2 or gases such as H_2, and nuclear waste storage. A decrease in the wetting phase (typically, water) content is known to modify the velocity distribution and thus the associated transport phenomena. In particular, it can lead to the development of regions of wetting fluid of very low velocities, including regions where it is trapped, and connected preferential channels of high velocity [*de Gennes*, 1983]. The dependence of the velocity field distribution on the saturation degree is expected to strongly impact solute transport, mixing, and chemical reactivity that take place within one of the immiscible phases (usually, the aqueous phase). The need to account for saturation-dependent mixing has been highlighted by studies focusing on the mixing of recently infiltrated water with "old" resident water in catchments [e.g., *Legout et al.*, 2007; *Brooks et al.*, 2009]. This effect has been quantified recently by introducing "ad hoc" dynamic partial mixing coefficients in catchment transport models [*Hrachowitz et al.*, 2013].

Numerous works have measured an increased dispersion when decreasing saturation [e.g., *Sato et al.*, 2003; *Nutzmann et al.*, 2002; *Maraqa et al.*, 1997; *Haga et al.*, 1999; *Padilla et al.*, 1999; *Toride et al.*, 2003; *Guillon et al.*, 2013; *Russo*, 1993; *Russo et al.*, 1994; *Russo*, 1995a; *Roth and Hammel*, 1996; *Raoof and Hassanizadeh*, 2013; *Wildenschild and Jensen*, 1999; *Bromly and Hinz*, 2004]. Furthermore, the increase of flow heterogeneity with water desaturation has been shown to lead to dispersion processes that are non-Fickian to a larger extent [e.g., *Wildenschild and Jensen*, 1999; *Bromly and Hinz*, 2004; *Guillon et al.*, 2013], in particular in relation to mobile-immobile mass transfer processes described by nonequilibrium models, such as dual-continuum [*Nielsen et al.*, 1986; *Simunek and van Genuchten*, 2008] or Continuous Time Random Walks (CTRW) representations [e.g., *Cortis and Berkowitz*, 2004; *Zoia et al.*, 2010]. Although the mechanisms behind this change in dispersion regime are well understood, the explicit relationship between saturation and the non-Fickian transport parameters is still largely debated and likely nonuniversal [e.g., *Sahimi*, 2012]. While all these studies, mainly from laboratory experiments in disturbed or repacked soils,

Table 1. Main Control Parameters, for the Investigated Saturation Degrees S_w: Flow Q, Mean Velocity $\bar{v}$, Reynolds (*Re*), Péclet (*Pe*), and Capillary (*Ca*) Numbers

S_w	Q (mm^3 s^{-1})	$\bar{v}$ (mm s^{-1})	*Re* (-)	*Pe* (-)	*Ca* (-)
1.0	0.55	0.017	$5.49 \cdot 10^{-4}$	54	
1.0	1.375	0.043	$1.37 \cdot 10^{-3}$	135	
0.7	0.55	0.025	$7.87 \cdot 10^{-4}$	78	$2.04 \cdot 10^{-5}$
0.6	0.55	0.029	$9.18 \cdot 10^{-4}$	91	$2.38 \cdot 10^{-5}$

indicate an enhancement of dispersion when decreasing saturation, the opposite behavior, mainly from experiments in natural-undisturbed soils, has also been observed [e.g., *Hammel and Roth*, 1998; *Russo*, 2005; *Vanderborght and Vereecken*, 2007]. This phenomenon is explained in particular by the fact that an increase in saturation can correspond to an increase in flow rates, which induces larger velocity fluctuations for some soil structures. For anisotropic media it has also been observed that the effect of saturation on dispersion is dependent on the orientation of the mean flow direction with respect to the heterogeneities [e.g., *Russo*, 1995b; *Russo et al.*, 1998].

Unsaturated flows thus exhibit a rich scope of transport behaviors, which have been explored so far mainly through the analysis of solute-spreading properties. While the characterization of solute spreading is important to predict the spatial extent of solutes plumes or the distribution of transfer times in porous media, it does not directly inform about the actual mixing of solutes and the concentration distribution affecting chemical reaction processes [e.g., *Fluhler et al.*, 1996; *de Barros et al.*, 2012; *Chiogna et al.*, 2012; *de Anna et al.*, 2014a]. Mixing, in contrast, quantifies the distribution of concentration gradients within solutes plumes; these gradients control diffusive mass transfer and thus the evolution of concentration distributions [e.g., *Ottino*, 1989; *Kitanidis*, 1994; *Dentz et al.*, 2011]. While spreading and mixing are directly coupled, as spreading generally enhances mixing, the relationship between them is not direct [e.g., *Dentz et al.*, 2011]. In particular, a transport model fitting a breakthrough curve cannot, in general, predict chemical reactions resulting from solute mixing within the plume, since chemical reactions depend nonlinearly on concentration fluctuations which are not resolved by dispersion models [e.g., *Battiato et al.*, 2009]. While the number of studies addressing dispersion in unsaturated flows is significant, there has been much less work specifically targeting mixing processes and their consequences for chemical reactions under these conditions. A common view is that the existence of more pronounced preferential flow paths in unsaturated flow should induce faster traveltimes and thus decrease the time for solute mixing and chemical reactions [e.g., *Vanderborght et al.*, 2001; *Ursino et al.*, 2001; *Persson et al.*, 2005]. As discussed in the current study, this perception is not always correct as flow channeling may also increase concentration gradients and thus diffusive mass transfer and consequent reaction rates.

In this letter we quantify the impact of water saturation on mixing through novel pore-scale experimental imaging of solute concentrations in unsaturated flows. While most past studies have focused on Darcy scale heterogeneities, the presented experimental setup offers a pore-scale vision of transport processes, which is particularly relevant to the study of chemical reactions that depend nonlinearly on the microscale concentration distribution. We find that the formation of preferential flow paths in unsaturated flows largely enhances the mixing rate, and, consequently, the chemical reactivity, quantified here for large Damköhler number. In contrast to what is observed under saturated conditions, concentration gradients are found to be sustained in the direction transverse to the average flow through a coupling between non-Fickian longitudinal dispersion and diffusion into immobile zones transverse to preferential flow channels. Hence, these results uncover new mechanisms for the control of saturation on mixing and reaction processes.

2. Materials and Methods

The experimental flow cell is based on a horizontal analogous two-dimensional (2-D) porous medium consisting of a monolayer of cylindrical grains. The experimental setup allows capturing the incomplete mixing occurring within the pores from the measurement of (i) the solute concentration field in the liquid (wetting) phase [*de Anna et al.*, 2014b] and (ii) the spatial distribution of the two fluid phases (wetting and nonwetting).

The wetting fluid used is a 60–40% by weight *water-glycerol* solution dyed with Fluorescein, while *air* is used as nonwetting fluid; the viscosity ratio between the two fluids is 10^{-3}. In horizontal immiscible two-phase flows, the geometrical arrangement of the phases is controlled by the viscosity contrast between the two fluids

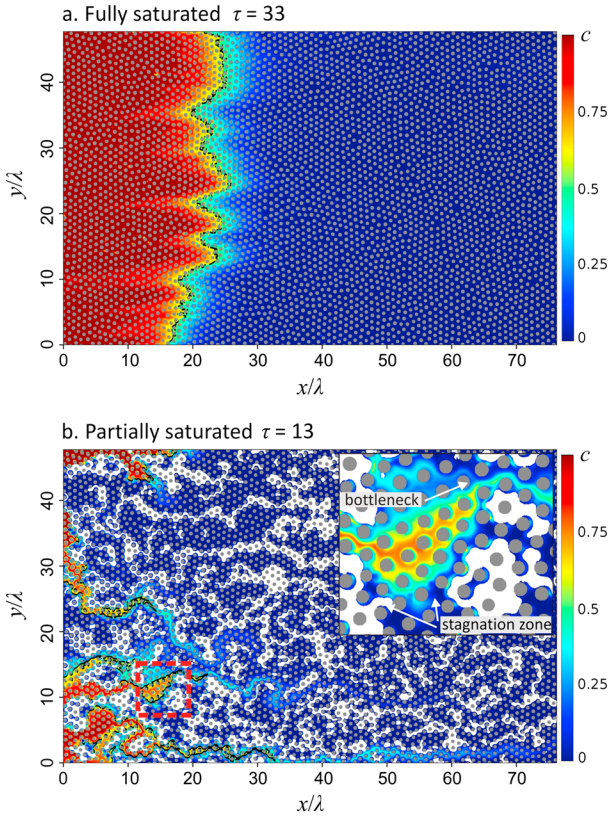

Figure 1. (a) Normalized concentration field $c(\boldsymbol{x}, \tau)$ obtained in fully saturated conditions at $\tau = t/t_a = 33$; it shows the concentration field with the centerline Γ superimposed in black. (b) $c(\boldsymbol{x}, \tau)$ under partially saturated conditions ($S_w = 0.7$) at $\tau = 13$. In stagnation zones the tracer is diffused, while at bottlenecks formed between air clusters, coalescence of tracer fingers takes place.

[*Lenormand*, 1990], the average displacement velocity [*Lenormand*, 1990; *Løvoll et al.*, 2004; *Toussaint et al.*, 2012], and how the fluids are injected into the medium. Here we obtain the phase geometry by injecting the two fluids together, in a manner similar to that of *Tallakstad et al.* [2009]; this method provides the possibility of imposing a spatially homogeneous saturation degree (in a statistical sense) with a geometric configuration of the phases that is realistic. A detailed description of the model dimensions, fluid properties (wetting and nonwetting phase), and experimental protocol is given in the supporting information.

The flow and transport regimes are characterized by four dimensionless numbers (Table 1). The wetting saturation S_w is the fraction of the total pore volume occupied by clusters of the wetting fluid. The Reynolds number, which compares the typical ratio of inertial forces to viscous forces, is $Re = \rho_w \bar{v} a/\mu_w$, where ρ_w is the density, $\bar{v}$ the average flow velocity, μ_w the viscosity of the wetting phase, and a the average pore throat. The capillary number, which quantifies the relative magnitude of viscous to capillary forces, is expressed as $Ca = \mu_w Q a^2/(\gamma \kappa A)$, where Q is the flow rate, γ the surface tension at the interface between the two fluid phases, κ the absolute permeability, and A the cross-sectional area in the direction normal to the average flow direction [e.g., *Méheust et al.*, 2002]. The Péclet number, which characterizes the relative importance of advective and diffusive effects during transport, is $Pe = \bar{v} a^2/(2D\lambda)$, where D is the molecular diffusion coefficient and λ the average pore size. Note that in this experimental setup the flow rate is decoupled from the water saturation. Hence, the two variables can be varied independently over a certain range. This is different from common Darcy scale experimental setups where the flow rate increases with saturation [e.g., *Vanderborght et al.*, 2001].

3. Results and Discussion

3.1. Concentration Fields

A snapshot of the concentration field of the invading fluorescent tracer, both under fully and partially saturated conditions is shown in Figure 1 for the same injection flow rate ($Q = 0.55$ mm^3 s^{-1}). The injected solution has a homogeneous nondimensional concentration $c = 1$ (see supporting information). The geometry of the mixing zone (where $0 < c < 1$) can be characterized by (i) its longitudinal extension σ (longitudinal standard deviation of the mean concentration), which quantifies the spreading of the invading solution within the host medium, and (ii) the length Σ of its center line Γ, defined as the set of locations at which $c = 1/2$. We shall call Γ the interface between the two solutions, though it is in effect the center line of a diffuse interface.

In the saturated case, $\sigma(t)$ increases approximately diffusively, as $t^{1/2}$ (data not shown here). In the unsaturated case, the presence of the air leads to a highly channelized flow, with large stagnation zones developing between air clusters. This broad distribution of velocities is expected to result in a superdiffusive spreading $\sigma(t)$ of the solute [e.g., *Wildenschild and Jensen*, 1999; *Bromly and Hinz*, 2004; *Cortis and Berkowitz*, 2004; *Zoia et al.*, 2010; *Guillon et al.*, 2013], associated to a flow organization in well-developed fingers (Figure 1) along

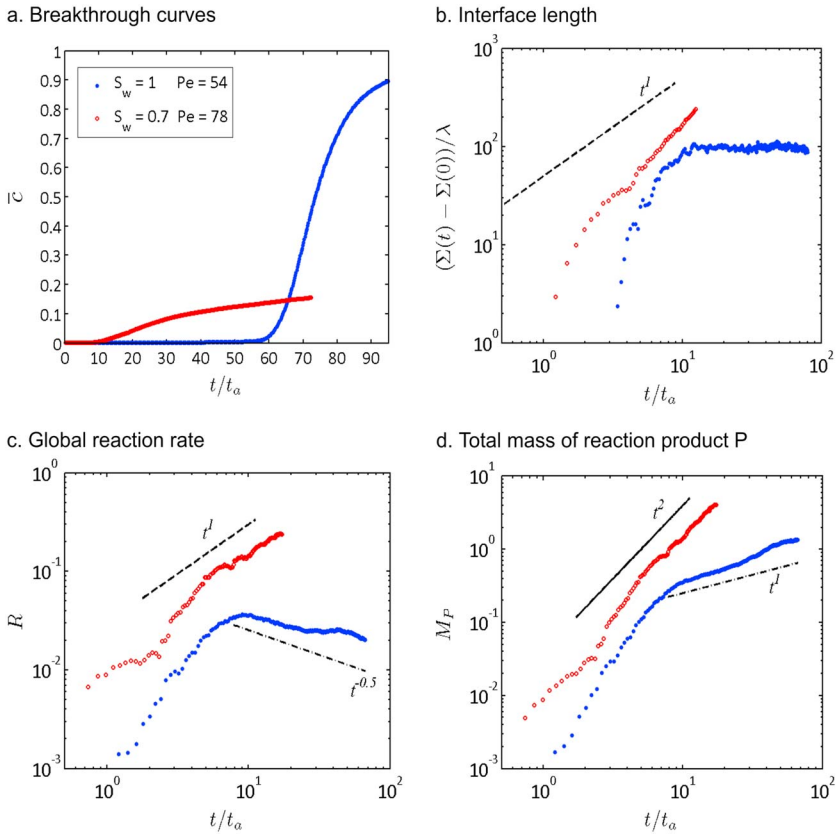

Figure 2. (a) Breakthrough curves (BTCs) measured at $x/\lambda = 63$ for fully saturated ($S_w = 1$ blue dots) and partially saturated conditions ($S_w = 0.7$ red circles). (b) Temporal evolution of $\Sigma - \Sigma(0)$, where Σ is the length of the center line Γ. (c) Temporal evolution of the global reaction rate R, which is obtained from the spatial integration of the local reaction rate r. (d) Total mass of reaction product, M_P; it is obtained from the temporal integration of R (see supporting information).

which the concentration gradient develops mainly in the direction transverse to the average flow. A measure of the impact of that spatial organization on solute transport is given by the breakthrough curves: under partially saturated conditions they are strongly asymmetric, with earlier breakthrough and much longer tailing than their saturated counterpart (Figure 2a).

The finger structure developed in the unsaturated cases also leads to a significant increase of the surface available for fluid mixing [e.g., *Jha et al.*, 2011]. This is visible in the temporal evolution of the interface length Σ in Figure 2b. In the saturated case, Σ initially increases and then stabilizes to a plateau value. The initial increase corresponds to the entrance of the mixing front into the porous media domain and its stretching by the flow heterogeneity [*Le Borgne et al.*, 2013]. This initial transient, also observed in experiments by *de Anna et al.* [2014b] in saturated conditions, disappears when finger merge transversally through diffusion, making the length of the mixing interface cease to increase. On the other hand, for partially saturated conditions, Σ increases faster than linearly in time (Figure 2b) and does not reach a plateau. Even though some finger coalescence does occur in bottlenecks, where flow lines are focused between air clusters (Figure 1b), that linear increase prevails through the continuous creation of new fingers. The strong deformation of the mixing interface, and the consequent enhancement of mixing, is analogous to observations made in Darcy scale heterogeneous flow topologies in saturated porous media [*de Barros et al.*, 2012; *Le Borgne et al.*, 2014].

This phenomenology was confirmed for different saturations and different Péclet numbers (see supporting information).

3.2. Mixing-Induced Reactivity $A + B \rightleftharpoons P$

In order to analyze the impact of saturation on chemical reactivity, we derive estimates of the local reaction rates that would be observed if the mixing of an injected liquid and a resident liquid, miscible with each other,

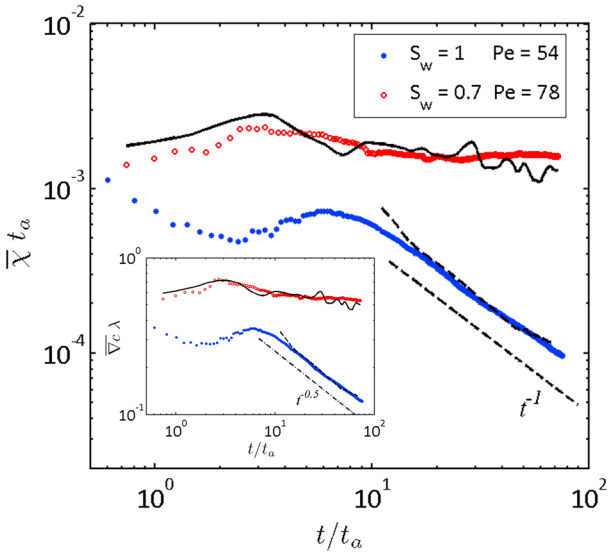

Figure 3. The main figure displays the time evolution of the mean scalar dissipation rate $\overline{\chi}(t)$ under fully ($S_w = 1$ blue dots) and partially saturated ($S_w = 0.7$ red circles) conditions. The insets shows the time evolution of the mean concentration gradient $\overline{\nabla c}(t)$. Estimates of $\overline{\chi}(t)$ from equation (4) are plotted for fully and partially saturated conditions as dotted and continuous line, respectively.

triggered a fast reversible reaction, i.e., a reaction (of characteristic timescale t_r) that is quasi-instantaneous with respect to advective mechanisms (of characteristic timescale t_a), that is, of Damköhler number $Da = t_a/t_r \gg 1$ [e.g., *Le Borgne et al.*, 2014]. For this we use the method presented by *de Simoni et al.* [2005, 2007] and *Willmann et al.* [2010], which allows quantifying the spatial distribution of local reaction rates r from the measured conservative concentration fields $c = c_A - c_B$ for a fast reversible reaction of known equilibrium constant K (see supporting information), according to the following relation:

$$r = \frac{2K}{(c^2 + 4K)^{3/2}} D \|\nabla c\|^2, \qquad (1)$$

where $\| \|$ denotes the vector magnitude.

The largest reaction rates are expected to be localized in areas of large concentration gradients. Hence, the spatial structure of concentration gradients is found to significantly impact the upscaled reactivity, i.e., the global reaction rate R, computed as the integral over the entire spatial domain of r (Figure 2c). In particular, while under saturated conditions the global reaction rate decreases after an initial increase, under unsaturated conditions its increase rate keeps approximately constant over the observation time (before mass starts leaving the domain). The late time reaction rate is higher in the unsaturated cases than in the saturated ones, even though we can only investigate times that are half a decade smaller due to the faster solute breakthrough. This translates directly into a large difference in the mass of the reaction product, M_P (Figure 2d). This behavior was confirmed for different saturations and different Péclet numbers (see supporting information).

The impact of mixing on the reaction rate is quantified through the product of the diffusion coefficient with the squared conservative concentration gradient (see supporting information). The integration of this term over the domain represents the scalar dissipation rate of concentration gradients [e.g., *Ottino*, 1989; *Le Borgne et al.*, 2010]. Thus, the temporal behavior of the global reaction rate is tightly linked to that of the scalar dissipation rate. In order to understand this behavior quantitatively, we analyze in details the dynamics of the concentration gradients in what follows.

3.3. Temporal Dynamics of Concentration Gradients

Figure 3 shows the temporal evolution of the mean concentration gradient $\overline{\nabla c}(t)$ and the mean scalar dissipation rate $\overline{\chi}(t)$ over the diffuse mixing interface, defined respectively as,

$$\overline{\nabla c} = \frac{1}{S_m} \int_{\Omega_m} dx\, dy\, \|\nabla c\| \qquad (2)$$

and

$$\overline{\chi} = \frac{1}{S_m} \int_{\Omega_m} dx\, dy\, D\|\nabla c\|^2. \qquad (3)$$

where S_m is the area of the mixing zone Ω_m defined as $\Omega_m = \{(x,y)|0.05 < c(x,y) < 0.95\}$.

In the fully saturated case and for different flow rates, the mean concentration gradient decays at large times after an initial quasi-constant transient. This scaling is in the form $\overline{\nabla c} \sim 1/\sqrt{t}$, as shown by the blue curve in Figure 3 (inset). This behavior is explained by the Fickian increase of the longitudinal dispersion length σ (see Figure 1) in the saturated medium. Indeed, after coalescence of early time fingers, the concentration

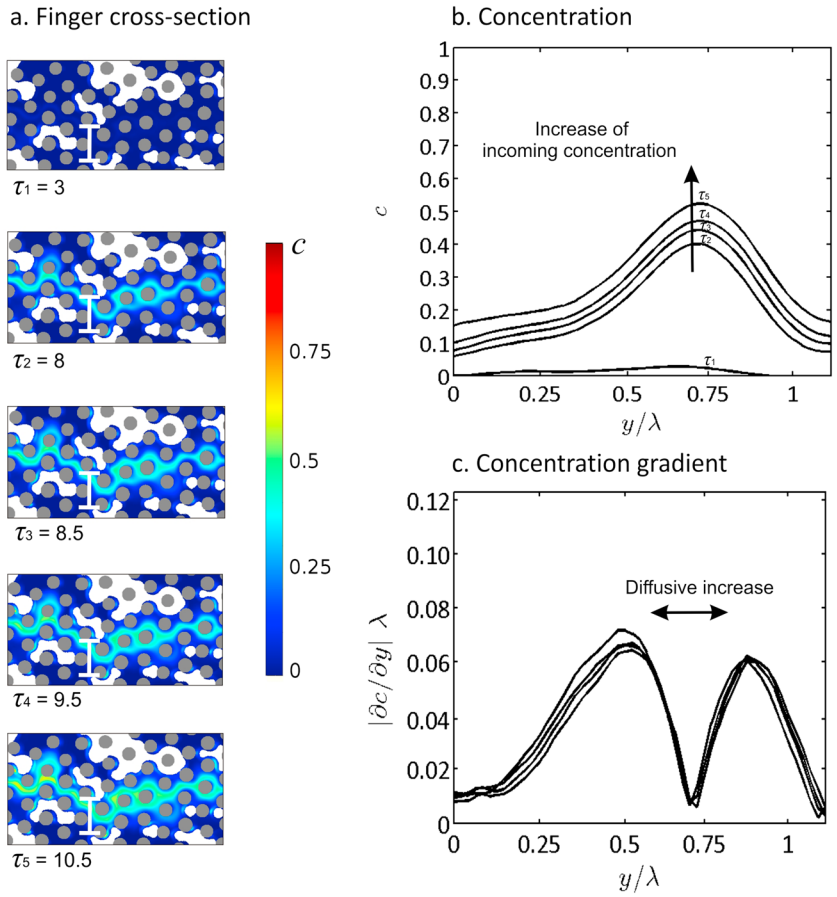

Figure 4. (a) Snapshots of one finger at different times ($\tau_i = t_i/t_a$) for a partially saturated test ($S_w = 0.7$). (b) Concentration profile along the vertical white segment indicated in the snapshots in Figure 4a, at different times. An increase of the incoming concentration is observed. (c) Profile of the concentration gradient $|\partial c/\partial y|$ at different times; $|\partial c/\partial y|$ is the absolute value of the derivative of the profile shown in Figure 4b. The direction of the diffusive widening of the figure is indicated by an arrow.

gradients are mostly oriented along the longitudinal direction. Hence, the mean concentration gradient may be approximated as $\overline{\nabla c} \approx 1/\sigma \sim 1/\sqrt{t}$, which provides a good prediction of the temporal evolution of $\overline{\nabla c}$ for saturated porous media at late times. Note that the early time behavior, controlled by a short initial fluid stretching regime, could also be modeled by a lamella-based model [e.g., *Le Borgne et al.*, 2013; *de Anna et al.*, 2014a].

In the partially saturated cases, $\overline{\nabla c}$ is always larger than in the saturated cases and decays slowly in time as shown by the red curve in Figure 3. This persistence of large concentration gradients is at the origin of the enhancement of chemical reactivity. In contrast to the saturated cases, concentration gradients are mostly oriented along the direction transverse to the average flow (Figure 1b). Elongated tracer fingers carry high concentrations that diffuse laterally into less mobile regions (see Figure 1b). Therefore, in the case of transport by an unsaturated flow, considering the concentration field at time t, we can approximate the characteristic transverse gradient at longitudinal position x in a finger as $\|\nabla c\|(x,t) \simeq 2\, c_f(x,t)/w_f(x,t)$, where c_f is the maximum finger concentration at x and $w_f/2$ is the finger half width at x. While the lateral finger size is expected to grow through diffusion, the maximum finger concentration c_f increases slowly in time as the result of the important longitudinal dispersion and the mixing processes (i.e., interaction with other fingers) upstream of location x (Figure 1b). In particular, critical bottlenecks (Figure 1b), which are known to focus a large part of the flow in unsaturated porous media [*de Gennes*, 1983], favor the coalescence of fingers with different mean velocities, thus leading to a slow increase of the downstream concentrations. This persistent slow increase of the maximum concentration is thus concomitant with a slow increase of the finger width w_f, leading to an approximately constant gradient over a large range of times (Figure 4).

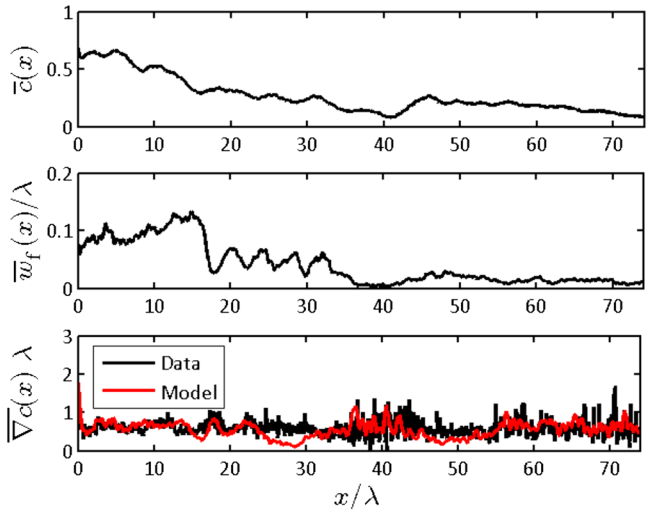

Figure 5. Dependence on x of the (top) mean concentration $\overline{c}(x,t) \simeq \overline{c}_f(x,t)$ and (middle) typical finger width $\overline{w}_f(x,t))$, for the concentration field of Figure 1b ($t/t_a = 13$). (bottom) The corresponding estimate of the average concentration gradient, $\overline{\nabla c} = 2\,\overline{c}_f/\overline{w}_f$, is compared to values obtained from a direct calculation.

3.4. The Role of Fingered Transport and Non-Fickian Dispersion on Mixing in Unsaturated Flows

As discussed above, we identify three main processes controlling mixing at the pore scale in unsaturated porous media: advective fingering, transverse diffusive mass transfer, and finger coalescence (Figures 1b and 4). In contrast to what is observed under saturated conditions [*Le Borgne et al.*, 2013; *de Anna et al.*, 2014a], continuous transverse coalescence of the solute fingers is limited by the presence of air clusters, so that no regime where concentration gradients are mostly longitudinal is observed; the concentration gradients remain mostly transverse to the average flow.

To quantify these mechanisms, we propose to estimate the concentration gradient averaged over the transverse direction y as $\overline{\nabla c}(x,t) \simeq 2\,\overline{c_f}(x,t)/\overline{w_f}(x,t)$, where the overline $\left(\overline{\ }\right)$ is to be understood as a an average over Ω_m and along the y only (see supporting information for details); this notation is identical to that of the global average used in equations (2) and (3), so to avoid any ambiguity, we indicate the space and time dependencies for all quantities mentioned below. We estimate the two factors $\overline{c_f}$ and $1/\overline{w_f}$ independently from the images and confirm the validity of this approximation (Figure 5). Note that $\overline{c_f}(x,t)$ is approximated as the average concentration in the mixing zone at longitudinal position x, $\overline{c}(x,t)$ (see supporting information for the detailed estimation of $\overline{c_f}$ and $\overline{w_f}$). Hence, the persistence of large concentration gradients can be understood from the ingredients presented in section 3.3, and consequently results from the spatial distribution and temporal dynamics of the two factors. The average concentration $\overline{c}(x,t)$ decays smoothly with the longitudinal position and differs from the profile observed for the saturated case. This is a characteristics of non-Fickian dispersion arising from the partially saturated conditions. As illustrated in Figure 1b, the high-velocity flow paths carry most of the tracer quickly through the domain, while the concentration increases slowly close to the inlet as the tracer invades the low-velocity regions. As expected, the typical finger width at longitudinal position x, $\overline{w_f}(x,t)$, is larger close to the inlet, where some of the stagnation zones have been invaded, than at the edge of the plume, where only fingers carry tracer. As both $\overline{c}$ and $\overline{w_f}$ decrease weakly with the distance from the tracer inlet, the average concentration gradient appears to depend only weakly on the longitudinal position. This is again in contrast to the saturated case where concentration gradients are localized in the mixing zone corresponding to the dispersing front.

We obtain an estimation of the global average concentration gradient, $\overline{\nabla c}(t)$, by integrating $\overline{\nabla c}(x,t)$ along the system length L, with a local weighting by the transverse extent of the mixing zone at position x and a normalization by the area of the mixing zone, S_m (see supporting information for details). This calculation yields

$$\overline{\nabla c}(t) = \frac{2}{S_m(t)} \int_0^L \mathrm{d}x\, \overline{c}(x,t)\, n_f(x,t), \tag{4}$$

where $n_f(x,t)$ is the typical number of fingers at longitudinal position x in the image recorded at time t.

This expression compares well with the direct measurement of $\overline{\nabla c}(t)$ (Figure 3), which validates our assumption that concentration gradients remain mainly transverse to the average flow under unsaturated conditions. Since the variance of the concentration gradient distribution, $\sigma^2_{\nabla c}$, can be computed as $\overline{(\nabla c)^2} - (\overline{\nabla c})^2$, the average scalar dissipation rate can simply be estimated from the average concentration gradient as $\overline{\chi} = D\left(\overline{\nabla c}^2 + \sigma^2_{\nabla c}\right)$. As $\sigma^2_{\nabla c}$ is found to be much smaller than the average concentration gradient squared, we use the simple approximation $\overline{\chi} \approx D\overline{\nabla c}^2$, where the average concentration gradient is given by equation (4). This relation provides a good estimate of the temporal evolution of the scalar dissipation rate over the range of investigated times (Figure 3). The persistence of large scalar dissipation rates in unsaturated porous media is thus the result of the finger dynamics (longitudinal finger development, transverse molecular diffusion, and occasional finger coalescence) as well as of the non-Fickian solute dispersion, which controls the concentration carried by fingers.

4. Conclusion

The presented experimental results shed new light on pore-scale mixing processes in unsaturated porous media. In particular, we uncover a basic mechanism by which mixing rates are significantly enhanced under unsaturated conditions. The first ingredient responsible for enhanced mixing is the formation of a ramified finger structure, shaped by the distribution of air clusters, which creates a large interface available for diffusive mass transfer. The second important process controlling mixing is non-Fickian dispersion, which leads to a persistent slow increase of finger concentrations, sustaining large concentration gradients. The third process is the limitation of finger merging by air clusters. These three processes induce concentration gradients that remain mainly normal to the average flow direction. Indeed, an estimate of the mean concentration gradient, $\overline{\nabla c}$, and mean scalar dissipation rate, $\overline{\chi}(t)$, based on these assumptions and from the measured finger width and mean concentration in fingers, compares well with direct measurements of $\overline{\nabla c}$ and $\overline{\chi}(t)$. Lowering the saturation and porous medium heterogeneity is expected to enhance flow fingering as a consequence of larger flow localization along better defined preferential flow paths and therefore also enhance mixing and reactivity.

We expect this mechanism to play an important role in controlling dilution and reaction processes in the vadose zone as well as in other natural and industrial systems. Though mixing enhancement is demonstrated here at the pore scale, we can postulate that it is expected to occur in unsaturated porous media where the above mentioned main ingredients are present. It could therefore be relevant at larger scales, depending on the medium geometry. But given the role played by air clusters, this mechanism of mixing enhancement would probably be efficient at scales not much larger than the size of the larger air clusters in the system. In our two-dimensional setup, the phase geometry exhibits no typical size for the air clusters, and the largest clusters are on the order of the system size [*Tallakstad et al.*, 2009], which makes the mixing enhancement particularly efficient.

Acknowledgments

J.J.-M. expresses his gratitude to Fondation Rennes 1. Y.M. acknowledges support from Rennes-Métropole through an A.I.S. grant from equipment. The authors gratefully acknowledge support from INSU/CNRS through the EC2CO program, under project AO2014-906387. The experimental work was also supported by the Interreg project CLIMAWAT, EU-RDF INTERREG IVA France (Channel)-England program.

The Editor thanks two anonymous reviewers for their assistance in evaluating this paper.

References

Battiato, I., D. M. Tartakovsky, A. M. Tartakovsky, and T. Scheibe (2009), On breakdown of macroscopic models of mixing-controlled heterogeneous reactions in porous media, *Adv. Water Res.*, *32*(11), 1664–1673.

Bromly, M., and C. Hinz (2004), Non-Fickian transport in homogeneous unsaturated repacked sand, *Water Resour. Res.*, *40*, W07402, doi:10.1029/2003WR002579.

Brooks, J. R., H. R. Barnard, R. Coulombe, and J. J. McDonnell (2009), Ecohydrologic separation of water between trees and streams in a Mediterranean climate, *Nat. Geosci.*, *3*, 100–104.

Chiogna, G., D. Hochstetler, A. Bellin, P. Kitanidis, and M. Rolle (2012), Mixing, entropy and reactive solute transport, *Geophys. Res. Lett.*, *39*, L20405, doi:10.1029/2012GL053295.

Cortis, A., and B. Berkowitz (2004), Anomalous transport in classical soil and sand columns, *Soil Sci. Soc. Am. J.*, *68*, 1539–1548.

de Anna, P., M. Dentz, A. Tartakovsky, and T. Le Borgne (2014a), The filamentary structure of mixing fronts and its control on reaction kinetics in porous media flows, *Geophys. Res. Lett.*, *41*, 4586–4593, doi:10.1002/2014GL060068.

de Anna, P., J. Jimenez-Martinez, H. Tabuteau, R. Turuban, T. Le Borgne, M. Derrien, and Y. Méheust (2014b), Mixing and reaction kinetics in porous media: An experimental pore scale quantification, *Environ. Sci. Technol.*, *48*, 508–516.

de Barros, F., M. Dentz, J. Koch, and W. Nowak (2012), Flow topology and scalar mixing in spatially heterogeneous flow field, *Geophys. Res. Lett.*, *39*, L08404, doi:10.1029/2012GL051302.

de Gennes, P. G. (1983), Hydrodynamic dispersion in unsaturated porous media, *J. Fluid Mech.*, *136*, 189–200.

de Simoni, M., J. Carrera, X. Sanchez-Vila, and A. Guadagnini (2005), A procedure for the solution of multicomponent reactive transport problems, *Water Resour. Res.*, *41*, W11410, doi:10.1029/2005WR004056.

de Simoni, M., X. Sanchez-Vila, J. Carrera, and M. Saaltink (2007), A mixing ratios-based formulation for multicomponent reactive transport, *Water Resour. Res.*, *43*, W07419, doi:10.1029/2006WR005256.

Dentz, M., T. Le Borgne, A. Englert, and B. Bijeljic (2011), Mixing, spreading and reaction in heterogeneous media: A brief review, *J. Contam. Hydrol.*, *120-121*, 1–17.

Fluhler, H., W. Durner, and M. Fluru (1996), Lateral solute mixing processes—A key for understanding field-scale transpor of water and solutes, *Geoderma*, *70*, 165–183.
Guillon, V., M. Fleury, D. Bauer, and M. Neel (2013), Superdispersion in homogeneous unsaturated porous media using NMR propagators, *Phys. Rev. E*, *87*, 043007.
Haga, D., Y. Niibori, and T. Chida (1999), Hydrodynamic dispersion and mass transfer in unsaturated flow, *Water Resour. Res.*, *35*(4), 1065–1077.
Hammel, K., and K. Roth (1998), Aproximation of asymptotic dispersivity of conservative solute in unsaturated heterogeneous media with steady state flow, *Water Resour. Res.*, *34*(4), 709–715.
Hrachowitz, M., H. Savenije, T. A. Bogaard, D. Tetzlaff, and C. Soulsby (2013), What can flux tracking teach us about water age distribution patterns and their temporal dynamics?, *Hydrol. Earth Syst. Sci.*, *17*, 533–564.
Jha, B., L. Cueto-Felgueroso, and R. Juanes (2011), Fluid mixing from viscous fingering, *Phys. Rev. Lett.*, *106*, 194502.
Kitanidis, P. K. (1994), The concept of the Dilution Index, *Water Resour. Res.*, *30*(7), 2011–2026.
Le Borgne, T., M. Dentz, D. Bolster, J. Carrera, J. R. de Dreuzy, and P. Davy (2010), Non-Fickian mixing: Temporal evolution of the scalar dissipation rate in heterogeneous porous media, *Adv. Water Res.*, *33*, 1468–1475.
Le Borgne, T., M. Dentz, and E. Villermaux (2013), Stretching, coalescence and mixing in porous media, *Phys. Rev. Lett.*, *110*, 204501.
Le Borgne, T., T. R. Ginn, and M. Dentz (2014), Impact of fluid deformation on mixing-induced chemical reactions in heterogeneous flows, *Geophys. Res. Lett.*, *41*, 7898–7906, doi:10.1002/2014GL062038.
Legout, C., J. Molenat, L. Aquilina, C. Gascuel-Odoux, M. Faucheux, Y. Fauvel, and T. Bariacn (2007), Solute transfer in the unsaturated zone-groundwater continuum of a headwater catchment, *J. Hydrol.*, *332*, 427–441.
Lenormand, R. (1990), Liquids in porous media, *J. Phys. Condens. Matter*, *2*(S), SA79.
Løvoll, G., Y. Méheust, R. Toussaint, J. Schmittbuhl, and K. J. Måløy (2004), Growth activity during fingering in a porous hele-shaw cell, *Phys. Rev. E*, *70*, 026301.
Maraqa, M., R. Wallace, and T. Voice (1997), Effects of a degree of water saturation on dispersivity and immobile water in sandy soil columns, *J. Contam. Hydrol.*, *25*, 199–218.
Méheust, Y., G. Løvoll, K. J. Måløy, and J. Schmittbuhl (2002), Interface scaling in a two-dimensional porous medium under combined viscous, gravity, and capillary effects, *Phys. Rev. E*, *66*, 051603.
Nielsen, D., M. T. van Genuchten, and J. Biggar (1986), Water flow and solute transport processes in the unsaturated zone, *Water Resour. Res.*, *22*(9S), 89S–108S, doi:10.1029/WR022i09Sp0089S.
Nutzmann, G., S. Maciejewski, and K. Joswig (2002), Estimation of water saturation dependence of dispersion in unsaturated porous media: Experiments and modelling analysis, *J. Hydrol.*, *25*, 565–576.
Ottino, J. M. (1989), *The Kinematics of Mixing: Stretching, Chaos, and Transport*, Cambridge Univ. Press, Cambridge, U. K.
Padilla, I. Y., T. C. J. Yeh, and M. H. Conklin (1999), The effect of water content on solute transport in unsaturated porous media, *Water Resour. Res.*, *35*(11), 3303–3313.
Persson, M., S. Haridy, J. Olsson, and J. Wendt (2005), Solute transport dynamics by high-resolution dye tracer experiments-image analysis and time moments, *Vadose Zone J.*, *4*, 856–865.
Raoof, A., and S. M. Hassanizadeh (2013), Saturation-dependent solute dispersivity in porous media: Pore-scale processes, *Water Resour. Res.*, *49*, 1943–1951, doi:10.1002/wrcr.20152.
Roth, K., and K. Hammel (1996), Transport of conservative chemical through an unsaturated two-dimensional Miller-similar medium with steady state flow, *Water Resour. Res.*, *32*(6), 1653–1663.
Russo, D. (1993), Stochastic modeling of solute flux in a heterogeneous partially-saturated porous formation, *Water Resour. Res.*, *29*, 1731–1744.
Russo, D. (1995a), On the velocity covariance and transport modeling in heterogeneous anisotropic porous formations: 2. Unsaturated flow, *Water Resour. Res.*, *31*, 139–145.
Russo, D. (1995b), Stochastic analysis of the velocity covariance and the displacement covariance tensors in partially saturated heterogeneous anisotropic porous formations, *Water Resour. Res.*, *31*(7), 1647–1658.
Russo, D. (2005), Stochastic analysis of solute mass flux in gravity-dominated flow through bimodal heterogeneous unsaturated formations, *Vadose Zone J.*, *4*, 939–953.
Russo, D., J. Zaidel, and A. Laufer (1994), Stochastic analysis of solute transport in partially saturated heterogeneous soil: 2. Prediction of solute spreading and breakthrough, *Water Resour. Res.*, *30*(3), 781–790.
Russo, D., A. Hadad, and A. Laufer (1998), A note on the orientation of the macrodispersion tensor in partially saturated heterogeneous porous formations, *Adv. Water Res.*, *21*(1), 63–70.
Sahimi, M. (2012), Dispersion in porous media, continuous-time random walks, and percolation, *Phys. Rev. E*, *85*, 016316.
Sato, T., H. Tanahashi, and H. A. Loáiciga (2003), Solute dispersion in a variably saturated sand, *Water Resour. Res.*, *39*(6), 1155, doi:10.1029/2002WR001649.
Simunek, J., and M. van Genuchten (2008), Modeling nonequilibrium flow and transport processes using HYDRUS, *Vadose Zone J.*, *7*, 782–797.
Tallakstad, K. T., H. A. Knudsen, T. Ramstad, G. Løvoll, K. J. Måløy, R. Toussaint, and E. G. Flekkøy (2009), Steady-state two-phase flow in porous media: Statistics and transport properties, *Phys. Rev. Lett.*, *102*, 074502.
Toride, N., M. Inoue, and F. J. Leij (2003), Hydrodynamic dispersion in an unsaturated dune sand, *Soil Sci. Soc. Am. J.*, *67*, 703–712.
Toussaint, R., K. J. Måløy, Y. Méheust, G. Løvoll, M. Jankov, G. Schäfer, and J. Schmittbuhl (2012), Two-phase flow: Structure, upscaling, and consequences for macroscopic transport properties, *Vadose Zone J.*, *11*(3), doi:10.2136/vzj2011.0123.
Ursino, N., T. Gimmi, and H. Fluhler (2001), Dilution of non-reactive tracers in variably saturated sandy structures, *Adv. Water Res.*, *24*, 877–885.
Vanderborght, J., and H. Vereecken (2007), Review of dispersivities for transport modeling in soils, *Vadose Zone J.*, *6*, 29–52.
Vanderborght, J., et al. (2001), Overview of inert tracer experiments in key belgian soil types: Relation between transport and soil morphological an hydraulic properties, *Water Resour. Res.*, *37*(12), 2837–2888.
Wildenschild, D., and K. H. Jensen (1999), Laboratory investigations of effective flow behavior in unsaturated heterogeneous sands, *Water Resour. Res.*, *35*(1), 17–27.
Willmann, M., J. Carrera, X. Sanchez-Vila, O. Silva, and M. Dentz (2010), Coupling of mass transfer and reactive transport for non-linear reactions in heterogeneous media, *Water Resour. Res.*, *46*, W07512, doi:10.1029/2009WR007739.
Zoia, A., M.-C. Néel, and A. Cortis (2010), Continuous-time random-walk model of transport in variably saturated heterogeneous porous media, *Phys. Rev. E*, *81*, 031104.

AGU PUBLICATIONS

Water Resources Research

RESEARCH ARTICLE

10.1002/2015WR017936

The flow of a foam in a two-dimensional porous medium

Baudouin Géraud[1], Siân A. Jones[1], Isabelle Cantat[1], Benjamin Dollet[1], and Yves Méheust[2]

[1]Institut de Physique de Rennes, UMR CNRS 6251, Université Rennes 1, Rennes, France, [2]Géosciences Rennes, UMR CNRS 6118, Université Rennes 1, Rennes, France

Key Points:
- We study the flow of a 2-D foam in a porous medium and monitor the bubble sizes *A* and velocities *V*
- We observe preferential and intermittent flow, bubble fragmentation, and correlation between *A* and *V*
- Large-scale models of subsurface foam flows may have to take this correlation into account

Correspondence to:
Y. Méheust,
yves.meheust@univ-rennes1.fr

Citation:
Géraud, B., S. A. Jones, I. Cantat, B. Dollet, and Y. Méheust (2016), The flow of a foam in a two-dimensional porous medium, *Water Resour. Res.*, *52*, doi:10.1002/2015WR017936.

Received 31 JUL 2015
Accepted 27 DEC 2015
Accepted article online 30 DEC 2015

Abstract Foams have been used for decades as displacing fluids for enhanced oil recovery and aquifer remediation, and more recently, for remediation of the vadose zone, in which case foams carry chemical amendments. Foams are better injection fluids than aqueous solutions due to their low sensitivity to gravity and because they are less sensitive to permeability heterogeneities, thus allowing a more uniform sweep. The latter aspect results from their peculiar rheology, whose understanding motivates the present study. We investigate foam flow through a two-dimensional porous medium consisting of circular obstacles positioned randomly in a horizontal transparent Hele-Shaw cell. The local foam structure is recorded in situ, which provides a measure of the spatial distribution of bubble velocities and sizes at regular time intervals. The flow exhibits a rich phenomenology including preferential flow paths and local flow nonstationarity (intermittency) despite the imposed permanent global flow rate. Moreover, the medium selects the bubble size distribution through lamella division-triggered bubble fragmentation. Varying the mean bubble size of the injected foam, its water content, and mean velocity, we characterize those processes systematically. In particular, we measure the spatial evolution of the distribution of bubble areas, and infer the efficiency of bubble fragmentation depending on the various control parameters. We furthermore show that the distributions of bubble sizes and velocities are correlated. This study sheds new light on the local rheology of foams in porous media and opens the way toward quantitative characterization of the relationship between medium geometry and foam flow properties. It also suggests that large-scale models of foam flows in the subsurface should account for the correlation between bubble sizes and velocities.

1. Introduction

Aqueous foams consist of air bubbles separated by films of an aqueous solution [*Weaire and Hutzler*, 1999; *Cantat et al.*, 2013] that contain surfactants to lower the surface tension. They are used in a number of industrial applications, including glass manufacturing, ore flotation, or firefighting technology [*Stevenson*, 2012]. Enhanced oil recovery (EOR) has been the first application for subsurface environments: injection of surfactant together with gas into the subsurface has been used as early as 50 years ago [*Patzek*, 1996] to generate foam in situ and improve oil sweep, in particular, in the framework of steam EOR [*Zhdanov et al.*, 1996]. More recently, foams have been used to remediate aquifers contaminated with nonaqueous phase liquids (NAPLs), in a manner very similar to EOR [*Hirasaki et al.*, 1997]. In both applications, the use of foams offers the following advantages: a reduction by 1 order of magnitude in the needed volume of solution for a given injection volume, since only about 10% of the foam consists of liquid solution, the rest being gas; a reduction of the needed amount of surfactant [*Roy et al.*, 1995a, 1995b], a better sweep of the defending fluid due to a more favorable mobility ratio with respect to the oil [*Huang et al.*, 1986], and diversion mechanisms resulting from the particular dissipation mechanisms at play when a foam flows through a porous medium: the foam tends to first occupy large permeability regions, where its low mobility causes later flow to sweep low-permeability regions [*Szafranski et al.*, 1998; *Huang and Chang*, 2000; *Jeong et al.*, 2000; *Jeong and Corapcioglu*, 2003].

A more recent application, which motivates the present study, is the remediation of vadose zone environments, and particularly of soils [*Chowdiah et al.*, 1998; *Jeong et al.*, 2000; *Wang and Mulligan*, 2004; *Zhong et al.*, 2010; *Shen et al.*, 2011; *Zhong et al.*, 2011]. In this context, the foam is used as carrier fluid for chemical amendments rather than as displacing fluid. In this respect, foams offer several advantages: they can be injected while maintaining a low water content in the treated zones, which is cheaper and particularly useful

for remediation of the vadose zone [*Zhong et al*., 2010]; their capacity to transport soil/colloidal particles [*Shen et al*., 2011] and bacteria [*Wan et al*., 1994] at air-water interfaces is high; transport of air along with the aqueous solution may enhance the efficiency of biodegradation [*Rothmel et al*., 1998; *Jenkins et al*., 1993]; in the case of in situ stabilization (of heavy metals, for example), a foam does not displace the target chemicals as much as a solution [*Zhong et al*., 2009, 2011]; they present a better sweeping efficiency than aqueous solutions due to a moderate sensitivity to gravity [*Zhong et al*., 2011]. In column experiments, a breaking of the foam front and consequent propagation of a wetting front ahead of the foam, which may help to optimally deliver the amendments in case of a heterogeneous reaction, has also been reported [*Zhong et al*., 2010].

The flow of bulk foams has been the subject of a vast amount of literature through the years [*Heller and Kuntamukkula*, 1987; *Weaire*, 2008; *Dollet and Raufaste*, 2014]. It occurs through sudden topological events allowing bubble rearrangement. Viscous dissipation within the films/lamellae is thus the dominant dissipation mechanism, resulting in a Herschel-Bulkley rheology; a yield stress σ_y must be overcome for the foam to start flowing, and the rheology under shear is shear thinning:

$$\sigma = \sigma_y + K\,\dot{\gamma}^n\,, \tag{1}$$

where σ is the shear stress, K the consistency, $\dot{\gamma}$ the strain rate, and the exponent n lies in the range [0.2; 0.4] [*Denkov et al*., 2005].

In contrast to bulk flow, when a foam flows inside a porous medium whose channels/dimensions are of the same order as the bubble size, a large part of the dissipation occurs in the wall films and in the Plateau borders that connect these films to the lamellae separating the flowing bubbles. Consequently, the foam rheology is expected to be different from that of bulk foam. Moreover, it strongly depends on the relative sizes of the pores and foam bubbles [*Heller and Kuntamukkula*, 1987]. The mobility of foams through porous media can be expressed in a manner similar to that of Newtonian fluids, using Darcy's law to relate the drop in hydraulic head over a length L of medium, Δh, to the apparent mean velocity, or Darcy velocity, v_d. The standard form of that law is $v_d = (\kappa\,\rho\,g/\mu)(\Delta h/L)$, where κ is the intrinsic permeability of the medium, ρ the mass density of the fluid, and μ its viscosity. For foam flow, it has been proposed that a Darcy law can be written provided that μ is replaced by an effective viscosity $\mu_{\text{eff}} = \mu_g + \beta/v^{1/3}$ [*Friedmann et al*., 1991; *Kovscek and Bertin*, 2003a], where μ_g is the gas viscosity, β is a parameter that depends on the medium geometry, on the foam formulation, and on its texture (that is, its average bubble size), and $v = v_d/\phi$ is the interstitial velocity, ϕ being the porosity of the medium. Combining the expression for the effective viscosity with Darcy's law and neglecting the gas viscosity yields a nonlinear relationship between the pressure and mean interstitial velocity:

$$v = \left(\frac{\kappa}{\beta\,\phi}\right)^{3/2}\left[\frac{\Delta(p+\rho\,g\,z)}{L}\right]^{3/2}, \tag{2}$$

where we have introduced the pressure p and altitude z. Note that the foam mobility through soils, $\kappa\,\rho\,g/\mu_{\text{eff}}$, has been measured to be relatively independent of the soil permeability, and when a dependence existed, the foam's mobility was observed to decrease with increasing soil permeability [*Chowdiah et al*., 1998].

For subsurface applications, the foam is usually generated in situ, by joint injection of surfactant solution and gas. In this framework, the gas is not present everywhere in the medium. The foam is then a dispersion of gas bubbles in a liquid, where the liquid is continuous and part of the gas is made discontinuous by liquid films [*Hirasaki and Lawson*, 1985]. The part of the gas that is not made discontinuous is trapped, while the rest flows as a continuous gas phase. The trapped gas phase represents a very large part (up to 70% or 80%) of the total gas present in the medium [*Kovscek and Radke*, 1994]. *Strong foams* are foams for which a significant part of the flowing gas is discontinuous, so that flow involves the costly displacement of liquid lamellae, rendering the mobility of the gas-liquid mixture much smaller than that of the gas alone. On the contrary, foams for which most of the gas is flowing as a continuous phase are called *weak foams*. What controls whether a foam is strong or weak is a complex issue, but the mean flow velocity and surfactant formulation [*Aronson et al*., 1994] play an important role. The mobilization and trapping of bubbles have been observed to be intermittent processes, due to the existence of preferential flow paths that change in time [*Kovscek and Radke*, 1994; *Cohen et al*., 1997]. Increasing the pressure head increases the portion of gas that

is flowing and renders the foam rheology shear thinning [*Hirasaki and Lawson*, 1985; *Falls et al*., 1989]. In this regime, where the discontinuous gas phase grows or shrinks depending on the applied pressure head, foam texture is the main control parameter for the foam mobility. In this respect, three fundamental mechanisms of lamella/film creation occur during foam generation within a porous medium: *leave-behind*, in which two gas fingers invade two adjacent and communicating liquid-filled pores, trapping a film of liquid in-between them after the pores have been fully invaded; *capillary snap-off*, in which the snap-off of liquid films at the throat between two pores separates a gas bubble in two [*Roof et al*., 1970; *Gauglitz and Radke*, 1990; *Kovscek and Radke*, 1994; *Kovscek et al*., 2007]; *lamella division*, in which a liquid film touching a solid grain while still attached to other grains on this perimeter separates into two films that travel on either side of the dividing grain [*Kovscek and Radke*, 1994]. Mechanisms of bubble disappearance are also at play when a foam flows through a porous medium; they consist mostly in (i) coarsening through gas diffusion and (ii) bubble coalescence by capillary suction. Bubble coarsening results from the diffusion of gas from smaller bubbles where the pressure and chemical potential are larger, to neighboring larger bubbles; it has been studied extensively in the context of bulk foams [*Cantat et al*., 2013]. In porous media, it is observed at locations where bubbles are trapped [*Kovscek and Radke*, 1994]. Bubble coalescence by capillary suction involves the sudden rupture of a lamella; it occurs when a lamella/film that has been sitting at a pore throat is displaced quickly into a pore volume much wider than the throat, and cannot adjust its liquid volume sufficiently fast to avoid rupturing [*Khatib et al*., 1988].

The impact of foam texture or structure on the pressure drop across a porous medium, and, consequently, on flow through that medium, has also been examplified in experimental and theoretical studies performed on systems of aqueous films confined in simple geometries: single film flowing across a biconical pore [*Rossen*, 1990; *Cox et al*., 2004; *Ferguson and Cox*, 2013], single bubble [*Bretherton*, 1961], or bubble trains [*Cantat et al*., 2004; *Terriac et al*., 2006] flowing in capillaries, two-dimensional monodisperse foams of various structures (e.g., staircase structures) flowing in a single channel [*Raven and Marmottant*, 2009; *Marmottant and Raven*, 2009], in parallel channels of different widths [*Jones et al*., 2013], or in parallel convergent-divergent channels [*Dollet et al*., 2014]. Note also that the reverse also holds: given confining shapes can select particular foam structures [*Drenckhan et al*., 2005]. Already in the seminal study by *Bretherton* [1961], a scaling of the pressure drop ΔP along the medium as a function of the mean foam velocity V in the form $\Delta P \propto V^{2/3}$ was demonstrated; it was later generalized to the more complex configurations mentioned above [*Cantat et al*., 2004; *Terriac et al*., 2006; *Raufaste et al*., 2009; *Jones et al*., 2013; *Dollet et al*., 2014]. Such a scaling is perfectly consistent with rheology measurements performed at the scale of a soil column or rock core and described by equation (2) above.

While much is already known qualitatively on the mechanisms of foam displacement in porous media, and many existing macroscopic models [e.g., *Kovscek and Radke*, 1994; *Kovscek et al*., 1995; *Fergui et al*., 1998; *Kornev et al*., 1999; *Alvarez et al*., 2001; *Kam et al*., 2003; *Dholkawala et al*., 2007] address the generation and macroscopic displacement of foams in porous media, experimental studies usually involve the use of core flooding units [*Fergui et al*., 1998; *Apaydin and Kovscek*, 2001; *Pang*, 2010] from which it is difficult to obtain detailed information on the local foam structure: only global quantities can be measured, and only qualitative information on local displacement dynamics is inferred. In recent years, experiments using X-ray microtomography [*Apaydin and Kovscek*, 2001; *Zitha et al*., 2006; *Nguyen et al*., 2007; *Du et al*., 2008; *Simjoo et al*., 2012] or γ ray attenuation [*Fergui et al*., 1998] have enabled limited visualization of foam flow, revealing regions of preferential occupation of the medium by the foam and providing spatially resolved measurement of liquid fractions, also under conditions of oil sweep [*Simjoo et al*., 2013]. Experiments based on micromodels consisting of pore networks [*Jeong et al*., 2000; *Chen et al*., 2005; *Ma et al*., 2012; *Jeong and Corapcioglu*, 2003], on the other hand, have mainly been used to investigate oil or NAPL sweep, and have not allowed precise bubble-scale observation of the foam kinematics, or only on a small subpart of the system [*Jeong and Corapcioglu*, 2005], for example, in order to assess the role of capillary snap-off on foam generation [*Kovscek et al*., 2007].

In this paper, we present a series of experiments performed on a transparent two-dimensional porous medium consisting of cylindrical grains. The setup allows for full in situ time-resolved measurement of the foam structure as well as of the bubble size and individual velocities, at the expense of dimensional reduction. Previous studies on analogous models with more simple geometries have evidenced the importance of foam structure on the distribution of flows between two parallel linear channels [*Jones et al*., 2013] and the potential impact of elastic effects on the foam mobility [*Dollet et al*., 2014]. In the following, we focus on flow characteristics already known from the literature but to our knowledge never addressed

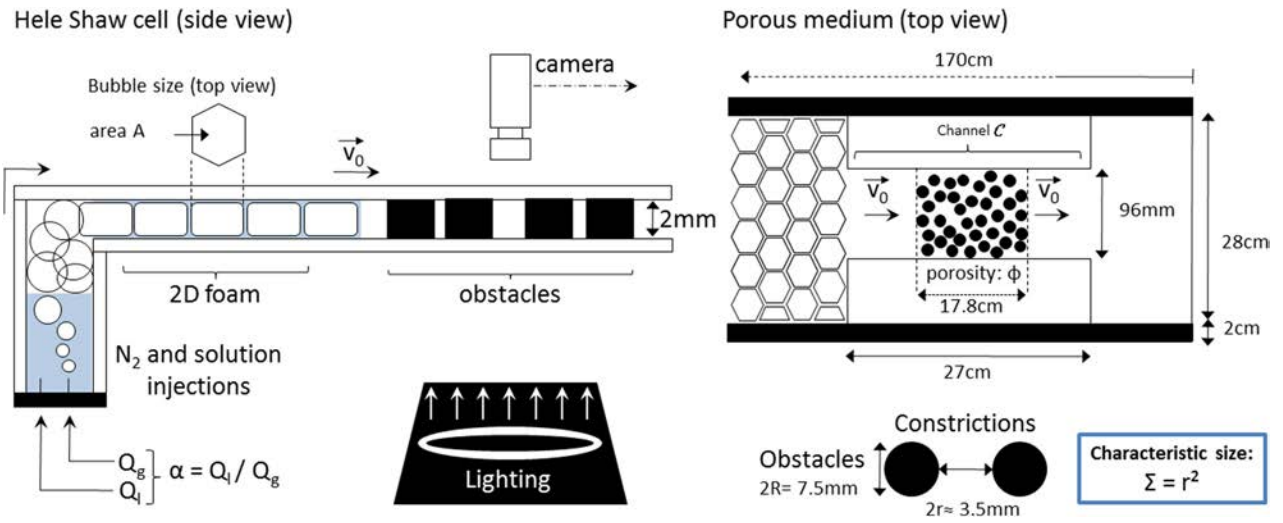

Figure 1. Sketch of the experimental setup: (left) side view and (right) top view.

experimentally with quantitative measurements: preferential flow and its relationship to the velocity probability density distribution, flow intermittency, and dynamics of the bubble size distribution. We inject into the medium a preexisting foam, so no continuous gas phase is present in our system.

The experimental methods are described in detail in section 2, while section 3 is devoted to a presentation and discussion of the results. In section 4, we summarize the findings and conclude.

2. Methods

2.1. Experimental Setup

We used an apparatus derived from the one described by *Jones et al*. [2013] (see Figure 1). The flow cell is a 170 $\times$ 32 cm^2 Hele-Shaw cell with a gap $h = 2$ mm between the glass plates. Obstacles positioned inside the Hele-Shaw cell define the pore geometry. The cell is enlightened by a circular fluorescent tube of diameter 37 cm, placed on a dark background and beneath the porous medium so as to optimize the contrast of foam films on the images. The foam structure is recorded at a regular time interval using a camera with a 1312 $\times$ 1082 resolution (Photon Focus, Alliance Vision). The acquisition rate is chosen according to the imposed flow rate and ranges from 5 to 100 Hz.

In the present study, the grains of the two-dimensional porous medium consist of monodisperse cylinders of diameter $2R = 7.5$ mm and of height equal to the cell thickness h, placed inside a narrow channel $\mathcal{C}$ near the outlet of the cell. The Hele-Shaw cell thus contains a two-dimensional porous medium. The channel $\mathcal{C}$ is 9.6 cm wide and 27 cm long, 17.8 cm of the length containing cylindrical grains. The obstacle positions were defined from a computer-generated geometry obtained by perturbing a diagonal regular mesh with a random displacement drawn from a Gaussian distribution; the process ensured that the porous medium always had a porosity $\phi = 0.5 \pm 0.02$.

2.2. Foam Generation and Flow

The foam is produced by injecting gas into a reservoir saturated with a foaming solution. A foam thus grows inside the reservoir and is displaced into the Hele-Shaw cell (see Figure 1). As they enter the cell, bubbles are squeezed between the top and bottom plates so that they are only separated from each other by vertical films (lamellae).

We used two kinds of foaming solutions in order to probe the influence of the film interfaces on the flows. We dissolved two kinds of sodium dodecyl sulfate (SDS) powders in water, one 99.9% pure and the other one 98.5% pure (Aldrich). Solution type 1 ($ST = 1$) refers to a solution obtained by dissolving 98.5% SDS in ultrapure water, solution type 2 ($ST = 2$) to one obtained from 99.9% SDS and ultrapure water. These solutions were prepared at the same surfactant concentration of 10 g/L.

Monodisperse foams are obtained by blowing nitrogen in the foaming solution at moderate gas flow rates ($Q_g \leq 200$ mL/min). The bubbles entrain the liquid from the reservoir as they leave it to enter the flow cell; we could measure the liquid flow rate Q_l from the decrease of the solution level in the reservoir with time. The resulting flux ratio $\alpha = Q_l/Q_g$ was on the order of a few percents, corresponding to what we qualify as *dry foams*. We also produced *wet* foams ($\alpha \simeq 10\%$) by injecting the solution into the cell using a peristaltic pump. These two techniques allowed us to investigate the behavior of foams of various liquid fractions ϕ_l and obtained from different surfactant solutions. Note that the *foam quality* $1-\phi_l$ is commonly used to characterize the amount of water within the foam.

The pressure variations in the cell remain orders of magnitude smaller than the atmospheric pressure. Consequently, the gas is safely assumed incompressible. In steady state, the volumetric fluxes of gas and liquid are thus uniform in the cell. The volumetric liquid fraction ϕ_l and the mean velocities $\langle v_l \rangle$ and $\langle v_g \rangle$ of the liquid and gas phases, respectively, are related to the flux ratio α as follows:

$$\alpha = \frac{\phi_l \langle v_l \rangle}{(1-\phi_l)\langle v_g \rangle} . \tag{3}$$

For comparable velocities and small liquid fractions, we would thus approximate $\alpha \simeq \phi_l$. In contrast to the mean gas velocity, however, the mean velocity of the liquid phase, $\langle v_l \rangle$, may differ from the measured bubble velocities and cannot be directly deduced from it. The liquid velocity is expected to be smaller than $\langle v_g \rangle$ in the wetting films on the top and bottom plates and larger than $\langle v_g \rangle$ in the meniscus network [*Wong et al.*, 1995]. Hence the parameters α and ϕ_l are a priori different, even though strongly correlated, and ϕ_l cannot be easily known. In the following, we therefore resort to the well-controlled experimental parameter α to characterize the foams, which are also identified by their solution type.

The length of the Hele-Shaw cell allows us to first produce the foam and fill the first part of the Hele-Shaw cell (see Figure 1) and then push this foam into the second part of the cell, where the obstacles are located. The gas and liquid fluxes Q_g and Q_l refer to the fluxes during the foam production, not during the measure. Q_g essentially defines the bubble size and Q_l/Q_g the liquid fraction. The gas flux is then modified to obtain the desired mean foam velocity. Bubble sizes and velocities were computed from image processing of the movies as explained in the following.

2.3. Image Treatment and Analysis

Images recorded at regular time intervals were analyzed using a custom made Matlab program. The processing consists of two parts: (i) the characterization of the porous medium and (ii) the analysis of the foam structure in time. The important steps of the entire process are shown in Figure 2, on a portion of the porous medium for clarity. Figure 2a shows a portion of a raw image. The white disks are the solid grains, while the dark polygons denote patches of double-sided bonding tape that are used to glue some of the grains to the Hele-Shaw cell. These polygons have been removed from all the foam structure snapshots that appear later in this article. Before each flow experiment, a picture of the empty 2-D porous medium is

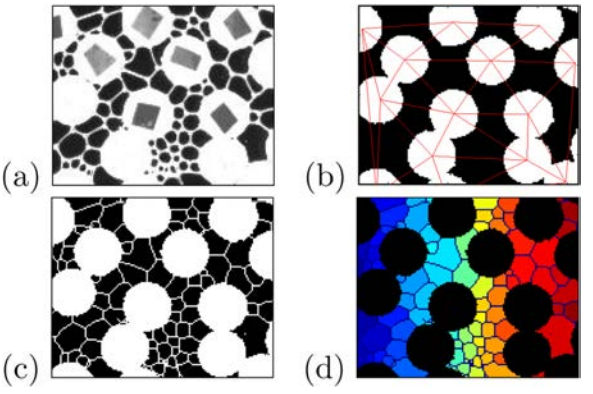

Figure 2. Successive steps in the image treatment: (a) raw image of the foam; (b) mask image defining the grains, with corresponding Delaunay triangulation superimposed; (c) binary image obtained from thresholding and skeletonizing the raw image (Figure 2a), and finally superimposing the mask (Figure 2b); (d) image with the different bubbles identified by different colors.

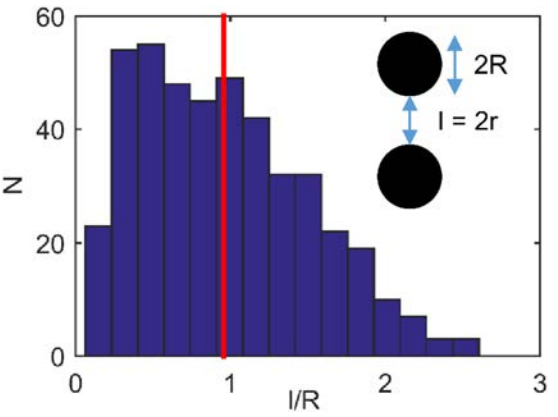

Figure 3. Distribution of the constriction widths / between neighbor obstacles. From this distribution, we define the length scale $r=\langle l\rangle/2$, which corresponds to the critical radius for a bubble to pass through a constriction without being deformed.

recorded. The binarization of this picture provides a "mask" that defines the geometry of the porous (and solid) space (see Figure 2b). This porous configuration is then characterized in the following manner. First, the positions of the entrance and exit of the porous medium are defined as the first and last segments perpendicular to the channel axis and that touch an obstacle. This definition then allows for a consistent measurement of the porosity. Second, a Delaunay triangulation provides the nearest neighbor obstacles for each grain, and consequently the *constriction* sizes, i.e., the distances l between nearest neighbors. The distribution of l is shown in Figure 3. We then define the distance r from the average value of l, as $r=\langle l\rangle/2$. This characteristic length scale of the disordered pore geometry is important for the foam flow process, since it corresponds to the critical radius of a bubble passing through the constriction without being deformed. We further define a characteristic size $\Sigma=r^2$, which we shall use to compare the bubble sizes to the geometry of the medium. In our experimental setup, we have $\Sigma \approx 3.2 \pm 0.3$ mm^2. For each flow image, the foam structure and dynamics are obtained through the following steps. First, the contrast is enhanced and the image is thresholded into a black and white image in which only the soap films and the obstacles remain visible. This image is then skeletonized, that is, all film widths are reduced to one pixel (Figure 2c). Note that the film width that is apparent on the raw picture is not the actual film width in the mid-plane of the cell, it corresponds rather to the transverse extent of the Plateau borders between the vertical films and the film that wets the cell's top plate; choosing a film width of one pixel is somewhat arbitrary but is much closer to the real film thickness. In the skeletonized picture, solid grains are then precisely defined from the mask obtained in (i). The skeletonized image is then inverted and a segmentation function of Matlab is used to identify the various bubbles and record their positions and areas (Figure 2d). Finally, we use a tracking algorithm to track each bubble between one image and the image recorded at the next acquisition time step. We thus infer bubble displacements during a time step, and from this, their velocities. The average velocity of the bubbles before entering the porous medium and after leaving it (while still in channel $\mathcal{C}$) are very close to each other, as expected. Their mean value V_0 is what we shall denote *velocity in the flow cell* in the following (see Figure 1); the mean interstitial velocity is thus expected to be V_0/ϕ.

2.4. Control Parameters for the Experiments

The parameters that define an experimental run are the following: the mean bubble area before the foam enters the porous medium, A_0, the flux ratio, $\alpha=Q_l/Q_g$, the gas flow rate, Q_g (during foam preparation), the mean foam velocity inside the flow cell, V_0, and the type of surfactant, *ST*. In this study, we present results from 45 experimental runs. The experimental parameters for these experiments are summarized in Table 1.

3. Results

In this section, we describe a set of general phenomena generic to foam flows in porous media. These processes are particularly interesting for applications such as subsurface remediation, but also from a fundamental point of view, since they are due to the peculiar nature of the foam and are not observed with Newtonian fluids. In this section, we often take some specific experiments as typical examples to illustrate the general phenomena involved, but we also perform a parametric study of the impact of the various control parameters on the investigated processes.

3.1. Preferential Flow Paths

Figure 4 (top) shows a snapshot of the flowing foam structure during experiment number 7. The velocity field, averaged over a duration of 100 s, is shown in Figure 4 (middle); preferential flow paths are clearly visible in this experiment. Nonuniform spatial distribution of foam mobility was previously observed by *Nguyen et al.*

Table 1. Control Parameters for the 45 Foam Flow Experiments[a]

Experiment	1	2	3	4	5	6	7
A_0/Σ	2.08	2.38	2.39	2.43	2.45	2.61	2.68
α	1.0	1.0	1.0	1.0	47.6	47.6	37.9
Q_g	28.3	28.3	28.3	28.3	22.5	22.5	28.3
V_0	1.34	3.44	0.82	1.44	0.75	1.75	2.54
ST	2	1	1	1	1	1	1
Experiment	8	9	10	11	12	13	14
A_0/Σ	3.16	3.18	3.19	3.35	3.44	3.49	3.94
α	21.4	21.4	21.4	21.4	1.5	1.5	1.5
Q_g	50.0	50.0	50.0	50.0	100.0	100.0	100.0
V_0	0.99	2.66	1.77	3.27	3.78	8.47	4.16
ST	1	1	1	1	2	1	2
Experiment	15	16	17	18	19	20	21
A_0/Σ	3.95	3.96	3.97	3.98	3.99	4.06	4.09
α	10.7	10.7	10.7	10.7	6.1	3.1	2.3
Q_g	100.0	100.0	100.0	100.0	100.0	100.0	200.0
V_0	5.11	4.59	3.68	1.12	3.95	4.19	8.07
ST	2	2	2	2	2	2	2
Experiment	22	23	24	25	26	27	28
A_0/Σ	4.11	4.12	4.17	4.25	4.31	4.35	4.36
α	10.7	10.7	10.7	0.6	10.7	1.5	1.5
Q_g	100.0	100.0	100.0	200.0	100.0	100.0	100.0
V_0	4.57	4.03	3.55	8.57	6.50	8.84	3.70
ST	2	2	2	2	2	2	1
Experiment	29	30	31	32	33	34	35
A_0/Σ	4.45	4.50	4.68	4.72	4.76	4.77	5.09
α	1.5	1.5	10.7	10.7	10.7	10.7	1.5
Q_g	100.0	100.0	100.0	100.0	100.0	100.0	100.0
V_0	1.84	0.44	1.78	3.49	0.99	2.76	6.61
ST	1	1	1	1	1	1	1
Experiment	36	37	38	39	40	41	42
A_0/Σ	5.13	5.15	5.37	5.39	5.43	5.52	5.54
α	1.5	1.1	1.5	1.5	10.7	10.7	10.7
Q_g	100.0	200.0	100.0	100.0	100.0	100.0	100.0
V_0	3.68	10.46	0.84	1.71	5.41	5.53	5.41
ST	1	2	1	1	2	2	2
Experiment	43	44	45				
A_0/Σ	6.22	6.31	6.48				
α	10.7	5.1	10.7				
Q_g	100.0	100.0	100.0				
V_0	6.33	20.57	6.13				
ST	2	2	2				

[a]The parameters are the ratio A_0/Σ of the initial mean bubble area to the characteristic size of the pores; the flux ratio α (here in %) and the gas flow rate Q_g (in mL·min^{-1}) used for the foam preparation; the mean foam velocity in the cell, V_0, in mm·s^{-1}; and the type of foaming solution, *ST*.

[2007] using X-ray tomography; they showed qualitatively that preferential flow paths existed. Figure 4 (bottom) shows a map of the pores in which the color for each pore indicates the ratio of its linear size (defined as the square root of its area) to that of the largest pore. A description of how the pores have been determined is given in Appendix A. Visual comparison between the maps of pores and local velocities shows that most preferential paths occur where a series of large pores are connected together. This is analog, for foam flow and at the pore scale, to a Darcy-scale phenomenon well known for water flow in soils: preferential flow generally occurs along paths of permeability larger than the average medium permeability.

The probability density function (PDF) of the velocity field shown in Figure 4 (middle) is shown in Figure 5. The PDF is rather widely distributed for the positive values of V_x, corresponding to the longitudinal flow direction. The inset shows the PDF in a semilogarithmic representation. The concavity of the curve on this plot indicates that the decay of the PDF is faster than an exponential one. The PDF also features a large

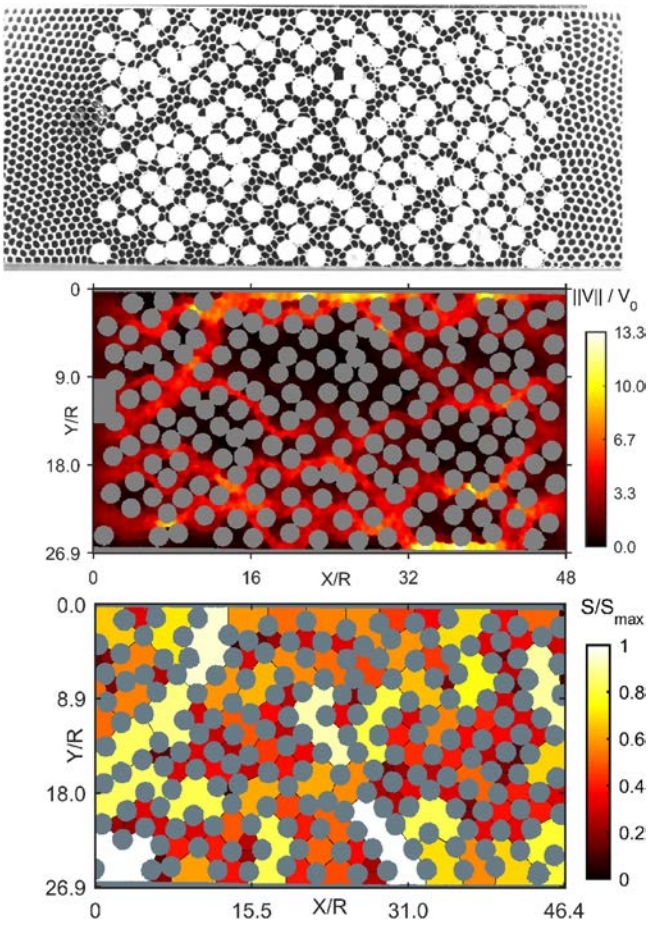

Figure 4. (top) Snapshot of the foam structure during experiment 7 ($A_0/\Sigma = 2.68$, $\alpha = 37.9\%$, $V_0 = 2.54$ mm/s). (middle) Map of normalized bubble velocities, averaged over 100 s, for the same experiment. (bottom) Spatial organization of the pores: the color of the pores indicates their linear size normalized by the linear size of the largest pore.

peak at small velocities, corresponding to bubbles trapped in regions of low flow velocity in-between closely set grains, and which oscillate around their trapping position, hence the negative values of the longitudinal velocity. These bubbles do not contribute to the flow inside the porous medium and play a role equivalent to the obstacles on short time scales. On each image, we define the trapped bubbles as the bubbles with an instantaneous velocity smaller than 0.2 V_0, the other ones being defined as the mobile bubbles. This arbitrary cutoff is qualitatively consistent with our observation of oscillating bubbles. The trapped bubbles in experiment 7 cover about 18% of the free area in the cell. The flow thus behaves as if the *effective* porosity of the porous medium, ϕ_{eff}, was 43% instead of 52%. This has been checked by computing the average velocity of mobile bubbles, $\langle V_x^m \rangle$. Indeed we find $\langle V_x^m \rangle = 2.5\, V_0$ while we expect 1.9 V_0 with a porosity of 52% and 2.3 V_0 with a porosity of 43%.

Finally, note that negative values of V_x can also be recorded for two other reasons: the first one is due to a few errors in the tracking of the bubbles. These events are rare and we estimate that their contribution to the computation leads to an uncertainty on the order of 0.1% on the PDF amplitude. The second one is the presence of regions in which the bubbles have to get around obstacles in such a manner that they happen to flow temporarily backward with respect to the main flow direction.

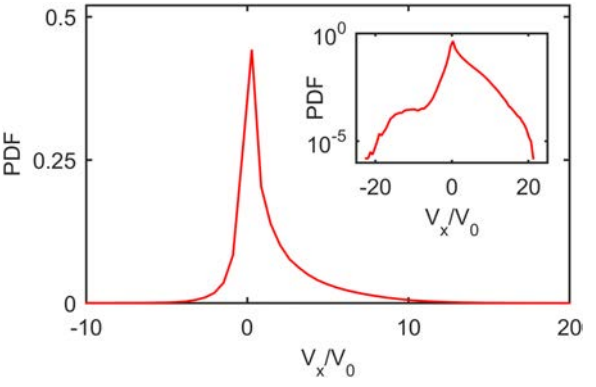

Figure 5. Probability density function of the velocity for experiment 7. The inset shows the PDF in semilogarithmic representation.

3.2. Local Intermittency

Let us now consider experiment number 5, which was performed under conditions identical to those of experiment number 7, except that the mean foam velocity V_0 was more than 3 times lower (see Table 1). Averaging the velocities over a time scale of 1 s, we observe that the velocity map changes with time (see Figure 6). The distribution of fluxes between channels is not permanent; local intermittency of the flow is observed, in spite of the constant, flow-driving, pressure gradient imposed between the inlet and outlet of the flow cell. The local flow intermittency results in fact from strong fluctuations

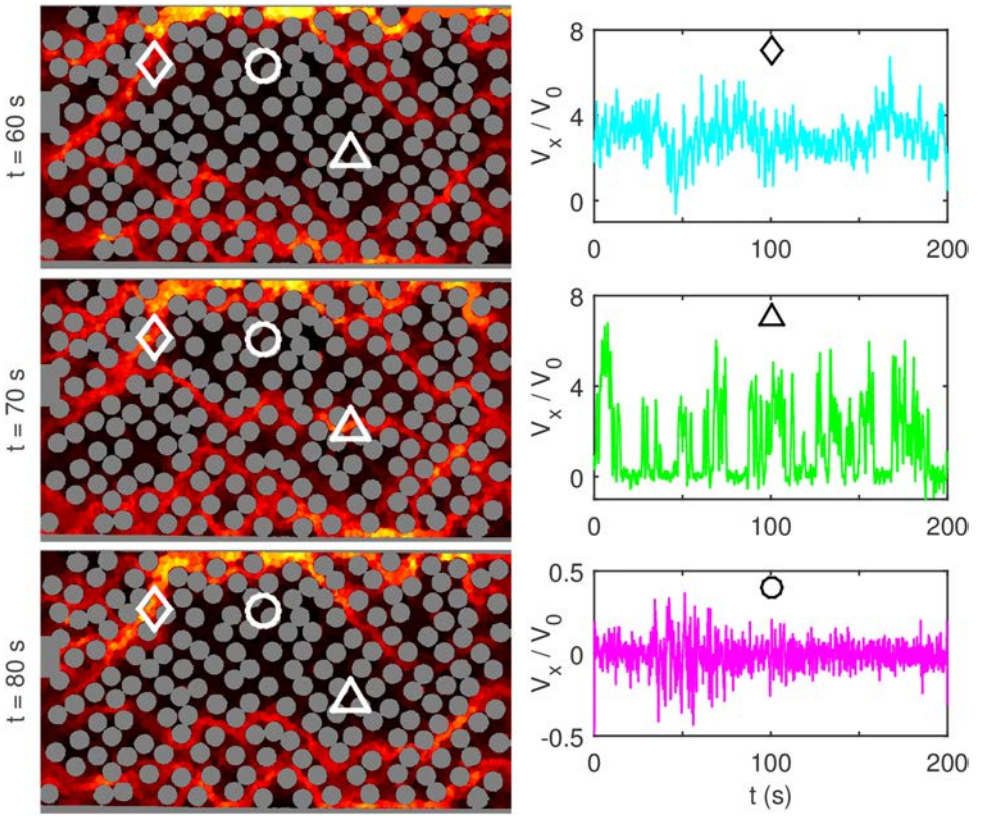

Figure 6. (left column) Example of local intermittency in the distribution of the local preferential channels in experiment 5. The experiment is performed in conditions similar to those of experiment 7, but with an entrance velocity more than 3 times lower. (right column) Evolution of the bubble velocity at the three positions indicated by three symbols on the velocity maps. The velocity maps and time evolutions of velocities are obtained by averaging the measurements over 1 s.

of the local pressure gradient, both in time and space: such fluctuations are essentially a Laplace pressure-related effect, that is, they correspond to fluctuations in time and space of the effective capillary force felt by each bubble. Indeed, when a film is in contact with two obstacles, its shape adapts to fulfill the contact condition at both ends, resulting in a curvature of the film and consequently in a Laplace pressure across the film, or equivalently in a capillary force along the normal to the film; depending on the film concavity, the capillary force can be an additional driving force, or on the contrary, a resisting force. The effective capillary force felt by the bubble is the sum of the capillary forces acting on all films along the bubble perimeter. For a given bubble, it varies in time depending on the geometry of the grains with which the bubble is in contact. From a Eulerian point of view (that is, seen in the fixed coordinate system of the laboratory), this translates into fluctuations in time and space of the local pressure gradient, as mentioned above.

In order to further illustrate this local intermittency, we have sampled the local longitudinal component V_x of the velocity in time, at three positions within the flow field shown in Figure 6: one at which preferential flow is always present (top, cyan line), one at which there is no preferential flow (bottom, pink line), and one at which preferential flow occurs in an intermittent manner (middle, green line). They are plotted in Figure 6 (right column) and are consistent with the visual observations. In the top plot, V_x fluctuates around a mean velocity $V_x = 3.0\ V_0$, while in the bottom plot, it is distributed symmetrically around a zero mean, with fluctuations smaller than $0.4\ V_0$. In the intermediate regime (middle plot), the velocity evolution exhibits alternating periods of very small velocities ($\lesssim 0.1\ V_0$) and positive velocities larger than the global average interstitial velocity $V_0/\phi \simeq 1.9\ V_0$. Note however that in this experiment, V_0 is very low, which results in an uncertainty of about 25% on its estimated value. In order for intermittency to be significant, the imposed pressure drop must not be too large with respect to capillary fluctuations, and therefore the average interstitial velocity must be low.

Intermittency is observed to be more pronounced for smaller bubbles. This is expected in view of the interpretation of intermittency provided above. Since the Laplace pressure across a single film is on the order of γ/r, with

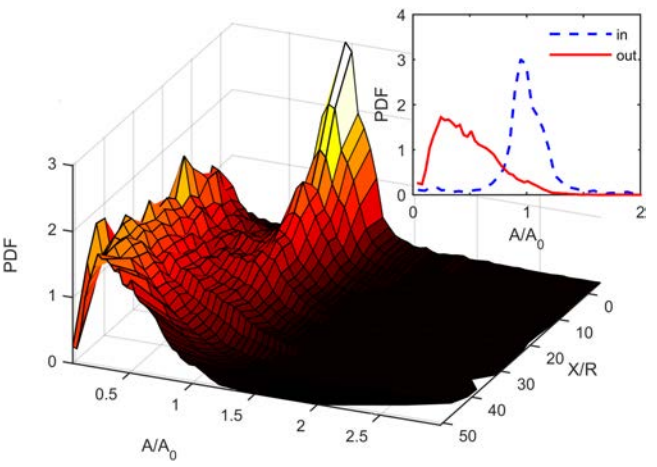

Figure 7. Evolution of the bubble area probability density function (PDF) along the medium, between the initial state (dashed blue line in the inset) and the final state (continuous red line in the inset) in experiment 28 ($A_0/\Sigma = 4.36$, $\alpha = 1.5\%$, $V_0 = 3.70$ mm/s). A/A_0 is the ratio of the bubble area to the initial average bubble area, A_0.

γ being the surface tension coefficient and r the half-distance between the two obstacles (see the inset of Figure 3), the averaging of capillary forces over all films along a bubble perimeter is likely to provide different results depending on the relative magnitudes of the mean bubble size and typical pore size in the medium. Bubbles much larger than the typical size between obstacles are limited by a large number of films in contact with two obstacles; under these conditions, the contribution of the capillary forces through individual films to the effective capillary force felt by one bubble average out statistically, so that the local pressure gradient felt by the bubble equals more or less the global, constant, pressure gradient. Smaller bubbles, on the contrary, are subjected to much larger local pressure fluctuations; in some configurations, capillary forces through individual films may add up along a bubble perimeter to produce a significantly resistive force which is able to overcome the mean driving force associated to the global pressure gradient: the small bubble is then trapped.

3.3. Selection of the Bubble Size Distribution by the Medium

3.3.1. Evolution in Time of the Bubble Size Distribution

For a large enough initial mean bubble size A_0, the outgoing foam is much more polydisperse than the incoming foam. Hence, the probability density function (PDF) for bubble areas evolves along the path through the porous medium. This PDF has been computed in windows of width 50 pixels along the longitudinal direction of the porous medium, which corresponds to an average obstacle diameter plus a constriction width $2(R + r)$. The evolution of the distribution as a function of the longitudinal coordinate (normalized by the typical obstacle radius) is shown in Figure 7 as a three-dimensional plot. As expected, the PDF for the incoming foam (also shown as a blue line in the two-dimensional plot of the inset) is peaked rather symmetrically around the mean bubble size. The PDF for the outcoming foam (also shown as a continuous red line in the 2-D plot of the inset in Figure 7), in contrast, is skewed, with a most probable value about 4 times smaller than that for the incoming foam, and a mean value also more than twice smaller than the incoming mean bubble size. The symmetrical peak of the PDF for the incoming foam (the dashed blue line in the figure inset) decays in time while the outlet distribution (the continuous red line in the figure inset) builds up. Clearly, the initial "mode" disappears while a new distribution, chosen by the medium and much broader, develops.

3.3.2. Size Adjustments Mechanisms

The bubble size distribution evolves under the effect of two mechanisms: lamella division and film breakage.

Lamella division is one of the three classically recognized mechanisms of foam generation in a porous medium [see *Kovscek and Radke*, 1994]. In contrast to the two other mechanisms (leave-behind and capillary snap-off), lamella division can also occur within a preexisting foam flowing through the medium, as illustrated in Figure 8. Let us consider a bubble that is being displaced along a pore whose lateral walls are defined by two grains, the rear film (or lamella) belonging to the bubble is in contact with each grain, on each side. If this film comes in contact with a third grain placed ahead of the two others, it divides into two films, each in its distinct pore. This leads to the formation of two bubbles from the unique bubble colored in red in Figure 8a. The combined area of the two resulting bubbles is identical to that of the initial single bubble within about 0.1%, despite the fact that the pressure within a bubble depends on the curvature radius of its interface and therefore on its size. Indeed, the capillary pressure across a lamella is about 3 orders of magnitude smaller than the pressure on either side of the lamella. The mechanism of bubble

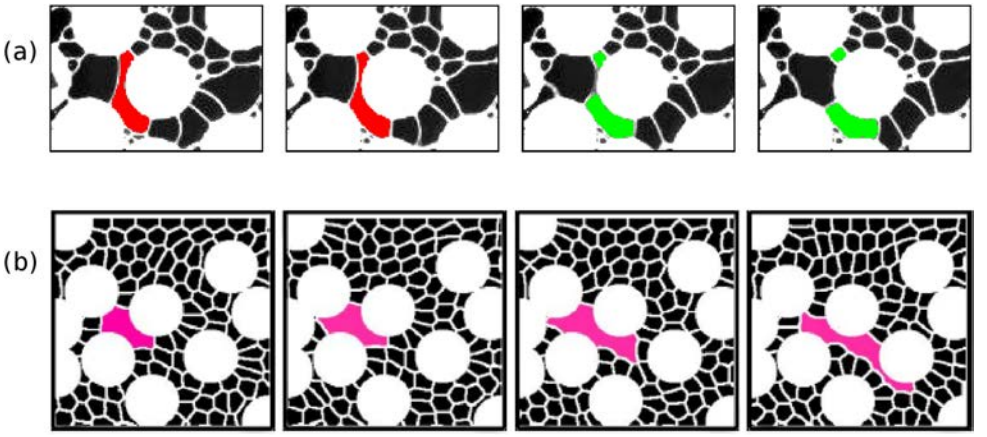

Figure 8. The two mechanisms of bubble size evolution: (a) fragmentation of a bubble by lamella division, and (b) film breakage. In Figure 8a, a bubble is shown just prior to the contact between its rear film and a grain; in Figure 8b, the film breakage triggers an escape of the bubble from the pore where it was initially trapped.

fragmentation resulting from the division of a film (or lamella) appears to be dominant in controlling the time evolution of the bubble size distribution in our system. Note that the effect of this mechanism was recently studied numerically by *Cox* [2015] on a bamboo foam meeting one or several obstacles. A bamboo foam is a foam that circulates in a narrow channel and whose lamellas all span the entire cross section of the channel [*Terriac et al*., 2006]; it corresponds to the simplest possible topology for a foam.

The second mechanism is film breakage, and was less frequently observed than bubble fragmentation in our system. Figure 8b provides an example of configuration in which film breakage provokes the merging of a bubble trapped between three grains and another bubble positioned outside of that "trap." Consequently, further film breakage occurs ahead of the bubble, allowing it to escape the trap.

If one considers that lamella division is the mechanism mainly controlling the evolution of the bubble area PDF shown in Figure 7, each bubble of the incoming foam will, by lamella division, fragment into two bubbles of sizes smaller than their "mother", and the mean bubble size is thus expected to decrease continuously as the foam progresses through the medium, meeting sites with a local geometry appropriate for lamella division. This is consistent with the three-dimensional plot in Figure 7.

Some authors indicate that mechanisms responsible for lamellae creation and destruction in porous media eventually balance each other, leading to a uniform texture of the flowing foam, a property that can be inferred from the near-linear dependence of the pressure drop along the medium as a function of the medium length [e.g., *Pang*, 2010]. In our experiments, we experience very few bubble disappearances according to the mechanisms described in section 1. Indeed, on the one hand bubble coarsening is not observed, even in aggregates of trapped bubbles, because the typical time scale for gas diffusion through the aqueous films remains much larger than the time of completion of our experiment. In any case, it would not be able to compete with the fast occurring bubble fragmentation. On the other hand, since in our porous medium pore throat widths are of the same order as pore sizes, film rupture due to capillary suction is unlikely, except for very large mean velocities that have not been investigated here.

3.3.3. Influence of the Various Parameters on Bubble Size Selection

We have systematically quantified the efficiency of bubble fragmentation, as a function of the experimental parameters presented in Table 1. For that purpose, we define an efficiency of fragmentation as

$$e_{fr} = \frac{A_0 - A_\infty}{A_0}, \tag{4}$$

where A_0 is the bubble size of the incoming foam and A_∞ the mean bubble size measured at the outlet of the porous medium. The fragmentation efficiency is 0 when A_∞ is identical to A_0, and reaches 1 when the A_∞ approaches 0.

In Figure 9, we show the values of e_{fr} for all 45 experiments, represented as a function of the initial average bubble area A_0 in three distinct plots, each one corresponding to one of the following ranges of flux ratio α:

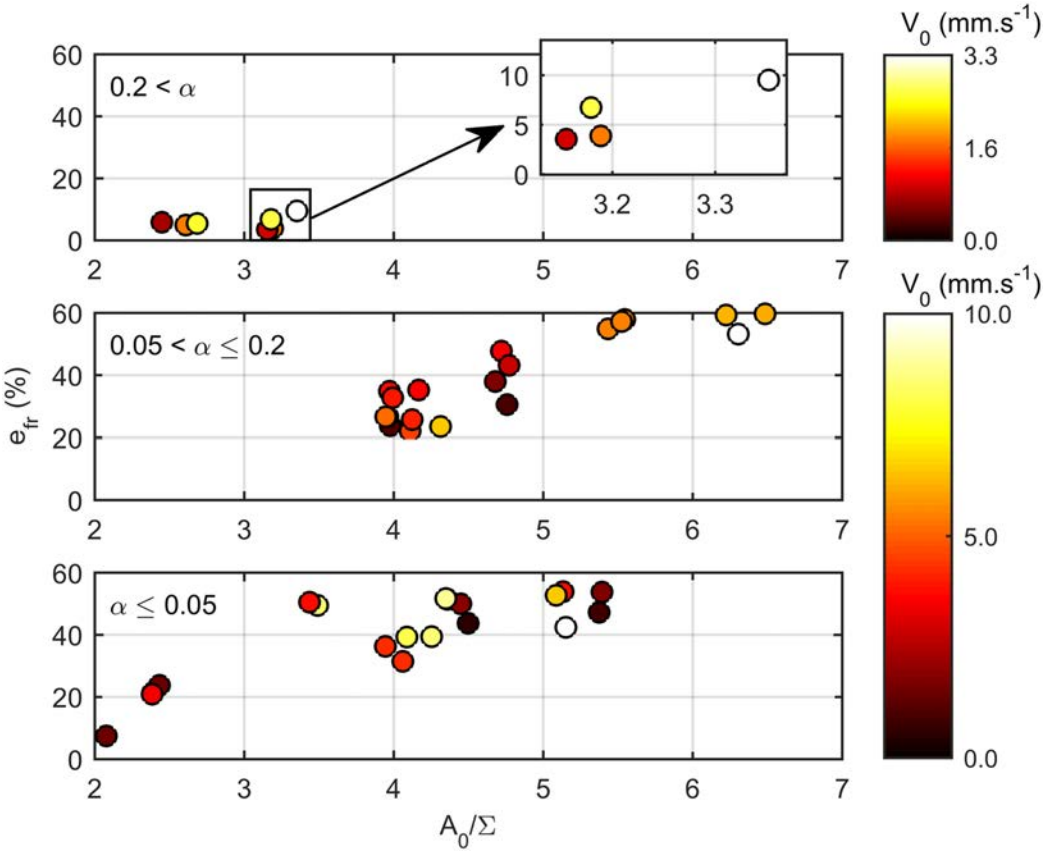

Figure 9. Fragmentation efficiency e_{fr} represented as a function of the mean bubble area of the incoming foam, A_0, normalized by the medium's characteristic length scale, Σ, for three ranges of flux ratio α: $\alpha > 0.2$ (top), $0.05 < \alpha \leq 0.2$ (middle), and $\alpha \leq 0.05$ (bottom). The color of the symbols indicates the entrance velocity V_0 during that experiment.

$\alpha \leq 0.05$ (the driest foams, bottom plot), $0.05 < \alpha < 0.2$ (middle plot), and $\alpha > 0.2$ (the wettest foams, top plot). Each colored disk corresponds to one experiment, and the color scale for the disks indicates the average foam velocity V_0 for the various experiments. We observed that the type of surfactant used for the foam preparation had a negligible impact on the measured fragmentation efficiency, all other parameters being equal. We therefore do not distinguish the types of surfactant in the plots. Notice that our experiments do not span the region of both larger A_0 and larger α values, because the foam generation and injection setup does not allow for a full independent control of bubble size and injection velocity.

This diagram shows that the efficiency depends mostly on the initial mean bubble area A_0 and flux ratio α, which controls the quality of the foam. It appears, within the limits of our sampling of the parameter space, that the fragmentation efficiency increases with the mean incoming bubble area and decreases with the flux ratio (or equivalently, increases with the foam quality). The observed dependence on the incoming bubble area is expected, as larger bubbles are more likely to be subjected to lamella division. Based on this division mechanism, we would also expect that the foam velocity should have little impact on the fragmentation efficiency. This hypothesis seems to be verified by our data, although it cannot easily be tested since experiments performed at different mean foam velocities also often differ in the mean bubble area of the incoming foam or the flux ratio. The influence of the flux ratio α on the fragmentation efficiency can be understood as follows: prior to lamella division, the lamella spans a large gap between two obstacles (Figure 8a), which enforces a significant deformation of the bubble that is about to split. Increasing α, hence increasing the liquid fraction, reduces the maximal deformation that a bubble can undergo before swapping neighbors. In the context of lamella division, it means that the bubbles have a larger probability to escape through one obstacle constriction instead of splitting.

In Figures 10 and 11, we provide examples of how the fragmentation efficiency depends on the foam quality and the mean velocity. In Figures 10a and 10b, we show two foams of similar initial average bubble size but

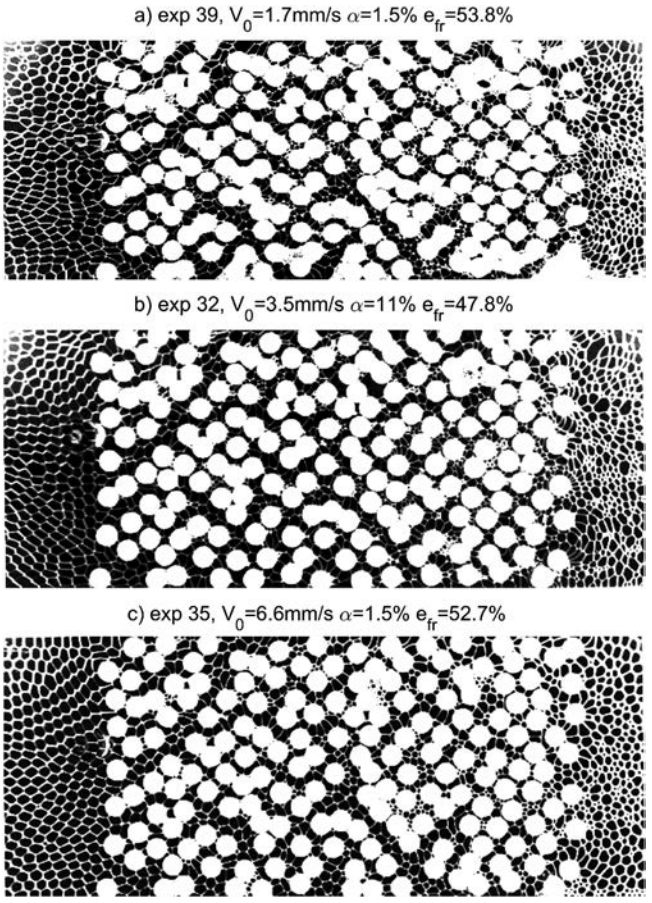

Figure 10. Effect of the initial foam quality and mean foam velocity on the bubble size selection. The corresponding experiments are (from top to bottom) experiments number 39, 32, and 35. A foam of (a) better quality (i.e., drier) is observed to be impacted differently than a foam of (b) lesser quality (i.e., wetter). The comparison of Figures 10a and 10c shows that the entrance velocity V_0 has little influence on the process.

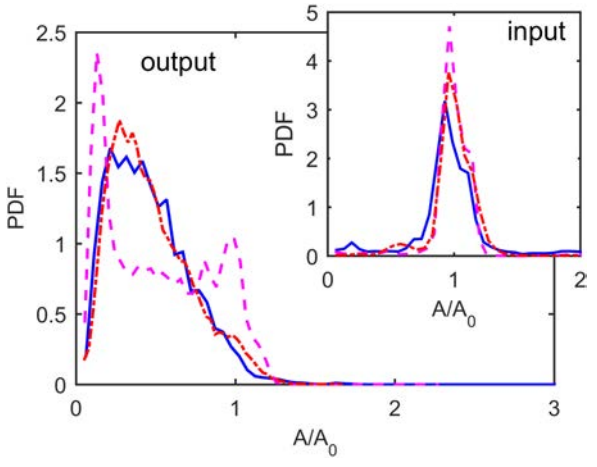

Figure 11. Size distributions recorded at the outlet of the porous medium for the same experiments as in Figure 10. Continuous blue line: same data as Figure 10a, magenta dashed line: same data as Figure 10b, and dashed-dotted red line: same data as Figure 10c. The inset shows the initial size distributions.

different qualities (flux ratio $\alpha = 1.5\%$ for (a) and $\alpha = 10.7\%$ for (b)). The foam of higher quality at the inlet (case (a)) exits the medium with a polydisperse bubble area distribution different from that of the lower-quality counterpart, as quantitatively shown in Figure 11. Figure 10c shows the same foam as the one of Figure 10a, but at a larger mean velocity ($V_0 = 1.71$ mm/s for (a) and $V_0 = 6.61$ mm/s for (c)). The polydispersity of the foam exiting the medium exhibits little dependence on the foam mean velocity. Those observations are consistent with the general behavior discussed in the previous paragraph.

3.4. Correlation Between Local Velocities and Bubble Sizes

Another important feature observed in our foam flows is the link between the bubbles' mobility and their size. Figure 12a shows a snapshot of experiment number 43, where different bubble areas can clearly be identified. The corresponding map of bubble sizes is shown in Figure 12b, and the corresponding normalized velocity field, integrated over 100 s, in Figure 12c. Visual comparison between the two suggests that larger bubbles follow paths of faster flow while smaller bubbles exhibit a smaller mobility, and can in particular be trapped in-between tightly set groups of three or four grains.

In order to investigate the correlations between bubble sizes and velocities quantitatively, we compare the velocity PDF for bubbles with areas larger than the average bubble area $\langle A \rangle$ (red crosses in Figure 13) to those for bubbles with areas smaller than $\langle A \rangle$ (blue solid circles in Figure 13). The velocity PDF for bubbles smaller than the average has more weight on low velocities than that for bubbles larger than the average. The velocity at which the population of larger bubbles starts dominating over that of smaller bubbles is 1.8 V_0, very close to the expected interstitial velocity V_0/ϕ. This analysis shows that small bubbles may

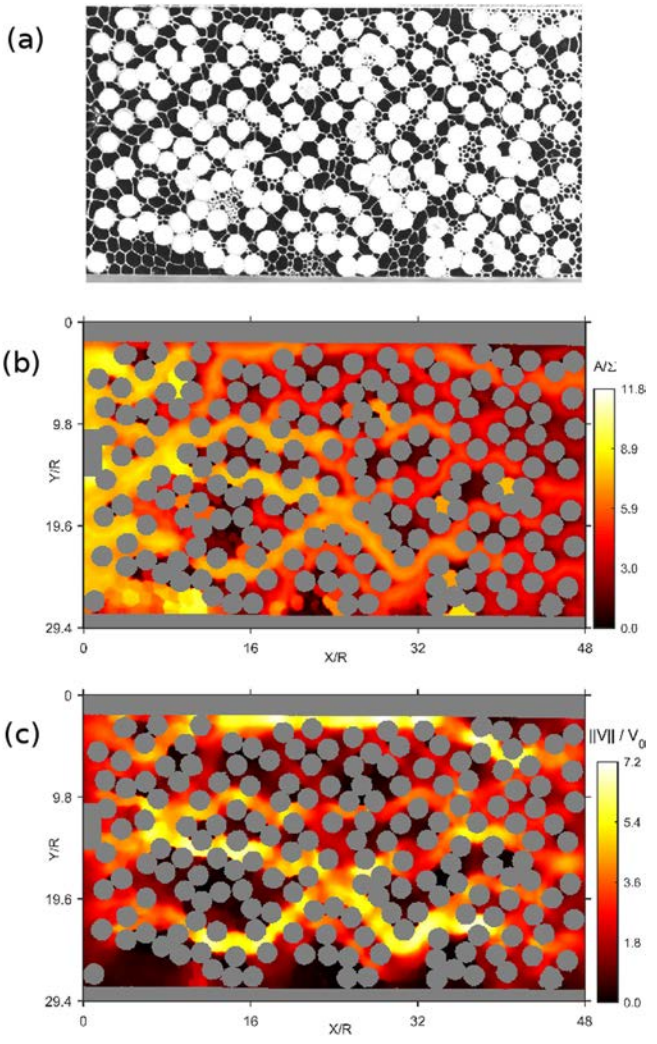

Figure 12. (a) Snapshot of experiment 43 ($A_0/\Sigma = 6.22$, $\alpha = 10.7\%$, $V_0 = 6.33$ mm/s). (b) Maps of normalized bubble sizes for the same experiment. (c) Maps of normalized bubble velocities.

flow faster than the mean flow velocity V_0/ϕ, but most of them flow slower, while the biggest bubbles show the opposite behavior.

A more systematic study of the correlation between bubble sizes and velocities as a function of the various experimental control parameters is based on the cross-correlation coefficient $C_{AV,}$ whose definition is given in Appendix B. In Figure 14, we show how the cross-correlation coefficient depends on the foam's polydispersity, (i.e., the relative width of the bubble area distribution, see Appendix B), for experiments with various flux ratios α indicated by the size of the symbols and fragmentation rates e_{fr} indicated by the color of the symbols. The positive value of $C_{AV,}$ observed for the entire data, evidences that the largest bubbles move, on average, faster than the mean flow. This effect is more pronounced at high size polydispersity, or, equivalently, high fragmentation efficiency. Figure 14 also evidences that the correlation between bubble sizes and velocities is all the larger as the foam is drier. Note that in our experiment, the liquid fraction and the size polydispersity (or, equivalently, the fragmentation efficiency) are correlated variables. This was shown in Figure 9 and is also apparent in Figure 14 where larger symbols have a darker color. Drier foams get more fragmented and reach a higher level of polydispersity, whereas the more monodisperse foams are the wetter ones. Thus, strictly speaking, we do not know whether the enhanced correlation between bubble size and velocity observed at large polydispersity in Figure 14 is due to the polydispersity in itself, or whether it is a consequence of the smaller liquid fraction.

Overall, this study demonstrates that larger bubbles are more likely to flow faster than smaller ones, but that this effect is only significant for sufficiently dry foams.

4. Summary and Conclusion

We have studied the flow of a preexisting two-dimensional foam inside a porous medium consisting of cylindrical solid grains, under conditions of discontinuous gas flow in the entire medium. Our experimental setup allows a direct visualization and quantitative analysis of phenomena previously reported for foam flow in porous media: preferential flow paths, flow intermittency, bubble trapping. Preferential flow paths were analyzed from the measurement of the full bubble velocity field. A significant portion of the bubble population was found to flow at velocities up to 4 times the mean interstitial velocity. Flow intermittency was shown to consist in a time evolution of the preferential flow paths' geometry, some of these paths being permanent and others being either active or inactive, depending on the time at which they are being observed. Furthermore, the distribution

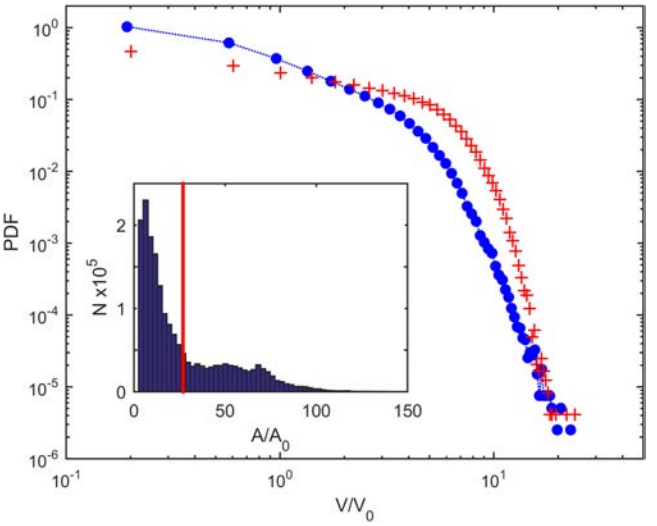

Figure 13. Probability distribution function (PDF) of the velocity field for bubbles of area in the ranges $0 \leq A \leq \langle A \rangle$ (blue solid circles) and $A > \langle A \rangle$ (red crosses), where $\langle A \rangle$ is the average normalized bubble size computed on the area map of Figure 12. The inset shows a histogram of the bubble areas, with $\langle A \rangle / A_0$ indicated by a vertical red line.

of bubble sizes was observed to evolve monotonically between the system inlet and its outlet, from the inlet symmetrical quasi-monodisperse probability density function (PDF) to a PDF with an skewed peak of most probable bubble size about 4 times smaller than the mean bubble size at the inlet. This systematic evolution toward smaller bubble sizes is consistent with the dominant bubble size evolution mechanism, namely bubble fragmentation by lamella division. A spatial correlation between bubble sizes and velocities was evidenced. The efficiency of the bubble fragmentation, as well as the correlation between bubble sizes and velocities, were measured as a function of various control parameters: the mean bubble size at the inlet, the foam quality, the mean flow velocity, and the type of surfactant used in the formulation of the foaming solution. The fragmentation efficiency depends mostly on the initial mean bubble size and foam quality; larger qualities and larger velocities enhance the foam polydispersity.

The correlation between bubble sizes and velocities has an important consequence in terms of foam rheology, which has been overlooked until now: in the relationship between the mean interstitial velocity and the pressure drop (equation (2)), the parameter β is proportional to the number of foam bubbles per unit volume [*Kovscek and Bertin*, 2003b], that is, for a 2-D foam, inversely proportional to the mean bubble area, so the prefactor in that equation is proportional to the mean bubble area. Since the mean bubble area in the channels of preferential flow is significantly larger than the global mean bubble area, the prefactor in equation (2) actually contains an implicit increasing dependence on the mean interstitial velocity v. Overall this weakens the dependence of v on the pressure drop and decreases the deviation of the foam's effective rheology from that of a Newtonian fluid. This behavior is expected to also be observed for 3-D foams flowing in subsurface porous media, and this all the more for media that are very heterogeneous and multiscale, and exhibiting preferential flows. The remediation of soils is among the applications in which this rheological property is expected to play a significant role. More generally, this study opens the way to quantitative characterization of the relationship between medium geometry and foam flow phenomenology. One possible application of this finding would be in large-scale models of subsurface foam flows: it could be beneficial to develop models that not only consider the dependence on the local velocity of the effective viscosity of the foam, but also explicitly account for the spatial distribution of bubble sizes

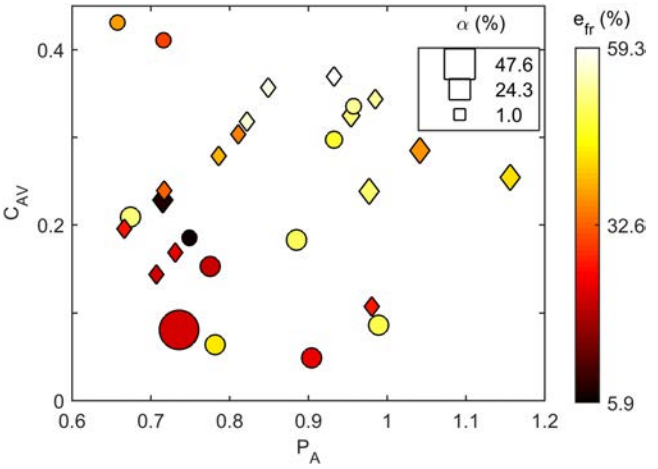

Figure 14. Evolution of the cross-correlation coefficient C_{AV} with the mean polydispersity P_A of the porous medium. Each experiment is represented by a symbol whose color indicates the value of e_{fr} and whose size indicates the flux ratio α. Two types of symbols are plotted: circles for experiments performed with solution 1, and diamonds for experiments performed with solution 2. The black squares indicate symbol areas corresponding to flux ratio values $\alpha = 1.0\%$, 24.3%, and 47.6%.

and the coupling between the local permeability of the medium and the effective viscosity of the foam (through the coupling of the permeability and the bubble size).

Remember though that in our system, mechanisms of bubble disappearance are quasi-inexistant: over the investigated time scale, foam coarsening by gas diffusion is negligible, while the ratio of the average pore size to the average pore neck size is not large enough to allow capillary suction to cause lamella rupture. Hence the bubble size distribution does not evolve toward a stationary state where mechanisms of lamella creation and destruction would balance each other. Future works will tackle the size selection mechanism in medium geometries with much more marked constrictions between pores, as well as in media with a different dimensionality, such as porous media columns commonly used by soil physicists and three-dimensional sand tanks. Another prospect is the modeling of the fragmentation process and its confrontation to the PDFs measured experimentally in the present study.

Appendix A: Pore Map Determination

The pore map of Figure 4 (bottom) is obtained in the following manner. A Delaunay triangulation is performed on the image that defines the grain (see red segments in Figure 2b). Then a number of these segments are removed selectively, and the pores are defined as the resulting continuous black areas. The segments removed are those which are significantly longer than their nearest neighbors: each segment $\mathcal{S}$ is selected for removal, or not, from a comparison of its length with respect to that of the four other segments constituting the two triangles that share the segment $\mathcal{S}$. More precisely, we compute the ratio of the length of $\mathcal{S}$ to the average length of the two shortest such segments. Performing this measurement on all segments, plotting the PDF of these "length ratios" provides a distribution with two weakly separated peaks, indicating two populations of segments. The segments belonging to the right peak (i.e., with the larger length ratios) were removed.

Appendix B: Definition of the Cross Correlation Between Bubble Sizes and Velocities

The cross-correlation coefficient between bubble sizes and velocities, $C_{AV,}$ is computed as follows. From the average area and velocity maps, we compute the average bubble size $\langle A\rangle$ and the standard deviation σ_A of bubble area values about $\langle A\rangle$, as well as the corresponding quantities for velocities, $\langle V\rangle$ and σ_V, respectively. The cross correlation is then given by:

$$C_{AV}=\frac{\langle \tilde{A}\tilde{V}\rangle}{\sigma_A\sigma_V}\,, \tag{B1}$$

with $\tilde{A}=A-\langle A\rangle$ and $\tilde{V}=V-\langle V\rangle$. We also define a measure of the polydispersity of the foam flowing inside the porous medium, by the ratio $P_A=\sigma_A/\langle A\rangle$. Note that we only process the data from the bubbles positioned inside the porous medium.

The coefficient C_{AV} is normalized to be on the order of unity. In Figure 14, its measured values are all positive, and around $C_{AV}=0.24\pm0.11$. This value indicates a rather weak correlation, which can be understood by looking at Figure 12, in which the average bubble size clearly decays throughout the channel; at the end of the channel, the size of the fastest bubbles corresponds to the size of the slowest ones at the entrance. The cross-correlation coefficient is then low since it is computed over all bubbles in the channels, not taking into account the decrease of the average bubble size along the length of the porous medium.

Acknowledgments
The authors acknowledge financial support from Région Bretagne (CREATE MOUSPORE). Y.M. is grateful to H. Bertin and L. Zhong for enlightening discussions. B.G. and B.D. thank Claire Bocher for experimental help. The authors commit to making their data available to any reader who requires it, once all results to be obtained from the data have been published.

References

Alvarez, J., H. Rivas, and W. Rossen (2001), Unified model for steady-state foam behavior at high and low foam qualities, *SPE J.*, *6*(03), 325–333.
Apaydin, O. G., and A. R. Kovscek (2001), Surfactant concentration and end effects on foam flows in porous media, *Transp. Porous Media*, *43*(3), 511–536.
Aronson, A., V. Bergeron, M. E. Fagan, and C. Radke (1994), The influence of disjoining pressure on foam stability and flow in porous media, *Colloids Surf. A*, *83*(2), 109–120.
Bretherton, F. (1961), The motion of long bubbles in tubes, *J. Fluid Mech.*, *10*(02), 166–188.
Cantat, I., N. Kern, and R. Delannay (2004), Dissipation in foam flowing through narrow channels, *Europhys. Lett.*, *65*(5), 726–732.
Cantat, I., S. Cohen-Addad, F. Elias, F. Graner, R. Hœhler, O. Pitois, F. Rouyer, and A. Saint-Jalmes (2013), *Foams. Structure and Dynamics*, translated by Ruth Flatman, Oxford Univ. Press, Oxford, U. K.
Chen, M., Y. Yortsos, and W. Rossen (2005), Insights on foam generation in porous media from pore-network studies, *Colloids Surf. A*, *256*(2), 181–189.

Chowdiah, P., B. R. Misra, J. J. Kilbane, V. J. Srivastava, and T. D. Hayes (1998), Foam propagation through soils for enhanced in situ remediation, *J. Hazard. Mater.*, *62*, 265–280.
Cohen, D., T. Patzek, and C. Radke (1997), Onset of mobilization and the fraction of trapped foam in porous media, *Transp. Porous Media*, *28*(3), 253–284.
Cox, S. (2015), Simulations of bubble division in the flow of a foam past an obstacle in a narrow channel, *Colloids Surf. A*, *473*, 104–108.
Cox, S. J., S. Neethling, W. R. Rossen, W. Schleifenbaum, P. Schmidt-Wellenburg, and J. J. Cilliers (2004), A theory of the effective yield stress of foam in porous media: The motion of soap film traversing a three-dimensional pore, *Colloid. Surf. A*, *245*(1–3), 143–151.
Denkov, N. D., V. Subramanian, D. Gurovich, and A. Lips (2005), Wall slip and viscous dissipation in sheared foams: Effect of surface mobility, *Colloids Surf. A*, *263*(1), 129–145.
Dholkawala, Z. F., H. Sarma, and S. Kam (2007), Application of fractional flow theory to foams in porous media, *J. Pet. Sci. Eng.*, *57*(1), 152–165.
Dollet, B., and C. Raufaste (2014), Rheology of aqueous foams, *C. R. Phys.*, *15*(8), 731–747.
Dollet, B., S. A. Jones, Y. Méheust, and I. Cantat (2014), Influence of the elastic deformation of a foam on its mobility in a model porous medium, *Phys. Rev. E*, *90*, 023006.
Drenckhan, W., S. Cox, G. Delaney, H. Holste, D. Weaire, and N. Kern (2005), Rheology of ordered foams—On the way to discrete microfluidics, *Colloids Surf. A*, *263*(1), 52–64.
Du, D.-X., A. N. Beni, R. Farajzadeh, and P. L. Zitha (2008), Effect of water solubility on carbon dioxide foam flow in porous media: An x-ray computed tomography study, *Ind. Eng. Chem. Res.*, *47*(16), 6298–6306.
Falls, A., J. Musters, and J. Ratulowski (1989), The apparent viscosity of foams in homogeneous bead packs, *SPE Reservoir Eng.*, *4*(02), 155–164.
Fergui, O., H. Bertin, and M. Quintard (1998), Transient aqueous foam flow in porous media: Experiments and modeling, *J. Pet. Sci. Eng.*, *20*(1), 9–29.
Ferguson, D., and S. Cox (2013), The motion of a foam lamella traversing an idealised bi-conical pore with a rounded central region, *Colloids Surf. A*, *438*, 56–62.
Friedmann, F., W. Chen, and P. Gauglitz (1991), Experimental and simulation study of high-temperature foam displacement in porous media, *SPE Reservoir Eng.*, *6*(01), 37–45.
Gauglitz, P., and C. Radke (1990), The dynamics of liquid film breakup in constricted cylindrical capillaries, *J. Colloid Interface Sci.*, *134*(1), 14–40.
Heller, J. P., and M. S. Kuntamukkula (1987), Critical review of the foam rheology literature, *Ind. Eng. Chem. Res.*, *26*(2), 318–325.
Hirasaki, G., and J. B. Lawson (1985), Mechanisms of foam flow in porous media: Apparent viscosity in smooth capillaries, *SPEJ Soc. Pet. Eng. J.*, *25*(02), 176–190.
Hirasaki, G., et al. (1997), Field demonstration of the surfactant/foam process for aquifer remediation, in *SPE Annual Technical Conference and Exhibition paper SPE 39292 presented at SPE Annual Technical Conference 698 and Exhibition*, Soc. of Pet. Eng., San Antonio, Tex.
Huang, C.-W., and C.-H. Chang (2000), A laboratory study on foam-enhanced surfactant solution flooding in removing n-pentadecane from contaminated columns, *Colloids Surf. A*, *173*(1), 171–179.
Huang, D. D., A. Nikolov, and D. T. Wasan (1986), Foams: Basic properties with application to porous media, *Langmuir*, *2*(5), 672–677.
Jenkins, K. B., D. L. Michelsen, and J. T. Novak (1993), Application of oxygen microbubbles for in situ biodegradation of p-xylene-contaminated groundwater in a soil column, *Biotechnol. Prog.*, *9*(4), 394–400.
Jeong, S.-W., and M. Y. Corapcioglu (2003), A micromodel analysis of factors influencing napl removal by surfactant foam flooding, *J. Contam. Hydrol.*, *60*(1), 77–96.
Jeong, S.-W., and M. Y. Corapcioglu (2005), Force analysis and visualization of napl removal during surfactant-related floods in a porous medium, *J. Hazard. Mater.*, *126*(1), 8–13.
Jeong, S.-W., M. Y. Corapcioglu, and S. E. Roosevelt (2000), Micromodel study of surfactant foam remediation of residual trichloroethylene, *Environ. Sci. Technol.*, *34*(16), 3456–3461.
Jones, S. A., B. Dollet, Y. Méheust, S. J. Cox, and I. Cantat (2013), Structure-dependent mobility of a dry aqueous foam flowing along two parallel channels, *Phys. Fluids*, *25*, 063101.
Kam, S., and W. Rossen (2003), A model for foam generation in homogeneous media, *SPE J.*, *8*(04), 417–425.
Khatib, Z., G. Hirasaki, and A. Falls (1988), Effects of capillary pressure on coalescence and phase mobilities in foams flowing through porous media, *SPE Reservoir Eng.*, *3*(03), 919–926.
Kornev, K. G., A. V. Neimark, and A. N. Rozhkov (1999), Foam in porous media: Thermodynamic and hydrodynamic peculiarities, *Adv. Colloid Interface Sci.*, *82*(1), 127–187.
Kovscek, A., T. Patzek, and C. Radke (1995), A mechanistic population balance model for transient and steady-state foam flow in boise sandstone, *Chem. Eng. Sci.*, *50*(23), 3783–3799.
Kovscek, A., G.-Q. Tang, and C. Radke (2007), Verification of roof snap off as a foam-generation mechanism in porous media at steady state, *Colloids Surf. A*, *302*(1), 251–260.
Kovscek, A. R., and H. J. Bertin (2003a), Foam mobility in heterogeneous porous media (II: Experimental observations), *Transp. Porous Media*, *52*, 37–49.
Kovscek, A. R., and H. J. Bertin (2003b), Foam mobility in heterogeneous porous media (I: Scaling concepts), *Transp. Porous Media*, *52*, 17–35.
Kovscek, A. R., and C. J. Radke (1994), Fundamentals of foam transport in porous media, in *Foams: Fundamentals and Applications in the Petroleum Industry*, edited by L. L. Schramm, chap. 3, pp. 115–163, ACS Publ., Washington, D. C.
Ma, K., R. Liontas, C. A. Conn, G. J. Hirasaki, and S. L. Biswal (2012), Visualization of improved sweep with foam in heterogeneous porous media using microfluidics, *Soft Matter*, *8*(41), 10,669–10,675.
Marmottant, P., and J.-P. Raven (2009), Microfluidics with foams, *Soft Matter*, *5*(18), 3385–3388.
Nguyen, Q. P., P. K. Currie, M. Buijse, and P. L. Zitha (2007), Mapping of foam mobility in porous media, *J. Pet. Sci. Eng.*, *58*(1), 119–132.
Pang, Z.-X. (2010), The blocking ability and flowing characteristics of steady foams in porous media, *Transp. Porous Media*, *85*(1), 299–316.
Patzek, T. W. (1996), Field applications of steam foam for mobility improvement and profile control, *SPE Reservoir Eng.*, *11*(02), 79–86.
Raufaste, C., A. Foulon, and B. Dollet (2009), Dissipation in quasi-two-dimensional flowing foams, *Phys. Fluids*, *21*, 053102.
Raven, J.-P., and P. Marmottant (2009), Microfluidic crystals: Dynamic interplay between rearrangement waves and flow, *Phys. Rev. Lett.*, *102*(8), 084501.
Roof, J. (1970), Snap-off of oil droplets in water-wet pores, *Soc. Pet. Eng. J.*, *10*(01), 85–90.
Rossen, W. R. (1990), Theory of mobilization pressure gradient of flowing foams in porous media: III. *Asymmetric lamella shapes, J. Colloid Interface Sci.*, *136*(1), 38–53.
Rothmel, R. K., R. W. Peters, E. St. Martin, and M. F. DeFlaun (1998), Surfactant foam/bioaugmentation technology for in situ treatment of tce-dnapls, *Environ. Sci. Technol.*, *32*(11), 1667–1675.

Roy, D., S. Kongara, and K. Valsaraj (1995a), Application of surfactant solutions and colloidal gas aphron suspensions in flushing naphthalene from a contaminated soil matrix, *J. Hazard. Mater.*, *42*(3), 247–263.

Roy, D., R. R. Kommalapati, K. T. Valsaraj, and W. D. Constant (1995b), Soil flushing of residual transmission fluid: Application of colloidal gas aphron suspensions and conventional surfactant solutions, *Water Res.*, *29*(2), 589–595.

Shen, X., L. Zhao, Y. Ding, B. Liu, H. Zeng, L. Zhong, and X. Li (2011), Foam, a promising vehicle to deliver nanoparticles for vadose zone remediation, *J. Hazard. Mater.*, *186*, 1773–1780.

Simjoo, M., Q. Nguyen, and P. Zitha (2012), Rheological transition during foam flow in porous media, *Ind. Eng. Chem. Res.*, *51*(30), 10,225–10,231.

Simjoo, M., Y. Dong, A. Andrianov, M. Talanana, and P. Zitha (2013), Ct scan study of immiscible foam flow in porous media for enhancing oil recovery, *Ind. Eng. Chem. Res.*, *52*(18), 6221–6233.

Stevenson, P. (2012), *Foam Engineering: Fundamentals and Applications*, John Wiley, Hoboken, N. J.

Szafranski, R., J. Lawson, G. Hirasaki, C. Miller, N. Akiya, S. King, R. Jackson, H. Meinardus, and J. Londergan (1998), Surfactant/foam process for improved efficiency of aquifer remediation, *Prog. Colloid Polymer Sci.*, *111*, 162–167.

Terriac, E., J. Etrillard, and I. Cantat (2006), Viscous force exerted on a foam at a solid boundary: Influence of the liquid fraction and of the bubble size, *Europhys. Lett.*, *74*(5), 909–915.

Wan, J., J. L. Wilson, and T. L. Kieft (1994), Influence of the gas-water interface on transport of microorganisms through unsaturated porous media, *Appl. Environ. Microbiol.*, *60*(2), 509–516.

Wang, S., and C. N. Mulligan (2004), An evaluation of surfactant foam technology in remediation of contaminated soil, *Chemosphere*, *57*(9), 1079–1089.

Weaire, D. (2008), The rheology of foam, *Curr. Opin. Colloid Interface Sci.*, *13*(3), 171–176.

Weaire, D., and S. Hutzler (1999), *The Physics of Foams*, Oxford Univ. Press., Oxford, U. K.

Wong, H., C. J. Radke, and S. Morris (1995), The motion of long bubbles in polygonal capillaries. Part 2. Drag, fluid pressure and fluid flow, *J. Fluid Mech.*, *292*, 95–110.

Zhdanov, S. A., A. Amiyan, L. M. Surguchev, L. M. Castanier, and J. E. Hanssen (1996), Application of foam for gas and water shut-off: Review of field experience, paper SPE 36914-MS presented at European Petroleum Conference, Soc. of Pet. Eng., Milan, Italy.

Zhong, L., N. P. Qafoku, J. E. Szecsody, P. E. Dresel, and Z. F. Zhang (2009), Foam delivery of calcium polysulfide to the vadose zone for chromium (vi) immobilization: A laboratory evaluation, *Vadose Zone J.*, *8*(4), 976–985.

Zhong, L., J. Szecsody, F. Zhang, and S. M. Mattigod (2010), Foam delivery of amendments for vadose zone remediation: Propagation performance in unsaturated sediments, *Vadose Zone J.*, *9*, 757–767.

Zhong, L., J. Szecsody, M. Oostrom, M. Truex, X. Shen, and X. Li (2011), Enhanced remedial amendment delivery to subsurface using shear thinning fluid and aqueous foam, *J. Hazard. Mater.*, *191*, 249–257.

Zitha, P., Q. Nguyen, P. Currie, and M. Buijse (2006), Coupling of foam drainage and viscous fingering in porous media revealed by x-ray computed tomography, *Transp. Porous Media*, *64*, 301–313.